eman ta zabal zazu

Universidad del País Vasco
Euskal Herriko Unibertsitatea

Towards a 3D hydrodynamic characterization from the joint analysis and blending of multiplatform observations for potential marine applications in the southeastern Bay of Biscay

Ivan Manso Narvarte

PhD Thesis 2021

Towards a 3D hydrodynamic characterization from the joint analysis and blending of multiplatform observations for potential marine applications in the southeastern Bay of Biscay

Presented by

Ivan Manso Narvarte

A thesis submitted to the University of the Basque Country for the degree of

DOCTOR OF PHILOSOPHY

Thesis Directors

Dr. Ainhoa Caballero Reyes (AZTI)

Dr. Anna Rubio Compañy (AZTI)

Department

Zoology and Animal Cell Biology

Doctoral programme

Marine Environment and Resources

University of the Basque Country

2021

eman ta zabal zazu

Universidad del País Vasco
Euskal Herriko Unibertsitatea

AZTI
MEMBER OF BASQUE RESEARCH & TECHNOLOGY ALLIANCE

The research carried out in this Dr. Philos thesis has been developed in AZTI (Pasaia, Spain). Ivan Manso-Narvarte was funded by a Doctoral Fellowship from the Department of Environment, Regional Planning, Agriculture and Fisheries of the Basque Government.

This Dr. Philos thesis, presented under the international mention from University of the Basque Country, was assessed by two scientific experts from non-Spanish research institutions:

- Dr. Annalisa Griffa, from the Institute of Marine Sciences, National Research Council of Italy (La Spezia, Italy).
- Dr. Enrico Zambianchi, from the Università degli Studi di Napoli Parthenope (Napoli, Italy).

Recommended citation: Manso-Narvarte, I., 2021. *Towards a 3D hydrodynamic characterization from the joint analysis and blending of multiplatform observations for potential marine applications in the southeastern Bay of Biscay*. PhD Thesis. Department of Zoology and Animal Cell Biology, University of the Basque Country, 277pp.

Neure familiarentzat

CONTENTS

AGRADECIMIENTOS – ACKNOWLEDGEMENTS VII

LIST OF ACRONYMS IX

LIST OF FIGURES XIII

LIST OF TABLES XXI

LABURPENA XXIII

RESUMEN XXIX

SUMMARY XXXV

CHAPTER 1: Introduction 1

1 Background 3
  1.1 Coastal observing systems 3
  1.2 Multisource data combination and data expansion 5
  1.3 Study area and motivation of the thesis 6

2 Introduction to the study area 7
  2.1 The Bay of Biscay 7
  2.2 The southeastern Bay of Biscay and the EusKOOS observatory 10
    2.2.1 Physical characteristics 10
    2.2.2 Biological, geochemical and environmental aspects related to hydrodynamics 12
    2.2.3 EuskOOS: the Basque coastal operational oceanography system 13

3 Hypothesis, aim and objectives 15
  3.1 Working hypothesis 15
  3.2 Aim and objectives 16

4 Structure of the thesis 16

CHAPTER 2: Data and Methods 17

1 Data 19
  1.1 EuskOOS coastal observing system 20
    1.1.1 The HFR system 20

1.1.2 Moorings 24
1.2 Complementary data in the area covered by EuskOOS 27
1.2.1. Gliders 27
1.2.2 Satellites 28
1.2.3 Drifters 31
1.2.4 The Bilbao-Vizcaya mooring 32
1.2.5 Research vessels 32
1.2.6 Oceanic and atmospheric models 34
1.3 Summary of the data used in each chapter 36
2. Methods 38
2.1 Geostrophic and wind-driven currents estimations 38
2.1.1 Across-track geostrophic currents from hydrographic glider data 39
2.1.2 Across-track surface geostrophic currents from altimeter data 41
2.1.3 Wind-driven currents from wind data 42
2.2 Data-reconstruction methods 44
2.2.1 The DCT–PLS method 44
2.2.2 The ROOI method 46
2.3 Lagrangian model 48
2.4 Summary of the methods used in each chapter 49
CHAPTER 3: Joint analysis of coastal altimetry and high-frequency radar data: observability of seasonal and mesoscale ocean dynamics in the Bay of Biscay 51
1 Introduction 53
2 Data and Methods 55
2.1 Data 55
2.1.1 HFR data 55
2.1.2 Altimetry data 56
2.1.3 Wind data and sea surface temperature images 57
2.2 Methods 58
2.2.1 Pointwise comparison 59
2.2.2 Along-track current comparison 61

2.2.3 Ekman currents ... 61

3 Results and Discussion ... 62

3.1 Statistical results ... 62

3.1.1 Pointwise comparison ... 63

3.1.2 Along-track current comparison ... 67

3.2 Observability of mesoscale processes in HFR and altimetry datasets ... 69

3.2.1 Observability of the IPC ... 70

3.2.2 Observability of mesoscale eddies ... 73

4 Summary and Conclusions ... 74

CHAPTER 4: The seasonal intensification of the slope Iberian Poleward Current ... 77

1 Introduction ... 79

2 Data and Methods ... 81

2.1 Data ... 81

2.1.1 HFR data ... 81

2.1.2 Mooring data ... 81

2.2 Method ... 82

3 Results and Discussion ... 82

CHAPTER 5: 3D reconstruction of ocean velocity from high-frequency radar and acoustic Doppler current profiler: a model-based assessment study ... 87

1 Introduction ... 91

2 Data and Methods ... 93

2.1 Assessment approach ... 93

2.2 Data-reconstruction methods ... 95

2.2.1 The ROOI method ... 95

2.2.2 The DCT-PLS method ... 96

2.3 Numerical simulations ... 97

2.4 Skill assessment ... 98

3 Describing the spatiotemporal variability in the study area ... 100

4 Results and Discussion ... 103

4.1 Data reconstruction ... 103

4.2 Sensitivity test: increased number of ADCPs 109

5 Summary and Conclusions 110

CHAPTER 6: 3D characterization of a coastal mode-water eddy from multiplatform observations and a data-reconstruction method 113

1 Introduction 115

2 Data and Methods 117

2.1 Multiplatform and multivariable data approach 117

2.1.1 Temperature, salinity, pressure and chlorophyll-a from glider profiles 118

2.1.2 Surface currents from HFR 118

2.1.3 Vertical profiles of potential density anomaly and currents from a moored buoy ... 119

2.1.4 Chl-a images and wind data 120

2.1.5 Numerical simulations 120

2.2 Method for the 3D reconstruction of the observed fields 120

2.2.1 The ROOI method 120

2.2.2 Implementation of the ROOI method 122

3 Results 125

3.1 Observed 3D properties of the eddy 125

3.2 Reconstruction of the 3D eddy current velocity fields 128

3.2.1 Skill of the reconstruction 128

3.2.2 Reconstructed 3D eddy current velocity fields and associated transports 128

4 Discussion 132

5 Conclusions 136

CHAPTER 7: Anchovy eggs and larvae advection in the southeastern Bay of Biscay 139

1 Introduction 141

2 Data 143

2.1 HFR and ADCP data 144

2.2 IBI data 145

2.3 Drifter data 145

2.4 BIOMAN data 146

3 Methods 146

3.1 Implementation of the ROOI method ... 147

3.2 The Lagrangian model ... 148

3.3 ROOI validation ... 148

3.4 Eggs and larvae advection simulations ... 152

4 Results ... 153

4.1 Simulations with ROOI ... 153

4.2 Simulations with HFRtot ... 157

4.3 Discussion ... 162

5 Conclusions ... 164

CHAPTER 8: Conclusions and Thesis ... 165

Conclusions ... 167

Thesis ... 169

REFERENCES ... 171

APPENDICES ... 191

CHAPTER 5 – APPENDIX A ... 193

Appendix A1: HFR and ADCP observations temporal cross-correlations ... 195

Appendix A2: RRMSD maps for ROOI with GLORYS-HR ... 197

Appendix A3: DCT-PLS RRMSD-U maps with higher colorbar values ... 199

Appendix A4: RMSD maps and spatial mean RMSD graphs ... 200

Appendix A5: Correlation between two variables ... 205

CHAPTER 6 – APPENDIX B ... 207

Appendix B1: Input variables ... 209

Appendix B2: Sensitivity tests ... 210

Appendix B3: ADCP data-gap filling ... 217

CHAPTER 7 – APPENDIX C ... 221

Appendix C1: ROOI parameter sensitivity test ... 223

Appendix C2: Sensitivity of Lagrangian simulations to the used forcing at different depths in the study area ... 225

CHAPTER 8 – APPENDIX D ... 229

Future Work ... 231

AGRADECIMIENTOS – ACKNOWLEDGEMENTS

Tras cuatro años de tesis puedo decir que ha sido un camino duro (con pandemia incluida) pero a la vez apasionante y estimulante en el que he aprendido muchísimo y que sin duda ha merecido la pena. Este camino me ha llevado a encontrarme con gente que además de la gente de toda la vida ha hecho que sea más fácil recorrerlo. Por ello, hay muchas personas a las que quisiera mostrar mi agradecimiento por toda la ayuda y el apoyo dados. Pido disculpas de antemano por si me olvido de alguien, ya sabéis que soy un poco despistado para estas cosas.

En primer lugar, quisiera mostrar mi más profundo agradecimiento a mis directoras de tesis Ainhoa y Anna por acogerme y guiarme durante estos años. Me habéis introducido al mundo de la oceanografía y he aprendido muchísimo de vosotras a muchos niveles. Vuestra actitud siempre positiva y vuestro entusiasmo han sido vitales para mí. ¡Gracias de todo corazón! Eskerrik asko bihotz-bihotzez!

A la gente de AZTI, gracias por vuestra amable ayuda tanto con dudas administrativas, como científico-técnicas, por pasarme datos o por lo que sea que necesitase. Eskerrik asko Julien, Unai, Lohitzune, Maria, Andrea, Alaitz, gente de TICs, y al resto de la gente que me ha echado un cable.

Mila esker ere nire unibertsitateko tutoreari, Ionan, paperekin eta tramiteekin emandako laguntzagatik. Thank you, Annalisa and Enrico, for your reviews of the thesis. Grazie!

I also would like to thank all the people who helped me in my stays and that have collaborated with me during these years. Merci Claire for hosting me in Toulouse and for the altimetry training in the first international collaboration of my life! Thank you also, Florence. Grazie mille all the people at CNR-ISMAR and also Lerici that made me feel at home. To Maristella and Annalisa for warmly hosting me and for all the help and guidance during my stay and also after. To the rest of the group: Lorenzo, Carlo, Giuseppe, Roberta, … and Laura who accommodated me at her house and helped me as if I was her nephew. Hope to see all you guys again at the Baracchetta or anywhere else! Thank you Erick for introducing and sharing your method with us. Gracias Biel por tenerme en Mallorca una semana y por enseñarme tanto en tan poco tiempo. Gracias también por tu ayuda y consejos en mis investigaciones. Merci Amandine and Matthias for hosting me in Bidart. Despite having to leave before expected due to the pandemic situation we kept working together and I kept learning a lot from you. Thank you also Jeff and Lucas for your collaboration in running the glider campaign and the subsequent investigation. It has been a pleasure to work with you. Finalmente, gracias Jano e Ismael por vuestra predisposición a ayudarme y por aconsejarme con las estimaciones Lagrangianas.

Becarios. Ese grupo que no sabría cómo definir. A medio camino entre cuadrilla y grupo de ayuda… o no lo sé… El caso es que ha sido un placer haberos conocido, haber entablado amistad y haber compartido alegrías, dudas, pintxos de tortilla, preocupaciones y planes todo junto o por separado. No voy a rememorar nada específico con cada persona o personas, que me dan las uvas… el día a día y las vivencias ahí están y os agradezco que seáis así de geniales. Mila esker! ¡Muchas gracias! Çok teşekkür ederim!

Lankidez gogoratu eta ez naiz kuadrilaz ahazten. 3 urte geneuzkanetik elkarrekin. Batzuk beranduago elkartu ere, baina beti familia bat bezala. Ezinezkoa da babesgabe sentitzea horrelako lagun talde batean. Bizitza osoa elkarrekin eman ondoren, zaila egiten zait tesi honetan pentsatzea zuengan pentsatu gabe. Beraz, horregatik eta infinito gauza gehiagorengatik: Mila esker! Aupa Kondarrak!

Desde un punto de vista ya más personal quisiera mostrar mi agradecimiento a mi familia. A los que se fueron y, por supuesto, a los que están, tanto allá por Valencia o Burgos o aquí al lado en Gros y Amara. En especial a mis padres. Aita eta ama, me lo habéis dado todo en la vida. Aunque a veces sea parco en palabras o un tanto inexpresivo, no sabría expresar cuánto os agradezco todo lo que hacéis y habéis hecho por mí, todo lo que me habéis enseñado y cuánto os admiro. A la amona porque me dejó marcado su arrojo y a la vez infinita bondad en la vida. Nere arreba Itsasori, elkarrekin bizitakoak eraman gaituelako gaur egun gauden lekura. Nahiz eta aspaldi bakoitzak bere bidea jarraitu, azken finean ez da harritzekoa askotan hain antzekoak izatea. Eta azkenik, Itxaso, eskerrik asko nigan sinesteagatik eta ni aguantatzeagatik nire momentu onenetan eta txarrenetan. Ezinbestekoa izan zara niretzat azken urteetan.

LIST OF ACRONYMS

Acronym	Definition
2D	Two-dimensional
3D	Three-dimensional
ADCP	Acoustic Doppler Current Profiler
ARGOS	Advanced Research and Global Observation Satellite
AUV	Autonomous Underwater Vehicles
AVHRR	Advanced Very High-Resolution Radiometer
BoB	Bay of Biscay
Chl-a	Chlorophyll-a concentration
CMEMS	Copernicus Marine Environment Monitoring Service ernicus Marine Environment Monitoring Service
CODAR	Coastal ocean dynamics applications radar
COSYNA	Coastal Observing System for Northern and Arctic Seas
CT	Conductivity Temperature
CTD	Conductivity Temperature Depth
CTOH	Center for Topographic studies of the Ocean and Hydrosphere
CUFES	Continuous Underway Fish Egg Sampler
DCT	Discrete Cosine Transform
DCTN	N-dimensional DCT
DCT-PLS	Discrete Cosine Transform Penalized Least Square
DINEOF	Data Interpolating Empirical Orthogonal Functions
DF	Direction Finding
DIVAnd	n-dimensional Data Interpolating Variational Analysis
DT	Dynamic Topography
EA	East Atlantic
EGO	Everyone's Gliding Observatories

ELS	Early Life Stages
ENACW	Eastern North Atlantic Central Water
EO	Earth Observation
EOF	Empirical Orthogonal Function
EPS-SG	EUMETSAT Polar System-Second Generation
EuskOOS	Basque coastal operational oceanography system
FML	Floating Marine Litter
GCV	General Cross-Validation
GDOP	Geometric Dilution Of Precision
GPS	Global Positioning System
HF	High-Frequency
HFR	High-Frequency Radar
HZG	Helmholtz–Zentrum Geesthacht
IBI	Ireland-Biscay-Iberia
IDCTN	Inverse DCTN
IPC	Iberian Poleward Current
IR	Infrared
IST	Instituto Superior Técnico
LF	Low-Frequency
MARETEC	Marine and Environmental Technology Research Center
MOHID	MOdelo HIDdrodinamico
MREA	Marine Rapid Environmental Assessment
MUSIC	MUltiple SIgnal Classification
MW	Mediterranean Waters
NAC	North Atlantic Current
NADW	North Atlantic Deep Waters
NAO	North Atlantic Oscillation
NEMO	Nucleus for European Modelling of the Ocean

NEODAAS	NERC Earth Observation Data Acquisition and Analysis Service
NRT	Near real time
OI	Optimal Interpolation
OLCI	Ocean and Land Colour Instrument
OMA	Open-boundary Modal Analysis
OSE	Observing System Experiments
OSSE	Observing System Simulation Experiments
PMW	Passive MicroWave
RDI	RD Instruments
RI	Research Infrastructure
rms	root-mean-square
RMSD	Root Mean Square difference
ROOI	Reduced Order Optimal Interpolation
RRMSD	Relative Root Mean Square Difference
RSS	Residual Sum of Squares
SD	Standard Deviation
SE-BoB	Southeastern Bay of Biscay
SHOM	Service Hydrographique et Océanographique de la Marine
SLA	Sea Level Anomaly
SOCIB	Sistema d’Observació i predicció Costaner de les Illes Balears
SOM	Self-Organizing Maps
SSH	Sea Surface Height
SST	Sea Surface Temperature
SWODDIES	Slope Water Oceanic eDDIES
TS	Temperature Salinity
UTC	Universal Time Coordinated
VA	Variational Analysis
WRF	Weather Research and Forecasting

LIST OF FIGURES

Figure	Caption	Page
1.1	(a) Some observing platforms of the RAIA observatory (from Bastos et al., 2016). (b) Scheme of the COSYNA observatory (from Baschek et al., 2017). (c) Scheme of some observing platforms that composed the SOCIB system in 2013 (from Tintoré et al., 2013).	4
1.2	Location of the Bay of Biscay (blue square) and the SE-BoB (study area; red square). Figure adapted from Google Earth.	6
1.3	Main characteristics of the mean circulation and hydrodynamic processes in the BoB (adapted from Ferrer et al., 2009). The red dotted lines depict the study area.	9
1.4	Distribution of the different observing platforms within EuskOOS. The colorbar depicts the bathymetry in meters	14
1.5	Observing platforms of EuskOOS. (a) Pasaia costal station. (b) Donostia mooring. (c) Matxitxako HFR antenna. (d) Coastal videometry. (e) Pasaia high-frequency tidal gauge.	15
2.1	Map of several components of the EuskOOS observing system. The HFR sites are depicted by red points, whereas the moorings are shown by blue diamonds. The grey dots show the grid points where the HFR system provides surface current fields. The grey lines depict the 200, 1000 and 2000 m isobaths.	20
2.2	(a) Higer receiver antennas, (b) Higer transmitter antenna and (c) Matxitxako transmitter antenna (upper antenna) and receiver antennas (bottom antenna).	21
2.3	Example of a real spectra where the red, green and blue colours correspond to each of the receiver antennas (courtesy of Qualitas Remos).	22
2.4	(a) Example of radial current vectors for Higer (red) and Matxitxako (blue) stations. (b) Scheme of the radial current vectors decomposed in zonal and meridional directions inside a circle of 10 km of radius centered at one grid point. (c) Example of a final current velocity field. (d) Example of the corresponding gap-filled OMA current velocity field.	24
2.5	(a) Donostia mooring. (b) Scheme of the mooring (by C. Hernandez).	25
2.6	A Seabird SBE37IM CT as the ones installed on EuskOOS slope moorings (from https://www.seabird.com).	26
2.7	An RDI Workhorse ADCP as the ones installed on EuskOOS slope moorings.	27
2.8	(a) Deployment of the glider. (b) Trajectories of the gliders.	28

2.9 Scheme of the altimetry principle and the reference surfaces (from https://www.aviso.altimetry.fr/en/techniques/altimetry/principle/basic-principle.html). 30

2.10 Jason-2 satellite's 248 and 213 tracks over EuskOOS observatory. 31

2.11 Scheme of a drifter similar to the ones used in this thesis (from https://www.aoml.noaa.gov/es/global-drifter-program/). 32

2.12 Distribution of egg abundance measurement stations with PairoVET in BIOMAN 33

2.13 (a) a PairoVET net. (b) Scheme of the CUFES system (from https://calcofi.org/field-work/underway-observations/cufes-fish-egg-survey.html). 34

2.14 Map of the model data points. The blue dots are points of IBI_ANALYSISFORECAST_PHY_005_001, red dots of IBI_REANALYSIS_PHYS_005_002 and GLOBAL_REANALYSIS_PHY_001_025, and green crosses of GLOBAL_REANALYSIS_PHY_001_030. The grey lines depict the 200, 1000 and 2000 m isobaths. 35

2.15 Map of the wind data points. The blue dots show the grid points where the WRF provides wind data, whereas the red square depicts the location of the Bilbao-Vizcaya mooring. The grey lines depict the 200, 1000 and 2000 m isobaths. 36

2.16 Scheme of the geometry used for estimating the geostrophic velocity shear between pressure levels P1 and P2 between profiles A and B separated by a distance L. 40

2.17 Scheme of the Ekman current generated by a 10 m s−1 wind at latitude 35º (from Stewart, 2008). 43

3.1 Study area, observational systems and main characteristics of the ocean circulation (figure modified from Rubio et al., 2018). The winter IPC is represented by blue solid arrows, whereas the blue hollow arrows show the mesoscale eddy regime (although only anticyclonic arrows are represented, eddies of anticyclonic and cyclonic polarity are observed in different locations along the slope). The bold black lines delimit the HFR total-current footprint. The black stars represent the HFR stations: Matxitxako (left) and Higer (right). Jason-2 tracks 213 and 248 are represented by black crosses and the part of the track used in this study is marked in red. Grey lines: 1000, 3000, and 4000 m isobaths. 55

3.2 Schematic view of the pointwise comparison and of the data used for this approximation. Jason-2's 213 and 248 tracks are depicted by orange lines. The HFR radial directions from both sites are represented by grey lines and the selected radial directions (from the Matxitxako site) for the pointwise comparison are plotted in red (the central radial orthogonal to the track) and in blue (the adjacent radials). Points E and W are the points where each of the HFR radial directions is orthogonal to the Jason-2's track directions. Around E, the blue and red crosses show the selected points of HFR radial directions where radial currents are averaged to obtain the corresponding values on the track (green crosses). Then, the along-track green crosses are averaged to obtain the corresponding HFR current values at the point at issue (the same process 60 is carried out for point W, but it is not represented in the figure). Grey lines: 200, 1000, and 2000 m isobaths.

3.3 Across-track $\mathrm{AC_G}$+$\mathrm{AC_E}$ and $\mathrm{AC_{HFR,R}}$. (a) CTOH, CMEMS, and HFR datasets at point E_R. (b) CTOH-HFR and CMEMS-HFR residuals at point E_R. (c) CTOH, CMEMS, and HFR datasets at point W_R. (d) CTOH-HFR and CMEMS-HFR residuals at point W_R. Black arrows depict the slope current intensifications mentioned in the text. 64

3.4 Monthly statistical parameters of the comparison between $\mathrm{AC_G}$ vs. $\mathrm{AC_{HFR,R}}$ and $\mathrm{AC_G}$+$\mathrm{AC_E}$ vs. $\mathrm{AC_{HFR,R}}$at points E_R and W_R for both altimetry products: (a) CTOH $\mathrm{AC_G}$ at point W_R, (b) CTOH $\mathrm{AC_G}$ at point E_R, (c) CMEMS $\mathrm{AC_G}$ at point W_R, and (d) CMEMS $\mathrm{AC_G}$ at point E_R. The normalized RMSD is the quotient between the RMSD and the values of the corresponding $\mathrm{AC_{HFR,R}}$. 66

3.5 Mean and variance values along track 248 of different datasets: (a) $\mathrm{AC_{HFR,T}}$, $\mathrm{AC_G}$ (CTOH) and $\mathrm{AC_G}$ (CMEMS); (b) $\mathrm{AC_{HFR,T}}$, $\mathrm{AC_G}$ (CTOH) +$\mathrm{AC_E}$ and, $\mathrm{AC_G}$(CMEMS)+$\mathrm{AC_E}$. In addition, correlation and RMSD values between (a) $\mathrm{AC_{HFR,T}}$ and $\mathrm{AC_G}$ and (b) $\mathrm{AC_{HFR,T}}$ and $\mathrm{AC_G}$+$\mathrm{AC_E}$. The grey-coloured area corresponds to the slope between the 200 and 1000 m isobaths, whereas the black line is the location of point *E*. The first point of the track is around 10.5 and 13 km away from the coast for CTOH and CMEMS, respectively. The spacing between the points is slightly different and the HFR points are the same as the CMEMS points. The first point in CTOH is removed because it is an outlier. Correlation values are not plotted for confidence levels under 90 %. 68

3.6 Time evolution from 1 January 2009 to 1 July 2015 along track 248 (y-axis shows distance to the first point of the track in kilometres) of (a) CMEMS SLA' (cm), (b) $\mathrm{AC_E}$ (cm $\mathrm{s^{-1}}$), and (c) $\mathrm{AC_{HFR,T}}$ (cm $\mathrm{s^{-1}}$). The distance from the first point of the track to the coast is around 6 km. The horizontal black lines delimit the slope area between the 200 and 1000 m isobaths. The black diamonds depict the IPC intensification signals whereas the black inverted triangles show the eddy events, all mentioned in the text. 70

3.7 Snapshots showing four slope current intensification events observed by HFR, altimetry, and SST (see the dates of the events depicted in Figure 3.6) in November 2009 (a), December 2010-January 2011 (b), January 2014 (c), and November 2014 (d). The small arrows depict the HFR current fields (not rotated) whereas the thick ones indicate the across-track $\mathrm{AC_G}$. The black line shows the altimeter's track. The colormap depicts the sea surface temperature (ºC) with values referenced in each colour scale. Note that the dates corresponding to the data are not the same for SST or for HFR and $\mathrm{AC_G}$ (specified in each panel's title). 71

3.8 Four mesoscale eddies observed in the study area. The dots show the points of track 248 of the CMEMS database. SLA' (cm) values are indicated in the colour scale. Black arrows depict the HFR current fields. Red arrows correspond to across-track $\mathrm{AC_G}$ derived from the SLA' values in the dots. Grey lines: 200, 1000, and 2000 m isobaths. Note that the scale of each kind of arrow is not the same. 73

4.1 Study area corresponding to the southeastern Bay of Biscay (northeastern Iberian Peninsula) and schematic view of the winter shelf-slope current and mesoscale regime (grey arrows, note that although only anticyclonic arrows are represented, eddies of anticyclonic and cyclonic polarity are observed in different locations along the slope). The nodes for the computation of HFR currents are shown by the grey dots. The stars provide the location of the HFR antennas in Matxitxako and Higer (Donostia) Capes. The black dots provide the location of the slope moorings used in this study and the black lines the surface cross-transects used to plot HFR along-slope currents in Figure 4.2. Bathymetry is given by the contours (in metre). 80

4.2 Figure 4.2. Hovmöller diagrams of along-slope surface currents derived from the HFR along the surface cross-transects shown in Figure 4.1, at the longitude of the (a) Matxitxako and (c) Donostia moorings. Hovmöller diagrams of along-slope current profiles up to 150 m depth from downward looking ADCP data in (b) Matxitxako (only for the period 2009–2013) and (d) Donostia moorings. The wind vectors from Bilbao Vizcaya mooring are shown in (e). A selection of winter (W*) and summer (S*) current events discussed more in detail in the text are identified at the top of (a) panel. 83

4.3 Figure 4.3. Spatial maps of cross-correlations between the low-pass filtered time series of the HFR along-slope velocity component at (a,b) Matxitxako and (c,d) Donostia locations and the rest of the nodes within the HFR footprint area for total currents (the maps for winter/summer are shown in (a) and (c)/(b) and (d) subplots, respectively). ADCP data cross-correlations along the vertical range of ADCP data for (e) Matxitxako and (f) Donostia and the along-slope velocity component for summer (stratified) and winter (well-mixed) periods. The confidence level is over 99 % for all the cross-correlations values plot in the figure. 84

5.1 (a) Location of the study area (red square). Map data © 2018 AND Data SIO, NOAA, U.S. Navy, NGA, GEBCO. Image IBCAO. Image: Landsat/Copernicus. (b) Close-up map of the study area. The winter IPC is represented by solid blue arrows. The grid used for the emulated HFR surface current fields is shown by blue crosses. The red dots provide the locations of the current vertical profiles that emulate the EuskOOS moorings: Matxitxako (red M) and Donostia (red D), whereas the black dots depict the location of the two extra moorings used for the 4-mooring scenario. The bold black lines delimit the winter reduced grid, whereas the dashed orange lines delimit the summer one. The grey lines show the 200, 500, 1000 and 2000m isobaths. 93

5.2 Scheme of the approach used to test the performance of the two data-reconstruction methods described in Sect. 2.2. The models used for SIMULATION 1 and SIMULATION 2 are presented in Sect. 2.3. 94

5.3 U (a, b) and V (c, d) temporal cross-correlations between the surface and the water column levels for winter (blue) and summer (red) periods. In the Matxitxako location (a, c) and in the Donostia location (b, d). 100

5.4 Temporal cross-correlation maps between the water column levels considered and the surface points of the HFR grid for U. (a, b, c, g, h, i) for the Matxitxako mooring and (d, e, f, j, k, l) 101 for the Donostia mooring. Different depths are considered: −12m (a, d, g, j), −52m (b, e, h, k) and −100m (c, f, i, l), for summer (a-f) and winter (g-l). The white gaps are the areas where the confidence level is less than 95 %. The black dots depict the locations of the current vertical profiles.

5.5 Temporal cross-correlation maps between the water column levels considered and the surface points of the HFR grid for V. (a, b, c, g, h, i) for the Matxitxako mooring and (d, e, f, j, k, l) for the Donostia mooring. Different depths are considered: −12m (a, d, g, j), −52m (b, e, h, k) and −100m (c, f, i, l), for summer (a-f) and winter (g-l). The white gaps are the areas where the confidence level is less than 95 %. The black dots depict the locations of the current vertical profiles. 102

5.6 RRMSD maps for the summer period between the reference fields and the outputs of the ROOI with GLORYS-LR for U (a, c, e) and V (b, d, f). Different depths are considered: −12 m (a, b), −52 m (c, d) and −100 m (e, f). The black dots depict the locations of the current vertical profiles. 104

5.7 RRMSD maps for the winter period between the reference fields and the outputs of the ROOI with GLORYS-LR for U (a, c, e) and V (b, d, f). Different depths are considered: −12 m (a, b), −52 m (c, d) and −100 m (e, f). The black dots depict the locations of the current vertical profiles. 104

5.8 RRMSD maps for the summer period between the reference fields and the outputs of the DCT-PLS for U (a, c, e) and V (b, d, f). Different depths are considered: −12 m (a, b), −52 m (c, d) and −100 m (e, f). The black dots depict the locations of the current vertical profiles. 106

5.9 RRMSD maps for the winter period between the reference fields and the outputs of the DCT-PLS for U (a, c, e) and V (b, d, f). Different depths are considered: −12 m (a, b), −52 m (c, d) and −100 m (e, f). The black dots depict the locations of the current vertical profiles. 106

5.10 Mean RRMSDs related to all the data-reconstruction methods for each depth considering the entire grid for the summer period (a, b) and for the winter period (c, d). U is shown in (a, c) and V in (b, d). 108

5.11 Mean RRMSD-U related to all the data-reconstruction methods for each depth considering the reduced grid domain for the summer period (a) and for the winter period (b). 108

5.12 The 4-mooring scenario RRMSD maps subtracted by the 2-mooring scenario RRMSD maps for winter at −52 m. Negative values mean a better performance in the 4-mooring scenario for U (a, b) and for V (c, d) for the ROOI (a, c) and for the DCT-PLS (b, d). The black dots depict the locations of current vertical profiles. 109

6.1 (a) Location of the study area (dashed red square). The winter slope current is represented by blue solid arrows, whereas the black arrows depict the usual location of anticyclonic eddies. (b) Close-up map of the study area. The grid points used to compute total high-frequency radar (HFR) currents are shown by gray dots, and the red triangles show the location of the HFR stations. The red square provides the location of the Donostia mooring. The dark and bright 116 gray crosses show the shallow and deep gliders' trajectories, respectively; while the black, magenta, and green ones show the position of the gliders during the three reconstruction periods (P1, P2, and P3 respectively). The blue dots and numbers show the positions of the anticyclonic eddy core (from the location of the maximum vorticity values). The point used for extracting the wind time series is depicted by the red point. The gray lines show the 200, 1000, and 2000 m isobaths.

6.2 In (a–c) the black dots show the positions of the eddy core, estimated from the location of the maximum of relative vorticity, overlaid to a snapshot of the high-frequency radar (HFR) low pass filtered (LP) field for a date within P1 (a), P2 (b), and the last detection date before P3 (c). In (a–c), the trajectory followed by the gliders is shown in black, magenta, and green colors, respectively, and the blue dots depict the position of the eddy core. (d–f) show satellite Chl-a (mg m^{-3}) images with the daily mean HFR fields superimposed (red arrows) showing the mentioned anticyclone. The gray lines show the 200, 1000, and 2000 m isobaths. (g) depicts the wind series (see location in Figure 6.1b). 124

6.3 Deep glider (a,e) salinity (psu), (b,f) θ (°C), (c,g) σ_θ (kg m^{-3}), and (d) Chl-a (mg m^{-3}). From −10 to −200 m for (a–d); and from −200 m to the bottom (gray area) for ((e–g), note the change in the color bar). In (a–d), the dashed black line depicts the 15 °C isotherm (representing the form of the seasonal thermocline), whereas in (e–g), the white line depicts the 11.5 °C isotherm (representing the form of the permanent thermocline). The X-axis shows the distance (in km) to the first point of the profile (from north to south in the maps shown in Figures 6.1b and 6.2c) and the Y-axis the depth in m. 126

6.4 Across-track Vgeos (cm s^{-1}) profiles corresponding to P3. The Vgeos was referenced to a level of no motion at −100 m for (a) and the integrated currents for (b). The positive values correspond to the eastward across-track currents, whereas the negative ones correspond to the westward currents. The X-axis shows the distance (in km) to the first point of the profile (from north to south in the maps shown in Figures 6.1b and 6.2c) and the Y-axis the depth in m. In (b) the bottom is depicted by dark gray color. 127

6.5 Reconstructed fields in P1. (a–c) show the current velocity fields and the relative vorticity for three depth levels. The gray lines show the 200, 1000, and 2000 m isobaths. The green crosses show the position of the gliders and mooring observations. The straight black line depicts section A. In (d), the relative vorticity in section A is shown along with the velocities perpendicular to it (gray contour lines). The values of the velocities are depicted in green in cm s^{-1}, and the 0 cm s^{-1} contour is marked in black. The positive/negative velocities correspond to northeastward/southwestward currents. The Y-axis shows the depth in m. 129

6.6 The same as Figure 6.5 but for P2. 130

6.7 The same as Figure 6.5 but for P3. 131

6.8 Across-track currents (in cm s^{-1}) along the deep glider trajectory in P3 for −50 m (asterisk) and 90 m (triangle). The red markers correspond to the Vgeos observed by the glider (as in 132

Figure 6.4b), whereas the black markers correspond to the reconstructed current velocities. Eastward currents have positive values whereas westward currents have negative values.

7.1 Location of the HFR antennas (blue triangles), the HFR grid points (grey points) that cover the study area and the location of the moorings (red points). Capbreton canyon, and Gironde and Adour rivers are also depicted. The grey lines show the 200, 1000 and 2000 m isobaths. 144

7.2 Drifter trajectories: drifter-1, drifter-2 and drifter-3 are depicted by magenta, black and grey points, respectively. The light grey lines show the 200, 1000 and 2000 m isobaths. 150

7.3 (a) Mean distance in function of time between real drifter trajectories and simulated trajectories using IBI reanalysis, ROOI, HFR and HFRtot data. HFRtot denotes the original non-filtered total HFR data. (b) The same for the distance normalized by the distance travelled by the real drifter. 151

7.4 Distribution of the 10.000 particles according to observations of the CUFES system at −3 (a, b) and of the PairoVET system −10 m (c, d). (a) and (c) correspond to the period centred on 10-05-2011, whereas (b) and (d) correspond to the period centred on 13-05-2013. The colorbar depicts the number of particles and the grey lines show the 200, 1000 and 2000 m isobaths. 153

7.5 Simulated particle density maps starting from 10-05-2011 (a-l) and 13-05-2013 (m-x) forced with ROOI at −3 and −10 m. −3 days means 3 days backwards and +3, +10, +20 and +30 days mean 3, 10, 20 and 30 days forwards, respectively. The colorbar depicts the number of particles. The grey lines show the 200, 1000 and 2000 m isobaths. 155

7.6 Location of the centres of mass at −3 (a) and −10 m (b) for 2011 (black crosses) and 2013 (red asterisks), corresponding to simulations forced with ROOI. −3 days means 3 days backwards and +3, +10, +20 and +30 days mean 3, 10, 20 and 30 days forwards, respectively. The green and purple lines show the trajectory of the centres of mass in 2011 and 2013, respectively. The grey lines show the 200, 1000 and 2000 m isobaths. 156

7.7 Simulated particle density maps starting from 10-05-2011 (a-f), 13-05-2012 (g-l), 13-05-2013 (m-r) and 08-05-2014 (s-x) forced with HFR data at −3 and −10 m. −3 days means 3 days backwards and +3, +10, +20 and +30 days mean 3, 10, 20 and 30 days forwards, respectively. The colorbar depicts the number of particles. The grey lines show the 200, 1000 and 2000 m isobaths. 159

7.8 Simulated particle density maps starting from 09-05-2016 (a-f), 09-05-2017 (g-l) and 13-05-2018 (m-r) forced with HFR data at −3 and −10 m. −3 days means 3 days backwards and +3, +10, +20 and +30 days mean 3, 10, 20 and 30 days forwards, respectively. The colorbar depicts the number of particles. The grey lines show the 200, 1000 and 2000 m isobaths. 160

7.9 (a) Location of the centre of mass at −3 m for different years, corresponding to simulations forced with HFR data. −3 days means 3 days backwards and +3, +10, +20 and +30 days mean 3, 10, 20 and 30 days forwards, respectively. The lines show the trajectory of the centres of mass. (b) zoomed for 2011, 2012 and 2013. (c) zoomed for 2014, 2016, 2017, 2018. The grey lines show the 200, 1000 and 2000 m isobaths. 161

LIST OF TABLES

Table	Caption	Page
1.1	Examples of data-reconstruction methods.	6
2.1	Summary of the data sources used in this thesis, the provided data and their spatial coverage.	19
2.2	Summary of the observing platforms/models and variables used in each chapter.	37
2.3	Summary of the methods used in each chapter.	49
3.1	Statistics at different points for the study period. r is the correlation parameter, and RMSD is the root mean square difference of the velocity anomalies between HFR and altimetry for different altimetry products (i.e., CMEMS and CTOH). The mean and the standard deviation (SD) are also estimated for each dataset. E and W are the points where HFR radial velocities are orthogonal to tracks 248 and 213, respectively (see Figure 3.1). E_R and W_R are the names given to those points in the pointwise comparison, whereas E_T is given in the along-track current comparison. Max_T, is the track point where the correlation r is maximal in the along-track current comparison (point 2.10º W, 43.82º N for CTOH and point 2.09º W, 43.80º N for CMEMS). RAD refers to HFR radial data for E_R and W_R and across-track rotated OMA anomaly currents for E_T and Max_T. There is no data in Max_T because they are different for each altimetry product. Both AC_G and AC_G+AC_E cases are considered.	63
3.2	NAO and EA indexes in the previous 2 months of the events. m–2 means 2 months before the event whereas m–1 means 1 month before.	72
5.1	Details of the numerical simulations used in this study. Note that T and S represent temperature and salinity, respectively.	98
5.2	Seasonal spatial correlation length scales for the emulated current velocity components U and V in the study area, for the summer and winter periods and in zonal and meridional directions. Note that the surface horizontal scales are shown in kilometres and that the vertical scales in depth at Matxitxako and Donostia mooring points are shown in metres.	99
5.3	Summary of the results of the reconstructions with ROOI (with GLORYS-LR) and DCT-PLS in terms of spatial mean RMSDs and RRMSDs for the entire and reduced grids, the summer and winter study periods, and different depths.	103
6.1	Summary of the observing platforms and datasets where θ denotes potential temperature, σ_θ denotes potential density anomaly, Vgeos denotes geostrophic current velocity, U (V) denotes the zonal (meridional) current velocity component, LP denotes low pass filtered and x, y, and z denote the zonal, meridional, and vertical directions, respectively.	117

6.2 Definition of the three periods in 2018 used for the reconstruction, with all times in UTC. Period P3 was also used for the vertical description of the eddy. 122

6.3 Root mean square differences (RMSDs) between the reconstructed and observed current velocities at the HFR and acoustic Doppler current profiler (ADCP) observation points (in cm s^{-1}). 128

7.1 Summary of the observing platforms and datasets used. LP means low pass filtered. 143

7.2 RMSD (in cm s−1), RRMSD and correlations between the Matxitxako ADCP observations and IBI reanalysis, ROOI, HFR and HFRtot data for both current components. HFRtot denotes the original non-filtered HFR data. General values are shown as well as values for different depths. Note that in the case of the HFR, comparisons are carried out between the surface and the water column. 149

7.3 Percentage of the particles that leave the domain during the simulations. 156

7.4 Percentage of the particles that leave the domain during the simulations. 162

LABURPENA

Kostaldeko ozeanoak biodibertsitate handiko funtsezko eremuak dira, eta prozesu biologikoak eta geokimikoak modu aktiboan gertatzen dira bertan. Gizartearen zati handi bat kostaldetik gertu bizi da eta bertan jarduera sozioekonomiko ugari garatzen dira, hala nola, merkataritza eta aisialdi arrantza, nabigazioa, turismoa, etab. Ondorioz, giza inpaktuaren eragina nabarmena denez zonalde horietan, kudeaketa jasangarriaren beharra sortzen da. Horrek, aldi berean, kostaldeko behaketa sistemen instalazioa bultzatzen du, eremu horien ezaugarriei eta egoerari buruzko funtsezko informazioa lortzeko. Hala ere, zonalde horien monitorizazioa zaila da: batetik, hidrodinamika konplexua delako; eta bestetik, behaketa plataformen instalazioa zaila izan daitekeelako. Aipatutako faktoreez gain, eragileen interesek behatokien diseinuan ere eragiten dute.

Kostaldeko behaketa sistemek emandako datuak prozesu hidrodinamikoak karakterizatzeko eta itsasoaren egoera monitorizatzeko garrantzitsuak diren arren, datu horien estaldura espaziala nahiko eskasa da, bereziki, ur zutabean zehar. Hortaz, behaketa plataformetako datuak edota ereduak konbinatzeko metodoak edo planteamenduak funtsezkoak dira 3D deskribapen osoagoa lortzeko.

Testuinguru orokor horren barruan, tesi honek Bizkaiko Golkoaren hego-ekialdea du kokagune (SE-BoB). Bertan, Capbreton kanoiak honakoak bereizten ditu: ekialde-mendebalde norabidea duen Espainiako kostaldea eta kontrako ipar-hego norabidea duen kostalde Frantsesa. Hori horrela, ezponda korrontea [poloranzko korronte iberiarra (IPC)] zirkulazioaren arduradun nagusienetakoa da. Neguan, ekialderantz egiten du Espainiako kostaldean eta iparralderantz Frantziako kostaldean zehar ur zutabearen lehen 300 m-etan; udan, berriz, fluxua alderantzikatu egiten da, korronte ahulagoak eta aldakorragoak ematen baitira. Era berean, ezponda korrontearen eta batimetria malkartsuaren arteko elkarrekintzak ~40 eta 60 km bitarteko azaleko diametroko eta ~1−5 asteko biziraupeneko zurrunbiloak eratzea dakar. Ezponda korronteaz gain, haizeak eragindako korronteak dira gainazaleko zirkulazioaren eragile nagusiak. Udazkenean eta neguan hego-mendebaldeko haizeek ipar-ekialderanzko zein ekialderanzko korronteak eragiten dituzte plataforma gainean; udaberrian eta udan, ostera, ipar-ekialdekoek mendebalderantz eta hego-mendebalderantz bultzatzen dituzte korronteak. Bestalde, plataformen gainean, mareek eta dentsitateak eragindako zirkulazioa ahula da, plataforma estuengatik eta dentsitate aldaketa esanguratsuak eragiten dituzten ibairik ez dagoelako. Beraz, korronteak batez ere haizeen eta horien aldakortasunaren mende daude. Halaber, ur zutabean, baldintzak nabarmen aldatzen dira

urtaroaren arabera, baldintza estratifikatuak eta nahasiak baitaude udan eta neguan, hurrenez hurren.

Ezaugarri horiek guztiak kontuan izanda, SE-BoBa hidrodinamika konplexuko zonaldea dela esan daiteke. Konplexutasun horrek eragin handia du ur masen eta horien osagaien banaketan, hala nola nutrienteen, fitoplanktonaren, arrain espezieen arrautzen eta larben, itsas zabor flotatzaileen eta abarren banaketan; eta, horrela, prozesu biologikoetan, geokimikoetan zein ingurugirokoetan eragiten du. Prozesu horien garrantzia eta kostaldeko erabiltzaileen beste premia sozial batzuk direla eta, Euskadiko Ozeanografia Operazionala Sistemak (EuskOOS) itsasoaren egoera monitorizatzen du euskal kostaldean zehar. Sistema horrek zonaldea hobeto ezagutzeko eta haren jarraipena egiteko ezinbesteko datuak ematen ditu. Era horretan, itsasertzetik urrunen dagoen kostaldeko gunea monitorizatzen duten EuskOOSeko behaketa plataformak bi dira. Batetik, goi maiztasuneko radar sistema (HFR), itsasertzetik 150 km itsas zabalerantz gainazaleko korronte abiadura eremuak orduan behin ematen dituena; eta, bestetik, ezponda espainiarrean ainguratutako bi buia (edo ainguraketa), korronteak eta datu hidrografikoak ematen dituztenak ur zutabean zehar (−200 m arte). Plataforma horiek emandako datuak SE-BoBn espazio-denboran zabalenak diren behaketak badira ere, haien estaldura espaziala erlatiboki eskasa da erabateko 3D karakterizazio baterako. Orduan, tesi honen helburu nagusia EuskOOSeko behaketa plataformek bai eta kanpoko datu iturriek ere (besteak beste gliderrak, sateliteak, deriba buiak, ikerketa ontziak eta ereduak) emandako datuak konbinatzea izan zen, zonaldeko hidrodinamika 3Dn karakterizatzeko. Konbinaketa hori aurrera eramateko datuak besterik gabe aldi berean aztertu ez ezik, haien artean nahastu ere egin ziren datu-berreraiketa metodoen bitartez espazialki zabaltzeko. Hori burutzean, eskuragarri dauden datuei balio handiagoa gehitu zitzaien. Era berean, metodo horiek itsas aplikazioetarako zuten egokitasuna ere ebaluatu zen. Hori guztia egiteko, tesi hau hainbat ikerketetan banatu zen.

HFRaren gainazaleko korronteak eta altimetriatik eratorritakoak elkarren osagarri izan daitezkeenez, adibidez, behaketak baliozkotuz edo espazio-denboran zabalduz, *3. kapituluan* (*1.* eta *2. kapituluak Sarrera* eta *Datuak eta Metodoak* atalei dagozkie, hurrenez hurren) bi sistemen arteko bat etortzea ebaluatu zen lehen aldiz SE-BoBn. Halaber, urtaroko eta mesoeskalako zenbait prozesuren baterako behagarritasuna ebaluatu zen, zehazkiago ezponda korrontea eta zurrunbiloak. Lehenik eta behin, altimetroaren trazarekiko norabide perpendikularrean korronteak 2009 eta 2015 urte artean alderatu ziren. Horretarako, HFRak korronte totalak neurtzen dituenez (geostrofikoak + ageostrofikoak), horiek iragazi egin ziren eta seinale ageostrofikoaren zati bat kendu eta altimetriatik eratorritako korronte geostrofikoetara gehiago hurbildu zen. Hori horrela, behaketa sistema bakoitzaren mugak eta funtzionamendu printzipio desberdinak gorabehera, haien arteko lotura ikusi zen, 0,64rainoko korrelazioekin. Frantziako ezpondaren gainean akordio hoberena ikusi zen; bertan, korronte geostrofikoaren seinalea korronte ageostrofikoen (haizeak eragindako korronteak, adibidez) eragin handiagoa duten beste zonalde batzuetan baino handiagoa baita. Horrez gain, haizeak eragindako korronteak altimetriatik eratorritakoei ere gehitu zitzaizkien, eta korrelazioa % 10 inguru handitu zen. Urtaroko eta mesoeskalako prozesuen detekzioari begira, bi behaketa plataformek akordio kualitatiboa erakutsi zuten ezpondako korrontea eta mesoeskalako zurrunbiloak hauteman baitzituzten lau gertaera independentetan.

Zirkulazio patroi nagusietako bat izanik, hainbat egilek aztertu dute dagoeneko ezponda korrontea. Azterketa horiek, batez ere, behaketa plataforma independenteen bitartez egin ziren, eta eskualde zehatzetan zentratzen ziren, adibidez, *3. kapituluan* egin genuen bezala (bertan azaleko seinalea baino ez zen aztertu). Beste analisi batzuek gainazaleko eta gainazalpeko behaketak ere konbinatu zituzten; hala ere, gainazaleko eta gainazalpeko korronteen abiadura behaketa serie zabalagoen eskuragarritasunak 3D azterketa osatuagoa ahalbidetzen zuen. Horixe da, hain zuzen ere, *4. kapituluaren* helburua. Horretan, Doppler efektuan oinarrituriko bi korronte profilagailu akustikok emandako ur zutabeko datuak (ADCP; EuskOOSeko aingura lekuetan kokatuak) eta HFRren gainazaleko datuak 2009 eta 2017 urte artean aztertu ziren batera. Konparazio kualitatiboek bi behaketa sistemek ezponda korrontearen urtarokotasuna detektatzen dutela erakutsi zuten, IPC seinalea neurtuz. Gainera, haizearen norabide aldaketa azkarrek eragindako gorabeherak ere hauteman zituzten bi plataformek. Halaber, konkordantzia espazial kuantitatibo bat ikusi zen gainazalean ainguratze puntuen eta gainerako radarraren sarearen puntuen artean, bai eta ainguraketetako ur zutabearen sakonera desberdinen artean ere. Horrek esan nahi du gainazaleko eta gainazalpeko korronteen artean erakutsitako aurreko konkordantzia kontuan hartuta, HFR eta ADCP datuen konbinazioa egokia dela ezponda korrontea 3Dn monitorizatzeko bai eta datu horiek nahasteko ere korronte abiadurak 3Dn zabaltzeko.

Jarraian, *5. kapituluan*, datuak berreraikitzeko bi metodoren trebetasuna eta bideragarritasuna ebaluatu ziren, erabilgarri dauden korronte abiadura behaketak 3Dn zabaltzeko. Horretarako, behaketa sistemen simulazio esperimentuen (OSSE) antzeko planteamendua erabili zen, hau da, zenbakizko simulazio bat erabili zen *benetako ozeano* gisa eta bertatik behaketak erauzi ziren. Behaketek EuskOOS behatokiaren konfigurazioa simulatu zuten (hau da, Espainiako ezpondan zehar ur zutabean zeuden bi ADCPen datuak eta HFRaren gainazaleko korronteak simulatu zituen). Ondoren, behaketa horiek nahastu egin ziren; eta, azkenik, berreraikitako korronte abiadura eremuak *benetako ozeanoarekin* alderatu ziren. Datuak berreraikitzeko ikuspegi ezberdinetan oinarritzen diren honako bi metodo hauek erabili ziren: batetik, kosinu diskretuen transformatuetan oinarrituriko karratu minimo penalizatuen metodoa (DCT-PLS); eta, bestetik, ordena murriztuko interpolazio optimoa (ROOI). DCT-PLSa karratu minimo penalizatuen erregresio ikuspegian oinarritzen da, behaketekiko fideltasuna eta emaitzaren leuntasuna orekatzen du; ROOI, berriz, datu historikoetatik (oro har, ereduetatik) lortutako kobariantza espazialen eta behaketen fusioan oinarritzen da. Ebaluazioak udako eta neguko periodoetan egin ziren, metodoek korronte eta baldintza bertikalen erregimen desberdinekiko duten sentsibilitatea aztertzeko. Bi metodoak ezponda korrontearen urtarokotasunarekiko sentikorrak zirela erakutsi zen. Errore maila onargarriak lortu ziren ur zutabearen lehen 150 m-etan, 0,55 eta 7 cm s^{-1} bitarteko batez besteko espazialekin (sakonera bakoitzerako) kasu gehienetarako, eta batez besteko 0,07−1,2 errore erlatiboekin (batez besteko koadratikoarekiko). Frantziako ezpondan zehar bi ADCP gehitzeak emaitzak hobetu zituen. Emaitzek bi metodoak zonaldeko 3D hidrodinamika karakterizatzeko tresna egokiak direla erakutsi zuten bakoitzak portaera ezberdinarekin. Alde batetik, DCT-PLSa hobeto dabil behaketa ugari dauden zonaldeetan, eta konfigurazio sinpleagoa du; bestetik, ROOIk hobeto funtzionatzen du behaketa urriko eskualdeetan, baina datu historikoak behar ditu kobariantzak estimatzeko (ereduetatik, gure kasuan), eta sarrerako parametro batzuen doiketa ere behar du.

Kostaldeko zurrunbiloak ur partzelen eta haien osagaien garraioa eragiten duten prozesu garrantzitsuak dira. Nahiz eta beste ikertzaile batzuek egitura ozeaniko hauen gainazaleko ezaugarriak SE-BoBn aztertu, gutxi dakigu ur zutabeko ezaugarriei buruz. Beraz, *6. kapituluan*, zenbait behaketa plataformatako datuak erabili ziren, kostaldeko zurrunbilo bat 3Dn karakterizatzeko glider misio batean zehar. Zehazkiago, bi gliderren, HFRaren, eredu baten eta satelite baten datuak batera erabili ziren. Behaketen aldi bereko analisiaz gain, eta aurretik ebaluatutako ROOI metodoari esker plataforma anitzeko behaketak ere erabili ziren (hau da, HFR datuak, glider eta ainguraketa batekoak) zurrunbiloaren korronte abiadura eremuak 3Dn berreraikitzeko. Zurrunbiloak ur modaleko zurrunbiloaren portaera erakutsi zuen, hots, isopiknak ur zutabearen goiko aldean goratuta zituen eta maila sakonagoetan hondoratua zituen zurrunbilo antizikloniko bat. Tamaina txikiagoa izan arren, zurrunbilo horrek SE-BoBn detektatutako gainerako zurrunbiloen antzeko ezaugarriak zituen gainazalean eta inguruko eskualdekoekiko antzeko ezaugarriak ur zutabean. Halaber, ROOI korronteen abiadura eremuak 3Dn berreraikitzeko gai izan zen ur zutabeko lehen 100 m-etan eta behaketa konfigurazio desberdinen pean. Hain zuzen ere, berreraiketak gliderretik eratorritako korronte geostrofikoekin bat etorri ziren gliderrak zurrunbiloaren nukleoa zeharkatu zuen periodoan. Hala ere, berreraiketak datu gehigarriekin baliozkotzea baliagarria izango litzateke horien sendotasuna are gehiago ziurtatzeko. Horretaz gain, berreraikitako eremuak zurrunbiloak eragindako plataforma zeharreko ur masen garraioa (kostalderantz edo itsaso zabalerantz) kalkulatzeko erabili ziren eta ikerketa esparruarekiko iparraldean modelatutako zurrunbiloek eragindako magnitude ordenako balioak lortu ziren. Kapitulu honetako analisiek ezaugarri hidrodinamikoen karakterizazio osoagoak lortzeko plataforma anitzeko behaketen konbinazioak duen potentziala erakutsi zuten. Bestalde, berreraikitako korronte abiadura eremuak beste gai batzuetan aplika zitezkeela ikusi zen, esate baterako, partikula pasiboen kostaldeko garraioan, hala nola nutriente, kutsatzaileak edo arrain pelagikoak haien bizitzako etapa goiztiarretan (ELS).

Azken kapituluak berreraikitako eremu horien aplikazio bat erakusten du. Zehazkiago, baldintza hidrodinamikoek antxoa europarraren (Engraulis encrasicolus) ELSko distribuzioan nola eragin dezaketen aztertzen da. Antxoa europarra Kantauriko arrantza espezie garrantzitsuenetako bat da; euskal arrantza sektoreko ekonomiaren oinarrietako bat. Antxoa europarraren arrautzak eta larbak ur zutabearen goiko aldean daude nagusiki. Hidrodinamikak espezie horren arrautzen eta larben garraioa eragiten du, errutea gertatu eta 30 egun ingurura arte, larbek igeri egiteko gaitasun nabarmenak garatzen dituztenean. Errute zonalde nagusiak Gironde eta Adour ibaietako lumak dira (Frantziako plataformaren gainean), baita plataformaren haustura-puntua ere kasu batzuetan. Aurretik egindako ikerketen arabera, arrautzen eta larben adbekzioa, batez ere, haizeak eragindako hego-mendebalderanzko korronte patroiari lotuta dago. Patroi horrek, oro har, plataformaren haustura-eremuetara, ezpondara eta itsaso zabalera bidaltzen ditu. Arrautzen eta larben adbekzioa errutearen ondoko 30 egunetarako simulatzen duten azterketak urriak dira, eta ez dira korronteen abiaduren behaketetan oinarritzen. Beraz, *7. kapituluan*, antxoa arrautzen eta larben adbekzioa simulatu zen 30 egunez, hidrodinamikak espezie horren ELSan duen eragina eta eragin horren urtetik urterako aldakortasuna ezagutzeko, behatutako korronte abiaduren datuetan oinarrituta. Hain zuzen, HFR nahiz ROOItik (HFR, ADCP bat eta eredu datuetatik berreraikita) eratorritako korronte abiadura datuak erabili ziren eta arrautzen hasierako distribuzioak BIOMANetik lortutako datuetan oinarritu ziren. BIOMAN urtero maiatzean egiten den kanpaina ozeanografikoa da, antxoaren errutea bere puntu gorenera iristen denean. Bertan, arrautza ugaritasunen distribuzio espazialak neurtzen dira −3 m-tan, eta ur-zutabeko lehenengo 100 m-etan integratuta ere. −3 m-tan lortutako datuetatik abiatuz simulazioak 2011tik 2018ra (2015 urtea ez zen simulatu korronte datu urritasunagatik) egin ziren HFRko korronteak erabilita, eta 2011 eta 2013rako ROOIrekin (beste urte batzuk ez ziren kontuan hartu, korronte datu urriak zirela eta). Ur zutabeko lehen 100 m-etako ugaritasunei dagokienez, −10 m-ko sakonera hautatu zen adierazgarritzat. Hala, -10 m-tako simulazioetarako ROOItik eratorritako korronteak erabili ziren 2011 eta 2013an. Emaitzek urte arteko aldakortasun handia erakutsi zuten distribuzio patroietan, bat-bateko zirkulazioaren aldakortasunaren menpe baitzeuden; haatik, oro har, larben zati batek Frantziako plataforma-haustura eta ezpondaren inguruan amaitzen zuen, beste ikerketa batzuetan ikusitako patroiarekin bat etorriz. Distribuzioak hainbat sakoneratako hidrodinamika ezberdinekiko sentikorrak direla ikusi eta 3Dko korronte abiadura eremuak izatearen garrantzia nabarmendu zen. Nahiz eta, normalean, larbak simulazio esparru barruan geratu, atxikipen handiagoa ikusi zen arrautzak plataformaren gainean erruten zirenean, plataformaren haustura gunean edo plataformatik kanpo ordez. Ikerketa honek ROOI metodoak itsas aplikazioetarako eta kasu honetan zehatzago 3D lagrangiar azterketetarako duen potentziala erakusten du. Gainera, eskuragarri dauden plataforma anitzeko behaketei balioa gehitzen die.

Tesi honetan, plataforma anitzen eta ereduen datuen konbinazioak karakterizazio hidrodinamiko osoago bat ahalbidetu zuen; EuskOOSeko zein beste behaketa plataformen balioa handitu zuen bitartean. Gainera, ROOI metodoa SE-BoBn prozesu hidrodinamikoak hobeto ulertzeko eta gainerako aplikazioetarako tresna erabilgarria dela ikusi ez ezik, beste zonaldetan aplikagarria ere bada. Tesi honetan lortutako emaitzek datuak berreraikitzeko metodoek eskaintzen dituzten aukerak gehiago ikertzeko bidea zabaltzen dute kostaldeko 3D prozesu hidrodinamikoak eta haiek eragindako ur garraioak zehazkiago karakterizatzeko, inguruko prozesu ozeanikoak hobeto ulertzeko nahiz kudeaketa jasangarriagoa lortzeko asmoz.

RESUMEN

Los océanos costeros son áreas esenciales de gran biodiversidad donde ocurren procesos biológicos y geoquímicos de manera activa. Gran parte de la humanidad vive en zonas cercanas a la costa y desarrolla una amplia gama de actividades socioeconómicas como la pesca comercial y recreativa, la navegación, el turismo, etc., siendo las zonas más productivas del mundo para la humanidad. Por tanto, estas se ven fuertemente afectadas por el impacto humano, lo que genera la necesidad de una gestión sostenible. Este requisito motiva la instalación de sistemas de observación costeras que proveen información esencial sobre las características y el estado de estas áreas. Sin embargo, la monitorización es complicada debido a la compleja hidrodinámica y muchas veces a la difícil accesibilidad para la instalación de las plataformas de observación. Además de los factores mencionados, los intereses de los diferentes actores también inciden en el diseño de los observatorios.

A pesar de que los datos proporcionados por los sistemas de observación costeras son cruciales para caracterizar los procesos hidrodinámicos y monitorizar el estado del mar, la cobertura espacial de estos datos es relativamente escasa, especialmente a lo largo de la columna de agua. Por lo tanto, los métodos o enfoques para combinar datos de diferentes plataformas de observación y/o modelos son clave para obtener una descripción 3D más completa.

Dentro de este contexto general, esta tesis se centra en el sureste del Golfo de Vizcaya (SE-BoB de sus siglas en inglés), que se caracteriza por un cambio brusco en la orientación de la costa de una dirección este-oeste a lo largo de la costa española a una dirección norte-sur a lo largo de la costa francesa, con el cañón de Cap Bretón separando ambas plataformas. La corriente de talud (Corriente Ibérica hacia el Polo (IPC de sus siglas en inglés)) es el principal responsable de la circulación, que en invierno fluye hacia el este a lo largo de la costa española y hacia el norte a lo largo de la costa francesa en los primeros 300 m de la columna de agua, mientras que en verano el flujo se invierte, mostrando corrientes más débiles y variables. La interacción de la corriente de talud con la batimetría abrupta del área desencadena la formación de remolinos que muestran diámetros superficiales de ~40 a 60 km y vidas de ~1 a 5 semanas. Además de la corriente de talud, las corrientes inducidas por el viento son los principales responsables de la circulación superficial que en otoño e invierno generan una deriva hacia el norte y hacia el este sobre la plataforma provocada por los vientos del suroeste, y en primavera y verano una deriva hacia el oeste y suroeste debido a vientos del noreste. Sobre las plataformas, la circulación inducida por las mareas y la densidad es débil debido a las plataformas estrechas y la ausencia de ríos que proporcionen variaciones significativas de densidad, estando las corrientes principalmente sujetas a los vientos y su variabilidad. En la columna de agua, las condiciones varían significativamente

dependiendo de la estación con condiciones estratificadas y de mezcla en verano e invierno, respectivamente.

La combinación de todas estas características hace del SE-BoB en un área de hidrodinámica compleja que tiene un gran efecto en la distribución de las masas de agua y sus constituyentes tales como nutrientes, fitoplancton, huevos y larvas de especies de peces, basura marina flotante, contaminantes, etc., influyendo así en los procesos biológicos, geoquímicos y ambientales. Dada la importancia de estos procesos, así como otras necesidades sociales de los usuarios costeros, el sistema de oceanografía operacional de la costa vasca (EuskOOS) monitoriza las condiciones del mar a lo largo de la costa vasca, aportando datos esenciales para un mejor conocimiento y seguimiento de la zona. Las plataformas de observación de EuskOOS que monitorizan la parte costera más alejada de la línea de costa son un sistema de radar de alta frecuencia (HFR de sus siglas en inglés) que proporciona campos horarios de corrientes superficiales desde la línea de costa hasta 150 km mar adentro y dos boyas fondeadas (o fondeos) que proporcionan datos de velocidad de la corriente y datos hidrográficos en la columna de agua (hasta –200 m) en el talud español. A pesar de que los datos proporcionados por estas plataformas componen las series de datos observacionales espaciotemporalmente más extensas en el área de estudio, su cobertura espacial es relativamente escasa para una caracterización 3D completa. Por tanto, el objetivo principal de esta tesis fue combinar los datos disponibles de las plataformas de observación de EuskOOS así como de fuentes de datos externas como gliders, satélites, boyas de deriva, embarcaciones de investigación y modelos para caracterizar en 3D la hidrodinámica del área. Dicha combinación se llevó a cabo mediante el análisis conjunto de los datos y la mezcla de datos con métodos de reconstrucción de datos que los expanden espacialmente, agregando así más valor a los datos disponibles. La idoneidad de dichos métodos para aplicaciones marinas también fue evaluada. Para ello, esta tesis se dividió en diferentes estudios.

Dado que las corrientes superficiales del HFR y las derivadas de la altimetría podrían complementarse entre sí, por ejemplo, validando las observaciones o expandiéndolas espaciotemporalmente, en el *Capítulo 3* (los *Capítulos 1* y *2* corresponden a las secciones de *Introducción* y *Datos y Métodos*, respectivamente) se evaluó la concordancia entre ambos sistemas por primera vez en el área de estudio. Al mismo tiempo, también se evaluó la observabilidad conjunta de ciertos procesos estacionales y de mesoescala, como la corriente de talud y los remolinos. En primer lugar, las corrientes en dirección perpendicular a la traza del altímetro se compararon entre 2009 y 2015. Para ello, dado que el HFR proporciona corrientes totales (geostróficas + ageostróficas), estas se filtraron, eliminando parte de la señal ageostrófica y acercándose más a las corrientes geostróficas derivadas de la altimetría. A pesar de las limitaciones de cada sistema de observación y sus diferentes principios de funcionamiento, se observó concordancia entre ellos con correlaciones de hasta 0,64 y con la mejor concordancia sobre el talud francés, donde la señal de la corriente geostrófica es mayor que en otras áreas más influenciadas por corrientes ageostróficas (tales como corrientes inducidas por el viento). Las corrientes inducidas por el viento también se sumaron a las derivadas de la altimetría aumentando las correlaciones en torno al 10%. En cuanto a la detección de procesos estacionales y de mesoescala, ambos sistemas detectaron la corriente de talud y los remolinos de mesoescala en cuatro eventos independientes, mostrando una concordancia cualitativa.

Siendo uno de los principales patrones de circulación, la corriente de talud ya ha sido analizada en el área de estudio por varios autores. Estos análisis fueron realizados principalmente por plataformas de observación independientes y se centraban en regiones específicas, por ejemplo, como hicimos en el *Capítulo 3* (donde solo se analizó la señal superficial). Algunos análisis también combinaron observaciones superficiales y subsuperficiales, sin embargo, la disponibilidad de series temporales de observaciones de velocidad de corrientes superficiales y subsuperficiales más extensas permitía un análisis 3D más completo. Este es precisamente el objetivo del *Capítulo 4*, donde se analizaron conjuntamente los datos en la columna de agua de dos perfiladores acústicos de corriente por efecto Doppler (ADCPs de sus siglas en inglés; coubicados en los fondeos de EuskOOS) y los datos superficiales del HFR entre 2009 y 2017. Las comparaciones cualitativas mostraron que ambos sistemas de observación detectan la estacionalidad de la corriente de talud, midiendo la señal IPC. Además, las fluctuaciones debidas a rápidos cambios en la dirección del viento también fueron detectadas por ambas plataformas. También se observó una concordancia espacial cuantitativa entre los puntos de fondeo y el resto de la malla del radar en superficie, y entre las diferentes profundidades en la columna de agua en los fondeos, lo que significa que teniendo en cuenta la concordancia anterior mostrada entre las corrientes superficiales y subsuperficiales, la combinación de datos HFR y ADCP es adecuada para monitorizar la corriente de talud en 3D y para mezclar esos datos para expandir las velocidades de la corriente en 3D.

A continuación, en el *Capítulo 5*, se evaluaron las habilidades y la viabilidad de usar dos métodos de reconstrucción de datos para expandir en 3D las observaciones de velocidad de corriente disponibles. Para ello se usó un enfoque similar a los experimentos de simulación de sistemas de observación (OSSE de sus siglas en inglés) en el que se utilizó una simulación numérica como *océano real*. Las observaciones se extrajeron del *océano real* simulando la configuración del observatorio EuskOOS (es decir, datos de dos ADCPs en la columna de agua a lo largo del talud español y de corrientes superficiales del HFR), luego se mezclaron y, finalmente, los campos de velocidad de corriente reconstruidos se compararon con el *océano real*. Los dos métodos de reconstrucción de datos fueron el método de mínimos cuadrados penalizado con transformadas de coseno discretas (DCT-PLS de sus siglas en inglés) y la interpolación óptima de orden reducido (ROOI de sus siglas en inglés), que se basan en diferentes enfoques. El DCT-PLS se basa en un enfoque de regresión de mínimos cuadrados penalizados que equilibra la fidelidad a las observaciones y la suavidad de la solución; mientras que el ROOI se basa en la fusión de las covarianzas espaciales, obtenidas a partir de datos históricos (generalmente de modelos), y las observaciones disponibles. Las evaluaciones se realizaron para períodos de verano e invierno con el fin de conocer la sensibilidad de los métodos a diferentes regímenes de corrientes y condiciones verticales (es decir, estratificado en verano y mezclado en invierno). De hecho, ambos métodos mostraron que eran sensibles a la estacionalidad de la corriente de talud. Se obtuvieron niveles de error aceptables en los primeros 150 m de la columna de agua, con valores espaciales promedio (para cada profundidad) para la mayoría de los casos de entre 0,55 y 7 cm s^{-1} y errores relativos promedio de 0,07 – 1,2 veces la media cuadrática. La adición de dos ADCPs a lo largo del talud francés mejoró los resultados. Los resultados mostraron que ambos métodos pueden ser herramientas útiles para caracterizar en 3D la hidrodinámica del área de estudio y que cada uno se comporta de manera diferente. El DCT-PLS funciona mejor en áreas bien muestreadas y tiene una configuración más simple, mientras que el ROOI funciona mejor en áreas submuestreadas, pero necesita datos históricos para estimar las covarianzas (de modelos en nuestro caso) y también necesita el ajuste de algunos parámetros de entrada.

Los remolinos costeros son procesos importantes que regulan el transporte de las parcelas de agua y sus componentes. Estas estructuras oceánicas ya fueron analizadas en superficie por otros autores en el área de estudio, sin embargo, poco se conoce sobre sus características en la columna de agua. Por lo tanto, en el *Capítulo 6*, se utilizaron datos de diferentes plataformas de observación para caracterizar en 3D un remolino costero durante una campaña glider. Más concretamente, se utilizaron conjuntamente datos de dos gliders, del HFR, de un modelo y de un satélite. Además del análisis conjunto de observaciones y gracias al método ROOI previamente probado en el área de estudio, también se utilizaron observaciones multiplataforma (es decir, datos HFR, glider y de un fondeo) para reconstruir en 3D los campos de velocidad de corriente del remolino. El remolino mostró un comportamiento de remolino de agua modal, es decir, un remolino anticiclónico con una elevación de las isopicnas en la parte superior de la columna de agua y un hundimiento en niveles más profundos. Aunque este remolino tuviera un tamaño ligeramente menor, presentaba características similares a otros remolinos detectados previamente en superficie en el área de estudio y en la columna de agua en regiones cercanas. El ROOI fue capaz de reconstruir en 3D los campos de velocidad de las corrientes en los primeros 100 m de la columna de agua bajo diferentes configuraciones observacionales, concordando con las corrientes geostróficas derivadas del glider en el período en el que el glider cruzó el núcleo del remolino. Sin embargo, una mayor validación con datos externos adicionales sería valiosa para asegurar la solidez de las reconstrucciones. Los campos reconstruidos también se utilizaron para estimar aproximadamente el transporte a través de la plataforma (hacia costa o hacia mar abierto) inducido por el remolino en la columna de agua, obteniendo valores del orden de magnitud de los remolinos modelados al norte del área de estudio. Los análisis llevados a cabo en este capítulo mostraron el potencial de la combinación de observaciones multiplataforma para obtener caracterizaciones más completas de diferentes características hidrodinámicas en el área de estudio. Por otro lado, se vio que los campos de velocidad de corriente reconstruidos podrían ser aplicados en otros temas, como por ejemplo el transporte costero de partículas pasivas tales como nutrientes, contaminantes o peces pelágicos en etapas tempranas de la vida (ELS de sus siglas en inglés).

El último capítulo muestra una aplicación de estos campos reconstruidos. Más concretamente se aplican al estudio de cómo las condiciones hidrodinámicas pueden influir en la distribución de la anchoa europea (Engraulis encrasicolus) en ELS. La anchoa europea es una de las especies pesqueras más importantes del Cantábrico y está considerada como uno de los pilares de la economía del sector pesquero vasco. Los huevos y larvas de anchoa europea se encuentran principalmente en la parte superior de la columna de agua. La hidrodinámica induce el transporte de huevos y larvas de esta especie hasta aproximadamente 30 días después del desove, cuando las larvas desarrollan habilidades natatorias significativas. Las principales áreas de desove son las plumas de los ríos Gironde y Adour (sobre la plataforma francesa) y también el punto de ruptura de la plataforma en algunos casos. Estudios previos indicaron que la advección de huevos y larvas está sujeta principalmente al patrón estacional de corriente hacia el suroeste inducido por el viento, que por lo general los dirige hacia áreas de ruptura de la plataforma, talud y mar abierto. Los estudios que simulan la advección de huevos y larvas considerando variabilidades mayores que la estacional para los 30 días posteriores al desove son escasos y no se basan en observaciones de velocidad de corrientes. Por lo tanto, en el *Capítulo 7*, se simuló la advección de huevos y larvas de anchoa durante 30 días, en base a los datos de velocidad de corriente observados, con el fin de conocer los efectos de la hidrodinámica en el ELS de esta especie y su variabilidad interanual. Más específicamente, se utilizaron datos de velocidad de corriente derivados de HFR y ROOI (reconstruidos del HFR, un ADCP y datos de modelo). Las distribuciones iniciales de huevos se basaron en datos de abundancia de huevos obtenidos de BIOMAN, que es una campaña oceanográfica realizada todos los años en mayo, cuando el desove de la anchoa alcanza su punto máximo, que proporciona datos espaciales de abundancia de huevos a –3 m y también integrados en los primeros 100 m en la columna de agua. Para el caso de datos de abundancia inicial a –3 m, las simulaciones se ejecutaron de 2011 a 2018 (excepto 2015 debido a la escasez de datos de corriente) forzadas con corrientes del HFR, y para 2011 y 2013 con ROOI (otros años no se tuvieron en cuenta debido a la escasa disponibilidad de datos de corrientes). Las abundancias integradas en los primeros 100 m en la columna de agua se asignaron a –10 m como profundidad representativa. Por tanto, a –10 m, los huevos y larvas fueron advectados forzados con ROOI para 2011 y 2013. Los resultados mostraron una alta variabilidad interanual en los patrones de distribución ya que estaban sujetos a la variabilidad de la circulación instantánea, sin embargo, generalmente parte de las larvas terminaban alrededor de la rotura de la plataforma y el talud francés, coincidiendo con el patrón de advección principal observado previamente en otros estudios. Las distribuciones finales también fueron sensibles a las diferentes condiciones hidrodinámicas a diferentes profundidades, destacando la importancia de tener campos de velocidad de corriente en 3D. Aunque, en general, las larvas se retuvieron en el área, se observó una mayor retención cuando los huevos se desovaron sobre la plataforma, en lugar de alrededor de las áreas de rotura de la plataforma o fuera de la plataforma. Este estudio muestra el potencial del método ROOI para aplicaciones marinas y en este caso más específicamente para estudios lagrangianos 3D, agregando valor a las observaciones multiplataforma disponibles.

En esta tesis, la combinación de datos multiplataforma y modelos permitió una caracterización más completa de la hidrodinámica del área de estudio, potenciando el valor de las plataformas de observación disponibles tanto de EuskOOS como externas. Además, el método ROOI emerge como una herramienta convincente para una mejor comprensión de los procesos hidrodinámicos y para aplicaciones marinas en el área y también aplicable en otras áreas. Los resultados obtenidos en esta tesis abren el camino hacia futuras investigaciones sobre las posibilidades que ofrecen los métodos de reconstrucción de datos para mejorar la caracterización de los procesos hidrodinámicos costeros 3D, y su transporte asociado, con el objetivo de una mejor comprensión de los procesos oceánicos en el área para una gestión más sostenible.

SUMMARY

Coastal oceans are key areas of great biodiversity where active biological and geochemical processes occur. A big part of humanity lives in nearby zones and develops a wide range of socio-economic activities such as commercial and recreational fisheries, navigation, tourism, etc., being the most productive areas in the world for mankind. Therefore, coastal areas are heavily affected by human impact, generating the need for sustainable management. This requirement drives the installation of coastal observing systems that provide key information about the characteristics and state of these areas. However, the monitorization is challenging due to the complex hydrodynamics and many times the accessibility for setting up the observing platforms. In addition to the aforementioned factors, the interests of the different stakeholders also affect the design of the observatories.

Despite the data provided by coastal observing systems being crucial for characterizing hydrodynamical processes and monitoring the sea state, the spatial coverage of these data is relatively scarce, especially along the water column. Therefore, methods or approaches to combine data from different observing platforms and/or models are key to obtain a more complete three-dimensional (3D) picture of coastal areas.

Within this general context, this thesis is focused on the southeastern Bay of Biscay (SE-BoB), which is characterized by an abrupt change in the orientation of the coast from an East-West direction along the Spanish coast to a North-South direction along the French coast, with the Capbreton canyon separating both shelves. The slope current (Iberian Poleward Current (IPC)) is the main driver of the circulation, which in winter flows eastward along the Spanish coast and northward along the French coast in the upper 300 m of the water column, whereas in summer the flow reverses, showing weaker and more variable currents. The interaction of the slope current with the abrupt bathymetry of the area triggers the formation of eddies that show surface diameters of ~40–60 km and lifetimes of ~1–5 weeks. In addition to the slope current, wind-driven currents are the main drivers of the surface circulation in the area that in autumn and winter generate a northward and eastward drift over the shelf triggered by southwesterly winds, and in spring and summer a westward and southwestward drift due to northeasterly winds. Over the shelves, tidal and density-driven circulation is weak due to the narrow shelves and the absence of rivers that provide significant density variations, being the currents chiefly subject to the winds and their variability. In the water column, conditions vary significantly depending on the season with stratified and well-mixed conditions around summer and winter, respectively.

The combination of all these features makes the SE-BoB an area of complex hydrodynamics that has a large effect on the distribution of water masses and its constituents such as nutrients, phytoplankton, eggs and larvae of fish species, floating marine litter, pollutants etc., thus influencing biological, geochemical and environmental processes. Given the importance of these processes as well as other social needs of coastal users, the Basque coastal operational oceanography system (EuskOOS) monitors the sea conditions along the Basque coast, providing invaluable data for a better understanding and follow-up of the study area. The observing platforms of EuskOOS that monitor the offshore area are a high-frequency radar (HFR) system which provides hourly surface current velocity fields up to 150 km off the coastline and two moorings which provide current velocity and hydrographic data in the water column (up to -200 m) in the Spanish slope. Despite the data provided by these observing platforms being the most spatiotemporally complete observational datasets in the study area, their spatial coverage is relatively scarce for a complete 3D characterization. Therefore, the main aim of this thesis was to combine the data available from the observing platforms of EuskOOS and also from external sources such as gliders, satellites, drifters, research vessels and models to 3D characterize the hydrodynamics of the study area. To that end, data were jointly analysed and also blended by data-reconstruction methods, which were tested as tools for expanding observations for marine applications, adding value to the available data. To achieve this aim, this thesis was divided into different studies.

Since HFR and altimetry-derived surface currents could complement each other by, for example, validating observations or spatiotemporally expanding them, an assessment of the agreement between both systems was first carried out in *Chapter 3* (note that *Chapter 1* and *2* correspond to the *Introduction* and *Data and Methods* sections, respectively). At the same time, the joint observability of certain seasonal and mesoscale processes such as the slope current and eddies was also evaluated. First, currents across the altimeter-track direction were compared from 2009 to 2015. Since the HFR provides total (geostrophic + ageostrophic) currents, they were filtered, thus removing part of the ageostrophic signal and approaching more to the altimetry-derived geostrophic currents. Despite the limitations of each observing system and their different working principles, concordance between them was observed with correlations up to 0.64 and with the best agreement over the French slope, where the signal of the geostrophic current is higher than in other areas more influenced by ageostrophic currents (e.g., wind-driven currents). Wind-induced currents were also added to the altimetry-derived ones improving the agreement by an increase in correlation of around 10 %. Concerning the detection of seasonal and mesoscale processes, both measuring systems detected the slope current and mesoscale eddies in four independent events, showing a qualitative agreement.

As one of the main circulation patterns, the slope current has already been analysed in the study area by several authors. These analyses were mostly made by independent observing platforms focused on specific regions, for instance, as we did in *Chapter 3* (where only the surface signal was analysed). Some analyses also combined surface and subsurface observations, however, the availability of extended surface and subsurface current velocity observations time series enabled a more complete 3D analysis of the slope current in the study area. This is precisely the objective of *Chapter 4*, where two acoustic current Doppler profilers (ADCPs; co-located on the EuskOOS moorings) and HFR data were jointly analysed from 2009 to 2017. The qualitative comparisons showed that both observing systems detect the seasonality of the slope current, measuring the IPC signal. Moreover, the fluctuations due to rapid wind direction changes were also detected by both platforms at the surface and along the water column. A spatial agreement was also observed between the HFR nodes at the mooring locations and the rest of the nodes of the radar grid at the surface, and among the different depths in the water column, meaning that considering the previous agreement shown between surface and water-column currents, the combination of HFR and ADCP data is suitable for monitoring the slope current in 3D and for blending those data to 3D characterize current velocities.

Then, in *Chapter 5*, the skills and the feasibility of using two data-reconstruction methods for expanding the available current velocity observations in 3D were assessed. To that end, a similar approach to observing system simulation experiments (OSSEs) was used where a numerical simulation was used as *true ocean*. The observations were extracted from the *true ocean* simulating the configuration of the EuskOOS observatory (i.e., two ADCP data in the water column along the Spanish slope and HFR surface currents), then, they were blended, and finally, the reconstructed current velocity fields were compared with the *true ocean* itself. The tested data-reconstruction methods were the discrete cosine transform-penalized least square (DCT-PLS) and the reduced order optimal interpolation (ROOI), which are based on different approaches. The DCT-PLS is based on a penalized least square regression approach that balances the fidelity to the observations and the smoothness of the solution; whereas the ROOI is based on merging the spatial covariances, obtained from historical data (usually from models), and the available observations. The assessments were made for summer and winter periods in order to find out the sensitivity of the methods to different current regimes and vertical conditions (i.e., stratified in summer and mixed in winter). Indeed, both methods showed that they were sensitive to the seasonality of the slope current. Acceptable error levels were obtained in the upper 150 m of the water column, with mean spatial values (for each depth) for most of the cases between 0.55 and 7 cm s^{-1} and mean relative errors of 0.07–1.2 times the root mean square. The addition of two ADCPs along the French coast improved the results. The results showed that both methods can be compelling tools to 3D characterize the hydrodynamics of the study area and that each method performs differently. The DCT-PLS performs better in well-sampled areas and has a simpler set-up, whereas the ROOI performs better in undersampled areas, but needs historical data for setting the covariances (from models in our case) and also needs the tuning of some input parameters.

Coastal eddies are important features that regulate the transport of water parcels and their constituents. These oceanic structures were already analysed at the surface by other authors in the study area, however, little was known about their characteristics in the water column. Therefore, in *Chapter 6*, data from different observing platforms were used to 3D characterize a coastal eddy during a glider campaign. More precisely, data from two gliders, the HFR, a model and a satellite were jointly used. In addition to the joint analysis of observations and thanks to the ROOI method previously tested in the study area, multiplatform observations (i.e., HFR, glider and mooring data) were also used to 3D reconstruct the current velocity fields of the eddy. The eddy depicted a mode-water eddy behaviour, that is, an anticyclonic eddy with an uplift of the isopycnals in the upper water column and a downlift at deeper levels. Although this eddy was slightly smaller, similar characteristics to the ones previously detected at the surface in the study area and in the water column at nearby regions were observed. The ROOI was able to 3D reconstruct current velocity fields in the upper 100 m of the water column under different observational configurations, agreeing with the glider-derived geostrophic currents for the period when the glider crossed the core of the eddy. However, further validation with additional external data is valuable in order to further ensure the robustness of the reconstructions. These reconstructed fields were also used to roughly estimate the cross-shelf transport induced by the eddy in the water column, providing values of the order of magnitude of modelled eddies to the north of the study area. The analyses carried out in this chapter, showcased the power of the combination of multiplatform observations for obtaining complete characterizations of different hydrodynamic features in the study area. At the same time, the use of reconstructed current velocity fields opens the door for further application to other issues, such as the coastal transport of passive particles like nutrients, pollutants or pelagic fish at early life stages (ELS).

In the last chapter, an application of these fields to the study of how hydrodynamic conditions can influence the distribution of the European anchovy (*Engraulis encrasicolus*) at ELS is showcased. The European anchovy is one of the most important fishing species in the Bay of Biscay and it is considered to be one of the pillars of the economy of the Basque fishing sector. European anchovy eggs and larvae are mainly located in the upper part of the water column. Hydrodynamics induce the transport of eggs and larvae of this species until around 30 days after spawning when larvae develop significant swimming abilities. The main spawning areas are the Gironde and Adour river plumes (over the French shelf) and also the shelf-break in some cases. Previous studies indicated that the advection of eggs and larvae are mainly subject to the seasonal wind-driven southwestward pattern, usually advecting them towards shelf-break, slope and open ocean areas. Studies simulating the advection of eggs and larvae that considered higher variabilities than the seasonal one for the 30 days after spawning are scarce and not based on current velocity observations. Therefore, in *Chapter 7*, the advection of anchovy eggs and larvae were simulated for 30 days in order to find out the effects of the hydrodynamics in the ELS of this species and its interannual variability based on observed current velocity data. More specifically, HFR and ROOI-derived (from HFR, one ADCP and model data) current velocity data were used. The initial egg distributions were based on egg abundance data obtained from BIOMAN, which is a survey run every year in May, when anchovy's spawning peaks, that provides spatial egg abundance data at -3 m and also integrated into the upper 100 m of the water column. For the initial abundance data case at -3 m, simulations were run from 2011 to 2018 (excepting 2015 due to scarce current data) forced with HFR currents, and for 2011 and 2013 with ROOI (other years were disregarded due to scarce current data availability). Abundances of the upper 100 m were allocated at -10 m as a representative depth. Therefore, at -10 m, eggs and larvae were advected forced with ROOI for 2011 and 2013. The results showed high interannual variability in the distribution patterns since they were subject to the variability of the instantaneous circulation, however, part of the larvae usually ended up around the French shelf-break and slope agreeing with the main advection pattern previously observed in other studies. Final distributions were also sensitive to the different hydrodynamic conditions at different depths, highlighting the importance of having current velocity fields in 3D. Although, in general, larvae were retained in the area, higher retention was observed when eggs were spawned over the shelf, instead of around the shelf-break or off-shelf areas. This study showcases the potential of the ROOI method for marine applications and in this case more specifically for 3D Lagrangian studies, thus adding value to the available multiplatform observations.

In this thesis, the combination of multiplatform and model data enabled a more complete characterization of the hydrodynamics of the study area, enhancing the value of the available observing platforms both from EuskOOS and external sources. Moreover, the ROOI method arises as a compelling tool for marine applications and for better understanding the hydrodynamic processes held in the area and also applicable in other areas. The results obtained in this thesis paves the way for further investigations on the possibilities that the data-reconstruction methods offer for improving the characterization of 3D coastal hydrodynamic processes, and their associated transport, aiming for a better understanding of the oceanic processes in the area for more sustainable management.

CHAPTER 1

Introduction

1 Background

The ocean covers 71 % of the Earth surface and is essential for regulating climate and weather. It hosts a large number of ecosystems and sustains human activities such as tourism, fishing and transport (Liu et al., 2015). Within the global ocean, coastal oceans represent a small fraction of its area, however, these areas are key since they host great biodiversity, regulate biogeochemical cycles (e.g., carbon and nutrients) and are the most highly productive regions in the world (Holt et al., 2017), providing a wide variety of resources for mankind (e.g., food, renewable energy, recreation, and transport). Indeed, a big part of humanity lives near coastal areas.

The coastal geometry is highly variable with features such as the shelf-breaks, underwater canyons, capes, promontories, estuaries etc. As we approach the coast, hydrodynamics gets more complex as additional processes of different spatiotemporal scales arise, ranging from the general oceanic circulation to higher frequency processes such as slope currents, coastal eddies, coastal upwelling/downwelling, fronts, and jets, among others. Although the monitorization of all these processes is challenging, the major importance of coastal areas has urged the setting-up of coastal observing systems for supporting societal needs and sustainable management of these areas.

1.1 Coastal observing systems

There are diverse configurations of coastal observing systems around the world, where the observing platforms' number, configuration and type vary. On the one hand, the physical, geological, and biological characteristics of the area determine the setting-up of one configuration or another. On the other hand, the needs of the different stakeholders play an important role in fixing the main aims, and therefore the design of the observatory. In this section, a few examples are presented aiming to briefly provide further context to what coastal observing systems are.

For instance, the RAIA observatory located in the North-Western Iberia (Bastos et al., 2016) aims to provide oceanic, biological and meteorological information by means of in situ measurements and numerical model simulations for a better monitorization and a deeper understanding of the study area, as well as for providing a wide variety of products for end-users (e.g., hydrodynamic and biogeochemical model outputs, fecal and pollution distributions, flood maps, oceanographic and meteorological predictions for shell fishing sectors…). The observatory uses data from multiple observing platforms such as moorings, drifting buoys, gliders, high-frequency radars (HFRs) and satellites among others (examples of some platforms are provided in Figure 1.1a) and uses tailored methodologies to monitor the area.

In Germany, the Coastal Observing System for Northern and Arctic Seas (COSYNA; Baschek et al., 2017) aims to better understand the complex interdisciplinary processes and the impact of anthropogenic activities in a changing environment. The observatory is focused on the German Bight and in Svalbard, an Arctic coastal location under strong pressure of global change. It is composed of many observing platforms such as poles, ferry boxes, underwater nodes, wave-buoys, acoustic current Doppler profilers (ADCPs), HFRs and gliders among others (see Figure 1.1b) that provide valuable long-term measurements, also assimilated in models for hindcasts, nowcasts, and forecasts. Moreover, all the data and products are disseminated for scientific or societal applications.

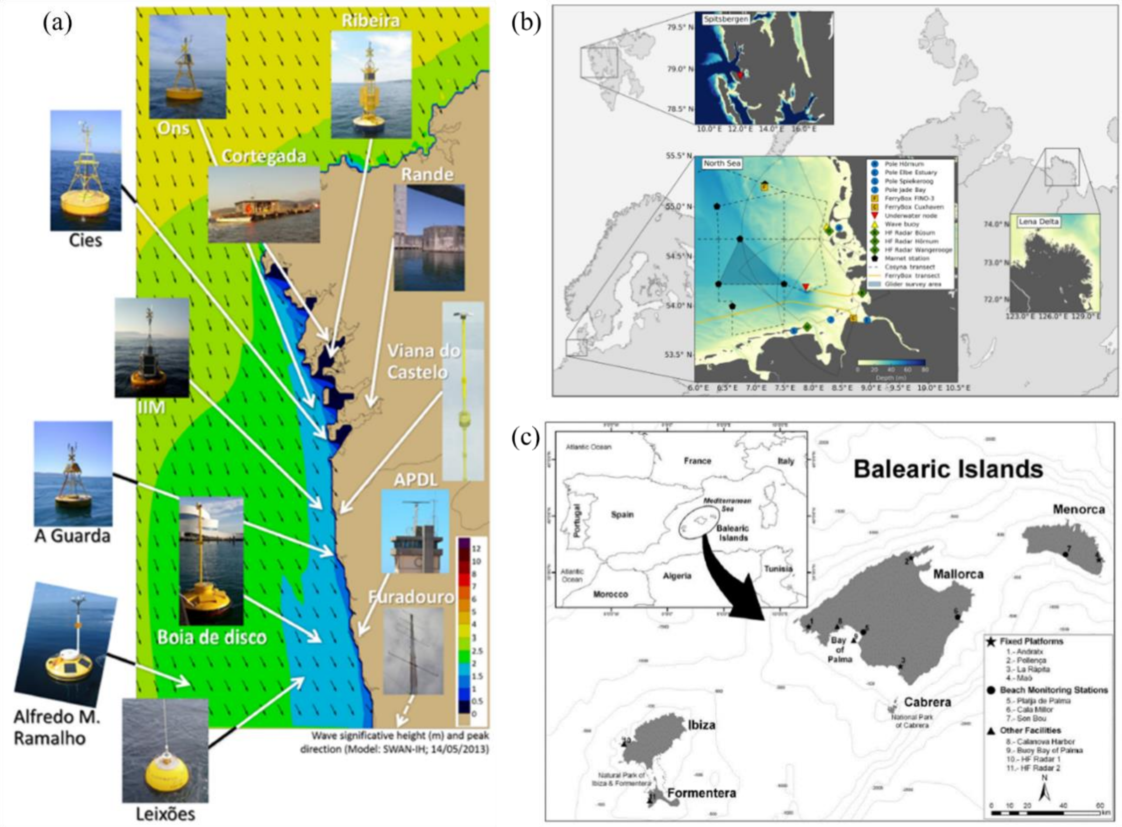

Figure 1.1. *(a) Some observing platforms of the RAIA observatory (from Bastos et al., 2016). (b) Scheme of the COSYNA observatory (from Baschek et al., 2017). (c) Scheme of some observing platforms that composed the SOCIB system in 2013 (from Tintoré et al., 2013).*

In the Balearic Islands, the SOCIB coastal observing and forecasting system (Tintoré et al., 2013) is composed of several observing platforms that extend from nearshore to open ocean. Such platforms are a two-site HFR system, gliders, fixed stations, coastal ocean research vessels, Lagrangian platforms and beach monitoring facilities (see Figure 1.1c). The SOCIB system provides oceanographic data and modelling services to support a wide range of scientific research on issues such as climate change, coastal processes, ecosystem variability etc. while fulfilling societal needs by backing a more science-based ocean and coastal management.

The above-mentioned configurations are only examples of some regional coastal observatories; however, there also exist infrastructures that gather different coastal observatories, like for instance the JERICO-RI in Europe, which is an integrated pan-European multidisciplinary and multiplatform research infrastructure dedicated to the observation of the coastal marine system. JERICO-RI aims to group dispersed coastal observatories around Europe for a better harmonization and consistency (https://www.jerico-ri.eu/, Farcy et al., 2019; Petihakis et al., 2015). The JERICO network constantly works for providing comprehensive observational data, while integrating new observing technologies for expanding its spatiotemporal coverage (Corgnati et al., 2018).

1.2 Multisource data combination and data expansion

One of the drawbacks of the observations in the open and coastal ocean is the spatiotemporally relatively sparse coverage, especially in the water column. Therefore, methodologies that allow combining different observing platforms or expanding the existing data are crucial in order to obtain a more complete picture. To that end, models and observations can be jointly used simply complementing each other, using the observations to validate model outputs or by assimilating the observations into the models. In coastal areas, the combination of observations and models provides an added value to the observations enabling them for a wide range of applications such as monitoring coastal sea level rise, decision-making support, sustainable coastal management, marine search and rescue, port operations etc. (De Mey-Frémaux et al., 2019).

Besides the models, data-reconstruction methods offer a straightforward way to expand observations to nearby areas with a low computational effort. Some of them are able to blend observations from different platforms and even model data. Some of these methodologies are shown in Table 1.1. These methods have been applied to oceanographic datasets for instance to reconstruct 2D current velocity fields (e.g., Barth et al., 2021; Fredj et al., 2016; Hernández-Carrasco et al., 2018b; Taillandier et al., 2006; Yaremchuk and Sentchev, 2009), 3D current velocity fields (e.g., Jordà et al., 2016; Chapman and Charantonis, 2017), sea surface temperature (SST) (e.g., Alvera-Azcárate et al., 2007; Esnaola et al., 2013; Kaplan et al., 1997), sea level rise (Church and White, 2006), sea level pressure (Kaplan et al., 2000), or sea surface salinity (Alvera-Azcárate et al., 2016).

In coastal areas, methods to expand the surface current velocity fields from HFR observations into the upper water column have been also developed in recent years. For instance, the use of multifrequency radars (Barrick, 1972; Broche et al., 1987; Paduan and Graber, 1997; Stewart and Joy, 1974; Teague et al., 2001) or the use of the secondary peaks in the radar echo spectra (Ivonin et al., 2004; Shrira et al., 2001) have been used to obtain the velocity shear. The “velocity projection” method has been also used to obtain subsurface current velocities (Gangopadhyay et al., 2005; Marmorino et al., 2004; Shen and Evans, 2002, 2001).

Table 1.1. Examples of data-reconstruction methods.

Name of the method	Reference
Optimal Interpolation (OI)	Gandin (1965)
Variational Analysis (VA)	Brasseur (1991)
Open-boundary Modal Analysis (OMA)	Kaplan & Lekien (2007)
Data Interpolating Empirical Orthogonal Functions (DINEOF)	Alvera-Azcárate et al. (2005) and Beckers & Rixen (2003)
Self-Organizing Maps (SOM)	Kohonen (1997)
Discrete Cosine Transform Penalized Least Square (DCT-PLS)	Garcia (2010)
Reduced Order Optimal Interpolation (ROOI)	Kaplan et al. (1997)
n-dimensional Data Interpolating Variational Analysis (DIVAnd)	Barth et al. (2014)

1.3 Study area and motivation of the thesis

The study area of this thesis is the coastal area of the southeastern Bay of Biscay (SE-BoB) (Figure 1.2).

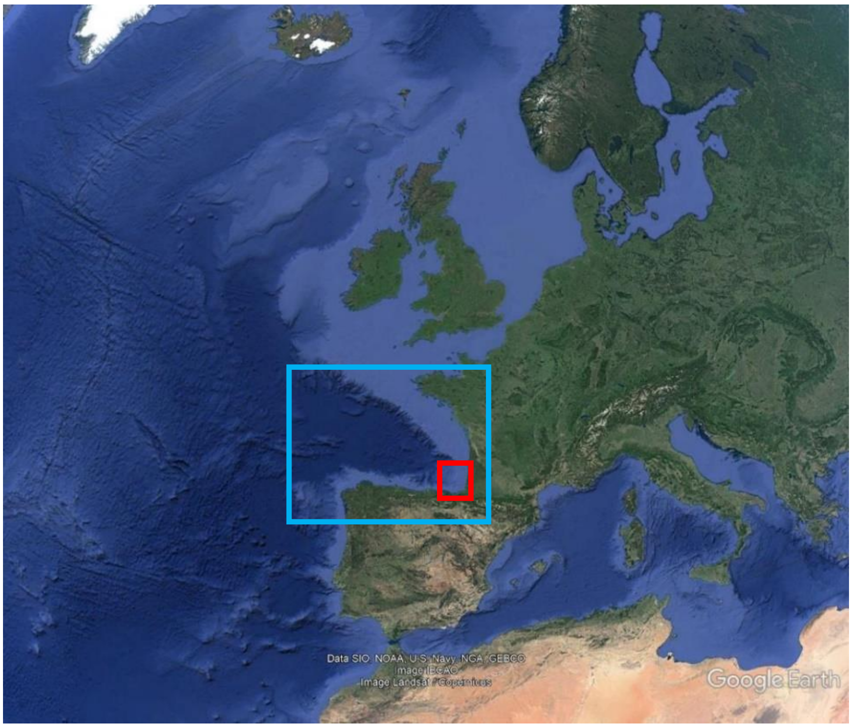

Figure 1.2. Location of the Bay of Biscay (blue square) and the SE-BoB (study area; red square). Figure adapted from Google Earth.

This is an area with complex hydrodynamics that influence different biological and environmental processes such as the advection of eggs and larvae of fish species, of floating marine litter (FML) or of oil spills or other harmful bodies (e.g., jellyfish, algal blooms) that potentially could reach the area. Moreover, they also regulate the transport and retention of phytoplankton and nutrient-rich coastal waters that sustain primary production and therefore the trophic chain. Thus, the monitorization of hydrodynamics is crucial in order to better understand all these processes and carry out sustainable management. This monitorization is continuously performed by the EusKOOS coastal observing system. The area furthest from the coastline is monitored by a HFR system that provides surface current velocity fields and by two moorings set over the Spanish slope that provide hydrodynamical and hydrographic data in the water column. The joint analysis of the data obtained from these observing platforms, as well as from other external platforms (e.g., gliders, drifters, satellites), provides essential information about the hydrodynamics of the SE-BoB.

Despite the invaluable information provided by the different observing platforms and their joint analysis, the spatial coverage is still sparse, especially in the water column. Therefore, a wider 3D characterization of the hydrodynamics is needed to better understand them and their influence on the biological, geochemical and environmental processes. To that end, in addition to the above-mentioned joint analysis, data-reconstruction methods that blend data from different sources and expand the available observations straightforwardly arise as interesting options.

2 Introduction to the study area

The SE-BoB is a complex area, highly influenced by the regional-scale hydrodynamics of the whole Bay of Biscay (BoB) as well as by other factors acting at local scale. In this section, first, the main physical characteristics of the bay are introduced in order to provide information about the surrounding of the study area. Then, the SE-BoB and the EusKOOS observatory are more specifically described.

2.1 The Bay of Biscay

The BoB is an embayment located in the eastern part of the North Atlantic Ocean. In the southern part, it is bounded by the Spanish coast, whereas in the western part it is bounded by the French coast. More specifically, it is latitudinally delimited between 43ºN and 49ºN and longitudinally delimited between 1ºW and 9ºW (Figure 1.3). The most important topographic characteristic of the area is the abrupt change in the orientation of the coast, which turns 90º from the East-West (E-W) oriented Spanish coast to the North-South (N-S) oriented French coast.

As described in Koutsikopoulos and Le Cann (1996) and Lavín et al. (2006) the shelf is narrow along the Spanish coast being 30−40 km wide and with steep slopes (10−12%). Along the French coast the shelf can be divided into two shelves: the Aquitanian shelf, located in the southern part, which is 50−150 km wide; and the Armorican shelf in the northern part, which is around 180 km wide. The French slope is much gentler than the Spanish one, with slopes of around 0.12%. There are numerous underwater canyons, being the main ones: the Capbreton canyon, located in the intersection between the Spanish and the French shelves; and the Cap Ferret canyon located in the Aquitanian shelf.

The general wind circulation is mainly driven by an atmospheric high-pressure area (Azores High) west of Portugal, and a low-pressure area (Iceland low) south of Iceland. Between these two areas, the prevailing winds range from the west to southwest, stronger in winter and weaker and more variable in summer. Therefore, within the BoB, southwesterly winds prevail during autumn and winter, whereas the wind regime changes to west and northwesterlies in summer (OSPAR, 2000).

With regard to the oceanic circulation, the BoB is located in an inter-gyre area between the North Atlantic current (in the subpolar gyre) and the Azores current (in the Northern part of the subtropical gyre). Therefore, the circulation is weak since it is located between cyclonic and anticyclonic regimes. In the Bay, the open ocean circulation is characterized by an anticyclonic circulation with upper water current velocities of around 1−2 cm s^{-1} (Koutsikopoulos and Le Cann, 1996; Pingree, 1993).

Over the slope, the mean currents are relatively weak (5−10 cm s^{-1}) and tend to flow poleward (Pingree and Le Cann, 1990), however, the currents have a strong seasonal variability. This seasonal slope current is known as the Iberian Poleward Current (IPC). During autumn and winter, it travels northward along the Portuguese coast and turns at a right angle in the northwestern Iberia, thus entering the BoB (Frouin et al., 1990; Haynes and Barton, 1990). The IPC intrudes warm and salty waters in the BoB and these intrusions are known as “Navidad Current” (Christmas current in Spanish) since they are usually observed in Christmas time along the Cantabrian coast (Pingree and Le Cann, 1992a). After entering the bay, it flows eastwards along the Spanish coast and, when it is intense enough, it meets the French coast and turns northwards reaching in some cases the Armorican slopes (Charria et al., 2013; Frouin et al., 1990; Garcia-Soto et al., 2002; Pingree and Le Cann, 1990, 1989). In spring and summer, the slope current is reversed with notoriously weaker velocities than in winter (Charria et al., 2013; Pingree and Le Cann, 1990; Rubio et al., 2013a; Solabarrieta et al., 2014).

Over the shelf, the circulation is mainly driven by winds, tides, and density gradients. The wind-induced currents depend on the prevailing wind regimes; therefore, the prevailing northwesterlies will induce southeastward currents in summer and the prevailing southwesterlies will induce northeastward currents in winter (Lavín et al., 2006). The principal tidal component that triggers currents is the semidiurnal tide, however, tidal currents depend on the width of the shelf. Therefore, such currents are strong over the French shelf whereas they are weak over the Spanish one (Le Cann, 1990). The two main sources of continental waters are the Loire and Gironde rivers along the French coast, inducing density currents generally towards the north due to the earth rotation (Koutsikopoulos and Le Cann, 1996).

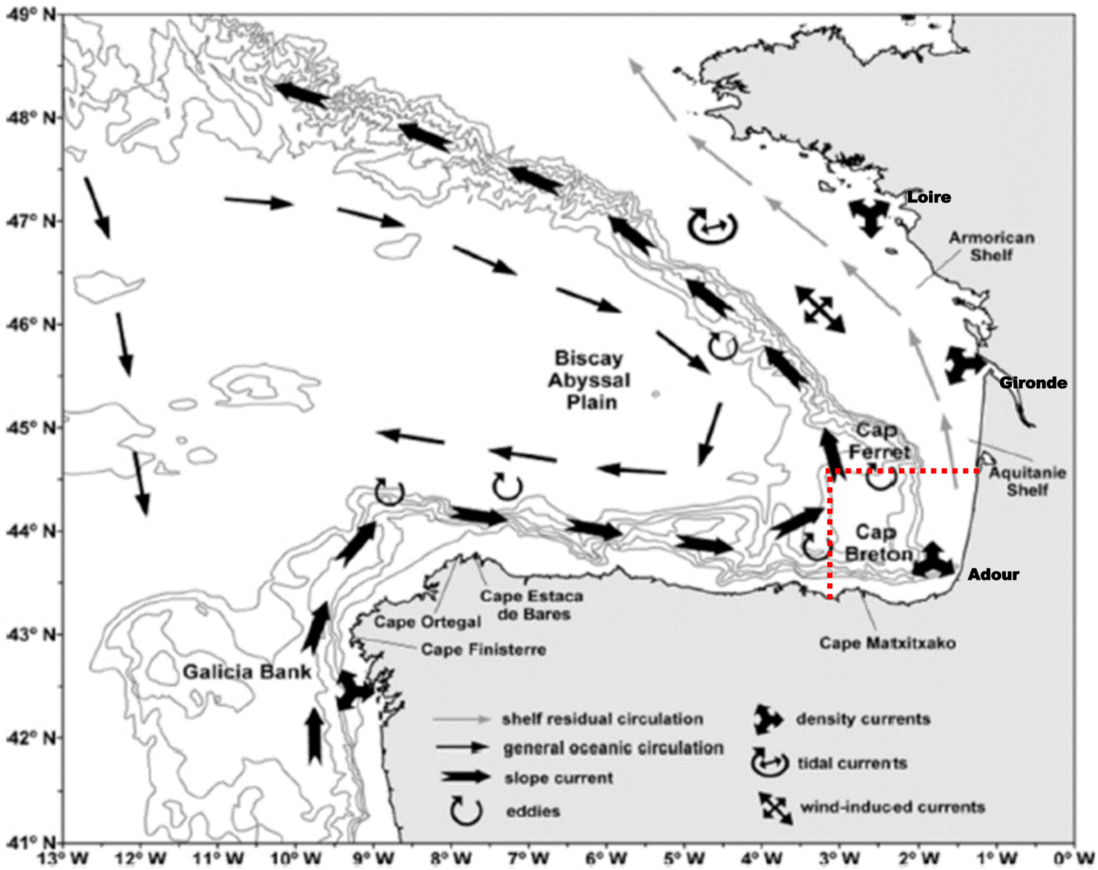

Figure 1.3. *Main characteristics of the mean circulation and hydrodynamic processes in the BoB (adapted from Ferrer et al., 2009). The red dotted lines depict the study area.*

Several studies have related the intensification of northward IPC with the northward favouring southwesterly winter wind regime (e.g., Garcia-Soto and Pingree, 2012; Haynes and Barton, 1990). On the other hand, the interannual variability of the IPC has been also associated with different teleconnections, like the North Atlantic Oscillation (NAO). Several authors have associated a negative NAO index in the preceding months of a January water warming over the slope due to the IPC (Esnaola et al., 2013; García-Soto, 2004; Garcia-Soto and Pingree, 2012; Garcia-Soto et al., 2002; Le Cann and Serpette, 2009; Le Hénaff et al., 2011), however, this relationship is not always fulfilled.

The complex topography causes instabilities in the slope currents that in turn form eddies that inject the shelf and slope water into the open ocean. These are the so-called SWODDIES (Slope Water Oceanic eDDIES; Pingree and Le Cann, 1992b), which are mainly generated in winter when the intensified IPC interact with the abrupt bathymetry. Indeed, in a recent study, Teles-

Machado et al. (2016) observed that a sudden decrease of southerly winds resulted in the development of instabilities in the IPC and generation of eddies in the vicinity of abrupt topographic areas such as canyons, promontories and capes. SWODDIES have diameters of 100 km and can be felt until 1500 m depth. They usually have lifetimes of one year and tend to drift westwards at 2 km/day favouring shelf-open sea exchanges (Pingree and Le Cann, 1992b). Nevertheless, the existence of eddies that remain quasi-stationary for months has been also studied, centered around 44°N−4°W (Caballero et al., 2016b, 2014, 2008b; Garcia-Soto et al., 2002; Pingree and Le Cann, 1992a, 1992b).

It has been observed that although in some of these anticyclonic SWODDIES deep waters are downlifted, the surface ones are uplifted, being a typical behavior of mode-water eddies (McGillicuddy et al., 1999). For instance, Fernández et al. (2004) observed that the seasonal pycnocline of the AE6 anticyclone was uplifted up to 30 dbar, showing a mode-water behavior. The opposite structure also exists, that is, cyclonic eddies where the upper waters are downlifted and deeper waters uplifted. These structures are called cyclonic “thinnies” (named by McGillicuddy, 2015), and a cyclonic “thinny” in addition to a mode-water eddy were observed in the southern part of the BoB by Caballero et al. (2016b) during a glider campaign.

Concerning the hydrography, the upper waters are composed by the Eastern North Atlantic Central Water (ENACW), where two kinds of waters are found: a southern branch of the North Atlantic Current (NAC) (Pollard et al., 1996) and a subtropical branch of Azores current that moves northeastward along the Iberian Peninsula coast (Pingree, 1997; Valencia et al., 2004). The core (bottom) of the ENACW is placed at about −350 (−500) m with a potential density (σ_θ) of 27.1−27.2 (27.2−27.3) (Somavilla et al., 2009). Below the upper waters, the intermediate waters are mainly composed of Mediterranean Waters (MW), and below, the North Atlantic Deep Waters are found (NADW) (Valencia et al., 2004).

2.2 The southeastern Bay of Biscay and the EusKOOS observatory

The main topographic feature of the study area (red square in Figures 1.2 and 1.3) is that the Spanish coast turns 90º to the French coast, with the Capbreton canyon separating both shelves. The complexity of biological, geochemical and environmental processes, as will be described in the following subsections, evidence the need for an infrastructure that monitors the hydrodynamics in the study area. This is fulfilled by EuskOOS.

2.2.1 Physical characteristics

The slope current (IPC) is the main driver of the circulation that in winter flows in the upper 300 m of the water column (Le Cann and Serpette, 2009). As described in the previous section, it flows eastwards along the Spanish coast and northwards along the French coast. Indeed, the surface current velocity fields provided by an HFR system in the study area corroborate this pattern (Solabarrieta et al., 2014). In addition, Rubio et al. (2013a) observed mean slope current velocities of 40−50 cm s^{-1} and 20−30 cm s^{-1} in the upper 150 m of the water column in two slope moorings located in front of cape Matxitxako (Matxitxako mooring) and San Sebastian (Donostia mooring) respectively (see Figure 1.4), from November to January between 2007 and 2009. Also, Solabarrieta et al. (2014) observed maximum current velocities of 70 cm s^{-1} in Matxitxako mooring. The slope current was better sampled in Matxitxako mooring than in Donostia mooring since the latter is anchored in the area where the slope changes the orientation and where the Capbreton canyon is located (Rubio et al., 2013a). The situation in summer changes, with a reversed flow that is 3 times weaker and more variable than in winter (Solabarrieta et al., 2014).

Along with the slope circulation, wind-induced currents are the main drivers of the surface circulation in the area (e.g., Lazure, 1997; Solabarrieta et al., 2015). During autumn and winter, southwesterly winds dominate and generate northward and eastward drift over the shelf. The wind regime changes to the NE during spring, when it causes currents to turn towards the W and SW along the Spanish coast and with a similar situation during summer. However, the weakness of the winds and the greater variability in the direction make currents more variable in the latter seasons (González et al., 2004; Lazure, 1997; Solabarrieta et al., 2015). During spring and summer, the prevailing weak and not persistent northeasterly winds produce weak coastal upwelling. In autumn and winter, when stronger and more persistent southwesterly winds predominate, more frequent and intense coastal downwelling events are triggered (Borja et al., 1996).

Note that over the shelf, the currents are mainly wind-induced since tidal currents are weak due to the narrow shelf and the lack of rivers that induce large density currents (González et al., 2004; Ibañez, 1979). In the study area, the main source of continental water is the Adour river (Valencia et al., 2004), however, the extension of the river plumes in this area is highly variable, being their effect subject to oceano-meteorological conditions (Ferrer et al., 2009). North to the study area the Gironde river also provides important inputs of continental waters that can easily reach the study area.

In the upper water column, hydrographic properties measured by Matxitxako and Donostia slope moorings show a marked seasonal variability. Whilst in winter, the water column is well-mixed, in summer, is stratified with mean thermocline depths ranging from −30 to −50 m (Rubio et al., 2013a). Indeed, the surface currents have a higher correlation with subsurface currents during winter than during summer (Rubio et al., 2013a; Solabarrieta et al., 2014).

Surface signatures of several coastal anticyclonic SWODDIES were observed centered around 43.8°N−2.5°W (Rubio et al., 2018). These SWODDIES originated mainly in winter after the relaxation of strong winter slope current events and had diameters of ~40–60 km and lifetimes of ~1–5 weeks.

2.2.2 Biological, geochemical and environmental aspects related to hydrodynamics

Hydrodynamics has a large effect on the environment and biology in the BoB (e.g., Koutsikopoulos and Le Cann, 1996; Lavín et al., 2006). Although in the SE-BoB nutrients are mainly provided by rivers (mainly by Adour and Gironde), oceanic structures such as eddies can also uplift them from deep waters to the photic layer, thus favouring phytoplankton growth. Typically, anticyclones tend to downwell nutrients in their cores, whereas cyclones tend to upwell them. However, it has been observed that some anticyclonic SWOODIES tend to uplift waters in the upper water column in the southern BoB (e.g., Caballero et al., 2016b; Fernández et al., 2004; Garcia-Soto et al., 2002; Pingree and Le Cann, 1992b) showing higher chlorophyll-a (Chl-a) abundances in their cores compared to the surrounding waters. Moreover, Caballero et al. (2016b) observed higher retention rates of Chl-a in anticyclones than in cyclones near the study area and suggested that anticyclones provide more favourable conditions for primary production. Therefore, the presence of SWODDIES in the study area could influence the distribution of phytoplankton and affect primary production.

The transport and retention patterns of water parcels vary at interannual, seasonal, and even daily scales in the study area, influenced by oceanic processes such as the general circulation, wind-driven currents, mesoscale eddies, and fronts (Rubio et al., 2020). For instance, Rubio et al. (2018) observed that eddies can induce surface cross-shelf water export as well as their retention in the area. However, little is known about cross-shelf transport and retention patterns in the water column.

These transport and retention patterns influence many biological, geochemical and environmental processes in the SE-BoB. The fate of phytoplankton and nutrient-rich waters depends directly on them, influencing primary production and hence the sustainability of the trophic chain. Transport patterns also influence the distribution of eggs and larvae of European anchovy (*Engraulis encrasicolus*), which is considered one of the pillars of the economy of the Basque fishing sector. Food availability and the predation risk are important factors to be considered to understand its recruitment. In addition, hydrodynamics also plays a role in that process mainly in early life stages (ELS). In the SE-BoB the main spawning areas are the Gironde and Adour river plumes and partially the shelf-break areas, and the spawning peaks in May-June (Motos et al., 1996). Several studies suggest that, in general, larvae are advected from the shelf to off-shelf areas (shelf-break, slope and open ocean) of lower predation risk but still productive enough, usually in a southwestward direction driven by northeasterly winds (Boyra et al., 2016; Cotano et al., 2008;

Irigoien et al., 2008; Uriarte et al., 2001). However, this pattern is variable since it is affected by different factors such as the variability of the wind regime (Irigoien et al., 2008). Later, larvae return to the shelf as mobile juveniles. Borja et al. (1998, 1996) observed that high recruitment is related to northeasterly upwelling-favouring wind regimes probably due to the off-shelf transport that it produces, which at the same time is linked to the negative East Atlantic (EA) teleconnection (Borja et al., 2008). On the other hand, Irigoien et al. (2008) suggested that the coincidence in space and time of SWODDIES with anchovy spawning could favour its recruitment by advecting eggs and larvae to off-shelf areas and still retaining them near the shelf-break.

From an environmental perspective, the SE-BoB is an area prone to accumulate marine litter (Declerck et al., 2019; Pereiro et al., 2019; Van Sebille et al., 2012) and unlike expected, the sea-based origin of FML represents a remarkably higher contribution than the land-based one (Ruiz et al., 2020). During summer, the FML shows significant retention in the southern area due to the wind-driven circulation, whereas during autumn and winter, the prevailing northward circulation favours coastal flushing (Declerck et al., 2019). Destang-Quelen et al. (2019) observed similar patterns.

Hydrodynamics also have a direct influence on the advection of oil spills that could be discharged due to shipping accidents. For instance, in 2002 the Prestige oil tanker sank off the northwestern coast of Spain releasing 63,700 tons of fuel. The oil slick rapidly reached the coastline of Galicia and progressively the coasts of the BoB. The arrival of the black tide to the northern Iberian coastline showed the need for platforms that allow monitoring the ocean dynamics in the study area (González et al., 2008). Other dangerous bodies could also reach the Basque coast such as the jellyfish which has shown to be strongly affected by wind-driven surface currents (Ferrer et al., 2015).

2.2.3 EuskOOS: the Basque coastal operational oceanography system

EuskOOS (www.euskoos.eus) is the Basque coastal operational oceanography system that belongs to the Basque Government and is operated by Euskalmet (the Basque Meteorological Agency) with the expert advice of AZTI. EuskOOS has three main goals: to provide an accurate description of current sea conditions along the Basque coastline, to offer ongoing forecasts of future sea conditions and to supply ocean-meteorological products to Basque coastal users. For that purpose, EuskOOS' observing system is equipped with several observing platforms along the Basque coast that have been installed sequentially in time since 2003 (Figures 1.4 and 1.5):

- The Matxitxako and Donostia moorings: Deep water buoys that provide meteorological data such as air temperature, atmospheric pressure, wind direction and intensity, visibility, and solar radiation; as well as temperature, salinity, and water current data in the upper 200m of the water column. Since 2013, the Matxitxako buoy is not working anymore.

- The Bilbao, Pasaia and Mutriku coastal stations: Fixed stations that provide wave height and period, seawater temperature at 5 depths, sea surface height (tide), atmospheric pressure, air temperature, wind direction and intensity, visibility, and solar radiation data.
- The Bermeo and Pasaia high-frequency tidal gauges provide sea level data.
- The Matxitxako and Higher HFR antennas: These are the antennas of the HFR (CODAR) system that provide surface current velocity data.

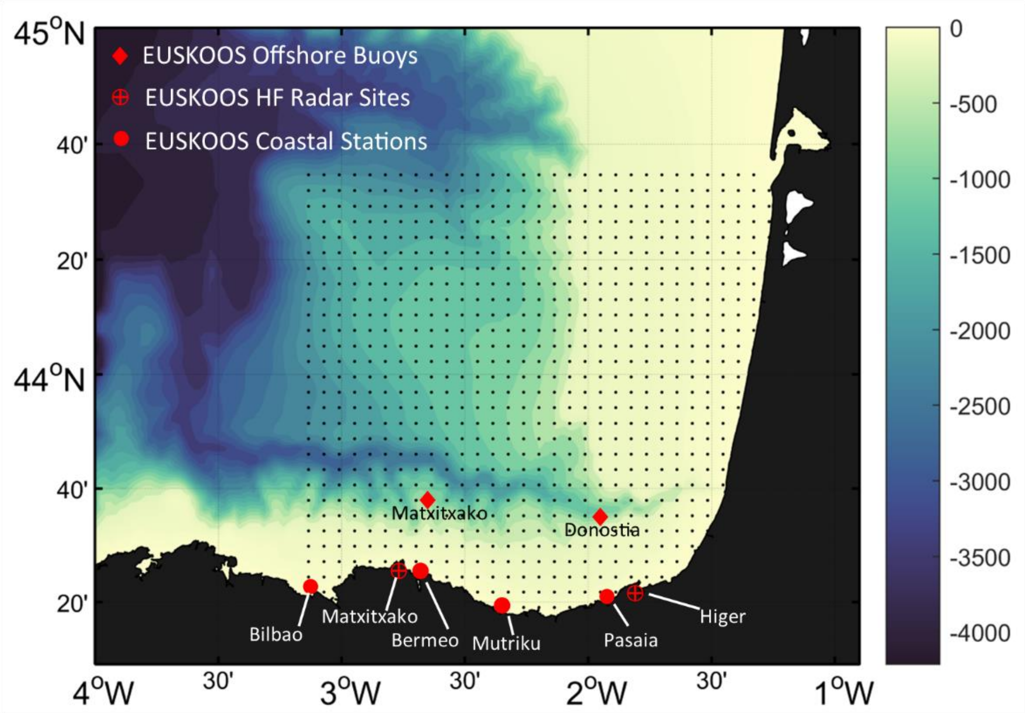

Figure 1.4. *Distribution of the different observing platforms within EuskOOS. The colorbar depicts the bathymetry in meters.*

All the data provided by these platforms are connected to European data portals like EMODnet (https://www.emodnet-physics.eu/Portal/) and Copernicus (https://marine.copernicus.eu/), excepting the tidal gauges and the Mutriku coastal station. Additionally, coastal videometry stations are set along the largest beaches of the Basque coast and a forecast model provides surface current, temperature, and salinity information.

Observations are used for better characterizing the physical, biological, geochemical and environmental oceanic processes of the area such as the ones shown in previous sections, as well as for several applications related to different needs. For instance, the availability of oceano-meteorological data series has permitted to better understand the link between several variables and the potential damage of extreme coastal events or to improve the warning service to alarm the population. The data from EuskOOS could be also used in pollution control or maritime rescue and safety issues by predicting the direction of spills in order to local authorities make decisions, by forecasting the arrival of jellyfish and algal blooms to our coasts and beaches, or by searching for people in shipwrecks events or falling into the sea. In addition, EuskOOS data is available for those in charge of the management and safety of activities carried out along the coast such as diving, sports sailing, recreational fishing, beach football competitions etc.

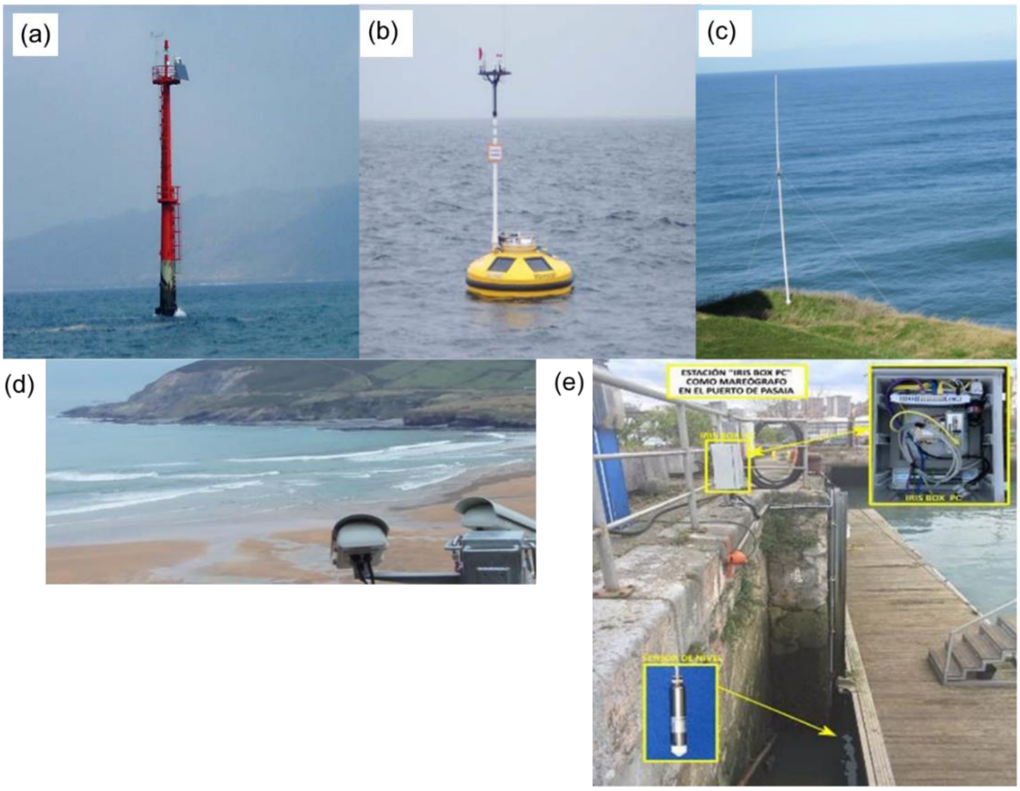

Figure 1.5. *Observing platforms of EuskOOS. (a) Pasaia costal station. (b) Donostia mooring. (c) Matxitxako HFR antenna. (d) Coastal videometry. (e) Pasaia high-frequency tidal gauge.*

3 Hypothesis, aim and objectives

3.1 Working hypothesis

The working hypothesis is a “provisional, working means of advancing investigation” which could lead to the discovery of unforeseen, but relevant facts during the progress of the research (Dewey, 1938; Shields and Tajalli, 2006). As such, the working hypothesis has helped to establish the connection between the questions posed for the research and the evidence observed, and it can be constructed as follows:

“*SE-BoB submesoscale to seasonal coastal hydrodynamic processes and their associated transports are only resolved partially by the different available observing systems, a more complete characterization of their complex 3D hydrodynamics (towards potential marine applications) can be obtained by the combination of multiplatform and model data.*”

3.2 Aim and objectives

Since little is known about the 3D circulation in the SE-BoB, the main aim of this thesis is to combine the available observations by jointly analysing them and blending them to 3D reconstruct current velocity fields by data-reconstruction methods obtaining tools to 3D characterize the hydrodynamics of the area for better describing physical, geochemical, environmental, and biological processes.

In order to fulfil the general aim, specific objectives are set:

1. To obtain a diagnosis of the agreement between surface currents measured by altimetry and HFR over the SE-BoB and to evaluate the observability of certain seasonal and mesoscale processes by both measuring systems in the study area. (*Chapter 3*)
2. To showcase the combination of HFR and ADCP data for monitoring the slope current (IPC) and its seasonal variability in the SE-BoB. (*Chapter 4*)
3. To assess and compare the skills of two data-reconstruction methods in terms of current velocities to evaluate the feasibility of using such methods in the study area for blending multiplatform observations. (*Chapter 5*)
4. To characterize the 3D properties of a coastal mode-water eddy and quantify the induced cross-shelf transport by means of a multiplatform data approach and a data-reconstruction method, while assessing the skills of the method for reconstructing mesoscale processes in the study area. (*Chapter 6*)
5. To simulate the advection of European anchovy eggs and larvae in the study area for several periods forced with current velocity observations, from HFR data and reconstructed fields, for the first time for a better understanding of the effect of the hydrodynamics in the ELS of this species. (*Chapter 7*)

4 Structure of the thesis

The next chapter (*Chapter 2*) describes the data and methods used along the thesis. Then, in the following five chapters (*Chapters 3*−7), different research themes are presented. Due to the disparity of the contents addressed during those chapters each one is presented as an individual scientific paper with its own sections and writing style. In this manner, some redundant information has been inevitably included in the *Introduction* and *Data and Methods* sections. Note that *Chapter 7* does not correspond to a scientific paper, but it has been formatted as such since its contents can be potentially submitted to a journal. In the last chapter (*Chapter 8*), the main conclusions and the thesis are presented.

CHAPTER 2

Data and Methods

In order to fulfil the objectives of this thesis, data from different sources and several methodologies including 3D data-reconstruction methods and Lagrangian diagnostics were used. Before presenting the main results of the thesis in the following chapters, data and methods are here introduced. Although many of the information will be repeated along the thesis, a more complete description is here provided showcasing that the combination of the multiplatform data, model data and methods enable a more complete 3D picture of the study area.

1 Data

In this section, the observing platforms and models used in this thesis are described as well as the data obtained from them. The observational data provided by different platforms are complementary in space and time as evidenced in Table 2.1. While the EuskOOS HFR and moorings were specifically set to monitor the study area and provide the most spatiotemporally complete real time observational data, a set of complementary observations and models were also used, depending on the needs of the different studies undertaken. In the case of models, although they cover the 3D space and provide invaluable information, the provided data is not fully real but simulated.

The depicted observing platforms and the models are widely used data sources for the characterization of oceanic properties and circulation. Indeed, these data sources are currently considered mature, being the role played by the technological advances in the last decades crucial in their evolution.

Table 2.1. *Summary of the data sources used in this thesis, the provided data and their spatial coverage.*

Source	Provided data	Spatial coverage
HFR	Current velocities	Surface grid
Moorings	Temperature, Salinity and Current velocities / Wind velocities	Vertical profiles / Surface point
Gliders	Temperature, Salinity and Chl-a concentration / Integrated currents	Vertical profiles along trajectories / One value for each vertical profile
Satellites	SST, Chl-a concentration and SLA	Surface maps and straight tracks
Drifters	Water parcel trajectories	Horizontal trajectories
Research vessels	Anchovy (*Engraulis encrasicolus*) eggs abundances	Transects perpendicular to the coast
Models	Temperature, Salinity, and Current velocities / Wind velocities	3D grid / Surface grid

1.1 EuskOOS coastal observing system

Coastal hydrodynamics in the SE-BoB, are operationally monitored by the EuskOOS coastal observing system. In addition to a series of coastal stations (see *Section 2.2.3* in *Chapter 1*), the monitorization of the SE-BoB is carried out by one HFR system since 2009 and one slope mooring (Donostia mooring) since 2007 located along the Spanish coast. In the period 2007–2013, an additional slope mooring (Matxitxako mooring) was also located along the Spanish slope (see Figure 2.1).

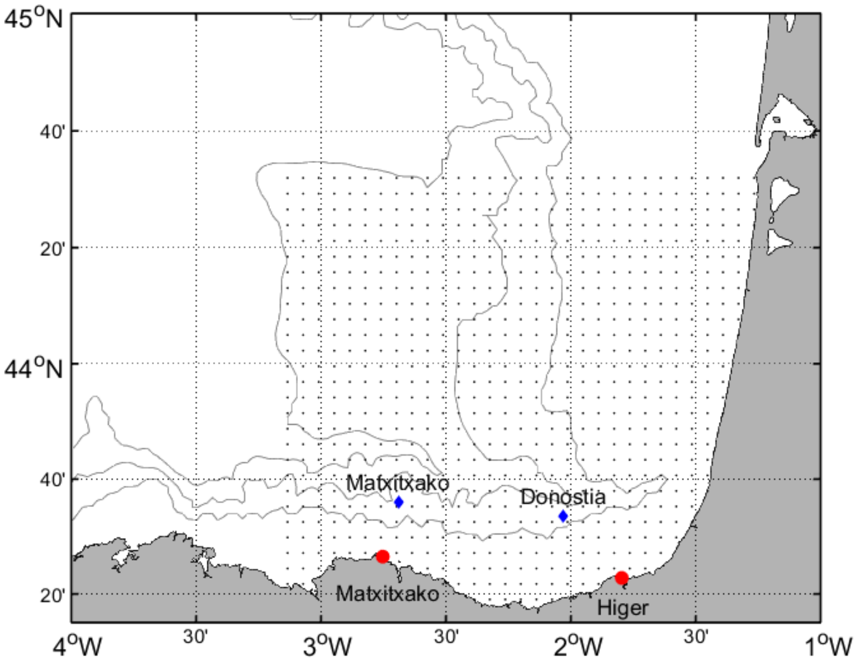

Figure 2.1. *Map of several components of the EuskOOS observing system. The HFR sites are depicted by red points, whereas the moorings are shown by blue diamonds. The grey dots show the grid points where the HFR system provides surface current fields. The grey lines depict the 200, 1000 and 2000 m isobaths.*

1.1.1 The HFR system

In general, HFR systems are composed of antennas located at least at two separated sites that send radio waves to the ocean surface and use the signal backscattered by the waves to infer the radial velocity of the surface current, toward or away from each antenna. Typically operating in the 3–30 MHz band, HFRs can provide real-time measurements with a relatively wide spatial coverage (up to 200 km from the coast) and high spatial (300 m–10 km) and temporal resolution (one hour or less). The resolution, maximum range, and integration depth (ranging from tens of cm to 1–2 m) depend on the operating frequency and the used bandwidth (see Rubio et al., 2017).

Figure 2.2. *(a) Higer receiver antennas, (b) Higer transmitter antenna and (c) Matxitxako transmitter antenna (upper antenna) and receiver antennas (bottom antenna).*

The HFR EuskOOS system is a CODAR (SeaSonde) system that consists of two sites located strategically in capes: Higher and Matxitxako (see Figures 2.1 and 2.2). Each site consists of a transmitter and 3 receiver antennas set together (two loop antennas oriented orthogonal to each other and one monopole antenna). The transmitter antennas work at a central frequency of 4.463 MHz with an operational bandwidth of 30 kHz. The footprint area covers ~150 km off the coast and the integration depth is ~1.5 m. The system has provided hourly current velocity fields gridded onto a 5 km resolution regular orthogonal mesh since 2009, with some interruptions mostly due to maintenance stops or malfunctioning related to severe atmospheric conditions. Since the deployment of the HFR system, the receiving antenna pattern of the two HFR sites has been calibrated at least every 2 years. The performance of this system and its potential for the study of ocean processes and transport patterns have already been demonstrated by previous works (Rubio et al., 2018, 2011; Solabarrieta et al., 2016, 2015, 2014).

The working principle of the HFRs is based on the Bragg scattering. An omnidirectional signal of λ wavelength is sent by the transmitter and the signal is backscattered by the wave crests. When the wavelength of the waves is $\lambda/2$, the backscattered signals in radial direction interfere constructively since they travel an extra distance proportional to λ and therefore are in phase. This is the Bragg scattering phenomena and it will result in a resonant intensity peak in the detected spectra (first order Bragg peak, see Figure 2.3). The range each spectrum corresponds to is determined by the time the signal needs to go and come back to the transmitter/receiver antennas. In our case, one spectrum is obtained every 17 minutes for each range and in order to remove noise and unwanted echoes from ships the spectrum is running averaged twice finally obtaining an hourly spectrum. From these spectra the radial current velocities can be inferred due to the doppler shift (Δf) between the modelled position of the wave's peaks (f_w) and the observed position of the peaks shifted by the currents (see Figure 2.3).

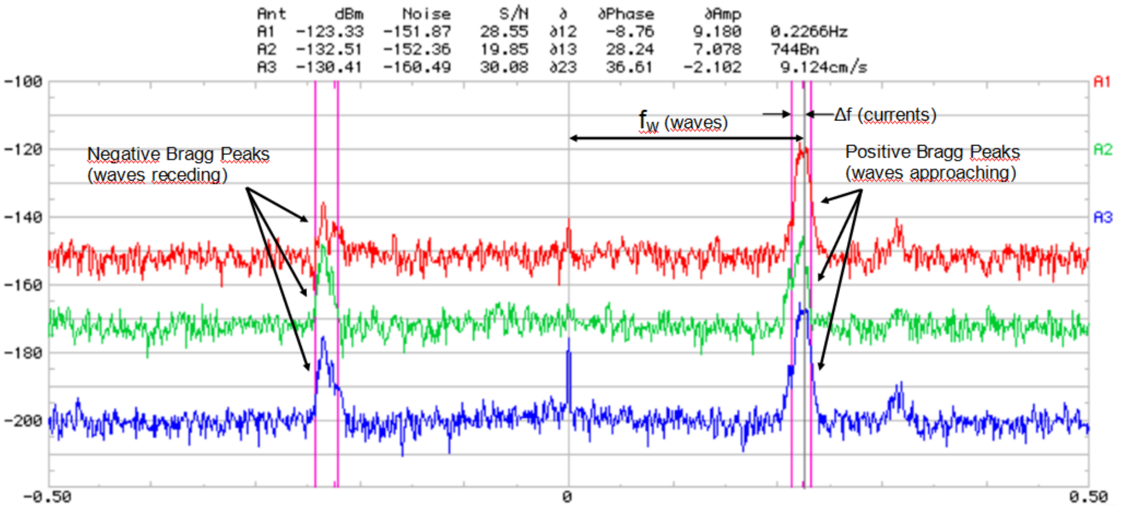

Figure 2.3. *Example of a real spectra where the red, green and blue colours correspond to each of the receiver antennas (courtesy of Qualitas Remos).*

To estimate the angle where the radial current velocities come from (i.e., the bearing) the CODAR systems use the Direction Finding (DF) method (Kohut and Glenn, 2003). However, in practice, a more robust algorithm developed by Schmidt (1986) called MUSIC (MUltiple SIgnal Classification) is used. Thus, hourly current velocities in radial directions are obtained for a given grid of bearings, built using a fixed angular resolution of 5º, with typical errors between 2–3 cm s^{-1} (Figure 2.4a).

In order to obtain surface current velocity maps, radial current velocities are combined in a regular orthogonal grid of 5 km resolution. To that end, the radial current velocities are decomposed in zonal and meridional directions and a least-square fitting is carried out considering all the velocities inside a circle of 10 km of radius centered at each grid point (Figure 2.4b). This is made using the HFR_Progs Matlab package (https://cencalarchive.org/~cocmpmb/COCMP-wiki/index.php/Main_Page#HFR_Progs_Documentation), based on Gurgel (1994) and Lipa & Barrick (1983).

When the angle between the radials from the two radar sites is too small, the orthogonal direction is not well resolved. This is the so-called Geometric Dilution Of Precision (GDOP; Chapman et al., 1997) and it usually occurs at the edges of the grid and along the baseline that connects the two radar sites. Thus, the data obtained from areas where angles between radials are lower than 30º are disregarded (as shown in Figure 2.4c). To ensure the best quality of the data, currents are also post-processed using procedures based on velocity and variance thresholds, signal-to-noise ratios, and radial total coverage, following the recommendations of Corgnati et al. (2018) and Mantovani et al. (2020). Since May 2019 EuskOOS HFR data are sent in real time towards the European HFR node and Copernicus Marine Environment Monitoring Service (CMEMS) In Situ TAC and shared as part of the current products INSITU_GLO_UV_NRT_OBSERVATIONS_013_048 and INSITU_GLO_UV_L2_REP_OBSERVATIONS_013_044 at https://marine.copernicus.eu/access–data. In addition, EuskOOS HFR data is available at EMODnet European data portal as part of the EP_MAP_RVFL_001 product at https://catalogue.emodnet–physics.eu.

Spatial and temporal data gaps are habitual in HFR current velocity fields due to GDOP and other errors due to severe atmospheric conditions, severe ocean wave conditions, radio interferences, software and hardware malfunction etc. Different techniques are used to fill spatial gaps in HFR datasets, being the open-boundary modal analysis (OMA, Kaplan and Lekien, 2007) the most widely extended one. Indeed, in addition to the standard total current maps, the EuskOOS HFR fields are routinely spatially gap-filled by this method (as in Figure 2.4d) with HFR_Progs. This method is based on the estimation of a set of linearly and time independent modes, estimated before they are fit to the data, which describe all the possible current patterns. Then the weight given to each mode is estimated by fitting them to velocity measurements. In our case 85 OMA modes, built setting a minimum spatial scale of 20 km, were used.

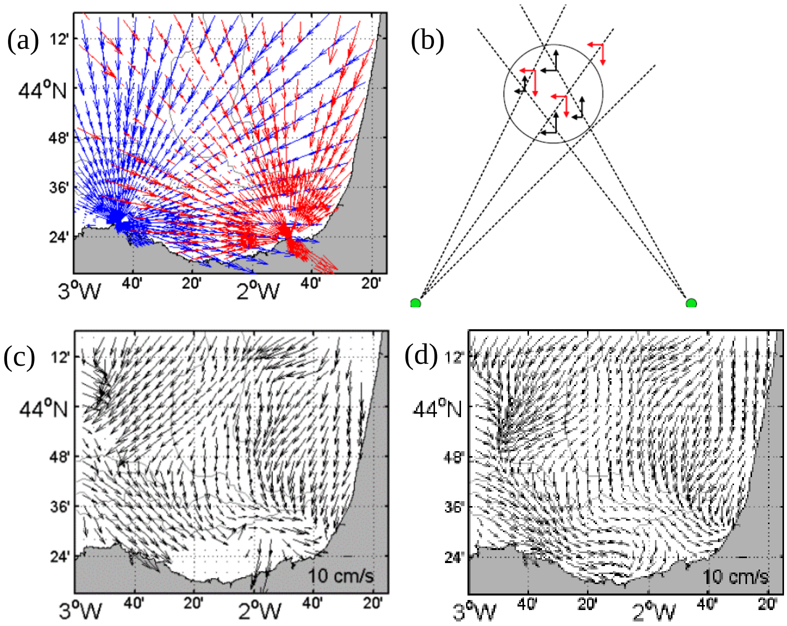

Figure 2.4. *(a) Example of radial current vectors for Higer (red) and Matxitxako (blue) stations. (b) Scheme of the radial current vectors decomposed in zonal and meridional directions inside a circle of 10 km of radius centered at one grid point. (c) Example of a final current velocity field. (d) Example of the corresponding gap-filled OMA current velocity field.*

1.1.2 Moorings

The Donostia mooring is anchored in a water depth of 550 m in the Spanish slope (at –2.03º E, 43.56º N, see Figure 2.1) and has been providing data since 2007. The Matxitxako mooring was anchored in a water depth of 450 m in the Spanish slope (at –2.69º E, 43.6º N, see Figure 2.1) and provided data from 2007 to 2013. In this thesis, data from both moorings (Wavescan buoys) were used to analyse the hydrographic and hydrodynamic properties of the water column, therefore, although other parameters were also measured by different sensors (see *Section 2.2.3 in Chapter 1*), only details about salinity, temperature, pressure, and current velocity measurements are provided in this section. The hydrographic data are measured by conductivity and temperature (CT) devices and one conductivity, temperature, and depth (CTD) device, whereas current velocities are measured by a downward-looking ADCP (see Figure 2.5). The data is sent in real-time to land by satellite connection; however, it is also stored in the individual sensors and recovered at each maintenance operation (~every 6–9 months). The performance of these sensors has been already demonstrated, for instance in Ferrer et al. (2009), Rubio et al. (2013a, 2011) and Solabarrieta et al. (2014). The mooring data is available as part of the CMEMS INSITU_IBI_NRT_OBSERVATIONS_013_033 product at https://marine.copernicus.eu/access–data.

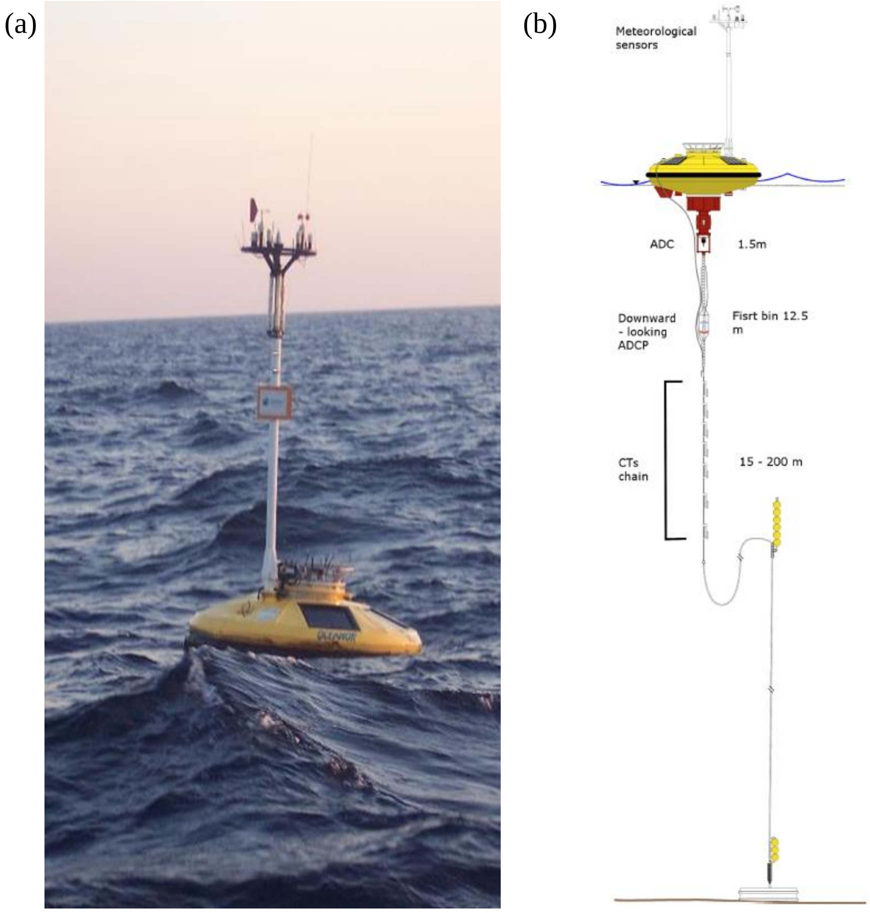

Figure 2.5. *(a) Donostia mooring. (b) Scheme of the mooring (by C. Hernandez).*

1.1.2.1. CTs and CTDs

CTDs are devices that can be set along the mooring line to measure conductivity (from which salinity can be derived), temperature and pressure. With salinity and temperature, density data can be also inferred, thus providing a complete description of the hydrography of the water column. Note that when they only have temperature and salinity sensors, it is called CT. The temperature is measured by a thermistor, whereas salinity is estimated by measuring the conductance of a submerged probe from which, with the probe’s dimensions, conductivity is obtained and thus salinity is estimated. The pressure is measured by a strain gauge sensor that detects the external pressure exerted on the gauge.

At the EuskOOS moorings, several CTs (Seabird SBE37IM) provide hourly temperature and conductivity data at –10, –20, –30, –50, –75 and –100 m. In addition, a CTD is located at –200 m. These data are quality controlled following standard procedures (Petit de la Villéon et al., 2005).

__Figure 2.6.__ A Seabird SBE37IM CT as the ones installed on EuskOOS slope moorings (from https://www.seabird.com).

1.1.2.2. ADCP

ADCPs measure current velocities at different depths, providing profiles of current velocities at several predefined bins, along the water column. The working principle is the Doppler effect. An acoustic signal pulse is sent from the transducer and then backscattered by small particles or plankton that drift along with the currents. Since these particles are moving towards or away from the transducer, the backscattered signal has a Doppler shift with respect to the emitted one, therefore, the current velocity in the beam radial direction is estimated by the difference in frequency between both signals. The combination of radial current velocities from differently oriented beams enables the estimation of horizontal and vertical currents. The measurements for different ranges are differentiated by range-gating the backscattered signal of each pulse.

The EuskOOS downward-looking ADCP (RDI Workhorse) works at a frequency of 150 kHz providing hourly current velocities with bins of 8 m depth starting at a depth of –12.26 m and extending down 200 m along the water column. For the raw ADCP data, beam amplitude and correlation magnitudes and vertical velocity errors were used for the data processing and quality tests, following Bender and DiMarco (2009).

Figure 2.7. *An RDI Workhorse ADCP as the ones installed on EuskOOS slope moorings.*

1.2 Complementary data in the area covered by EuskOOS

In this section additional data sources to the EuskOOS observing platforms used in this thesis are described.

1.2.1. Gliders

Gliders are Autonomous Underwater Vehicles (AUVs) that profile the water column through different routes (e.g., Davis et al., 2002; Rudnick, 2016). These type of AUVs do not use propellers or propulsive machinery for underwater manoeuvring and are silent and easy in underwater environment (reduce acoustics signal and pollutions). Gliders propel themselves by changing buoyancy and using wings to produce forward motion “flying” underwater along slightly inclined paths. The buoyancy is controlled by a change in volume generated by filling an external oil bladder and pitch and roll can be controlled by modifying the internal mass distribution to achieve the desired angle of ascent/descent. They follow saw-tooth patterns, and during each surfacing, a two-way communication system via satellite is established. Data is downloaded in near real time (NRT) from land and new commands for navigation are sent at each surfacing. The high efficiency of the propulsion system enables gliders to be operated for several months, during which they can cover thousands of kilometres.

Temperature, salinity, pressure, Chl-a and integrated currents data from one glider mission were used in this thesis: the BB-Trans glider mission (see Figure 2.8). This mission was run by AZTI (Pasaia, Spain) in collaboration with the Helmholtz-Zentrum (Geesthacht, Germany) in the frame of the Jerico-Next European project Transnational Actions (https://www.jerico–ri.eu/ta/selected–projects/second–call/bb–trans/), from 16 May 2018 until 14 June 2018. During this mission, two Teledyne Slocum Electric G2 gliders were deployed: the Sebastian shallow-water glider (0–100 m depth) and the Comet deep-water glider (0–1000 m depth). Temperature, salinity and pressure data were obtained from a CTD (Seabird SBE41 at 1 Hz), whereas the Chl-a data were obtained from a fluorescence-turbidity (Wetlabs FLNTU at 1 Hz) sensor. The average water column current velocities or integrated current velocities were obtained thanks to the differences between the glider and position fixes (measured with GPS) along their trajectories.

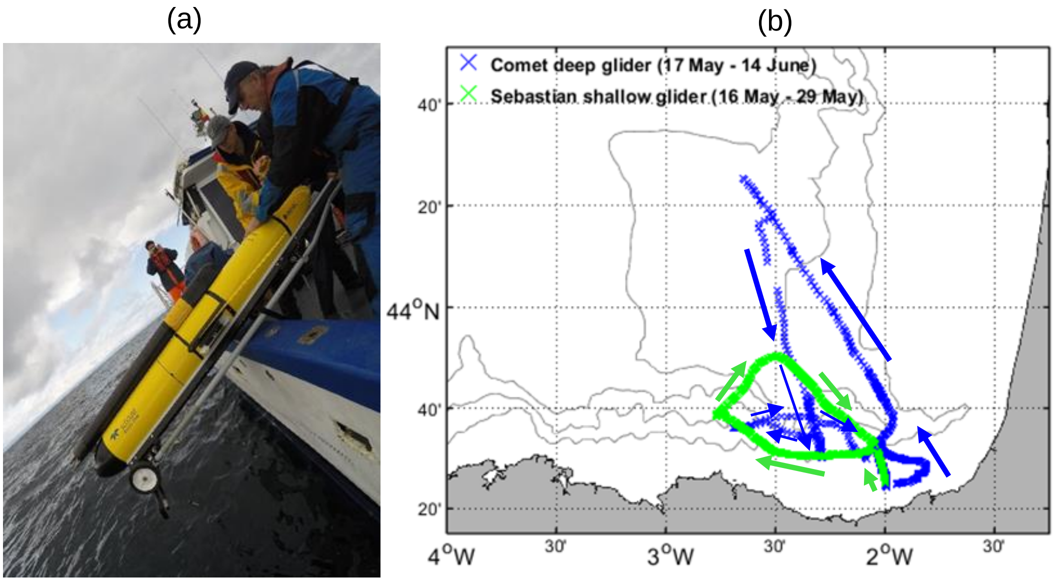

Figure 2.8. *(a) Deployment of the glider. (b) Trajectories of the gliders.*

Comet provided data from 17 May to 14 June 2018, whereas Sebastian provided data from 16 May to 29 May 2018 following the trajectories shown in Figure 2.8. After the glider mission, the data were processed, quality controlled and made freely available by the Everyone's Gliding Observatories (EGO; https://www.ego-network.org/) project and the national programs that contribute to it. In practice, a post-processing was carried out, where the data flagged as bad data during the processing were removed as well as the data corresponding to excessive or low glider vertical velocities.

1.2.2 Satellites

The constellation of the different satellites currently and previously measuring different parameters of the global ocean, contributes to the Earth Observation (EO). These data allow a global and continuous monitoring of the ocean with different resolution and revisit time, depending on the characteristic of the mission (e.g., orbit at which the satellites are located). The EO variables used in this thesis measured by sensors onboard satellites were SST, Chl-a, and sea surface height (SSH). SST and Chl-a measurements are carried out by passive sensors, that is, sensors that measure the radiation emitted by other bodies; whereas the SSH is measured by active sensors, which use their own electromagnetic radiation to illuminate the target and then analyse the backscattered radiation. The active sensors that measure the SSH are called altimeters.

1.2.2.1 SST and Chl-a measurements

SST measurements are carried out by infrared (IR) and passive microwave (PMW) radiometers that measure the radiation emitted by the sea surface. IR measurements are strongly affected by scattering and emission from clouds, whereas MW measurements (6–10 GHz) are considerably insensitive, except where there is heavy rainfall. Conversely, the advantage of IR radiometers is that they provide much higher spatial resolutions (1–4 km at nadir). In any case, good calibration of the sensors and correction algorithms due to atmospheric attenuation are needed to obtain accurate SST measurements (e.g., O'Carroll et al., 2019).

Ocean colour measurements are obtained by the backscattered sunlight out of the ocean after interacting with the water and its constituents. The main constituent is the phytoplankton, which has several photosynthetic pigments, primarily Chl-a. Chl-a concentration is estimated from ocean colour data by algorithms that relate the received signal and the Chl-a colour. For this, careful calibrations of the sensor, as well as atmospheric correction schemes must be applied (e.g., Groom et al., 2019).

In this thesis, the daily 1km resolution SST and Chl-a data were retrieved from the IR Advanced Very High-Resolution Radiometer (AVHRR) onboard the EUMETSAT Polar System-Second Generation (EPS-SG) satellite and the Ocean and Land Colour Instrument (OLCI) sensor onboard the Sentinel-3A satellite, respectively. These data corresponded to NERC Earth Observation Data Acquisition and Analysis Service (NEODAAS) and the CMEMS OCEANCOLOUR_ATL_CHL_L3_NRT_OBSERVATIONS_009_036 products, respectively.

1.2.2.2 SSH measurements

The basic principle of the altimetry technology is to send a radar signal to the sea surface and then to measure the reflected return echo. The time needed for the signal to go and come back determines the distance between the altimeter and the sea surface, called the range (see Figure 2.9 for more clarity about the general scheme and the reference surfaces). A physically based model (Brown, 1977) is adjusted to the resulting signal, called waveform, providing different parameters, including range. To reduce the measurement noise, the result is averaged. The satellite altitude is estimated relative to a reference ellipsoid, which is a mathematical surface that approximates Earth's form. Therefore, by subtracting the range to the satellite altitude (orbit), and by applying several corrections (e.g., tropospheric and ionospheric effects on the radar wave, sea surface bias, geophysical corrections), the SSH is obtained: SSH = orbit – range – corrections.

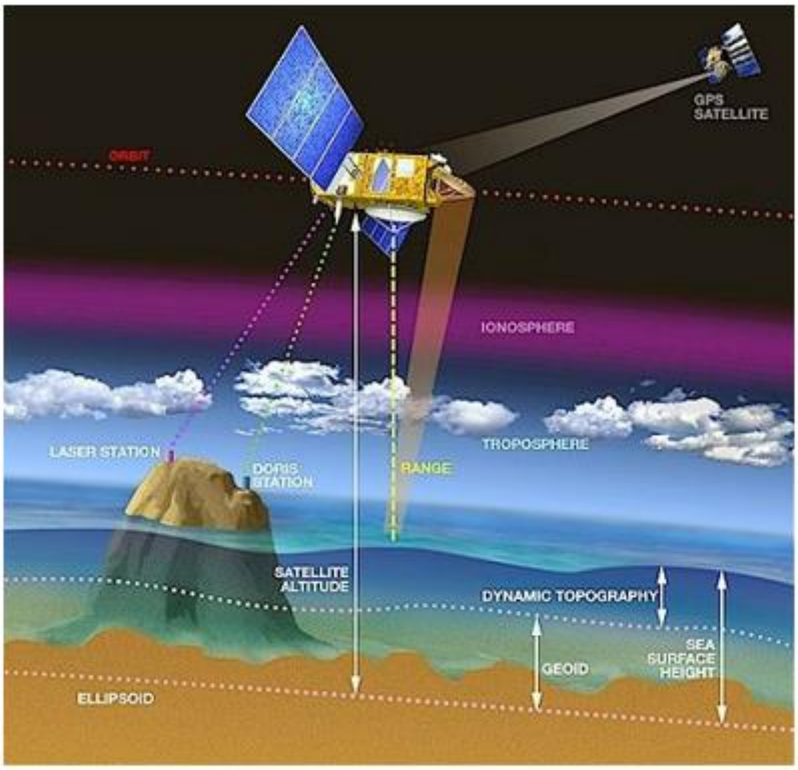

Figure 2.9. *Scheme of the altimetry principle and the reference surfaces (from https://www.aviso.altimetry.fr/en/techniques/altimetry/principle/basic-principle.html).*

However, the SSH does not provide oceanographic information since the gravitational forces differ along the ellipsoid. To remove this effect, the SSH must be referenced to the geoid, which is the equipotential surface the ocean would have only considering centrifugal and gravity forces. The surface height referenced to the geoid is called dynamic topography (DT), however, since the geoid is not measured with enough accuracy, a temporal mean of the SSH is subtracted to the SSH to obtain an accurate measurement of the ocean topography (referenced to a temporal average (Le Traon et al., 2003)), namely, the sea level anomaly (SLA):

$$\mathrm{SLA} = \mathrm{SSH} - \langle \mathrm{SSH} \rangle \qquad (2.1)$$

Altimeters provide invaluable data for observing ocean circulation (Le Traon and Morrow, 2001). However, measurements are degraded at 10–50 km from the coast since the footprint of altimeters are contaminated by the land and because of the inaccuracy in geophysical (atmospheric and tidal) corrections (Bouffard et al., 2010). Nowadays, several research groups are focused on improving coastal altimetry measurements and indeed this field has experienced great improvements in recent years (e.g., Restano et al., 2020).

In this thesis, along-track SLA data were used from Jason-2 satellite’s 248 and 213 tracks that cover the EuskOOS footprint area (see Figure 2.10). Two data products, with a revisit period of

~10 days and an along-track resolution of ~7 km were used. These products are the CTOH-XTRACK provided by the Center for Topographic studies of the Ocean and Hydrosphere (CTOH) and a preliminary version of the 2018 update of the reprocessed global ocean along-track level-3 data provided by CMEMS. Although they provide the same information, they are differently processed. The former is spatially filtered with a 40-km cut-off spatial Loess filter and it is specifically processed for coastal areas, whereas the latter, is spatially filtered with a 65-km cut-off spatial Lanczos filter and it is a reprocessed level-3 product.

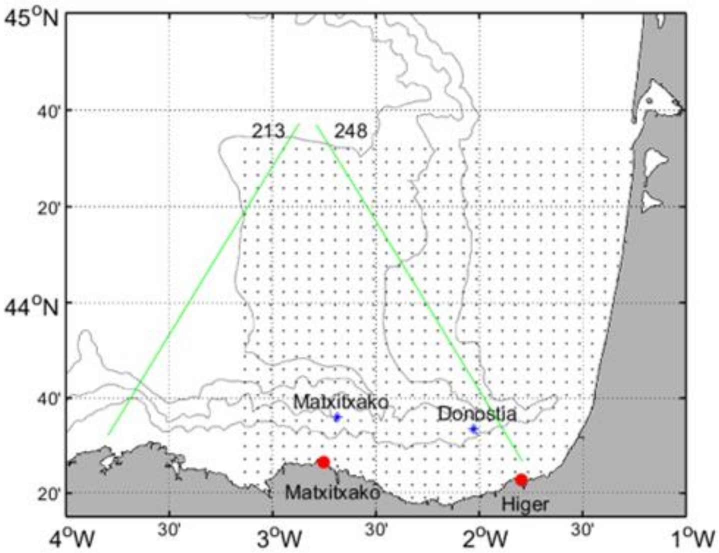

Figure 2.10. *Jason-2 satellite's 248 and 213 tracks over EuskOOS observatory.*

1.2.3 Drifters

Drifters are floating instruments that follow the water parcels' movement. The most typical drifter design consists of a surface float linked to a holey sock drogue by a thin cable (see Figure 2.11). These drogues are necessary to significantly lower the influence of direct wind and can be centered at different depths, making the movement of the drifter representative of those depths. Drifters measure their location; however, they can contain additional sensors that measure other parameters such as SST, barometric pressure, salinity, wave height (in absence of drogue), wind speed and direction, and optical magnitudes. Drifters are powered by batteries and the data are transmitted to satellites from where they are sent to land-based data centers.

In this thesis datasets from 3 different drifters were used. Two of them corresponded to the ARCADINO cruise run in the Bay of Biscay (Charria et al., 2013), whereas the other one was operated by the SHOM (Service Hydrographique et Océanographique de la Marine). These drifters were linked to a holey sock drogue centered at –15 m and their positions were hourly transmitted by an ARGOS localization system. The data were post-processed by quality controlling procedures based on velocity thresholds and visual inspection of the positions.

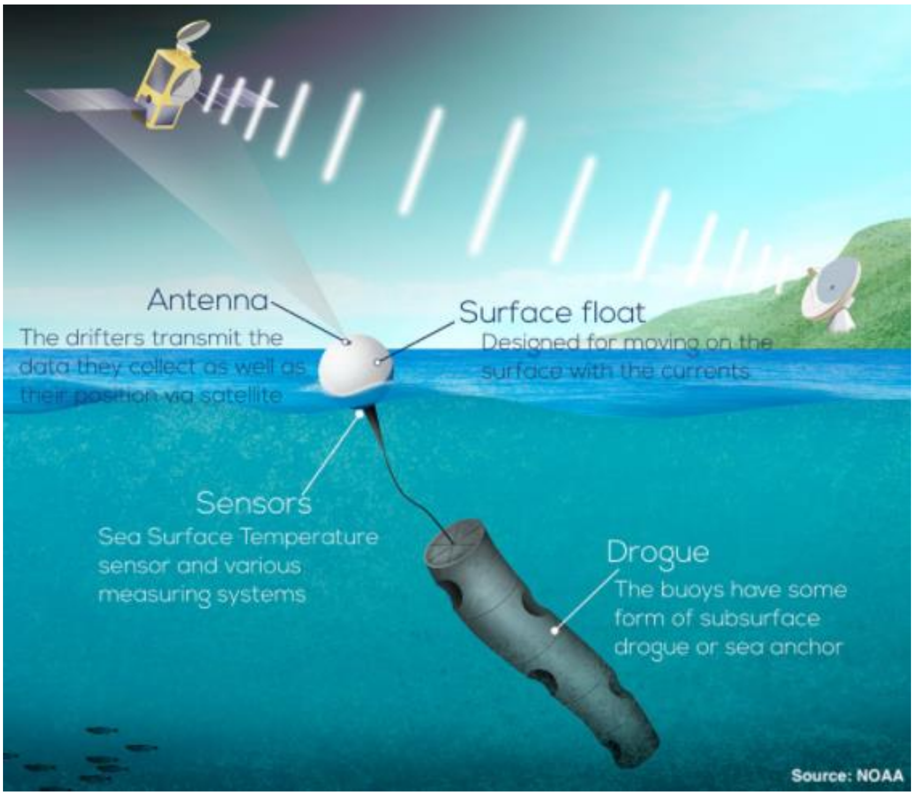

Source: NOAA

Figure 2.11. *Scheme of a drifter similar to the ones used in this thesis (from https://www.aoml.noaa.gov/es/global-drifter-program/).*

1.2.4 The Bilbao-Vizcaya mooring

This mooring (SeaWatch) located in the study area is anchored in a water depth of 580 m (at –3.04º E, 43.64º N, see Figure 2.15) and belongs to Puertos del Estado (the Spanish Government). The Bilbao-Vizcaya mooring owns meteorological sensors that provide hourly wind direction and speed data, used in this thesis. The mooring data is available as part of the CMEMS INSITU_IBI_NRT_OBSERVATIONS_013_033 product at https://marine.copernicus.eu/access–data.

1.2.5 Research vessels

Ships or research vessels are another way to obtain data in coastal areas. They are specifically designed ships or old ships reused and adapted to carry out oceanographic surveys. Therefore, they are capable to carry a wide variety of sensors to obtain information of the surveyed area.

In this thesis data from a research vessel used in BIOMAN oceanographic survey is used. This survey aims to estimate the anchovy biomass in the BoB at the end of spring and it is run every year in May since 1987. It consists of collecting different type of data along 15 nmi (nautical miles)-separated transects perpendicular to the coast (see Figure 2.12). In areas of high egg abundance (e.g., river plumes) the transects are separated 7.5 nmi. It also aims to investigate the relationships of the ocean characteristics and the population of anchovy; therefore, hydrographic data are also collected. In this thesis anchovy egg abundance data is used, which is sampled by means of two systems (see Figure 2.13):

- The Continuous Underway Fish Egg Sampler (CUFES; Checkley et al., 1997). It is an instrument located onboard the research vessel that pumps water at -3 m onboard to record the eggs with a net of 350 μm mesh size. Since the samples are immediately checked it provides near real-time volumetric abundance estimations (the volume of the used water is measured by a flowmeter) under all sea conditions each 1.5 miles.
- The PairoVET net. It consists of 2-CalVET nets (Smith et al., 1985) (Smith et al., 1985) with a 150 μm mesh in a bongo-type configuration. Sampling stations are set every 3 nmi along the research vessels transect (this distance is changed to 6 nmi when eggs are absent) where the net is lowered until –100 m. Then it is lifted back and samples are managed onboard where anchovy eggs are sorted, identified and counted obtaining the number of eggs per 0.1 m^2.

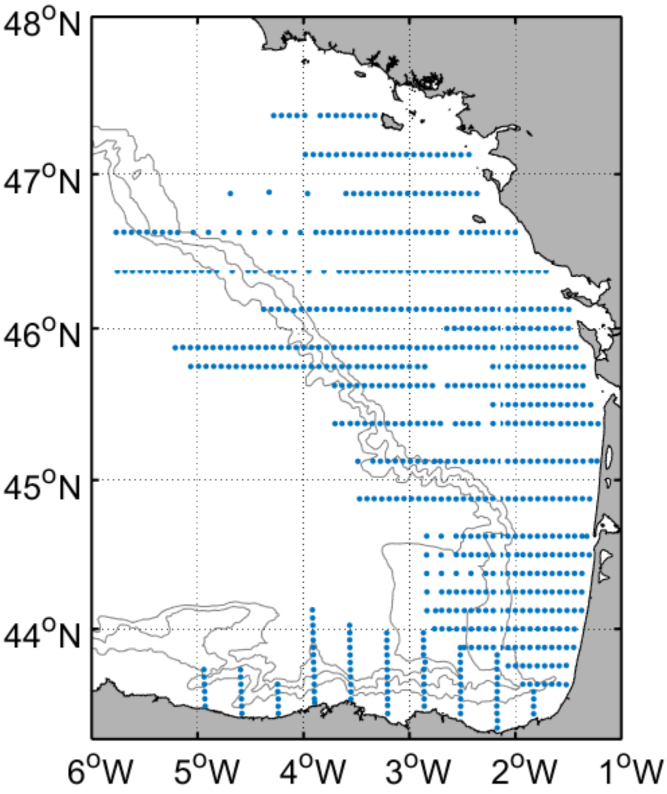

Figure 2.12. *Distribution of egg abundance measurement stations with PairoVET in BIOMAN 2011.*

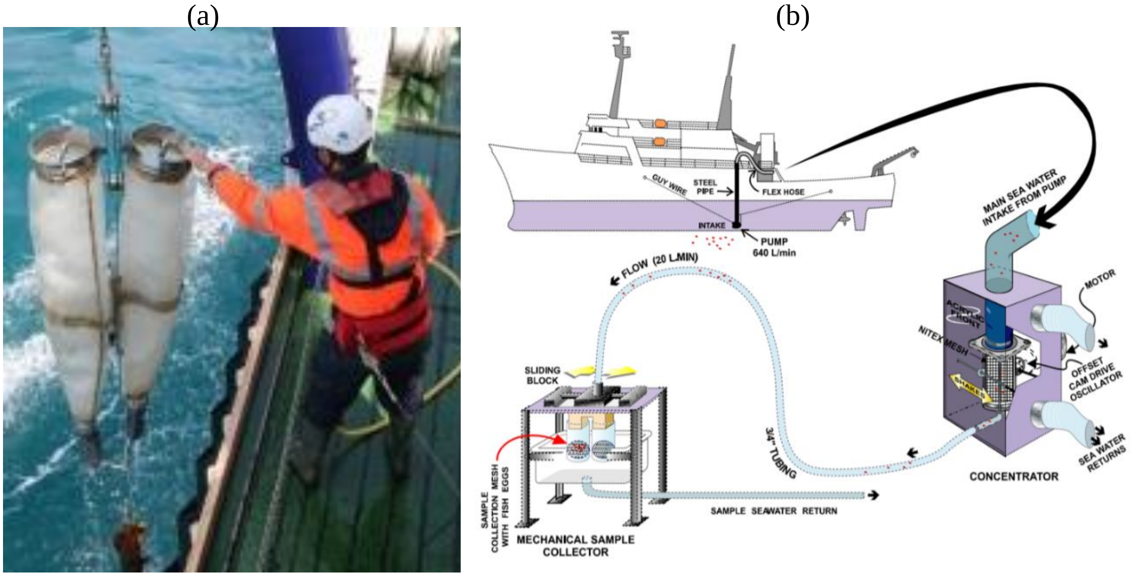

Figure 2.13. *(a) a PairoVET net. (b) Scheme of the CUFES system (from https://calcofi.org/field-work/underway-observations/cufes-fish-egg-survey.html).*

1.2.6 Oceanic and atmospheric models

Despite the long-term instrumental measurements, observational data are scarce in space (especially under the surface) and many times incomplete in time to obtain an integral description of the oceanic flows. In order to obtain a more complete description of the oceanic circulation, models can numerically solve the primitive equations of motion (i.e., the equation of state and the continuity and momentum equations) from some given initial and boundary conditions, thus simulating 3D ocean processes. Models have become invaluable tools for oceanographers in the last decades providing complete spatiotemporal 3D information, nevertheless, they are not able to fully reproduce the reality and have limitations. For instance, the primitive equations cannot be resolved analytically due to the non-linear terms and turbulence. The latter means that the information that lies between the grid points of the model is unknown, however, turbulence can be approximately parametrized. Although in the last decades the computational efficiency has experienced huge advances and provided remarkably improved simulations, it is still a limiting factor for obtaining the most possible accurate simulations.

Models can represent flows at different scales (global, regional or local) and can be oriented to solve the circulation of oceanic regions (simulation models) or some specific oceanic processes (mechanistic or academic models). On the other hand, atmospheric models provide invaluable information about the state of the atmosphere and data of atmospheric variables. Indeed, oceanic and atmospheric models can be even coupled.

The combination of models with observations can be valuable to obtain a more complete picture of the circulation, especially in coastal areas where oceanic processes are complex. Moreover, observations can be also assimilated into models or can be used to validate the outputs of the simulations (De Mey-Frémaux et al., 2019).

In this thesis, data products from various realistic ocean configurations of the NEMO model are used. Here they are briefly described, and further details are provided in *Chapters 5* and *7:*

- The IBI_REANALYSIS_PHYS_005_002 product, provided by CMEMS. It is a reanalysis product based on a realistic configuration of the NEMO model for the Iberian Biscay Irish region that assimilates in situ and satellite data and has a horizontal resolution of 0.083º x 0.083º (~6–9 km; red dots in Figure 2.14).
- The IBI_ANALYSISFORECAST_PHY_005_001 product provided by CMEMS. It is based on an eddy-resolving NEMO model for the Iberian Biscay Irish region and it provides forecast data as well as IBI downscaled analysis data with a horizontal resolution of 0.028º x 0.028º (~2–3 km; blue dots in Figure 2.14).
- The GLOBAL_REANALYSIS_PHY_001_030 product and the GLOBAL_REANALYSIS_PHY_001_025 products are also provided by CMEMS, based on a global configuration of NEMO model, which assimilate in situ and satellite data with horizontal resolutions of 0.083º x 0.083º (~6–9 km) and 0.25º x 0.25º (~20–28 km), respectively (red dots and green crosses in Figure 2.14, respectively). Conversely to the previous models, these are global models.

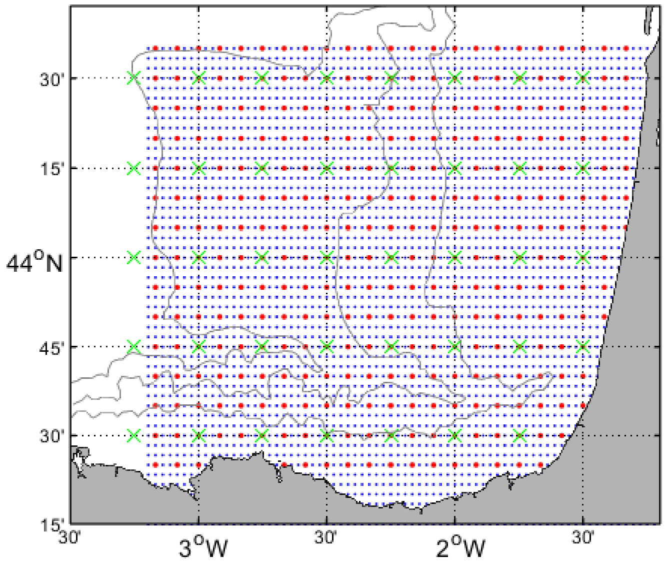

Figure 2.14. *Map of the model data points. The blue dots are points of IBI_ANALYSISFORECAST_PHY_005_001, red dots of IBI_REANALYSIS_PHYS_005_002 and GLOBAL_REANALYSIS_PHY_001_025, and green crosses of GLOBAL_REANALYSIS_PHY_001_030. The grey lines depict the 200, 1000 and 2000 m isobaths.*

Wind data from an atmospheric model is also used. This is the Weather Research and Forecasting model (WRF) provided by the meteorological agency of Galicia (MeteoGalicia). This model, with a native resolution of 12 km (see Figure 2.15), reproduces the offshore hourly wind fields of the SE-BoB with reasonable accuracy (Ferrer et al., 2010). For a detailed description of this model see (Skamarock et al., 2005).

Note that the reason for choosing wind data from the Bilbao-Vizcaya mooring or from the WRF model depends on the analysis scenario. If we are interested in the circulation along the Spanish slope the appropriate dataset is the one from the Bilbao-Vizcaya mooring, whereas if we want to analyse open water areas the WRF data are the adequate ones.

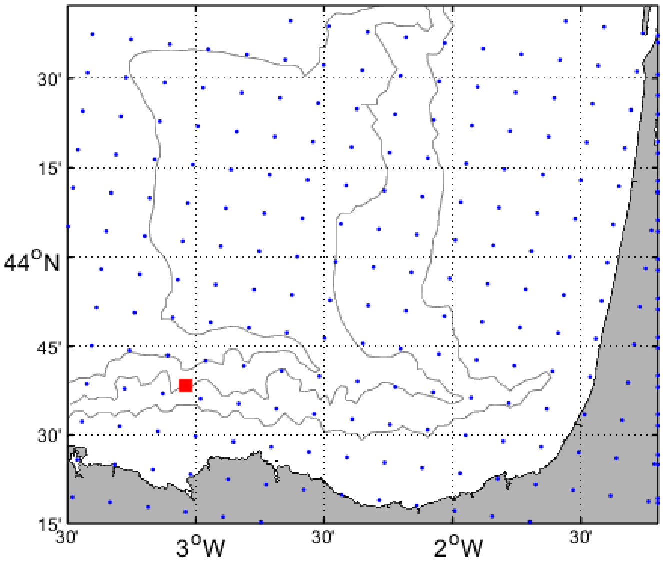

Figure 2.15. *Map of the wind data points. The blue dots show the grid points where the WRF provides wind data, whereas the red square depicts the location of the Bilbao-Vizcaya mooring. The grey lines depict the 200, 1000 and 2000 m isobaths.*

1.3 Summary of the data used in each chapter

Since several data sources used in this thesis have been described in this section Table 2.2 summarizes all of them and their corresponding variables used in each Chapter.

Table 2.2. *Summary of the observing platforms/models and variables used in each chapter.*

Observing Platforms/Models	**Variable**	**Chapter 3**	**Chapter 4**	**Chapter 5**	**Chapter 6**	**Chapter 7**
HFR	Current velocity	✓	✓		✓	✓
EuskOOS mooring (CT)	Temperature, Salinity				✓	
EuskOOS mooring (ADCP)	Current velocity		✓		✓	✓
Glider	Temperature, Salinity, Chl-a, Integrated currents				✓	
Satellite infrared	SST	✓				
Satellite ocean color	Chl-a				✓	
Satellite altimetry	SLA	✓				
Drifter	Position					✓
Oceanic model	Current velocity			✓	✓	✓
Oceanic model	Temperature, Salinity				✓	
Atmospheric model	Wind velocity	✓			✓	
Bilbao-Vizcaya mooring	Wind velocity		✓			
Research Vessel	Anchovy egg abundance					✓

2. Methods

In addition to the multiplatform observations and model data presented in the previous section, the formulation that allows to infer new variables from the observed data as well as the methods that expand the observations enable a more complete characterization of the study area. Moreover, Lagrangian approaches can give new insights into characteristics of water masses and about physical and biological processes. In this section, the formulations and methods used in this thesis are described along with the used Lagrangian model.

2.1 Geostrophic and wind-driven currents estimations

The equations of motion (Eq. (2.2–2.4)) that govern water circulation are here presented in order to support the description of the magnitudes derived from glider, altimeter and wind data in the following subsections. The motion in the ocean is the result of the balance between Coriolis, pressure gradient, gravity, and frictional forces (for complete derivation see Chapter 7 in Stewart (2008)):

$$\frac{du}{dt} = \frac{\partial u}{\partial t} + u\frac{\partial u}{\partial x} + v\frac{\partial u}{\partial y} + w\frac{\partial u}{\partial z} = -\frac{1}{\rho}\frac{\partial p}{\partial x} + fv + F_x \tag{2.2}$$

$$\frac{dv}{dt} = \frac{\partial v}{\partial t} + u\frac{\partial v}{\partial x} + v\frac{\partial v}{\partial y} + w\frac{\partial v}{\partial z} = -\frac{1}{\rho}\frac{\partial p}{\partial y} - fu + F_y \tag{2.3}$$

$$\frac{dw}{dt} = \frac{\partial w}{\partial t} + u\frac{\partial w}{\partial x} + v\frac{\partial w}{\partial y} + w\frac{\partial w}{\partial z} = -\frac{1}{\rho}\frac{\partial p}{\partial z} - g + F_z \tag{2.4}$$

where u, v and w are the zonal, meridional and vertical current velocity components respectively, ρ is water density, F_i are frictional forces, p is pressure, and g acceleration of gravity. f is the Coriolis parameter defined as $f = 2\Omega sin\varphi$, where φ is the latitude and Ω the rotation rate of the earth (Ω=7.292x10^{-5} radians s^{-1}). Note that the Coriolis force in the vertical direction has been neglected (in Eq. (2.4)) since it is much smaller than the gravity force and it is usually ignored (Stewart, 2008).

For an ocean in equilibrium (i.e., no accelerations) the terms in the left-hand side of the momentum equations (Eq. (2.2–2.4)) are null, and the momentum equations become linear. Therefore, it is possible to divide the velocities into the velocities driven by pressure gradients (geostrophic currents: u_g, v_g) and the velocities driven by frictional forces (such as wind-driven (Ekman) currents: u_e, v_e).

2.1.1 Across-track geostrophic currents from hydrographic glider data

As mentioned above, temperature, salinity, pressure and Chl-a data from glider observations were used in this thesis. From the temperature and salinity data, density data can be inferred, from which geostrophic current velocities are estimated in the across-track direction of the glider.

The geostrophic currents are those which are in equilibrium between the Coriolis force and the horizontal pressure gradients. The pressure gradients induce a flow that is deflected in perpendicular direction to the flow to the right (left) by the Coriolis force, in the northern (southern) hemisphere. Thus, from Eq. (2.2–2.4) we obtain the geostrophic equations:

$$\frac{1}{\rho}\frac{\partial p}{\partial x} = f v_g \tag{2.5}$$

$$\frac{1}{\rho}\frac{\partial p}{\partial y} = -f u_g \tag{2.6}$$

$$\frac{1}{\rho}\frac{\partial p}{\partial z} = -g \tag{2.7}$$

Taking the vertical derivative in Eq. (2.5, 2.6) and substituting the pressure derivative using the hydrostatic equation (i.e., Eq. (2.7)) the thermal wind equations are obtained:

$$\frac{\partial v_g}{\partial z} = \frac{1}{\rho f}\frac{\partial}{\partial x}\frac{\partial p}{\partial z} = \frac{-g}{\rho f}\frac{\partial \rho}{\partial x} \tag{2.8}$$

$$\frac{\partial u_g}{\partial z} = \frac{-1}{\rho f}\frac{\partial}{\partial y}\frac{\partial p}{\partial z} = \frac{g}{\rho f}\frac{\partial \rho}{\partial y} \tag{2.9}$$

showing that horizontal density gradients are related to vertical shear of geostrophic velocities.

In practice, this velocity shear is estimated between two pressure levels (P_1, P_2) in the water column by means of data between two hydrographic profiles (A, B), as the ones of the gliders, separated a distance L (see Figure 2.16). For this, a physical magnitude that accounts for the density of the profiles is considered, which is the change of geopotential ($d\Phi$). This is the amount of work needed to raise a unit mass a vertical distance dz. In the water column, this quantity can be estimated by changing the vertical dependence from distance to pressure by using the hydrostatic equation (Eq. (2.7)). Thus:

$$d\Phi = g\, dz = \frac{-1}{\rho} dp = -\alpha\, dp \tag{2.10}$$

where $\alpha = \alpha(S, t, p)$ is the specific volume (inverse of density) of seawater with salinity S, temperature t and pressure p. Then, integrating the thermal wind equations (Eq. 2.8, 2.9) in the vertical direction between two isobaric surfaces (P_1, P_2) and substituting $d\Phi$ the velocity shear of the perpendicular component (across-track) between A and B is obtained. If we consider the separation between A and B in the x-axis (y-axis), when finite differentiating L will be Δx (Δy) and the corresponding equation will be Eq. (2.11) (Eq. (2.12)):

$$v_{g2} - v_{g1} = \frac{-1}{f}\frac{\partial \Delta\Phi}{\partial x} = \frac{-1}{f}\frac{\Delta\Phi_B - \Delta\Phi_A}{\Delta x} \tag{2.11}$$

$$u_{g2} - u_{g1} = \frac{1}{f}\frac{\partial \Delta\Phi}{\partial y} = \frac{1}{f}\frac{\Delta\Phi_B - \Delta\Phi_A}{\Delta y} \tag{2.12}$$

Note that at P_2 the total geostrophic velocity is not obtained, but the velocity with respect to P_1. Therefore, P_1 is the so-called reference level and the velocity at P_1 must be known in order to obtain the total velocity.

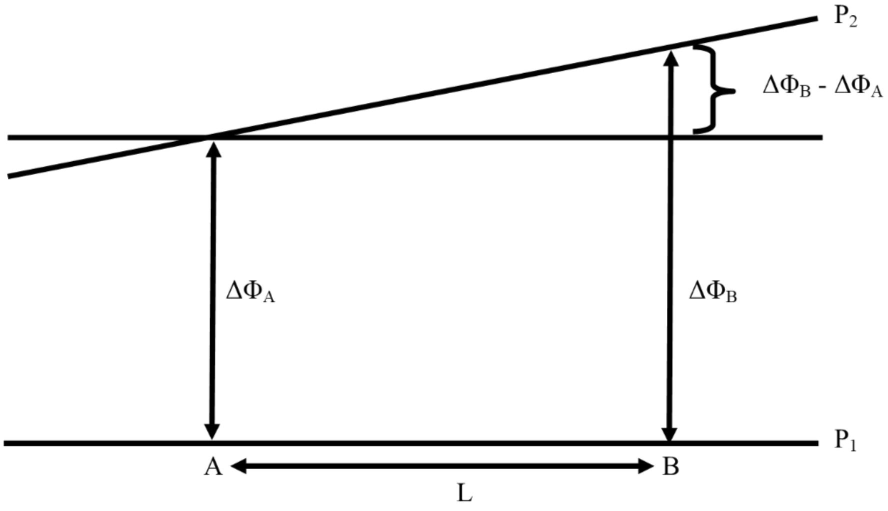

Figure 2.16. *Scheme of the geometry used for estimating the geostrophic velocity shear between pressure levels P_1 and P_2 between profiles A and B separated by a distance L.*

It is worth mentioning that in practice the specific volume anomaly (δ) is used instead of α. Such anomaly is estimated with respect to the arbitrary specific volume of seawater with S=35 psu, t = 0ºC and p (i.e., $\alpha(35,0,p)$). The specific volume can be written as:

$$\alpha(S,t,p) = \alpha(35,0,p) + \delta \tag{2.13}$$

therefore, when vertically integrating:

$$\Delta\Phi = \int_{P_1}^{P_2} \alpha(35,0,p)\,dp + \int_{P_1}^{P_2} \delta\,dp \tag{2.14}$$

The first term of the right-hand side of Eq. (2.14) is the same in A and B, therefore it is removed in Eq. (2.11, 2.12). Since the order of magnitude of $\alpha(35, 0, p)$ is one thousand times bigger than the δ's (Pond and Pickard, 1983), the only use of δ provides much more accurate estimations.

Also in practice, instead of the density the potential density is used, which is the density a water parcel has when it is adiabatically raised to a pressure reference level without change in salinity. The compressibility of the seawater makes the temperature of the water parcels sensitive to the influence of pressure. This, consequently, affect the density. Therefore, this effect of the pressure can be practically removed by considering the potential density referenced to a pressure level (to the surface in our case).

When different oceanic processes are studied (e.g., eddies), one way to know if the currents being measured are in geostrophic balance is by means of a dimensional analysis. In this case, the importance of the geostrophic balance can be estimated by the Rossby number (R_o) which is a dimensionless number that consists of the ratio of inertial force to Coriolis force:

$$R_o = \frac{U_s}{L_s f} \tag{2.15}$$

where U_s is a velocity scale, f the Coriolis factor and L_s is a horizontal length scale. A small (big) Rossby number means that the effect of Coriolis force is (is not) significant and the process would (would not) be largely in geostrophic balance. Indeed, it is considered that the Coriolis force is significant when the Rossby number is on the order of unity or less (Cushman-Roisin and Beckers, 2011).

2.1.2 Across-track surface geostrophic currents from altimeter data

Geostrophic current velocities can be inferred at the surface from altimetry data. Integrating the hydrostatic equation (Eq. (2.7)), the sea pressure (p) at a depth h beneath a level surface $z = 0$ (the geoid) can be obtained:

$$p = p_0 + \int_{-h}^{\eta} g\rho \, dz \tag{2.16}$$

where, p_0 is the atmospheric pressure and η is the height of the sea surface above or below the level surface. At the level surface h is 0, and g and ρ can be considered constant, therefore:

$$p = p_0 + g\rho\eta \tag{2.17}$$

Then, substituting this into the geostrophic equations (Eq. (2.5–2.6)) the surface geostrophic currents are obtained. In practice, η is the DT (SLA) data obtained from altimeters that provide geostrophic current (anomaly) velocities perpendicular to the altimeter track (i.e., across-track) by finite differentiating:

$$v_g = \frac{g}{f}\frac{\partial \eta}{\partial x} = \frac{g}{f}\frac{\Delta \eta}{\Delta x} \tag{2.18}$$

$$u_g = -\frac{g}{f}\frac{\partial \eta}{\partial y} = -\frac{g}{f}\frac{\Delta \eta}{\Delta y} \tag{2.19}$$

2.1.3 Wind-driven currents from wind data

The difference of velocity between the atmosphere and the ocean surface induces a stress on the ocean in the tangential direction, which is progressively spread to deeper layers. These are the wind-driven currents, and they were quantitatively theorized for the first time by Ekman (1905). He assumed a steady, homogeneous, horizontal flow subject to frictional forces driven by the wind in an infinitely deep water with no boundaries in a rotating earth. He also chose to relate the wind stress ($\vec{\tau}$) in one direction to the vertical water current velocity shear in such direction (i.e., $\tau_x \sim u_e$ and $\tau_y \sim v_e$) by means of a constant eddy viscosity (ν):

$$\vec{\tau} = \rho\nu\frac{\partial \overrightarrow{U_e}}{\partial z} \tag{2.20}$$

where $\overrightarrow{U_e} = U_e\ (u_e, v_e)$. Since for an ocean in equilibrium the momentum equations are linear, it is possible to extract the wind-driven flow from the equilibrium between Coriolis force and the wind stress (tangential pressure) vertical gradient (i.e., vertical friction) as:

$$f v_e = -F_x = \frac{-1}{\rho}\frac{\partial \tau_x}{\partial z} \tag{2.21}$$

$$f u_e = F_y = \frac{1}{\rho}\frac{\partial \tau_y}{\partial z} \tag{2.22}$$

Then, substituting Eq. (2.20) in Eq. (2.21, 2.22) the Ekman equations are obtained:

$$f v_e = -\nu\frac{\partial^2 u_e}{\partial z^2} \tag{2.23}$$

$$f u_e = \nu\frac{\partial^2 v_e}{\partial z^2} \tag{2.24}$$

The solution of these equations when the wind blows in the Y-direction (for simplicity) is:

$$u_e = \pm V_0\, cos\left(\frac{\pi}{4} + \frac{\pi}{D_e}z\right) e^{\left(\frac{\pi}{D_e}z\right)} \tag{2.25}$$

$$v_e = V_0\, sin\left(\frac{\pi}{4} + \frac{\pi}{D_e} z\right) e^{\left(\frac{\pi}{D_e} z\right)} \tag{2.26}$$

(+ for the northern hemisphere and – for the southern hemisphere)

where V_0 is the total Ekman surface current and D_e is the Ekman depth (i.e., the thickness of the layer affected by the wind stress):

$$V_0 = \frac{\tau_0}{\rho\sqrt{\nu f}} \tag{2.27}$$

$$D_e = \sqrt{\frac{2\nu}{f}} \tag{2.28}$$

where τ_0 is the total wind stress.

According to these results, surface water currents flow at 45º to the right (left) of the wind direction in the northern (southern) hemisphere. As depth increases, the current velocity decreases while there is a clockwise (anticlockwise) rotation in the northern (southern) hemisphere. This is the so-called Ekman spiral (see figure 2.17).

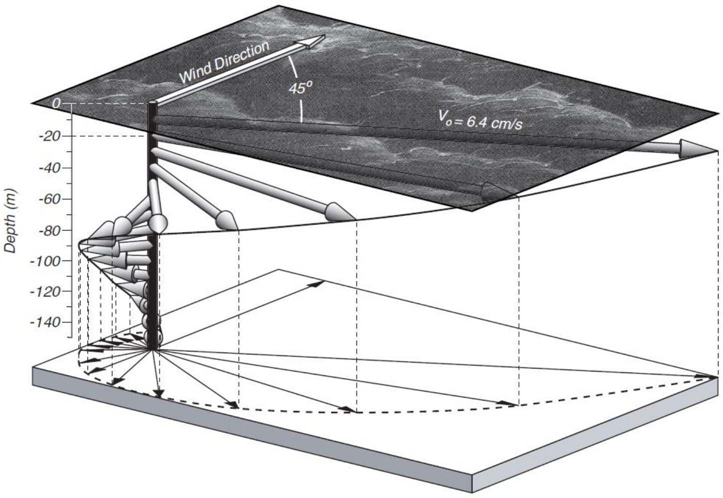

Figure 2.17. *Scheme of the Ekman current generated by a 10 m s*$^{-1}$ *wind at latitude 35º (from Stewart, 2008).*

However, Ekman currents are difficult to observe in the open ocean (Rio and Hernandez, 2003) and building on the work of Ekman (1905), several parametrizations have been suggested (e.g., D’Assaro et al., 1995; Davis et al., 1981; Pollard & Millard, 1970; Ralph & Niiler, 1999; Rio & Hernandez, 2003). In this thesis, the M1 model proposed by Rio and Hernandez (2003) is used since it already demonstrated good results in the study area (Caballero et al., 2008b). In this model, the wind stress and wind-driven currents are expressed by complex numbers (i.e., $\vec{\tau} =$

$\tau_x + i\tau_y$ and $\overrightarrow{U_e} = u_e + iv_e$), and constant eddy viscosity and water density are assumed in a slab-like flow (thus no Ekman spiral):

$$\overrightarrow{U_e} = \frac{b\vec{\tau}}{\sqrt{f}} e^{i\theta} \tag{2.29}$$

where b is the amplitude parameter related to the water density and eddy viscosity $\left(b = \frac{1}{\rho}\sqrt{\frac{2}{\nu}}\right)$ and θ represents the current rotation angle. These two parameters are obtained by adjusting the model to real data in the study area. From the fit of wind-stress measurements and drifter–derived currents in the Bay of Biscay, we use the following values obtained in Caballero et al. (2008b) for the study area: $b = 4.45\text{x}10^{-3}\ \text{m}^2\ \text{kg}^{-1}\text{s}^{1/2}$ and $\theta = -23.68^{\text{o}}$.

2.2 Data-reconstruction methods

Despite all the observational data presented in *Section 2.1* and their inter-complementarity, the full 3D coverage is still scarce. Models arise as a good option to obtain 3D data; however, they are not fully realistic. Data-reconstruction methods, although still do not provide fully realistic data, enable to directly expand in situ observations to the whole study domain with a low computational effort. In this thesis, current velocity fields were reconstructed from observations by two data-reconstruction methods, which are the discrete cosine transform-penalized least square method (DCT–PLS) and the reduced order optimal interpolation method (ROOI).

2.2.1 The DCT–PLS method

The DCT–PLS method, based on a penalized least square regression approach, was proposed by García (2010). The method has been used with oceanographic data, for instance accurately reconstructing HFR current velocity fields (in 2D) along the mid-Atlantic coast of the United States (Fredj et al., 2016) or gap-filling HFR current velocity fields in the Gulf of Manfredonia (Sciascia et al., 2018). Here the basics of the method are explained. For more details on the complete mathematical derivation see Garcia (2010) or Fredj et al. (2016).

Given some observational data (V), the method aims to find the best fitting model ($\hat{V}$), which is based on discrete cosine transforms (DCTs) and one smoothing (fitting) parameter s. The fitting model is as follows:

$$\hat{V} = IDCTN[\Gamma^N \circ DCTN(V)] \tag{2.30}$$

where, N denotes the dimensionality of the data (i.e., N=3 for a 3D grid), $DCTN$ refer to N-dimensional cosine transform ($IDCTN$ is the inverse), ∘ means element-wise product and Γ^N is a tensor of rank N:

$$\Gamma^N = 1^N \div (1^N + s\Lambda^N \circ \Lambda^N) \tag{2.31}$$

Here, ÷ means element-wise division, 1^N is an N-rank tensor of ones and Λ^N is the following N-rank tensor:

$$\Lambda^N_{i_1,\dots,i_N} = \sum_{j=1}^{N} \left(-2 + 2\cos\frac{(i_j - 1)\pi}{n_j} \right) \tag{2.32}$$

where n_j denotes the size of Λ^N (or the number points in the j$^{\text{th}}$ dimension) and i_j the position in the j$^{\text{th}}$ dimension.

The best fitting parameter s is obtained by cross-validating the created model against observations. The classical concept of cross-validation consists of separating part of the observations as test data (test set) and use the rest of the data to train the model (train set) to finally test the performance of the model on the test set. The created model can be tested by the trade-off (F) between the bias of the fitting (residual sum of squares, RSS) and the variance of the results of the created model (penalty term P):

$$F = RSS + P = ||y - \hat{y}||^2 + s||D\hat{y}||^2 \tag{2.33}$$

where y is the data of the test set, $\hat{y}$ is the data of the created model and D is a second-order difference derivative. This procedure is repeated for different test and train sets and a cross-validation score is obtained as $E[F]$. The best-fitting parameter s is the one that minimizes this score. In practice, this parameter is obtained by minimizing a general cross-validation (GCV) score based on $E[F]$ introduced by Craven and Wahba (1978) (see also Fredj et al. (2016) and García (2010) for derivation).

When we have outliers or missing data, the fitted data is obtained iteratively, thus reconstructing the data that were observationally noisy or absent. The iterative fitting model is as follows:

$$\hat{V}_{k+1} = IDCTN\left[\Gamma^N \circ DCTN\left(W^m \circ W^{bs} \circ \left(V - \hat{V}_k\right) + \hat{V}_k\right)\right] \tag{2.34}$$

where k is the number of the iteration, W^m is a weight matrix that masks missing values when accounting for the residual $\left(V - \hat{V}_k\right)$ and W^{bs} is a bisquare weight matrix that minimizes the effect of outliers. Note that V are the observations with the missing values interpolated by the nearest neighbour and that they do not change between iterations. For the first iteration $\hat{V}_k = V$ and the missing values are set to 0 in $\hat{V}_k$. Also note that at each iteration, the corresponding best-fitting parameter s is estimated by minimizing the GCV score (as mentioned above). The iteration procedure is convergent and it is done until the difference between the solution of an iteration and the previous one is very small (i.e., the result converge).

In conclusion, this is a method based on DCTs and one smoothing parameter approach consisting of a penalized least square criterion that minimizes the balance between the fidelity of the data, measured by the RSS, and a penalty term that reflects the noisiness of the smooth data. The method can deal with missing data, enabling the reconstruction in nearby areas of the observations.

The MATLAB code for implementing the method was a black box courtesy of Dr. Erick Fredj from the Jerusalem College of Technology (Israel).

2.2.2 The ROOI method

The ROOI method is based on Empirical Orthogonal Function (EOF) decomposition and was first proposed by Kaplan et al. (1997) to reconstruct SSTs from sparse data. Since then, it has been applied for different variables such as sea level pressure (Kaplan et al., 2000), SLAs (Church and White, 2006), or 3D velocity fields (Jordà et al., 2016).

In this thesis, the ROOI is used to reconstruct current velocity fields in a 3D grid from sparse observations data. The method is based on the observations and on the historical information of the study area, which is used to set the relationships between all the 3D grid points and the observation points. We can start by defining a state matrix $Z(r,t)$, where r is the m-vector of spatial locations (3D grid + observation points) and t the n-vector of times. Note that the elements of Z are anomalies with respect to the mean value (at each n point) to gain accuracy in the reconstruction. Then, a spatial $m\ x\ m$ covariance matrix that sets the spatial relationships between all the points can be computed as $C = n^{-1}ZZ^T$, and an EOF decomposition can be applied:

$$C = U\Lambda U^T \tag{2.35}$$

where U is an $m\ x\ m$ matrix whose columns are the spatial modes (EOFs) and Λ is the $m\ x\ m$ diagonal matrix of eigenvalues. Then, Z can then be exactly reproduced as:

$$Z(r,t) = U(r) \cdot \alpha(t) \tag{2.36}$$

in which the amplitude can be computed as $\alpha = U^T Z$. In practice, the data at every grid point are not known, but only at a limited set of N locations (observation points), being usually $N \ll m$.

Therefore, U cannot be computed from actual observations and historical data, usually from a model, is used to represent the actual statistics. This means, that historical data is used to estimate the covariance matrix, and hence U and Λ. An aspect to be considered is that fitting high order modes may introduce unwanted noise in the reconstruction. Thus, the Eq. (2.36) is truncated to include only the M leading EOFs, so that the contribution of the higher-order modes (accounting for local, small-scale features) is neglected:

$$Z_M(r,t) = U_M(r) \cdot \alpha_M(t) \tag{2.37}$$

The next problem is that obviously the amplitudes (α_M) cannot be obtained as in Eq. (2.36), since now we do not know Z. Instead, the M amplitudes can be determined under the constraint that the reconstructed Z_M fits the observations available at each time step while minimizing a cost function that takes into account the observational error and the role of neglected modes (see Kaplan et al., 1997, 2000, for the complete derivation). In particular, at each time t_i the solution for the M-vector of amplitudes $\alpha_M(t_i\,)$ is that minimizing the cost function:

$$\begin{aligned} S(t_i) = {} & [H(t_i)U_M\alpha_M(t_i) - Z^0(t_i\,)]^T R^{-1}[H(t_i)U_M\alpha_M(t_i) - Z^0(t_i)] \\ & + \alpha_M(t_i)^T \Lambda_M^{-1} \alpha_M(t_i) \end{aligned} \tag{2.38}$$

where $Z^0(t_i\,)$ is the N-vector of observations available at time t_i and $H(t_i)$ is an $N\ x\ m$ sampling operator whose elements are either 0 or 1 in such a way that it ‘extracts’ from vector $U_M \cdot \alpha_M(t_i\,)$ the values corresponding to the locations where observations are available and discards the others. Λ_M is a diagonal matrix that contains the M largest eigenvalues of the covariance matrix. R is an $N\ x\ N$ matrix accounting for the error covariance and consists of two terms:

$$R = \Sigma + HU'\Lambda'U'^T H^T \tag{2.39}$$

The term Σ is the observational error covariance, which is a diagonal matrix $\Sigma = \sigma_0^2 I$, where σ_0^2 is the observational error variance and I the identity matrix. The second term in R accounts for the errors introduced for ignoring higher-order modes (‘ indicates the eigenvalues and modes of the omitted modes). The first term in the cost function (Eq. 2.38) accounts for the deviation between observations and reconstruction, whereas the second term prevents from giving too much weight to higher-order modes (the higher the mode, the lower the eigenvalue, and therefore the higher the penalization). The latter is useful in the case where a high M number of EOFs are considered, thus avoiding giving too much variance to grid points which are far from the observation points. Then, as mentioned, minimizing the cost function the amplitude is obtained:

$$\alpha_M(t_i\,) = PU_M^T H^T R^{-1} Z^0(t_i\,) \tag{2.40}$$

where $P = (U_M^T H^T R^{-1} H U_M + \Lambda_M^{-1})^{-1}$.

In summary, using the ROOI, the data at a 3D grid can be reconstructed by merging (i) the spatial modes of variability (usually computed from a model), and (ii) the temporal amplitudes obtained using the available observations. Note that once Z is obtained, the mean value that was initially subtracted is finally added. In our case, the ROOI method is used to reconstruct current velocities, however, observations do not necessarily have to be current velocities, and other variables (e.g., hydrographic variables or SLA data) can be also used.

Note that each grid point (i.e., each m or each row of Z), corresponds to one variable. Thus, if two velocity components are used, there will be twice the number of grid points. The same applies if we want to add any other variable, thus the way to incorporate them is simply enlarging the matrix Z with additional rows: one for each grid point at which the new variable is available.

Note that although the explained variance of the M number of modes selected in each of the following chapters is not explicitly shown, such modes explain most of the variability of the historical data.

2.3 Lagrangian model

Although the Eulerian approach (i.e., description of oceanic properties in time at given locations) has historically been predominant in ocean studies, studies from a Lagrangian perspective (i.e., description of the trajectory of a water parcel and its properties) have increased in the last decades (Van Sebille et al., 2018). In recent years models that simulate the trajectories of passive particles have been widely used to track oil (e.g., Paris et al., 2012) floating debris (e.g., Declerck et al., 2019; Lebreton et al., 2012), nutrients (e.g., Chenillat et al., 2015), larvae (e.g., Paris et al., 2005; Phelps et al., 2015), etc.

In this thesis, trajectories of passive particles were simulated by the MOHID ("MOdelo HIDdrodinamico") modelling system (Neves, 2013), which was developed by MARETEC (Marine and Environmental Technology Research Center) at the Instituto Superior Técnico (IST) that belongs to the Universidade de Lisboa. The MOHID modelling system is programmed in ANSI FORTRAN 95 and is divided into diverse numerical tools: MOHID Water, MOHID Land and MOHID Soil. Obviously, in this thesis, the MOHID Water tool (Braunschweig et al., 2004) was used which is a 3D hydrodynamic model coupled to different modules such as Module WaterProperties, Module Turbulence and Module Lagrangian among others that compute different physical and biogeochemical processes. In our case, the Lagrangian module (Leitão, 1996) was used to simulate the mentioned trajectories, which allows explicit Euler, Multi-Step Euler and 4th order Runge-Kutta integration schemes. In the study area, this module was already used in Declerck et al. (2019) providing realistic results. The different conditions attributed to the simulations in this thesis such as the grid size, the boundary conditions at the coast, numerical particle release point, frequency and time, the diffusion coefficient etc. are presented in *Chapter 7* (when MOHID is used).

2.4 Summary of the methods used in each chapter

Table 2.3. *Summary of the methods used in each chapter.*

Methods	**Chapter 3**	**Chapter 4**	**Chapter 5**	**Chapter 6**	**Chapter 7**
Across-track v_g from glider data				✓	
Across-track v_g from altimeter data	✓				
Wind-driven currents from wind data	✓				
ROOI			✓	✓	✓
DCT-PLS			✓		
Lagrangian model (MOHID)					✓

CHAPTER 3

Joint analysis of coastal altimetry and high-frequency radar data: observability of seasonal and mesoscale ocean dynamics in the Bay of Biscay

Abstract

Land-based coastal high-frequency radar (HFR) systems provide operational measurements of coastal surface currents (within 1−3 m depth) with high spatial (300 m−10 km) and temporal (≤ 1 h) sampling resolutions, while the near-continuous altimetry missions provide information, from 1993 until today, on geostrophic currents in the global ocean with typical along-track and temporal sampling resolutions of > 7 km and > 9 days, respectively. During the last years, the altimetry community has made a step forward in improving these data in the coastal area, where the data present lower quality than in the open ocean. The combination of HFR and altimetry measurements arises as a promising strategy to improve the continuous monitoring of the coastal area (e.g., by expanding the measurements made by HFR to adjacent areas covered by the altimetry or by validating/confirming improvements brought by specific coastal algorithms or new altimeter missions). A first step towards this combination is the comparison of both datasets in overlapping areas.

In this study, a HFR system and two Jason-2 satellite altimetry products with different processing are compared over the period from 1 January 2009 to 24 July 2015. The results provide an evaluation of the performance of different coastal altimetry datasets within the study area and a better understanding of the ocean variability contained in the HFR and altimetry datasets. Both observing systems detect the main mesoscale processes within the study area (the Iberian Poleward Current and mesoscale eddies), and the highest correlations between radar and altimetry (up to 0.64) occur in the slope where the Iberian Poleward Current represents a significant part of the variability in the circulation. Besides, the use of an Ekman model, to add the wind-induced current component to the altimetry-derived geostrophic currents, increases the agreement between both datasets (increasing the correlation by around 10 %).

The contents of this chapter were published as:

Manso-Narvarte, I., Caballero, A., Rubio, A., Dufau, C., Birol, F., 2018. Joint analysis of coastal altimetry and high-frequency (HF) radar data: observability of seasonal and mesoscale ocean dynamics in the Bay of Biscay. Ocean Sci. 14, 1265–1281. https://doi.org/10.5194/os-14-1265-2018.

1 Introduction

Ocean dynamics result from a combination of processes of different timescales and space scales. However, and mainly due to technical limitations, this complexity cannot be captured by the existing observational systems if each observing technique is analysed individually since they are designed for resolving certain scales. Nowadays, there is a growing tendency to combine different observing systems for a more complete description and understanding of ocean dynamics. Current observatories are designed to monitor, in an operational way, the ocean environment to support the human activities concentrated on the coast (Liu et al., 2015). In recent years, great effort has been focused on the development and improvement of these platforms. In the framework of European projects such as JERICO (2007-2013) and JERICO-NEXT (2014-ongoing, http://www.jerico-ri.eu) progress has been made, on the one hand, regarding the improvement and creation of coastal observatory networks and, on the other hand, regarding the applications of these observatories for addressing European marine policies. As an example, the latter project aims to integrate emerging methodologies and technologies to proceed towards the automated monitoring at a high temporal and spatial resolution of wider areas in order to provide the best possible data and products necessary for the implementation of the European Marine Strategy Framework Directive. For this purpose, there is ongoing research on assessing the interconnection among physics, biogeochemistry, and biology at different spatial and temporal scales. In addition to the development of coastal observatories, there are global initiatives, such as the GLOBCURRENT project (2014−2017; http://www.globcurrent.org/), aimed at advancing in the evaluation of the synergy of satellite sensors and in situ data for the quantitative estimation of ocean surface currents (e.g., Rio et al., 2014).

Among the different methodologies to retrieve surface currents, two are particularly interesting due to their high potential complementarity: satellite altimetry and land-based high-frequency (HF) radar (HFR) systems. The former technique consists in a constellation of altimeters onboard satellites measuring the global sea level, with a revisit period greater than a week and a track distance around tens of kilometres. These continuous sea level series are today close to completing 25 years of data, resolving the ocean dynamics from mesoscale to near-climate scale. HFRs are designed to measure the local ocean surface dynamics with a high time and space resolution. However, altimetry and HFR do not capture exactly the same dynamics. Altimetry detects surface currents that are in geostrophic equilibrium (by excluding the direct response of the surface layer to the wind and then part of the high-frequency variations), whereas HFRs measure surface total currents, i.e., the geostrophic and ageostrophic components (like wind-driven and inertial currents or the wave-induced Stokes drift; e.g., Ardhuin et al., 2009; Laws, 2001; Paduan and Graber, 1997).

Besides the effort made for collecting data from different platforms, methods for combining these data are under development. Recent studies focused on the evaluation of the performance of altimetry using HFRs, concluded that HFRs offer a way to improve the validation of altimetry products for coastal areas (Chavanne and Klein, 2010; Liu et al., 2012; Pascual et al., 2015; Roesler et al., 2013; Troupin et al., 2015). One of the most extended approaches found in the literature to study the synergy between altimetry and HFR data consists in the comparison of the total across-track currents in the along-track direction (e.g., Morrow et al., 2017; Pascual et al., 2015; Troupin et al., 2015). The combination of HFR and altimetry could help to potentiate their strengths by, for example, expanding the spatial and temporal coverage of the HFR systems or evaluating and correcting the altimetric signal near the coast.

In this study, we focus on the south-eastern Bay of Biscay (SE-BoB), which is characterized by the presence of canyons (e.g., Capbreton canyon), by an abrupt change in the orientation of the coast, and by a narrow shelf and slope. The winter surface circulation in the SE-BoB is mainly related to the Iberian Poleward Current (IPC), which affects the upper 300 m of the water column. In winter, the IPC flows over the slope, advecting warm surface waters (Charria et al., 2013; Le Cann and Serpette, 2009) eastwards along the Spanish coast and northwards along the French coast (Figure 3.1). In summer, the flow is reversed, being 3 times weaker than in winter (Solabarrieta et al., 2014). Overlaid to the density-driven slope circulation, wind-induced currents are the main drivers of the surface circulation in the area (e.g., Lazure, 1997; Solabarrieta et al., 2015). During autumn and winter, south-westerly winds dominate and generate northward and eastward drift over the shelf. The wind regime changes to the NE during spring, when it causes sea currents to turn toward the W-SW along the Spanish coast. The summer situation is similar to that of spring, but the weakness of the winds and the greater variability in the direction of the general drift make currents more variable (González et al., 2004; Lazure, 1997; Solabarrieta et al., 2015). In addition to these processes, mesoscale eddies in the SE-BoB are generated, mainly during winter, by the interaction of the IPC with the abrupt bathymetry (Pingree and Le Cann, 1992b) (Figure 3.1). The combination of these processes makes the SE-BoB an area of interesting complexity.

The existence of a long historical time series of surface current fields from a long-range HFR system in the area provides an invaluable opportunity to explore the benefit of a combined analysis of satellite and land-based remote-sensing ocean currents. This HFR network (two sites; see Figure 3.1) is part of the coastal observatory of the SE-BoB, also composed of a network of oceano-meteorological coastal stations and two slope buoys. The performance of this system and its potential for the study of ocean processes and of transport patterns in the area have already been demonstrated by previous work (e.g., Rubio et al., 2018; Solabarrieta et al., 2015). With regard to the usefulness of altimetry for describing ocean dynamics in the BoB, several studies have proven its suitability to study processes that go from mesoscale (Caballero et al., 2016b, 2014, 2008b; Dussurget et al., 2011; Herbert et al., 2011) to climate scale (e.g., Pingree, 2005).

The main objectives of this study are first to obtain a diagnosis of the agreement of the surface currents measured by altimetry and HFR over the SE-BoB and, second, to evaluate the observability of certain mesoscale processes by both measuring systems.

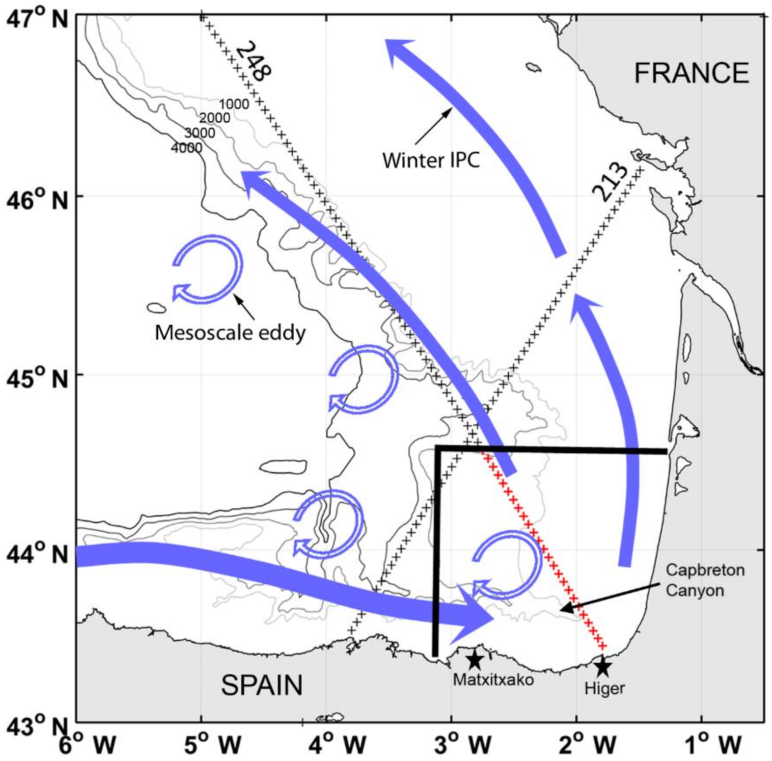

Figure 3.1. *Study area, observational systems and main characteristics of the ocean circulation (figure modified from Rubio et al., 2018). The winter IPC is represented by blue solid arrows, whereas the blue hollow arrows show the mesoscale eddy regime (although only anticyclonic arrows are represented, eddies of anticyclonic and cyclonic polarity are observed in different locations along the slope). The bold black lines delimit the HFR total-current footprint. The black stars represent the HFR stations: Matxitxako (left) and Higer (right). Jason-2 tracks 213 and 248 are represented by black crosses and the part of the track used in this study is marked in red. Grey lines: 1000, 3000, and 4000 m isobaths.*

2 Data and Methods

2.1 Data

2.1.1 HFR data

HFRs are remote-sensing instruments that send radio waves to the ocean surface and use the signal backscattered by the waves to infer the radial velocity of the surface current (toward or away from each HFR antenna). They can measure surface currents over wide areas with high spatial (300 m−10 km) and temporal (≤ 1 h) resolution. In this study, surface currents were obtained by means of two long-range HFR antennae. These antennae emit at a central frequency of 4.46 MHz and with an operational 30 kHz bandwidth. They are located at Matxitxako and Higer capes (Figure 3.1) and have provided operational data since 2009 (with some interruptions mostly due to maintenance stops or malfunctioning related to severe atmospheric conditions). The averaged Doppler backscatter spectrum obtained from the received signal (in a 3 h window) is processed to obtain hourly radial currents using the MUSIC algorithm (Schmidt, 1986). The coverage of radial data is up to 150 km, and the range cell and angular resolution are set to 5 km and 5º, respectively. Radial data are quality controlled using advanced procedures based on velocity and variance thresholds, signal-to-noise ratios, and radial total coverage. Since the deployment of the HFR system, the receiving antenna pattern of the two HFR sites has been calibrated at least every 2 years. A more detailed description of the system and of the HFR data validation exercises are provided by Solabarrieta et al. (2016, 2015, 2014) and Rubio et al. (2018, 2011).

To obtain total currents gridded onto a 5 km resolution regular orthogonal mesh, a least mean square algorithm (spatial interpolation radius of 10 km) was applied by using the HFR_Progs Matlab package (https://cencalarchive.org/~cocmpmb/COCMP-wiki/index.php/Main_Page#HFR_Progs_Documentation), based on Gurgel (1994) and Lipa and Barrick (1983). Then, using the same grid, radial velocities were processed with HFR_Progs to generate spatially gap-filled open-mode analysis (OMA) total currents (Kaplan and Lekien, 2007). In order to generate hourly total fields, 85 OMA modes, built setting a minimum spatial scale of 20 km, were used. A first analysis of the comparisons between HFR and altimetry showed that the results obtained using total currents generated by least mean squares and OMA were very similar. Thus, only results using OMA currents are presented in this work.

The typical spatial scales resolved by the HFRs depend on the resolution of the data and thus mainly on the operation frequency of the systems (Rubio et al., 2017). For the SE-BoB, the spatial scales resolved are typically of O(15−20) km.

2.1.2 Altimetry data

The basic principle of altimetry technology is to send a radar signal to the sea surface and then to measure the reflected return echo. The time needed for the signal to go and come back determines the distance between the altimeter and the sea surface (called the range). A physically-based model (Brown, 1977) is adjusted to the resulting signal, called waveform, providing different parameters, including range. To reduce the measurement noise, the result is averaged and the final data rate is classically (and in our case) 1 Hz (i.e., one datum every 7 km along the satellite track). By subtracting the range to the satellite orbit altitude (with respect to the reference ellipsoid) and by applying several corrections (e.g., tropospheric and ionospheric effects on the radar wave, sea surface bias), the sea surface height (SSH) is obtained (SSH = orbit – range – corrections). To retrieve the total geostrophic currents, in balance with the SSH gradients, the surface height must be referenced to the geoid; this height is called dynamic topography (DT). However, since geoids are not known with enough accuracy, only geostrophic anomaly currents can be accurately derived from sea level anomaly (SLA). The SLA is referenced to a temporal average (Le Traon et al., 2003) by subtracting a mean profile to the SSH (SLA = SSH – < SSH >). For more information about the SLA and the reference surfaces, the reader is referred to https://www.aviso.altimetry.fr/en/techniques/ altimetry/principle/basic-principle.html.

The two different along-track SLA time series used herein come from Jason-2's 248 and 213 tracks from cycle 18 to 259 and with a revisit period of 10 days. Track 248 covers the HFR footprint area, whereas track 213 only crosses a small area at the NW of the HFR total-current coverage (Figure 3.1); therefore, track 213 is only useful for the comparison with HFR radial data.

One of the altimetry datasets used in this study is the CTOH (Center for Topographic studies of the Ocean and Hydrosphere)-XTRACK product (http://ctoh.legos.obs-mip. fr/products/coastal-products/coastal-products-1/sla-1hz), which provides SLA data specifically processed for coastal areas. The filtered version of the product was used, meaning that a 40 km cut-off spatial Loess filter (Cleveland and Devlin, 1988) was also applied in order to reduce the remaining noise in the along-track SLA. For the same Jason-2 altimeter measurements, a differently processed dataset was also used to assess possible discrepancies between the two altimetric products. This product is a preliminary version of the 2018 update of the reprocessed global ocean along-track level-3 data provided by the Copernicus Marine Environment Monitoring Service (CMEMS). As for the CTOH-XTRACK product, data filtered with a 65 km cut-off spatial Lanczos filter (Pujol et al., 2016) were used. Note that, on the one hand, the accuracy of altimetry data is lower in the 20-30 km coastal band, so it might be a source of differences between altimetry and HFR data, and that, on the other hand, the larger the oceanic signal (larger signal-to-noise ratio), the lower this effect will be observed to be. In the SE-BoB, part of the slope (characteristically narrow) is located within the 20-30 km coastal band; therefore, the altimetry data will be affected by this inaccuracy in this area.

2.1.3 Wind data and sea surface temperature images

Hourly wind data from the Weather Research and Forecasting model (WRF; http://mandeo.meteogalicia.es/ thredds/catalogos/WRF_2D/catalog.html) were provided by the meteorological agency of Galicia (MeteoGalicia). This model, with a native resolution of 12 km, reproduces the offshore wind fields of the SE-BoB with reasonable accuracy (Ferrer et al., 2010). In this study, the WRF gridded fields were interpolated to the Jason-2 along-track points. Due to the cloudy weather in the SE-BoB, the most appropriate infrared sea surface temperature (SST) images were selected one by one from the AVHRR (Advanced Very High Resolution Radiometer) sensor series of 1 km resolution to process level-2 SST maps.

2.2 Methods

Since the time resolution of the altimetry (~ 10 days) is lower than that of the HFR (hourly), the HFR current data were filtered using a low-pass filter, based on a 10-day running average. The objective was to remove the high-frequency (HF) signals contained in the data (see, for instance, Solabarrieta et al., 2014) and part of the ageostrophic signals to make the HFR data closer to the measurements from altimetry. Several tests were carried out to determine the sensibility of the results to the temporal window chosen for the filter. For that purpose, 2-, 5-, 10- and 15-day low-pass filter configurations were tested, and the resulting currents were compared to those derived from the SLA. The 10-day filtered HFR currents provided the highest correlation with the altimetry data. It is worth noting that the 10-day running average filtered out a significant part of the wind-induced currents, except for the low-frequency (LF) Ekman component.

Since from the altimetry data used here we can only obtain sea surface anomaly currents, as explained in *Section 2.1.2*, the comparisons with the radar data were carried out in terms of anomaly. In order to obtain the HFR anomaly currents ($\mathrm{AC_{HFR}}$), the temporal average of the HFR currents (V) for the study period was subtracted from the series of low-pass HFR currents (Eq. 3.1). Then, to obtain SLA relative to the same period, the average SLA for the study period was subtracted to the SLA series (Eq. 3.2).

$$\mathrm{AC_{HFR}} = \mathrm{V} - < \mathrm{V} >_{t1-t2} \tag{3.1}$$

$$\mathrm{SLA'} = \mathrm{SLA} - < \mathrm{SLA} >_{t1-t2} \tag{3.2}$$

Hence, the time referenced SLA' and $\mathrm{AC_{HFR}}$ were obtained as suggested in Pujol et al. (2016), where $t1$ = 1 January 2009 and $t2$ = 24 July 2015. Hereafter, when referring to $\mathrm{AC_{HFR}}$ computed using Eq. (3.1), we will use $\mathrm{AC_{HFR,R}}$ to refer to current anomalies computed directly from the radial HFR components and $\mathrm{AC_{HFR,T}}$ to refer to current anomalies computed from total OMA HFR currents.

Concerning the altimetry velocity, across-track geostrophic anomaly currents ($\mathrm{AC_G}$) were inferred by means of the finite-difference geostrophic velocity equation (Eq. 3.3):

$$\mathrm{AC_G} = \frac{g}{f}\frac{\Delta \mathrm{SLA}'}{\Delta x} \tag{3.3}$$

where g is the acceleration of gravity, f is the Coriolis parameter, x is the along-track distance, and SLA' is the time referenced SLA. AC_G was estimated along the altimeter track by a three-point central difference operator with positive direction northeastwards (southeastwards) along track 248 (213).

For the statistical comparison between AC_G and AC_{HFR}, two different strategies were used. The first and simplest approach is the comparison of HFR radial across-track currents with altimetry across-track currents at two given points (explained in *Section 2.2.1*), which permits the direct use of radial HFR currents. The second approach is the along-track comparison (explained in *Section 2.2.2*) of total OMA HFR and altimetry across-track currents, which provides additional information on the spatial variability of the agreement between both datasets. Finally, in order to take into account the LF Ekman component that remains in the low-pass-filtered HFR data, a model for the computation of this component was used (explained in *Section 2.2.3*).

2.2.1 Pointwise comparison

This method, previously applied in Liu et al. (2012), consists in a direct comparison between HFR and altimetry data at a certain point, where one of the HFR radial directions (red lines in Figure 3.2) crosses the altimeter track perpendicularly. This approximation allows us to directly use $AC_{HFR,R}$, which are in the same direction as the across-track AC_G. This method was applied for Jason-2 altimeter tracks 213 and 248 shown in Figure 3.1, by using the corresponding $AC_{HFR,R}$ measured by the Matxitxako antenna at two points: point *E* on track 248 and point *W* on track 213 (Figure 3.2). Note that the radials from Higer station were not used, since they did not provide any orthogonal radial direction for track 248 and were too gappy for track 213 due to the large distance between this track and the antenna. Point *E* is located near the Capbreton canyon at 43.75º N, 2.05º W, 46.86 km from the coast and at a depth of 500 m (on the slope), whereas point *W* is located at 43.80º N, 3.58º W, 40.73 km from the coast and at a depth of 3000 m (on the abyssal plain). It is worth noting that by using directly radial currents, additional errors that propagate in the combination of HFR radials into HFR OMA currents are avoided.

In order to make the computations more robust to the potential absence of HFR or altimetry data at points *W* and *E*, nearby points were considered to obtain the across-track currents (Figure 3.2). With regard to $AC_{HFR,R}$, radial directions of ±5º (blue lines in Fig 3.2) away from the orthogonal radial direction (red lines in Figure 3.2) were also considered. For each of the three radials, the points in a range of ±5 km from the track were selected (blue and red crosses). Then, the across-track $AC_{HFR,R}$ in our point was obtained by firstly averaging the values for each radial, so that only three values along the track were obtained (green crosses in Figure 3.2). Finally, the three values were again averaged to get the corresponding across-track $AC_{HFR,R}$ (black dot in Figure 3.2).

On the other hand, the AC_G in the three along-track points considered for the HFR case (i.e., the green crosses in Fig 3.2) were averaged to obtain the AC_G in the central point (i.e., *E* and *W*). This permitted us to ensure a similar spatial smoothing for both datasets. It must be mentioned that for point *W* and for the CTOH altimetry product, the AC_G points were located between the along-track HFR points, so instead of considering three along-track points, two points on each side of the central point (*W*) were selected.

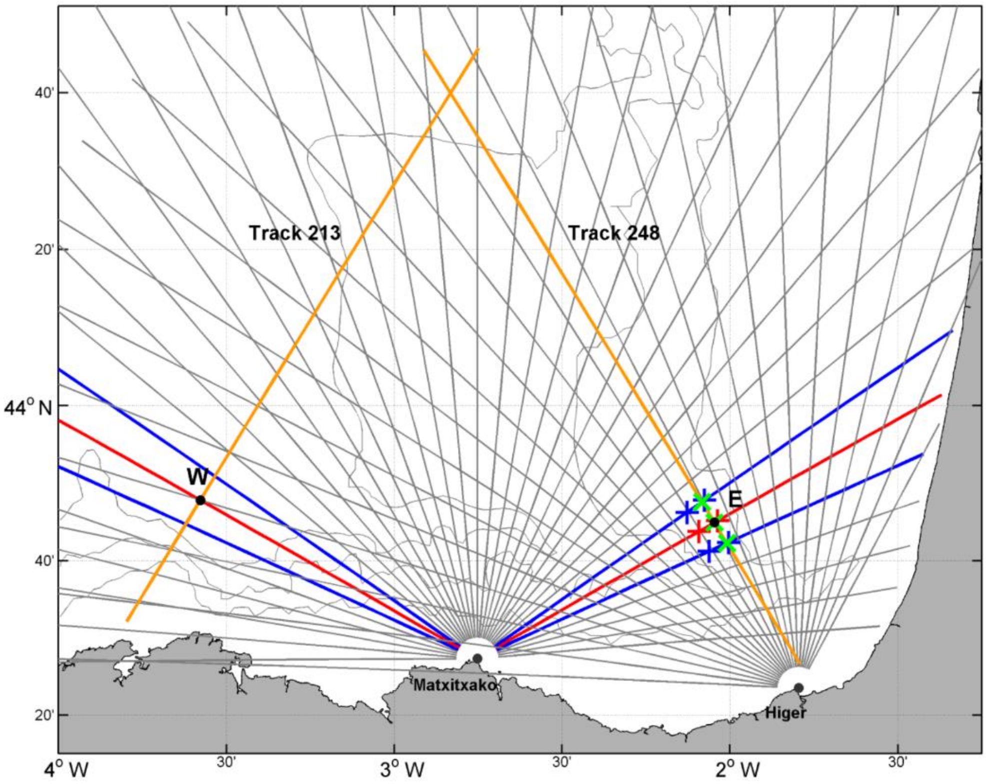

Figure 3.2. *Schematic view of the pointwise comparison and of the data used for this approximation. Jason-2's 213 and 248 tracks are depicted by orange lines. The HFR radial directions from both sites are represented by grey lines and the selected radial directions (from the Matxitxako site) for the pointwise comparison are plotted in red (the central radial orthogonal to the track) and in blue (the adjacent radials). Points E and W are the points where each of the HFR radial directions is orthogonal to the Jason-2's track directions. Around E, the blue and red crosses show the selected points of HFR radial directions where radial currents are averaged to obtain the corresponding values on the track (green crosses). Then, the along-track green crosses are averaged to obtain the corresponding HFR current values at the point at issue (the same process is carried out for point W, but it is not represented in the figure). Grey lines: 200, 1000, and 2000 m isobaths.*

2.2.2 Along-track current comparison

In order to compare HFR and altimetry data from the coast to the open ocean, across-track $AC_{HFR,T}$ and AC_G were compared along track 248. For that purpose, $AC_{HFR,T}$ was interpolated into the along-track altimetry points, and it was rotated to the across-track direction. Then, for each along-track AC_G point, the average with its four adjacent points was calculated. As in the previous case, this permitted us to ensure a similar spatial smoothing for both datasets. The sensitivity to the number of adjacent points considered was tested, and this approach was the one that provided the best adjustment to the HFR data.

2.2.3 Ekman currents

Ekman currents were estimated to evaluate what their contribution to LF currents in the area was, and how this component contributed to part of the differences observed between HFR and altimetry. Three different ways of calculating Ekman currents were tested to infer which one provided the best results in the comparisons: the rule of thumb that states that the surface currents are 3 % of the wind velocity; Ekman equations for the surface (Ekman, 1905); and the model M1 proposed in Rio and Hernandez (2003). Ultimately, the M1 model offered the best results:

$$\vec{u}_{ek} = \frac{b\vec{\tau}}{\sqrt{f}} e^{i\theta} \tag{3.4}$$

where f is the Coriolis parameter, $\vec{u}_{ek}$ is the Ekman current vector (meridional and zonal components), b is the amplitude parameter, θ is the phase parameter, and $\vec{\tau}$ is the wind stress vector (meridional and zonal components) that was obtained by means of the bulk-flux formula (Stewart, 2008):

$$\vec{\tau} = \rho_{air} C_d |\vec{w}| \vec{w} \tag{3.5}$$

where ρ_{air} is the density of the air (1.22 kg m^{-3}), $\vec{w}$ is the wind vector, and C_d is the drag coefficient proposed by Large and Pond (1981). b and θ were acquired by adjusting the model (by a least-square fit) to the real data in the study area. These parameter values were taken from Caballero et al. (2008a), where from the fit of wind stress measurements and drifter-derived currents of the Bay of Biscay to Eq. (3.4), the following results were obtained: $b = 4.45 \cdot 10^{-3}$ m^2 kg^{-1} $s^{1/2}$ and $\theta = -23.68^{\circ}$. Once the parameters were obtained, $\vec{u}_{ek}$ was estimated using the wind data series described in *Section 2.1.3*.

Ekman currents were initially computed at the locations of the WRF model nodes. Then, for the pointwise comparison, a similar procedure as with $AC_{HFR,R}$ and AC_G was followed. First, they were interpolated in *E*, in *W*, and at their adjacent along-track points (i.e., the green crosses in Figure 3.2) and rotated to obtain the across-track component. Subsequently, they were averaged to obtain the across-track Ekman current velocity at *E* and *W*. For the along-track current comparison, they were interpolated to the altimetry along-track points, and then, rotated to get the across-track component. Ekman currents were also 10-day running averaged to remove the HF Ekman signal. Since comparisons were made in terms of anomaly currents, Ekman anomaly currents (AC_E) were estimated by subtracting the average value of the study period like in Eqs. (3.1) and (3.2). For considering wind-induced currents in the comparisons they were added to AC_G, and this is indicated as AC_G+AC_E.

The results of all the comparisons described above are presented in terms of the correlation coefficient (*r*) (with a confidence level of 100 % and 90 % for the pointwise comparison and the along-track current comparison, respectively) and the root mean square difference (RMSD) between the across-track currents measured by each system from 1 January 2009 and to 24 July 2015. In addition, the mean and the standard deviation (SD) of such currents were also analysed. Hereinafter, points *E* and *W* will be called differently depending on the used comparison method. Since the HFR radials are used at the pointwise comparison, the crossing points are called E_R and W_R. In the along-track comparison, point *E* is precisely one of those along-track points. Therefore, considering that the rotated $AC_{HFR,T}$ are used in this comparison, the point is named E_T. The points along the track where *r* is maximal (point 2.10º W, 43.82º N for CTOH and point 2.09º W, 43.80º N for CMEMS) are also called Max_T. All these points and their statistics are displayed in Table 3.1, as well as in Figures 3.3–3.5, and they are discussed in the next section. Moreover, in Figure 3.5, apart from the results of E_T and Max_T, the results for all the track 248 are also shown.

Note that the HFR-altimetry comparisons were carried out for the CMEMS and CTOH datasets and that each comparison was also made with and without adding AC_E.

3 Results and Discussion

3.1 Statistical results

Table 3.1 provides an overview of the statistical results of the HFR-altimetry comparison at points E_R and W_R for the pointwise method and at points E_T and Max_T for the along-track method. In general, the comparison between AC_{HFR} and AC_G (AC_{HFR} and AC_G+AC_E) shows maximum correlations of 0.64 (0.70).

Table 3.1. *Statistics at different points for the study period. r is the correlation parameter, and RMSD is the root mean square difference of the velocity anomalies between HFR and altimetry for different altimetry products (i.e., CMEMS and CTOH). The mean and the standard deviation (SD) are also estimated for each dataset. E and W are the points where HFR radial velocities are orthogonal to tracks 248 and 213, respectively (see Figure 3.1).* E_R *and* W_R *are the names given to those points in the pointwise comparison, whereas* E_T *is given in the along-track current comparison.* Max_T*, is the track point where the correlation r is maximal in the along-track current comparison (point 2.10º W, 43.82º N for CTOH and point 2.09º W, 43.80º N for CMEMS). RAD refers to HFR radial data for* E_R *and* W_R *and across-track rotated OMA anomaly currents for* E_T *and* Max_T*. There is no data in* Max_T *because they are different for each altimetry product. Both* AC_G *and* AC_G+AC_E *cases are considered.*

		r		RMSD (cm s^{-1})		Mean ± SD (cm s^{-1})		
		CMEMS	CTOH	CMEMS	CTOH	CMEMS	CTOH	RAD
E_R	AC_G	0.53	0.48	7.4	7.5	0.3±8.7	−0.1 ±8.5	0.1±5.9
	$AC_G + AC_E$	0.64	0.59	7.1	7.4	0.3±9.7	−0.2±9.4	
W_R	AC_G	0.61	0.64	9.2	7.8	−0.2±11.9	0.2±9.9	0.0±9.3
	$AC_G + AC_E$	0.67	0.70	8.9	7.4	−0.1±12.8	0.2±10.6	
E_T	AC_G	0.56	0.53	7.1	6.5	−0.1±8.2	−0.3±7.6	0.2±5.4
	$AC_G + AC_E$	0.65	0.62	7.1	6.4	−0.1±9.3	−0.4±8.6	
Max_T	AC_G	0.60	0.55	6.5	6.1	−0.2±7.9	−0.2±7.2	-
	$AC_G + AC_E$	0.68	0.65	6.6	6.0	−0.3±8.9	−0.3±8.3	

3.1.1 Pointwise comparison

Concerning the pointwise comparisons between AC_G and $AC_{HFR,R}$ it can be observed that *r* depends on the location as well as on the altimetry product considered (see Table 3.1). In any case, the addition of AC_E increases *r* by 6 %−11 % for both altimetry products: from 0.53 and 0.48 to 0.64 and 0.59 in E_R and from 0.61 and 0.64 to 0.67 and 0.70 in W_R for CMEMS and CTOH, respectively. The RMSD also decreases between 0.1 and 0.4 cm s^{-1} showing that, in general terms, the addition of AC_E improves the agreement between $AC_{HFR,R}$ and AC_G. However, it adds variability: the SD for AC_G+AC_E increases with respect AC_G by 0.7−1.0 cm s^{-1}. It should be pointed out that the SD of $AC_{HFR,R}$ is lower than the SD of AC_G (where CMEMS's variability is higher than CTOH's), probably due to the filtering of HF signals applied to the radar or because the finite-difference operator used to estimate AC_G increases the variability. The same effect was observed in Liu et al. (2012) and in Verron et al. (2018).

The time series of $AC_{HFR,R}$ and AC_G+AC_E for both altimetry products at points E_R and W_R show global agreement and all the datasets depict similar variabilities (Figure 3.3). However, the largest variability is observed in W_R also shown in Table 3.1 (as SD). Although in Figure 3.3 it is difficult to detect any differences between locations and datasets, the lowest RMSD is observed in E_R for CMEMS AC_G+AC_E (RMSD=7.1 cm s^{-1}), while the RMSD rises up to 8.9 cm s^{-1} in W_R for CTOH AC_G.

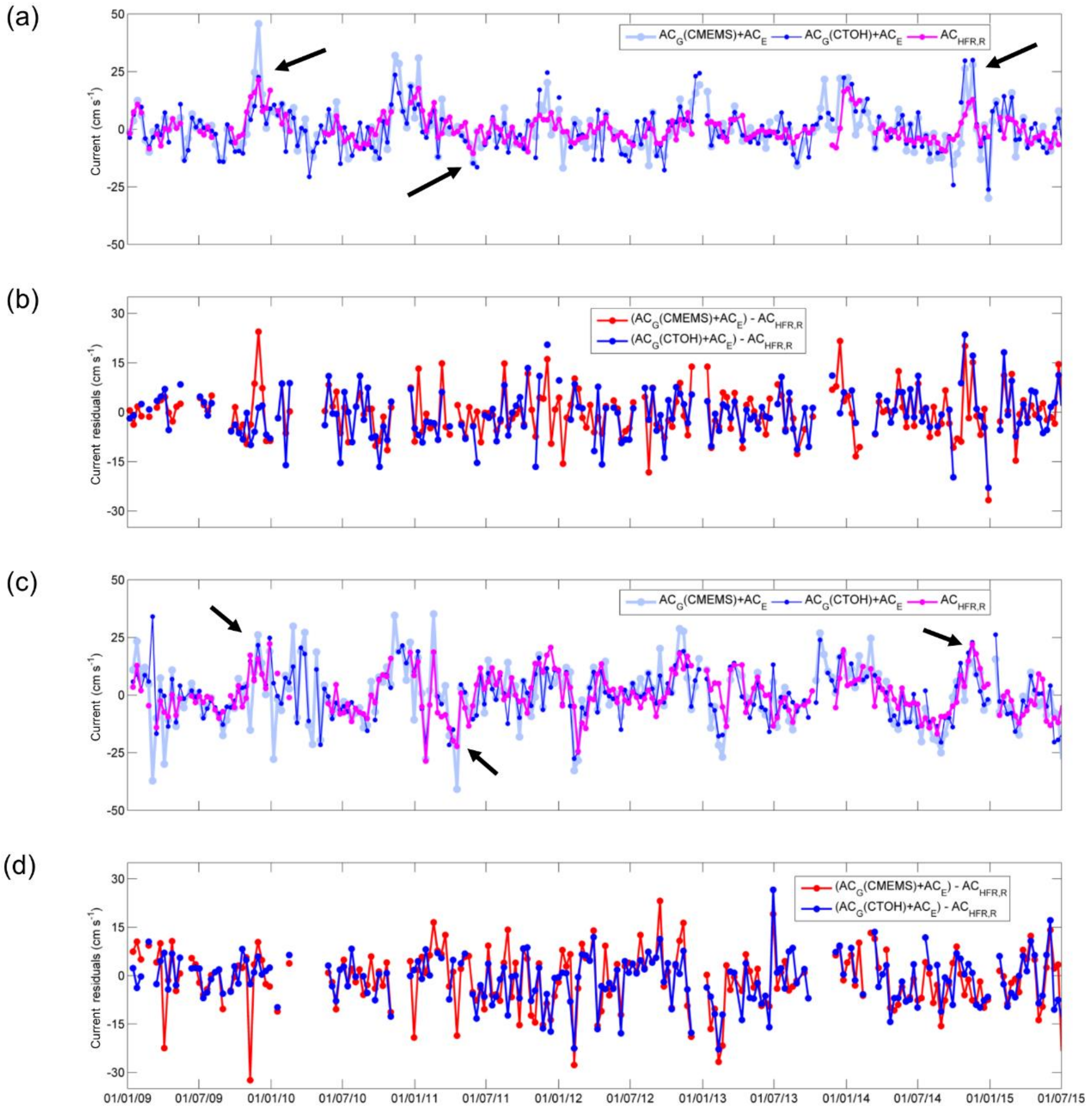

Figure 3.3. *Across-track AC_G+AC_E and $AC_{HFR,R}$. (a) CTOH, CMEMS, and HFR datasets at point E_R. (b) CTOH-HFR and CMEMS-HFR residuals at point E_R. (c) CTOH, CMEMS, and HFR datasets at point W_R. (d) CTOH-HFR and CMEMS-HFR residuals at point W_R. Black arrows depict the slope current intensifications mentioned in the text.*

In terms of correlation, the results suggest greater agreement in W_R (0.67 and 0.70 for CMEMS and CTOH AC_G+AC_E, respectively) than in E_R (0.64 and 0.59 for CMEMS and CTOH AC_G+AC_E, respectively). This could be explained by the fact that point W_R is located in a deeper area and is more influenced by the IPC that flows over the slope. The IPC shows lower variability at point E_R than at point W_R, where the signal of the slope current is more persistent. These spatial differences agree with what was observed in the area by Rubio et al. (2013a) from the analysis of the ADCP (Acoustic Doppler Current Profiler) time series of two buoys located over the slope in locations comparable to points *E* and *W*. These authors suggest that while there is a clear along-slope transport with intense mesoscale variability at Matxitxako buoy (slightly east from point *W*), at Donostia buoy (close to point *E*) the influence of the slope circulation was less significant. The lower current velocities and lower vertical coherence observed at the Donostia buoy during winter could be linked to the complex bathymetry, which might force the IPC to flow over deeper grounds out of the point measured by the buoy. This could also explain why the addition of AC_E increases more *r* in E_R (by 11 %) than in W_R (by 6 %), where the circulation has a stronger geostrophic component.

With regard to the performances of the two altimetry products, it must be highlighted that CTOH shows higher (lower) *r* (RMSD) in W_R, while CMEMS shows higher (lower) *r* (RMSD) in E_R (see Table 3.1). However, the differences are small and do not permit us to draw conclusions on their relative accuracy. In E_R (W_R) when *r* is higher for CMEMS (CTOH) than for CTOH (CMEMS), the RMSD is lower in the former. Therefore, the higher the correlation, the smaller the difference between AC_G(+AC_E) and $AC_{HFR,R}$. However, the difference in the RMSD is not related to the difference in *r*.

The residuals between AC_G+AC_E and $AC_{HFR,R}$ for each altimetry product show that in W_R (Figure 3.3d), the residuals' amplitudes are larger for CMEMS than for CTOH, agreeing with the higher RMSD values observed for CMEMS. In E_R the similar RMSD values observed for both altimetry products agree with the similar amplitudes of the residuals in Figure 3.3b.

The IPC winter intensification is visible in all datasets, being stronger for AC_G+AC_E (for both altimetry products) than for $AC_{HFR,R}$. There are some remarkable intensifications, for instance in November 2014, when a strong peak is shown in all the series and where the $AC_{HFR,R}$ signal is higher in W_R than in E_R (see black arrows in Figure 3.3a and c), approaching AC_G+AC_E. There is another remarkable intensification in winter 2009, when the IPC shows a pronounced peak (see black arrows in Figure 3.3a and c), especially in E_R, where AC_G (CTOH)+ AC_E is very similar to $AC_{HFR,R}$. This intensification is not so clear at point W_R, but it is still noticeable compared to the rest of the period. Equatorward slope current intensifications can be also observed throughout the whole period, as for instance in May 2011, where the peak is more prominent in W_R than in E_R (and even more for CMEMS) (see black arrows in Figure 3.3a and c).

Since the presence of a stronger IPC signal is expected to improve the correlation between HFR and altimetry and the IPC shows marked seasonality, a monthly analysis was carried out for AC_G, AC_G+AC_E and $AC_{HFR,R}$ at E_R and W_R (with each altimetry product). Thus, monthly values of several statistical parameters were estimated as shown in Figure 3.4, computed considering all the available data for each month during all the study period.

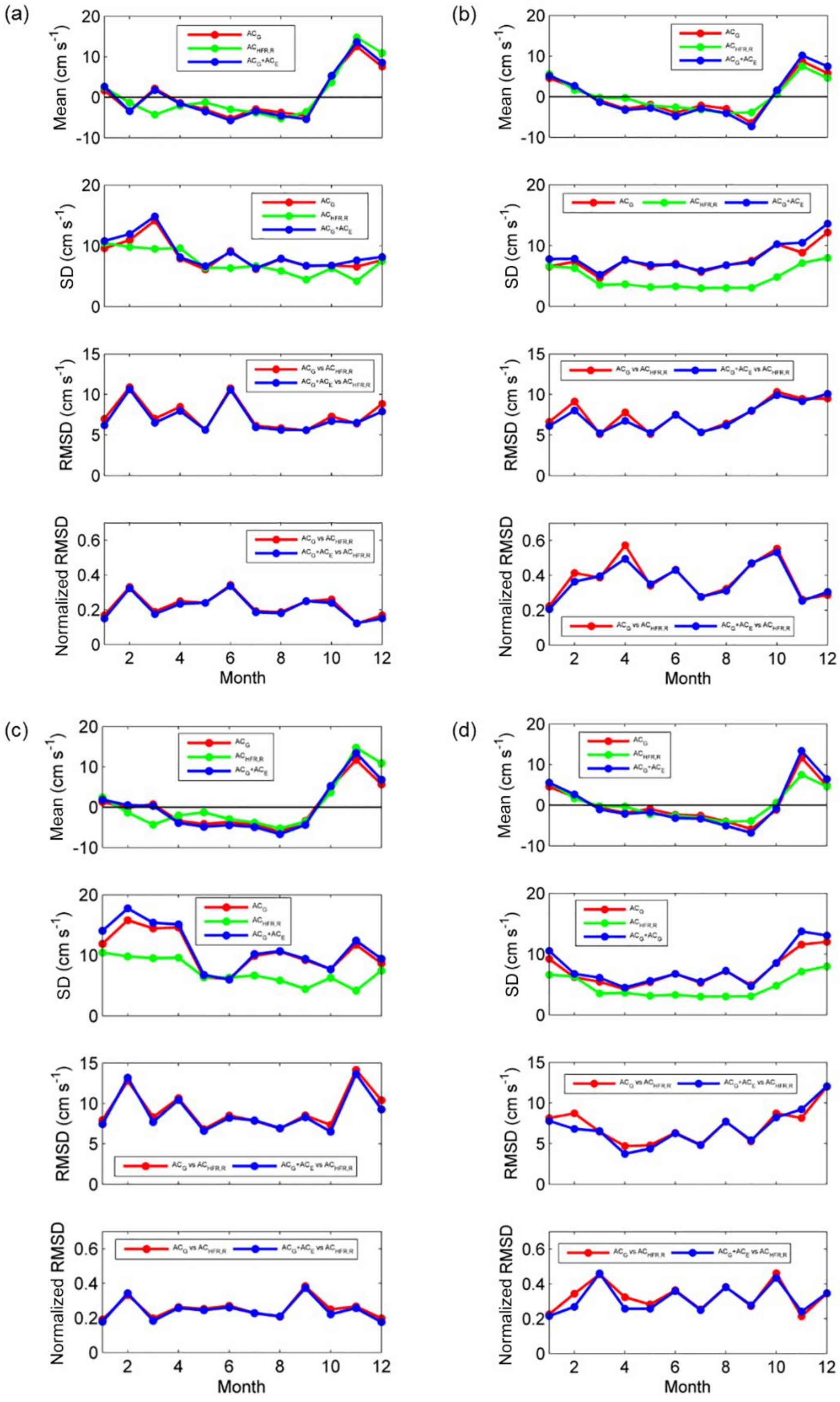

Figure 3.4. *Monthly statistical parameters of the comparison between* AC_G *vs.* $AC_{HFR,R}$ *and* AC_G+AC_E *vs.* $AC_{HFR,R}$ *at points* E_R *and* W_R *for both altimetry products: (a) CTOH* AC_G *at point* W_R*, (b) CTOH* AC_G *at point* E_R*, (c) CMEMS* AC_G *at point* W_R*, and (d) CMEMS* AC_G *at point* E_R*. The normalized RMSD is the quotient between the RMSD and the values of the corresponding* $AC_{HFR,R}$*.*

It can be observed that in terms of monthly mean currents, the three time-series have the same tendency and that there is a low discrepancy among them, as well as between the two altimetry products. The winter poleward current intensification is evident from October to January with a maximum in November (ranging for all datasets from 7.5 to 13.4 cm s^{-1} in E_R and from 11.7 to 14.8 cm s^{-1} in W_R). In E_R, the current intensification is still perceptible in February, whereas in W_R there is a small increase in March for $AC_G(+AC_E)$ but not for $AC_{HFR,R}$. From March to September the mean is weak, with a slight decrease reaching the minimum in September (ranging from 7.3 to 3.9 cm s^{-1} in E_R for all datasets and from 5.4 to 3.6 cm s^{-1} in W_R) and showing an equatorward weak mean slope current for that period. The addition of AC_E slightly strengthens the intensity of the slope currents for both poleward and equatorward directions. This can be explained by the general wind patterns of the area, which are in agreement with the main local geostrophic regime, although winter south-westerlies are stronger than the summer north-easterlies (e.g., Herbert et al., 2011; Solabarrieta et al., 2015).

$AC_{HFR,R}$ shows the lowest monthly SD values along all the period (Figure 3.4), agreeing with previous observations (see Table 3.1). AC_G SD values are slightly increased by the addition of AC_E, especially in winter when winds are stronger. At point E_R, the tendency of the SD is similar to that of the mean, being slightly higher in January and then stable (with small oscillations) until September. In the last 3 months of the year, it is increased. Therefore, there is higher variability in late autumn and winter, probably due to the slope current intensification and the stronger winds. At point W_R, the highest variability takes place in the first 4 months of the year. This increase is coherent with the intensification of the slope current and the development of an anticyclonic structure in March and especially in April near Torrelavega canyon (Caballero et al., 2014). Afterwards, the variability is practically maintained, with small oscillations and an increase in $AC_G(+AC_E)$ for CMEMS.

Regarding the RMSD, the patterns are similar to those of the SD of $AC_G(+AC_E)$, but with higher fluctuations. In general, the addition of AC_E improves the results by a slight decrease in the RMSD. The major differences between AC_G and AC_G+AC_E time-series are observed in February and April at point E_R. This can be clearly seen in the normalized RMSD, which measures the value of the RMSD with respect to the values of $AC_{HFR,R}$.

3.1.2 Along-track current comparison

Mean, variance, *r* and RMSD values were computed along track 248 as shown in Figure 3.5 in order to study the spatial differences in the comparison between $AC_{HFR,T}$, AC_G and AC_G+AC_E data. Temporal statistics considering all the study period for each point of the track are plotted as a function of the distance to the first point of the track.

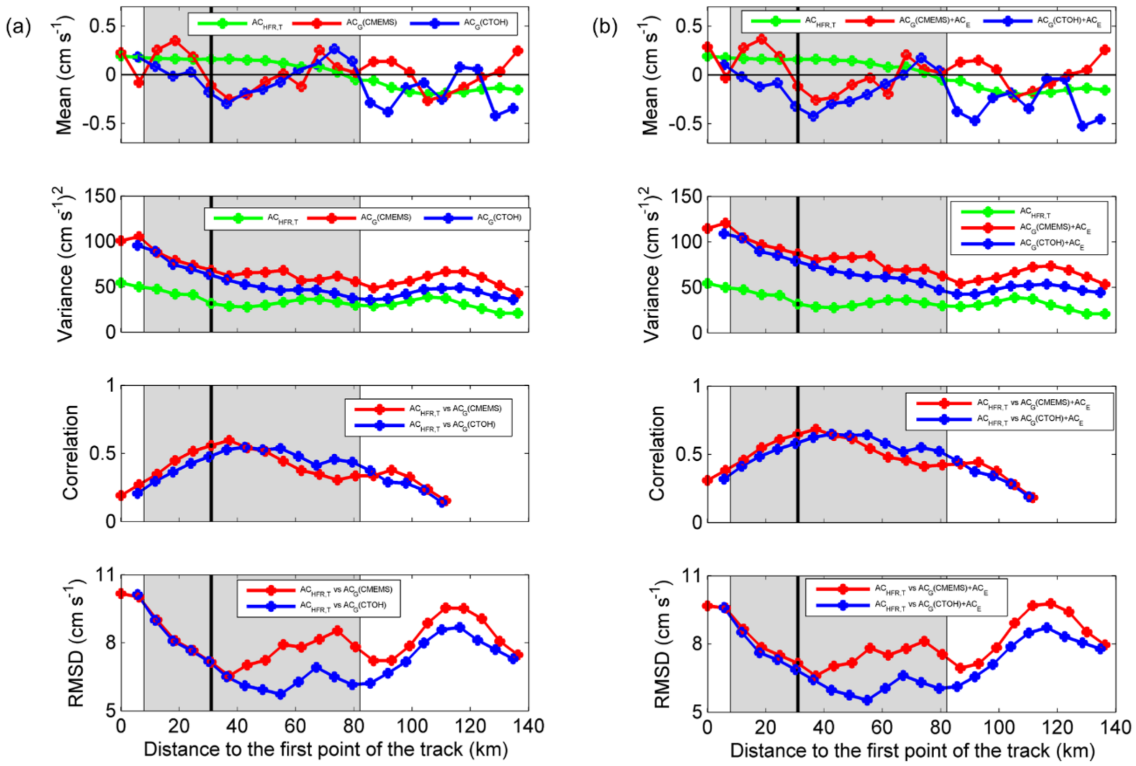

Figure 3.5. *Mean and variance values along track 248 of different datasets: (a) $AC_{HFR,T}$, AC_G (CTOH) and AC_G (CMEMS); (b) $AC_{HFR,T}$, AC_G (CTOH) $+AC_E$ and AC_G(CMEMS)$+AC_E$. In addition, correlation and RMSD values between (a) $AC_{HFR,T}$ and AC_G and (b) $AC_{HFR,T}$ and AC_G+AC_E. The grey-coloured area corresponds to the slope between the 200 and 1000 m isobaths, whereas the black line is the location of point E. The first point of the track is around 10.5 and 13 km away from the coast for CTOH and CMEMS, respectively. The spacing between the points is slightly different and the HFR points are the same as the CMEMS points. The first point in CTOH is removed because it is an outlier. Correlation values are not plotted for confidence levels under 90 %.*

$AC_{HFR,T}$ show mean values close to zero along all the track, with low fluctuations. Currents are oriented poleward over the shelf and upper slope over grounds shallower than 1000 m (i.e., until the point where the track leaves the slope current area). From there on, the mean is oriented equatorward. The mean AC_G is also close to zero; however, it shows larger fluctuations, changing between positive and negative values along the track, with a lack of agreement between both altimetry products at some points. Nevertheless, it should be pointed out that in any case, the mean anomaly currents are very weak and that the high SD values compensate for changes in the mean values. The addition of AC_E does not cause any spatial variation, and it barely changes the values. With regard to the variability, it is higher close to the coast. For AC_G, it slowly decreases as it gets away from the first point of the track, until the 1000 m isobath of the slope is reached (where the grey area ends in the figure). From there on, it is kept almost constant with a slight local maximum at around 120 km from the first point. For $AC_{HFR,T}$, the variability decreases until the point E_T is reached (where the Capbreton canyon area ends), and afterwards, it is also almost constant, with two maximums at around 60 and 105 km from the first point. It can be once again observed that the addition of the AC_E slightly increases the variability, that the variability in AC_{HFR} is lower than that of AC_G, and that CMEMS's variability is higher than CTOH's. The novelty is that all these results are now provided all along the track.

The highest r is observed between the 200 and 1000 m isobaths of the slope, where the IPC signal is the strongest, and thus the geostrophic component measured by the HFR is also stronger. At the points furthest from the coast, the r decreases. This can be linked to the absence of a strong and persistent geostrophic component and a higher signal-to-noise ratio for the HFR data (which increases as we get away from the antennas).

The maximum (minimum) values of r (RMSD) occur at around 37 and 45 km from the first point of the track for CMEMS and CTOH, respectively (Max_T points). These values could be explained by the fact that those points are located in the middle of the slope, where the slope current is stronger and where they are out of the Capbreton canyon area. At the same time, in that area, the slope current direction is nearly orthogonal to the track, so that the across-track component is stronger. For CTOH, the values around the maximum are relatively high, that is why the maximum is not a prominent peak. The same happens for CMEMS, but with a sharper peak and higher value (see Table 3.1). The addition of AC_E increases the r by 8 %−10 % as can be seen in Table 3.1 (for E_T and Max_T points).

In general, the addition of AC_E slightly increases (decreases) the r (RMSD), all along the track. This fact is not perceptible in the figure, where it seems that the addition of AC_E does not make any difference, but it can be observed in the values of Table 3.1 (except at point E_T for CMEMS data where it does not change).

3.2 Observability of mesoscale processes in HFR and altimetry datasets

In order to provide a complementary insight into the synergies and differences between HFR and altimeter data, in this section, the observability of different processes detected by HFR and altimetry is qualitatively analysed. Since the data are spatially filtered (for AC_G) or time filtered (for AC_{HFR} and AC_E), the detectable processes are mesoscale, seasonal, and interannual processes, such as mesoscale eddies and the IPC. Only CMEMS data are used for this analysis since the statistical results are very similar for both altimetry products and CMEMS data have fewer spatiotemporal data gaps in the study period and area, which is more suitable for monitoring ocean processes.

3.2.1 Observability of the IPC

Along-track values of SLA', across-track AC_E and across-track $AC_{HFR,T}$ for all the study period are shown in Figure 3.6. The highest SLA' values are observed during late autumn and winter, whereas the lowest ones are observed in spring and summer, especially from March to July (Figure 3.6a). This is coherent with the contribution of the main driving factor of the seasonal SLA variability in the area, the steric effect. It was observed in Caballero et al. (2008b) that the maximum amplitude of sea level in the BoB is reached in October, whilst the minimum takes place in April. AC_E shows a poleward seasonality with intensifications mainly in autumn and winter (usually from November to February) and weaker equator-ward currents in spring and summer (usually from March to October) (Figure 3.6b). This fact agrees with the general wind pattern in the area. Along-track SLA' gradients indicate winter slope current intensifications (IPC events) mostly from November to January and from the coast to the 1000 m isobath, approximately. The poleward intensification in winter 2014/2015 is the most remarkable, as already described in Rubio et al. (2018). In spring and summer, the gradients are weaker and even suggest equator-ward currents along all the track.

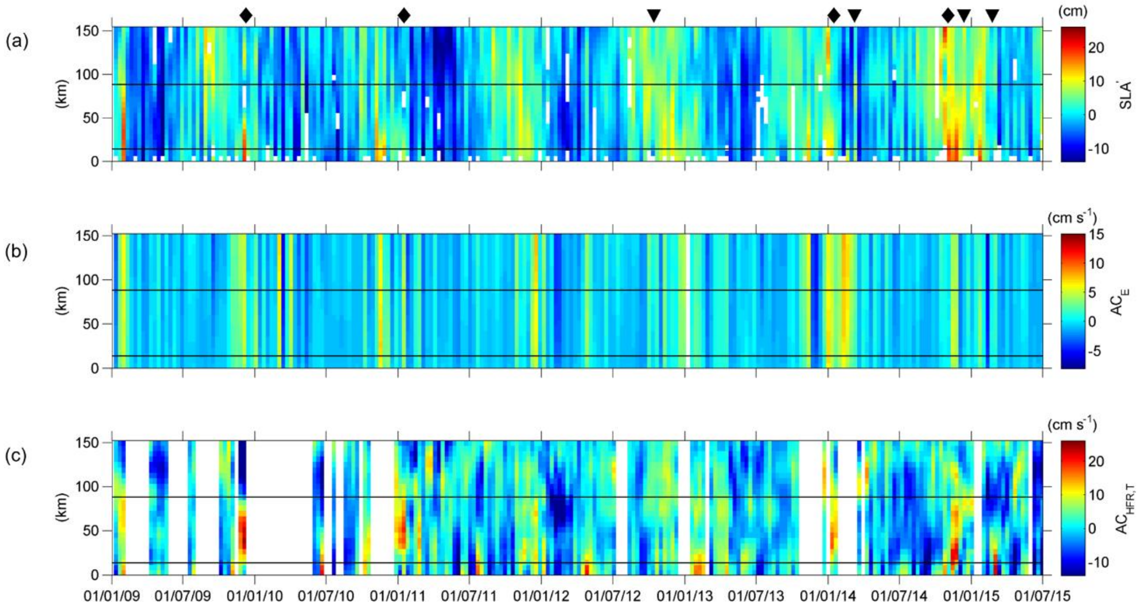

Figure 3.6. *Time evolution from 1 January 2009 to 1 July 2015 along track 248 (y-axis shows distance to the first point of the track in kilometres) of (a) CMEMS SLA' (cm), (b)* AC_E *(cm* s^{-1}*), and (c)* $AC_{HFR,T}$ *(cm* s^{-1}*). The distance from the first point of the track to the coast is around 6 km. The horizontal black lines delimit the slope area between the 200 and 1000 m isobaths. The black diamonds depict the IPC intensification signals whereas the black inverted triangles show the eddy events, all mentioned in the text.*

The IPC events are also detected by $AC_{HFR,T}$ in late autumn and winter, mainly in the points nearest to the coast between the 200 and 1000 m isobaths (Figure 3.6c). In spring and summer, although there are also several poleward current pulses, they are weaker. During this period, equatorward current pulses are also observed. From the joint analysis of SLA' and $AC_{HFR,T}$ data series, four main IPC events can be detected along the study period (Figure 3.6a and c).

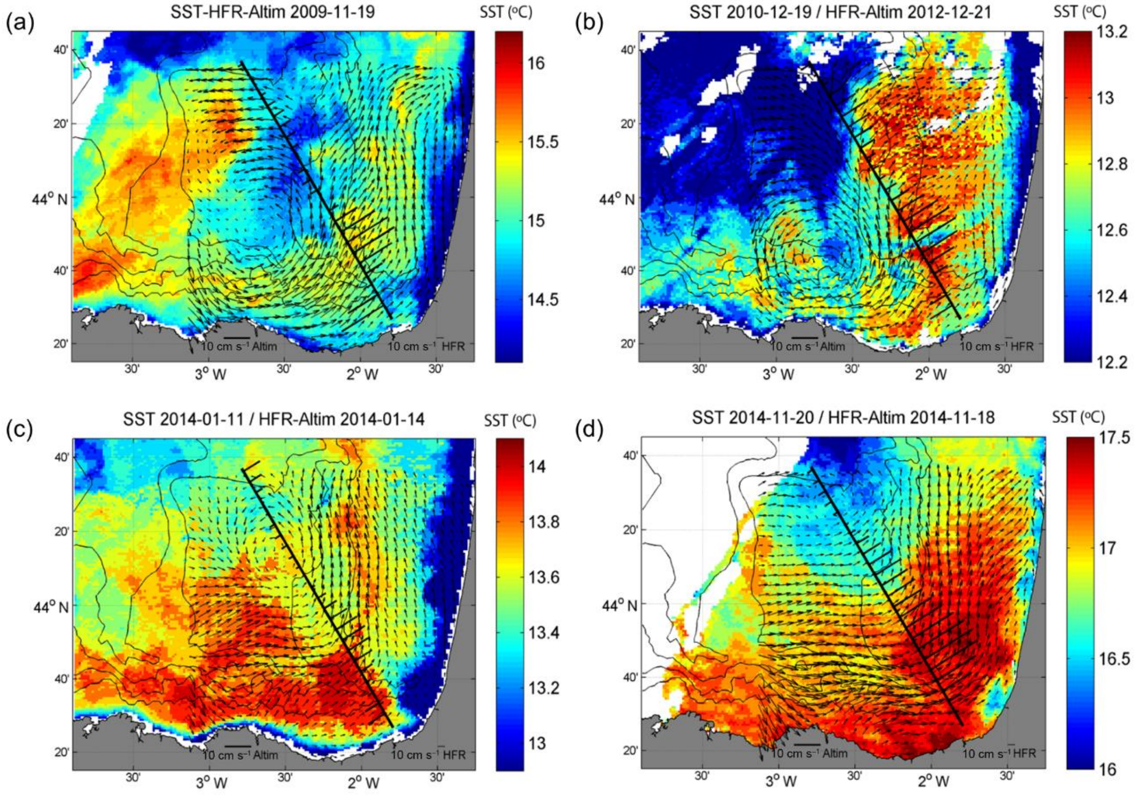

Figure 3.7. Snapshots showing four slope current intensification events observed by HFR, altimetry, and SST (see the dates of the events depicted in Figure 3.6) in November 2009 (a), December 2010-January 2011 (b), January 2014 (c), and November 2014 (d). The small arrows depict the HFR current fields (not rotated) whereas the thick ones indicate the across-track AC_G*. The black line shows the altimeter's track. The colormap depicts the sea surface temperature (ºC) with values referenced in each colour scale. Note that the dates corresponding to the data are not the same for SST or for HFR and* AC_G *(specified in each panel's title).*

More details on these events are provided in Figure 3.7, where four selected HFR total current field (obtained from OMA as explained in *Section 2.1.1*) snapshots are shown. Although each event is presented for a specific date, they last around 2–3 weeks (not shown), with the dates displayed in the figure being representative of all the period. Note that the SST maps do not show the same date as HFR snapshots and SLA' data, due to the limitations of this technique under cloudy conditions. For the four events, HFR total currents show a typical IPC spatial pattern, with poleward circulation along the slope intensifying between the 200 and 1000 m isobaths (Solabarrieta et al., 2015). The poleward patterns observed by the HFR agree with the AC_G observed along the altimetry track, which shows intensified poleward currents over the slope. For the four events, the SST images show that the current intensifications along the slope are related to an increase of 0.5−1 ºC over time (not shown), which is an increase in temperature previously observed in the study area or nearby (e.g., Esnaola et al., 2013; García-Soto, 2004; Le Cann and Serpette, 2009). The spatial extension of the warm water masses and the IPC along the French shelf/slope depends on the event, and it coincides with the area where the highest agreement between AC_G and HFR total currents is observed. During the IPC event of November 2009, the warm water tongue is closer to the coast. In this event, the strongest agreement between AC_G and HFR total currents is observed over the slope, while they disagree in the north-western area of the domain. Otherwise, during December 2010, the warm water extends over adjacent off-shore areas, as well as the area presenting the strongest agreement between HFR and the altimeter. In three of the four events, AC_G and HFR total currents show a lower fit over the shelf. These observations corroborate the results obtained in *Section 3.1*, where the best statistical results are obtained for the data pairs inside the slope area (Figure 3.5).

As one of the possible drivers of the IPC interannual variability, the relationship between the IPC and the NAO (North Atlantic Oscillation) in the BoB was described in Garcia-Soto et al. (2002) and Garcia-Soto (2004). They concluded that for strong IPC years, January water warmings (as a signal of the IPC) were related to negative NAO index values in the previous months (November, December). In addition, Le Cann and Serpette (2009) and Le Henaff et al. (2011) also observed negative NAO indexes during the preceding November and December months to intense IPC events in January. Esnaola et al. (2013) found that the NAO was the most recurrent teleconnection among different teleconnections with significant relationship with the IPC in winter months. For example, they also observed that positive Eastern Atlantic (EA) index values were related with the IPC.

Table 3.2. *NAO and EA indexes in the previous 2 months of the events. m–2 means 2 months before the event whereas m–1 means 1 month before.*

Event	NAO		EA	
	m–2	m–1	m–2	m–1
November 2009	1.62	–0.61	0.59	0.96
January 2011	–1.84	–1.8	0.24	–0.49
January 2014	0.81	0.79	0.09	1.2
November 2014	1.72	–0.87	0.2	1.02

For the four events studied here, the relationship between the IPC intensification and NAO and EA indexes is shown in Table 3.2 (data obtained from http://www.cpc.ncep.noaa.gov/data/teledoc/telecontents.shtml). In general, the NAO (EA) indexes are negatively (positively) related to the IPC in strong intensification periods; however, this relationship does not always apply (see, for instance, the events of 2011 and 2014 where a negative EA index and a positive NAO index are observed, respectively). Moreover, the intensity of the currents is not related to the amplitude of the index, leading to the same conclusion as Le Cann and Serpette (2009) and Le Hènaff et al. (2011).

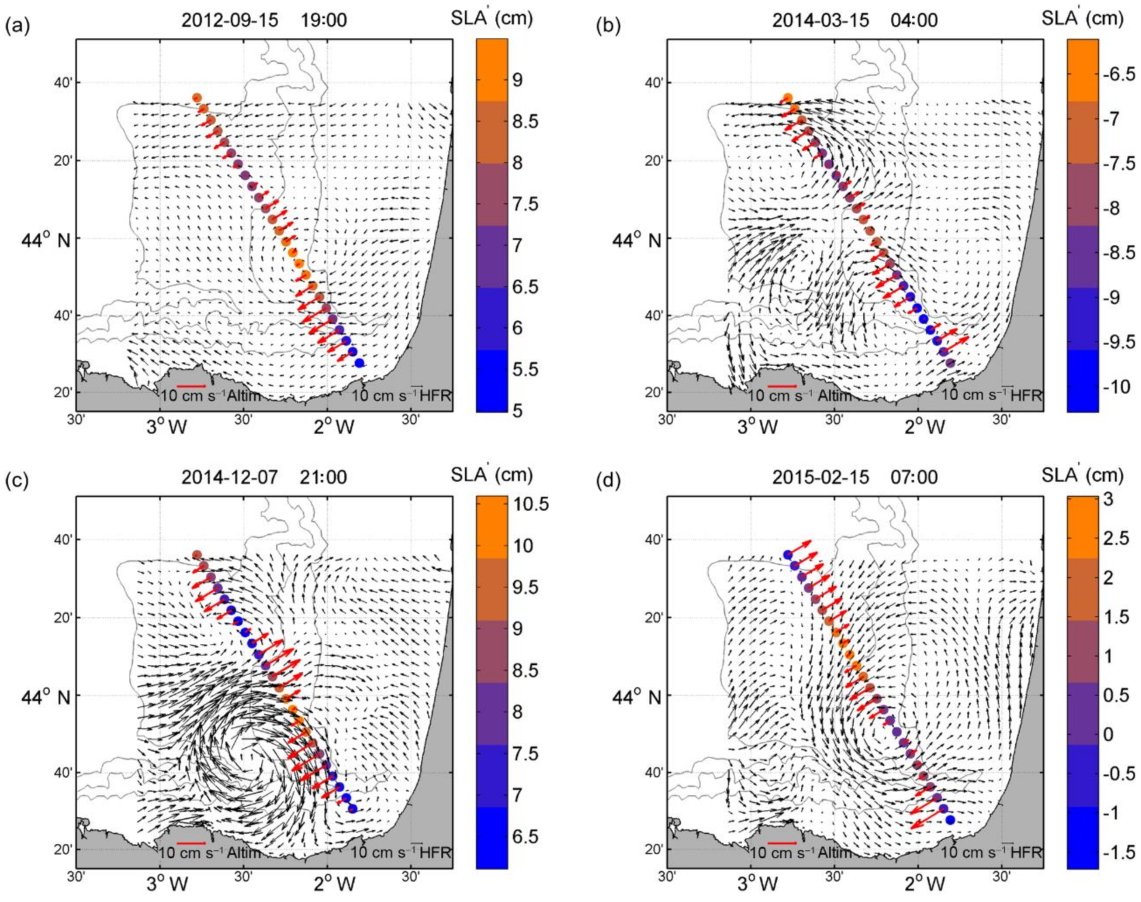

Figure 3.8. Four mesoscale eddies observed in the study area. The dots show the points of track 248 of the CMEMS database. SLA' (cm) values are indicated in the colour scale. Black arrows depict the HFR current fields. Red arrows correspond to across-track AC_G derived from the SLA' values in the dots. Grey lines: 200, 1000, and 2000 m isobaths. Note that the scale of each kind of arrow is not the same.

3.2.2 Observability of mesoscale eddies

Figure 3.8 shows four examples of eddies detected by the HFR and the altimeter. Although the effect of the presence of mesoscale eddies has not been explored in terms of statistical results, there is a qualitative agreement between AC_G and HFR total currents when eddies are observed in the area covered by the two measuring systems. This happens when either the eddies cross the track of the altimeter or when the size of the eddies, whose centre is located off the track, is large enough to be observable by altimetry. Across-track AC_G are generally in agreement with the HFR current fields, mainly in terms of current directions. For example, on 15 September 2012, the altimeter crosses a small anticyclone located to the north of the Capbreton canyon head. The maximum SLA' and minimum AC_G near the core of the eddy and the patterns of the SLA' and

AC_G north and southwards of the core agree with the structure detected by the HFR. An eddy with similar diameter and located near the same area is observed on 15 February 2015. In this case, the eddy is cyclonic, and though the HFR and altimetry currents in the area occupied by the structure agree with each other, this is not the case in the rest of the track. During winter, on 15 March 2014, a cyclone is detected by both datasets near the head of the Capbreton canyon, in addition to another cyclone in the north-western part of the domain. Finally, on 7 December 2014, an anticyclone, more energetic than all the former eddies, is observed over the Capbreton canyon. This anticyclone was analysed by Rubio et al. (2018), showing that it had an important role in the offshore transport of coastal waters. North of this eddy, the altimetry and the HFR detect a cyclonic circulation, but in this case, it is not clear from the HFR total current fields that the structure is an eddy.

4 Summary and Conclusions

In this study, we have investigated the synergies and differences between land-based HFR and satellite altimetry, two remote-sensing techniques that provide measurements of the ocean surface currents at different temporal and spatial scales. A general agreement between HFR and altimetry was observed in the study area, with correlations ranging up to 0.7. The comparisons were carried out in terms of time anomaly of currents, following different approaches with radial and total OMA HFR data. In all cases the addition of the LF Ekman component (AC_E) to the geostrophic component (AC_G) improved the results.

The best agreement between both datasets was observed in the slope area, mainly between 200 and 1000 m isobaths, where the surface circulation was dominated by a more energetic geostrophic component. In the coastal area, the agreement between both datasets was lower. AC_G have higher variability than AC_{HFR}, which could be explained by the error propagation in the finite-difference operator that estimates the geostrophic velocity from SLA' or by a more effective filtering of HF signals in the radar data (where HF signals can be efficiently removed using a running average temporal filter).

In terms of monthly mean currents, north-eastward currents were observed in all datasets in late autumn and in winter, while weaker north-eastward and south-westward currents were observed in spring and summer. In the winter period, higher variability was also observed at points *E* and *W*, possibly related to a more energetic slope current regime. Additionally, high variability was observed at point *W* in March-April, probably linked to an anticyclonic structure near Torrelavega canyon.

Four IPC events were isolated and described further by means of additional SST data. From this analysis, we conclude that during the IPC intensifications the qualitative agreement between

AC_G and HFR total currents is great and well related to the SST anomalies. In addition, a relationship between strong IPC events with negative (positive) NAO (EA) indexes in the previous months was detected for three of the four events. On the other hand, although the effect in terms of statistical results of the presence of mesoscale eddies was not explored, there is a qualitative agreement between AC_G and HFR total currents when eddies are observed in the area.

The low correlation between HFR and altimetry observed in some areas and periods can be due to several factors. It is worth noting that both technologies are based on different physical approaches to measure currents, at different spatial and temporal scales, and work under different physical assumptions. Besides, the quality of the radar data is expected to decrease in the furthest points from the antennae and varies as a function of the angle formed by the radial current components used for total current estimations (affecting the along-track comparison). Altimetry also has its own limitations and might have errors in the data editing procedure or in the corrections.

Future work should be oriented towards a better understanding of the relationship of the surface circulation and the dynamics of the subsurface layers by means of the combination of remote observations with data in the water column. Since the comparison near the shoreline is inconsistent, another future work line could be the investigation of the assumptions of geostrophic balance in the coastal area and the merging of altimetry and radar measurements to improve both products. In addition, further comparison with HFR data and higher-resolution coastal altimetry products would enable a better understanding of the differences between both observing systems.

CHAPTER 4

The seasonal intensification of the slope Iberian Poleward Current

Abstract

The combination of surface high-frequency radar (HFR) data and data from acoustic Doppler current profiler (ADCP) moorings is showcased as a promising approach for the monitoring of the slope currents in the southeastern Bay of Biscay and the Iberian Poleward Current seasonal intensification. Persistent and intense eastward currents are observed during winter periods and affect the measured water column down to 150 m depth. During summertime, stronger vertical shear is observed, both during eastward and westward current events. Strong fluctuations occur in parallel to intense north-northwestern and southern wind changes in both seasons. This variability is expected to have a significant impact on the residence time and the water exchanges between the coast and the open ocean in the area.

The contents of this chapter were published as:

Rubio, A., Manso-Narvarte, I., Caballero, A., Corgnati, L., Mantovani, C., Reyes, E., Griffa, A., Mader, J., 2019. The seasonal intensification of the slope Iberian Poleward Current. Copernicus Marine Service Ocean State Report. J. Oper. Oceanogr. 3, 13–18. https://doi.org/10.1080/1755876X.2019.1633075

1 Introduction

The Iberian Poleward Current (IPC) drives the ocean slope circulation in the southeastern Bay of Biscay from the surface down to 300 m depth. The intensification and variability of this current at seasonal and shorter scales can have a significant impact on the marine environment in this coastal area since it can modulate the residence time of nutrient-rich waters, pollutants, planktonic organisms as well as the water exchange between the coast and the open ocean. The monitoring and forecast of the surface and subsurface variability of currents in coastal areas is key for their accurate management where a myriad of socio-economic activities coexist (e.g., commercial and recreational fisheries and navigation, tourism, industry, ports and harbours, etc.). While coastal numerical models can provide three-dimensional (3D) fields of currents and enable the computation of Lagrangian quantities with application to biological, geochemical and environmental issues, the joint analysis of multi-platform observations, with complementary spatial coverage, is an interesting approach for a better understanding of the 3D coastal circulation and the validation of the models. In this contribution, we combine high-frequency radar (HFR) hourly surface current maps with acoustic Doppler current profiler (ADCP) data and wind measurements from three moorings to showcase their use to continuously monitor and analyse the IPC seasonal variability along the period 2009–2017 and its intensification under certain prevailing wind conditions.

The IPC is one of the main along-slope flows that promote transboundary interactions along the Atlantic margin of Europe. In the southeastern Bay of Biscay (see Figure 4.1), the IPC is a persistent feature and affects the 0–300 m depth layer in the area. Together with the presence of slope eddies that grow from current instabilities and the wind-induced circulation, this has a significant impact on the surface transport patterns, the residence times and the water exchange between the coast and the open ocean (Rubio et al., 2018).

The IPC flows over the slope, advecting warm surface waters eastwards (northwards) along the Spanish (French) coast (Le Cann and Serpette 2009; Herbert et al. 2011; Charria et al., 2013) during winter. The flow is reversed and three times weaker (Solabarrieta et al., 2014) during summer. In addition to this markedly seasonal density-driven circulation, variability at shorter scales is observed linked to wind-induced currents (e.g., Solabarrieta et al., 2015), mesoscale eddies (e.g., Rubio et al. 2018), tides and inertial motions (e.g., Rubio et al., 2013a). The generation of slope eddies occurs mainly in winter when the IPC interacts with the abrupt bathymetry (Pingree and Le Cann, 1992b; Teles-Machado et al., 2016). During autumn and winter, southwestern winds dominate and generate northward and eastward drift over the shelf. The rest of the year the winds are much weaker and less persistent, which makes wind-driven currents more variable (González et al., 2004; Lazure 1997; Solabarrieta et al., 2015). The observation and monitoring of the surface and subsurface current, together with its variability is thus crucial to obtain an accurate estimation of the coastal transport in this area and to evaluate its potential impacts on the coastal ecosystem.

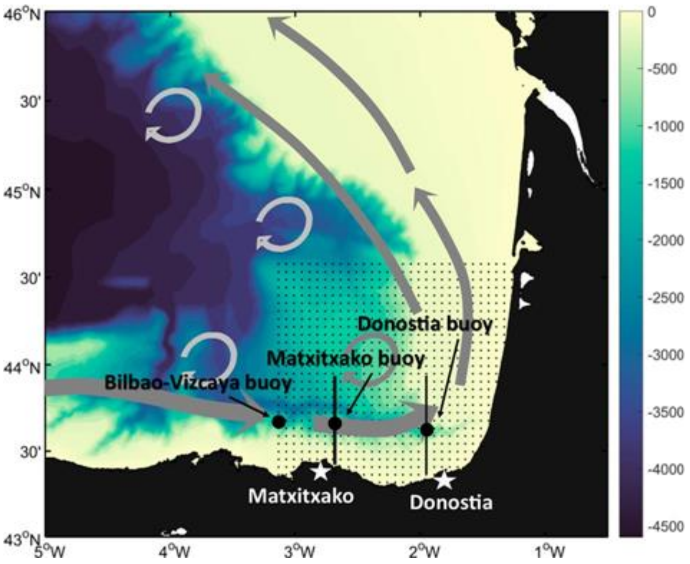

Figure 4.1. *Study area corresponding to the southeastern Bay of Biscay (northeastern Iberian Peninsula) and schematic view of the winter shelf-slope current and mesoscale regime (grey arrows, note that although only anticyclonic arrows are represented, eddies of anticyclonic and cyclonic polarity are observed in different locations along the slope). The nodes for the computation of HFR currents are shown by the grey dots. The stars provide the location of the HFR antennas in Matxitxako and Higer (Donostia) Capes. The black dots provide the location of the slope moorings used in this study and the black lines the surface cross-transects used to plot HFR along-slope currents in Figure 4.2. Bathymetry is given by the contours (in metre).*

Several previous works have focused on the study of different aspects of the IPC variability in the area by using remote sensing data (e.g., Herbert et al., 2011), moorings (Rubio et al., 2011), drifters (e.g., Charria et al. 2013), and HFR (e.g., Solabarrieta, 2014) independently. Moreover, Solabarrieta et al. (2014) jointly analysed HFR and one ADCP data observing a good agreement between the along-slope currents measured by both observing systems, especially during periods of intense IPC. Despite providing relevant results, the latter study was carried out for a short period (2009-2011) and only for one profile along the water column. Therefore, this study contributes to spatiotemporally enlarge the analysis made in Solabarrieta et al. (2014) for observing and monitoring the surface and subsurface currents and their variability, to accurately estimate the coastal transport in the southeastern Bay of Biscay. To that end, we combine data from HFR hourly surface current maps with ADCP water column velocity profiles from two slope moorings and wind velocity from a third mooring and monitor the IPC seasonal variability along the period 2009–2017 and its intensification under certain prevailing wind conditions.

2 Data and Methods

2.1 Data

In the next subsections, the HFR, mooring ADCP and wind data used are presented. Note that the HFR and ADCP data were 48-hour low-pass filtered by a 10th order digital Butterworth filter to obtain the sub-inertial currents. The same filter was applied to the wind data as well.

2.1.1 HFR data

HFR is a land-based remote sensing technology that can infer ocean surface currents over wide areas (distances from the coast over 150 km) with high spatial (300 m–5 km) and temporal (≤ 1 h) resolution. Nowadays, HFRs are the unique technology that can offer such a continuous observation of surface coastal current patterns over wide areas at high-spatial resolution and thus the possibility to monitor the associated transports. The combination of HFR data with water-column data is especially interesting since it can broaden the application of this technology to biological, geochemical and environmental issues since nutrients, plankton or pollutants can be located deeper in the water column and not only follow surface dynamics.

The HFR system located in the southeastern Bay of Biscay is part of the Basque Operational Oceanography System (EuskOOS; www.euskoos.eus/en/). It works at a central frequency of 4.46 MHz and a 30 kHz bandwidth and provides surface hourly current maps in an area up to 150 km from the coast (Figure 4.1). HFR surface currents are quality controlled using advanced procedures based on velocity and variance thresholds, noise to signal ratios and radial and total coverage (Rubio et al., 2011, 2018; Solabarrieta et al., 2014, 2015, 2016), and reprocessed (for obtaining gap-filled surface currents) using the Open-boundary Modal Analysis (OMA; Kaplan and Lekien, 2007). The historical HFR data used here cover the whole period 2009–2017.

2.1.2 Mooring data

Hourly wind data and current profiles in the water column are obtained from 3 moorings (see locations in Figure 4.1). More precisely, winds are obtained from the Bilbao Vizcaya mooring (which belongs to Puertos del Estado (the Spanish Government)) and we use current data from two buoys (of EuskOOS) moored over the upper part of the slope with a downward-looking ADCP (150 kHz, 8 m vertical bins, up to 200 m): Matxitxako mooring historical data spanning the period 2007–2013 and Donostia mooring the period 2007–2017. While the slope buoys' data time coverage is irregular, and no data are available for the Matxitxako buoy after August 2013, the HFR data coverage is quite good from the end of 2010.

2.2 Method

To explore the variability of the current we follow a two-step approach. First, the data series are analysed jointly to identify the main variability patterns in relation to the seasonal cycle and winds, exploiting the spatial complementarity of the measurements for characterising the variability in the horizontal and vertical extension of the current. Second, we compute spatial maps and vertical profiles of temporal cross-correlation (with a confidence level of 99 %) of the along-slope velocity measurements between (i) the HFR nodes at the mooring locations and the rest of the nodes within the HFR footprint, and (ii) the ADCP vertical levels. The latter approach aims to obtain an estimation of the area and levels where the point-wise current measurements from the HFR and the moorings can be considered as representative of the whole slope area. The areas and levels containing high cross-correlation values between measurements provide thus the 3D volume that can be well monitored by the combination of the two observing systems.

3 Results and Discussion

The along-slope current is marked by strong seasonal variability (Figure 4.2). Persistent and intense eastward currents are observed during winter periods and affect the measured water column down to 150 m depth agreeing with Solabarrieta et al. (2014). The cross-shore extension of the winter eastward current shows significant variability, being some of the winter events constricted to the shelf-slope area of the Matxitxako mooring (W2), while others show higher extension being observed up to 43.9°N (W3, W4 or W5). Remarkable differences between the two mooring locations are also observed (see also Rubio et al. 2011): the signature of the slope current is much stronger at Matxitxako, and generally weaker and less stable at Donostia mooring. Moreover, observed intensifications of the eastward winter current are also weaker at the Donostia location and more constrained to the slope (latitudes between 43.5 and 43.75° N). The strongest eastward currents are observed in periods of intense north-northwestern winds, particularly during wintertime. During some of the winter periods (e.g., W1 in Donostia or W4, see Figure 4.2), the strong fluctuations together with altering east/west intense currents occur in parallel to intense north-northwestern and southern wind changes. In December 2014, the wind-induced intensification of the slope current and its subsequent relaxation triggered the generation of an intense anticyclonic eddy described in Rubio et al. (2018) (see also Figure 4.2a: intense countercurrent after W4 event). The signature of the eddy at the Donostia latitudinal transect is less intense and less persistent but can be observed to be vertically coherent down to 150 m depth.

During summertime, stronger vertical shear is observed, both during eastward (S1, S2) and westward (S3 and S4) current events. In 2014, 2015 and 2016 intense summer westward currents (S3, S4) are observed in both locations. The westward event during July and August 2016 is especially remarkable because of its intensity and persistence, although it is limited to the surface (of a few tens of meters).

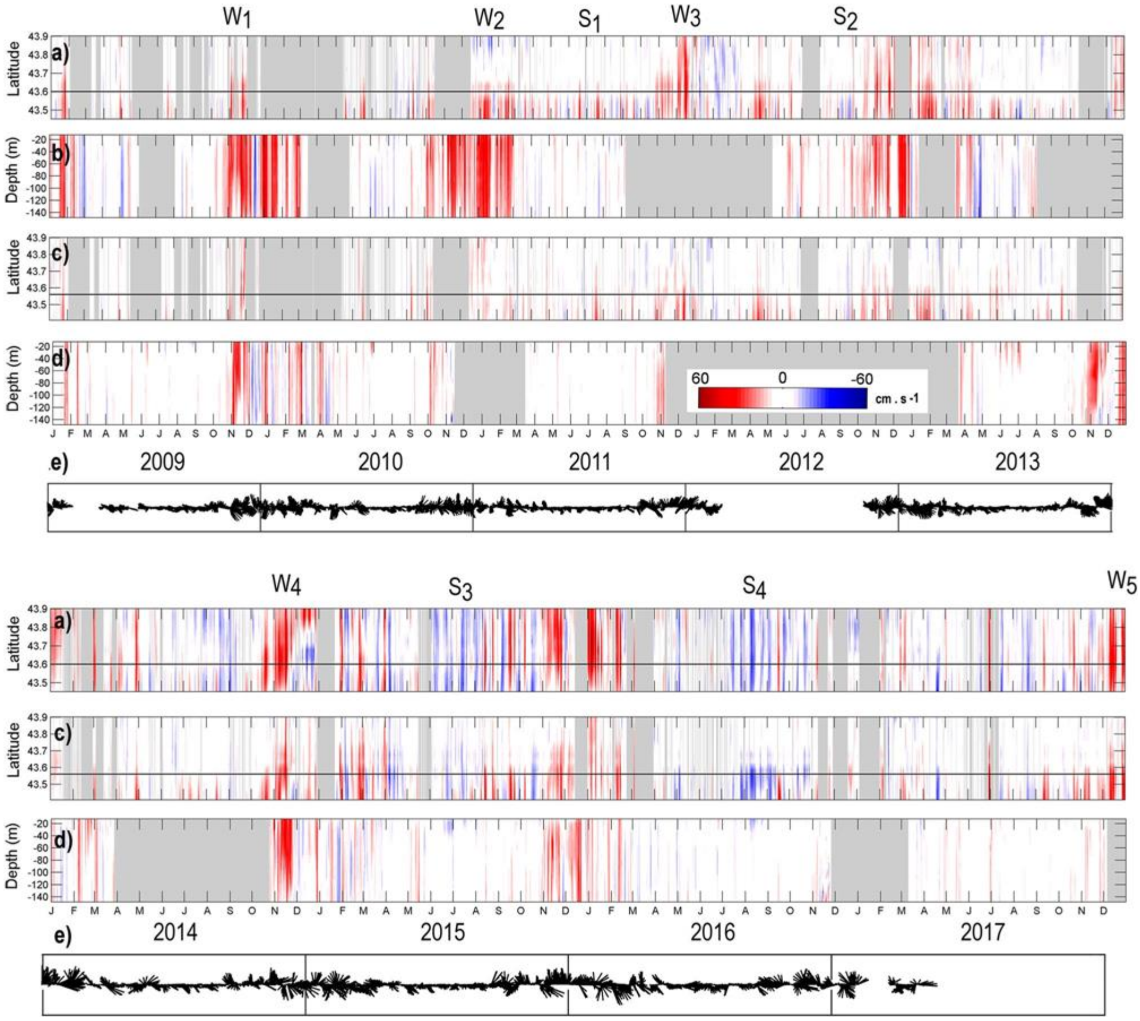

Figure 4.2. Hovmöller diagrams of along-slope surface currents derived from the HFR along the surface cross-transects shown in Figure 4.1, at the longitude of the (a) Matxitxako and (c) Donostia moorings. Hovmöller diagrams of along-slope current profiles up to 150 m depth from downward looking ADCP data in (b) Matxitxako (only for the period 2009–2013) and (d) Donostia moorings. The wind vectors from Bilbao Vizcaya mooring are shown in (e). A selection of winter (W) and summer (S*) current events discussed more in detail in the text are identified at the top of (a) panel.*

The cross-correlation maps for the sub-inertial along-slope component (Figure 4.3a–d) show high correlations between Matxitxako and Donostia locations and the nearby areas over the shelf and slope, from 1°30′ to 3°W, and from the coast to 43°50′. In winter, cross-correlation values over 0.6 are observed in the area between 43°50′N and the Spanish coast. This is due to the persistent and spatially homogeneous surface signature of the winter slope current flowing eastwards along the Spanish slope. In the case of Matxitxako mooring (which samples very well the core of the slope current) an area of high cross-correlation values (over 0.5) is also observed along the French slope (Figure 4.3a). We relate this to the surface signature of the slope current in this area where, due to the change of orientation of the bathymetry, it flows to the north-northwest (so the variability of the east-west component of the flow over the French slope is well correlated with east-west flow changes at Matxitxako mooring location). As mentioned before, the seasonal variability is weaker at Donostia location, being less evident the influence of the winter current regime (Figure 4.3c,d). Vertically, the cross-correlation is also seasonally modulated (Figure 4.3e,f), and shows significant spatial differences. The highest cross-correlations at 150 m are observed in winter in Matxitxako, which is again in coherence with a stronger slope current influence at this location. The strongest stratification in summer leads to a higher vertical shear and makes the correlation drop up to 0.5 at 60 and 50 m in Matxitxako and Donostia, respectively. From this level to 150 m the decay in the correlation is again much higher in Donostia, which indicates that other than the absence of a vertically coherent slope regime is favouring a stronger vertical shear in this area of complex bathymetry.

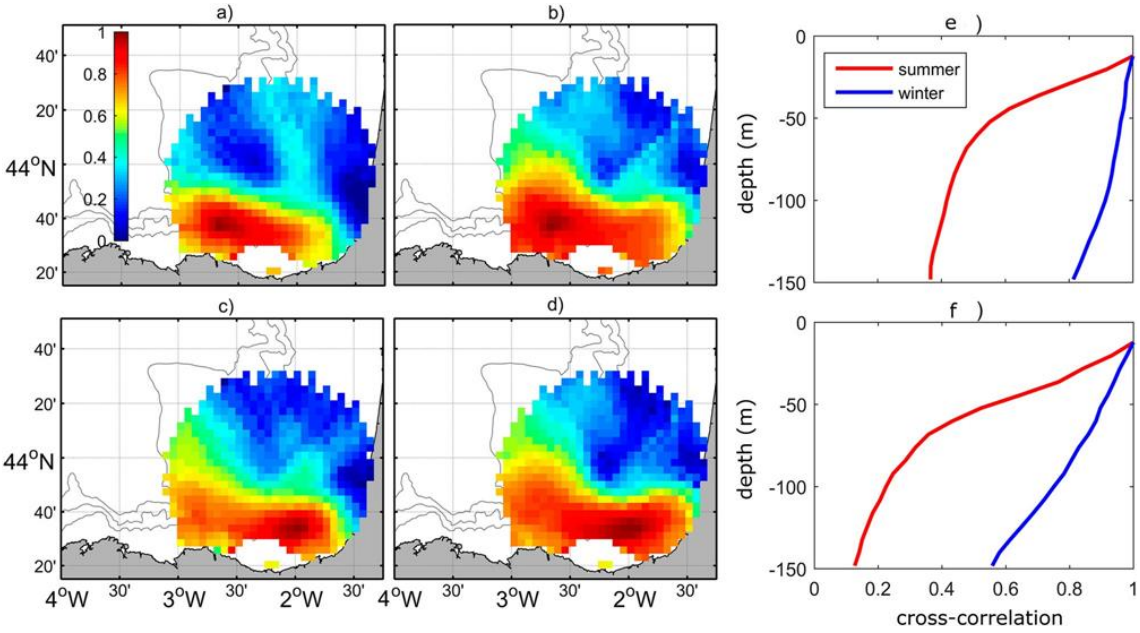

Figure 4.3. *Spatial maps of cross-correlations between the low-pass filtered time series of the HFR along-slope velocity component at (a,b) Matxitxako and (c,d) Donostia locations and the rest of the nodes within the HFR footprint area for total currents (the maps for winter/summer are shown in (a) and (c)/(b) and (d) subplots, respectively). ADCP data cross-correlations along the vertical range of ADCP data for (e) Matxitxako and (f) Donostia and the along-slope velocity component for summer (stratified) and winter (well-mixed) periods. The significance level is over 99 % for all the cross-correlations values plot in the figure.*

Recent work has shown the impact of the slope circulation and its variability on the residence time and the water exchange between the coast and the open ocean in the southeastern Bay of Biscay (Declerck et al., 2019; Rubio et al., 2018). The monitoring and forecast of the surface ocean variability are key for the accurate assessment of the distribution and transport of organic and inorganic matter, in this area where different human activities coexist (commercial and recreational fisheries and navigation, tourism, industry, etc.). From our results, the combination of surface HFR data and data from ADCP moorings arises as a promising approach for the monitoring and characterisation of the IPC seasonal variability and its intensification under certain prevailing wind directions. Moreover, our analysis of the spatial and temporal coherence in the seasonal and mesoscale variability observed by independent observing systems is a first step in the blending of both datasets, for an improved real-time monitoring of 3D coastal transports in the area. Besides, the use of these datasets for the improvement of the existing numerical models, through validation and data assimilation, would potentially enable enhanced forecast skills. Operational gap-filled HFR coastal surface currents could also be used to monitor the transport properties of the surface flow, based on the Lagrangian approach, aiming to identify the different scenarios that favour the local retention and dispersal of shelf waters.

CHAPTER 5

3D reconstruction of ocean velocity from high-frequency radar and acoustic Doppler current profiler: a model-based assessment study

Abstract

The effective monitoring and understanding of the dynamics of coastal currents are crucial for the development of environmentally sustainable coastal activities in order to preserve marine ecosystems as well as to support marine and navigation safety. This need is driving the set-up of a growing number of multiplatform operational observing systems, aiming for the continuous monitoring of the coastal ocean. A significant percentage of the existing observatories is equipped with land-based high-frequency radars (HFRs), which provide real-time currents with high spatiotemporal coverage and resolutions. Several approaches have been used in the past to expand the surface current velocity measurements provided by HFR to subsurface levels, since this can expand the application of the technology to other fields, like marine ecology or fisheries. The possibility of obtaining 3D velocity current fields from the combination of data from HFRs with complementary data, such as the velocity current profiles provided by in situ acoustic Doppler current profiler (ADCP) moorings is explored here. To that end, two different methods to reconstruct the 3D current velocity fields are assessed by a standard approach conceptually similar to OSSEs (observing system simulation experiments), where 3D numerical simulations are used as *true* ocean in order to evaluate the performance of the data-reconstruction methods. The observations of currents from a HFR and ADCP moorings are emulated by extracting the corresponding data from the 3D *true* ocean and used as input for the methods. Then, the 3D reconstructed fields (outputs of the methods) are compared to the *true* ocean to assess the skills of the data-reconstruction methods. These methods are based on different approaches: on the one hand, the reduced order optimal interpolation uses an approximation to the velocity covariances (which can be obtained from historical data or a realistic numerical simulation) and on the other hand, the discrete cosine transform penalized least square is based on penalized least squares regression that balances fidelity to the data and smoothness of the solution. This study, which is based on the configuration of a real observatory located in the southeastern Bay of Biscay (SE-BoB), is a first step towards the application of the data-reconstruction methods to real data since it explores their skills and limitations. In the SE-BoB, where the coastal observatory includes a long-range HFR and two ADCP moorings inside the HFR footprint area, the results show satisfactory 3D reconstructions with mean spatial (for each depth level) errors between 0.55 and 7 cm s^{-1} for the first 150 m depth and mean relative errors of 0.07–1.2 times the rms value for most of the cases. The data-reconstruction methods perform better in well-sampled areas, and both show promising skills for the 3D reconstruction of currents as well as for the computation of new operational products integrating complementary observations, broadening the applications of the in situ observational data in the study area.

The contents of this chapter were published as:

Manso-Narvarte, I., Fredj, E., Jordà, G., Berta, M., Griffa, A., Caballero, A., Rubio, A., 2020. 3D reconstruction of ocean velocity from high-frequency radar and acoustic Doppler current profiler: a model-based assessment study. Ocean Sci. 16, 575–591. https://doi.org/10.5194/os-16-575-2020

1 Introduction

Multiplatform observing systems are arising in several areas of the coast for providing data at different spatiotemporal scales. The combination of such data is a powerful approach for a better monitoring and understanding of the 3D coastal circulation, which is a key aspect to support sustainable coastal activities, as well as to preserve marine ecosystems.

Among the different observing systems, high-frequency radar (HFR) technology offers a unique insight into coastal ocean variability by providing information at the ocean-atmosphere interface. It allows for a better understanding of the coupled ocean-atmosphere system and the surface ocean coastal dynamics. In addition, since HFR data can provide real-time measurements of currents with a relatively wide spatial coverage (up to 200 km from the coast) and high spatial and temporal resolutions (typically a few kilometres and 1 h), they have become invaluable tools in the field of operational oceanography. Recent reviews on this technology and its applications worldwide have been provided by several authors (Fujii et al., 2013; Paduan and Washburn, 2013; Roarty et al., 2019; Rubio et al., 2017; Wyatt, 2014). However, HFRs provide current data only at the surface, within an integration depth ranging from tens of centimetres to 1−2 m, depending on the operating frequency (see Rubio et al., 2017). Moreover, data coverage is not always regular and may contain spatial and temporal data gaps due to several environmental, electromagnetic and geometric causes (Chapman et al., 1997).

The propagation of HFR information along the water column is especially valuable as it may broaden the application of this technology to biological, geochemical and environmental issues since plankton or pollutants can be located deeper in the water column and not only follow surface dynamics. In the last years, several methods to expand the information of the HFR data to subsurface layers in the upper water column have been developed, such as the use of multifrequency radars to obtain the velocity shear (Barrick, 1972; Broche et al., 1987; Paduan and Graber, 1997; Stewart and Joy, 1974; Teague et al., 2001), the use of the secondary peaks in the radar echo spectra to obtain the velocity shear (Shrira et al., 2001; Ivonin et al., 2004) or the “velocity projection” method to obtain the velocities of the subsurface currents (Shen and Evans, 2001, 2002; Marmorino et al., 2004; Gangopadhyay et al., 2005). Besides, simple models that study the surface and vertical profiles have been developed (e.g., Davies, 1985a, 1985b, 1985c; Prandle, 1991, 1987, 1982). In addition, other approaches combine the HFR data with data in the water column provided by in situ moored instruments, remote sensing platforms or circulation numerical simulations to investigate the 3D circulation (e.g., Cianelli et al., 2015; De Valk, 1999; Jordà et al., 2016; O’Donncha et al., 2015; Ren et al., 2015).

In line with these approaches, and with the effort towards improving the integrated observation of the coastal area undertaken in the framework of JERICO-RI (http://www. jerico-ri.eu/, last access: 6 May 2020; through the JERICO-NEXT and JERICO-S3 projects), in this work, we explore the skills of two data-reconstruction methods that allow us to expand the surface information from HFRs to subsurface layers. The two methods used here have already shown good performance for the reconstruction of HFR current data and rely on different basic principles. On the one hand, the discrete cosine transform penalized least square (DCT-PLS), implemented by Fredj et al. (2016), is based on the fitting of a function. On the other hand, the reduced order optimal interpolation (ROOI), implemented by Jordà et al. (2016), uses an approximation to the velocity covariances to extrapolate observed information to the whole domain.

The study area is located in the southeastern Bay of Biscay (SE-BoB), which is characterized by the presence of canyons (e.g., Capbreton Canyon), by an abrupt change in the orientation of the coast and by a narrow shelf (see Figure 5.1). The winter surface circulation in the SE-BoB is mainly related to a slope current flowing, in the upper 300 m of the water column, eastwards along the Spanish coast and northwards along the French coast (the so-called Iberian Poleward Current, IPC) (Frouin et al., 1990; Haynes and Barton, 1990; Le Cann and Serpette, 2009; Peliz et al., 2003; Pingree and Le Cann, 1990, 1992a, 1992b) with maximum surface current speeds of 70 cm s^{-1} (Solabarrieta et al., 2014). In summer, the surface flow is reversed, being 3 times weaker than in winter (Solabarrieta et al., 2014). In the water column, the subsurface properties measured by two slope moorings show a marked seasonal variability (Rubio et al., 2013a). Whilst in winter the water column is well mixed and shows stronger currents (strongest currents ranging from 20 to 50 cm s^{-1}), in summer it is stratified with mean thermocline depths ranging from −30 to −50 m, with surface temperatures over 20 ºC and with weaker currents (strongest currents ranging from 10 to 20 cm s^{-1}). The multiplatform coastal currents observatory in this study area belongs to the Basque Operational Observing System (EuskOOS; http://www.euskoos.eus) and is composed by one long-range HFR (working at a central frequency of 4.46 MHz with an integration depth of ~1.5 m depth and with a footprint area that covers ~150 km off the coast) and two ADCPs located in two slope moorings (Matxitxako and Donostia moorings) along the Spanish coast.

The assessment of the performances of the data-reconstruction methods is carried out in terms of current velocities, using a model-based scenario based on the coastal observatory existing in the study area, where HFR and ADCP data showed good agreement for 3D monitoring the slope current (Rubio et al., 2019). Thus, the skills of two data-reconstruction methods are assessed and compared, aiming to give a first step towards their applicability for this specific case.

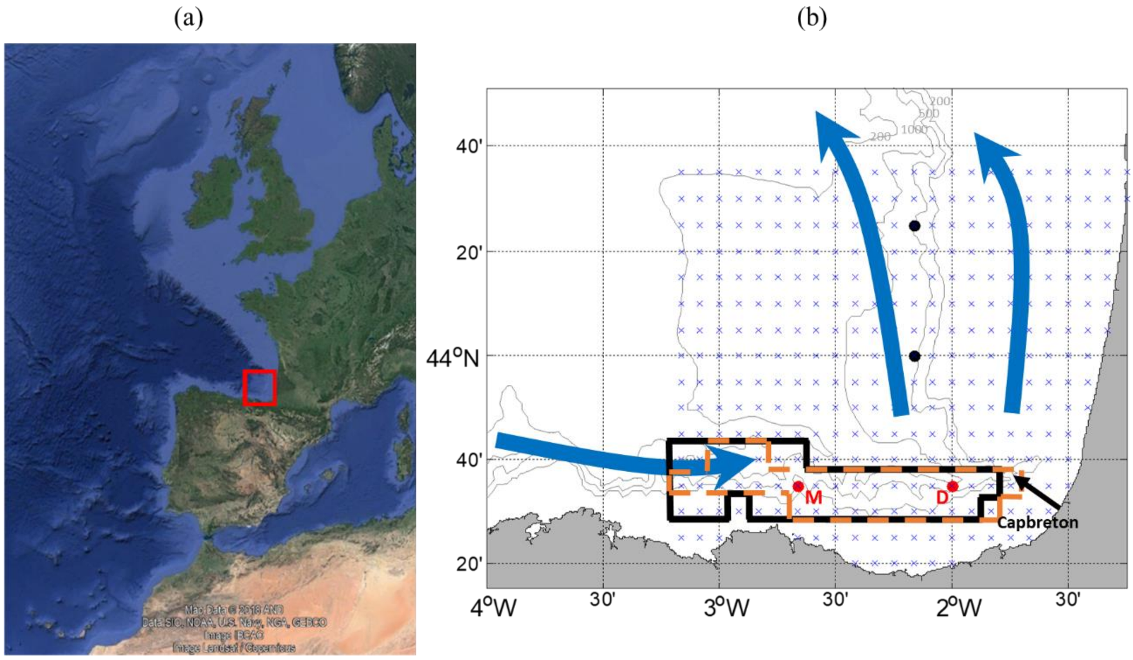

Figure 5.1. *(a) Location of the study area (red square). Map data © 2018 AND Data SIO, NOAA, U.S. Navy, NGA, GEBCO. Image IBCAO. Image: Landsat/Copernicus. (b) Close-up map of the study area. The winter IPC is represented by solid blue arrows. The grid used for the emulated HFR surface current fields is shown by blue crosses. The red dots provide the locations of the current vertical profiles that emulate the EuskOOS moorings: Matxitxako (red M) and Donostia (red D), whereas the black dots depict the location of the two extra moorings used for the 4-mooring scenario. The bold black lines delimit the winter reduced grid, whereas the dashed orange lines delimit the summer one. The grey lines show the 200, 500, 1000 and 2000m isobaths.*

2 Data and Methods

2.1 Assessment approach

The approach used for the analysis of the skills of the data-reconstruction methods is based on the use of a realistic numerical simulation as a *true* ocean, that provides both the emulated observations and the 3D reference field (hereinafter “reference field”) that will be used to assess the results of the 3D reconstruction. This is a well-established methodology inspired by the techniques used in observing system simulation experiments (OSSEs), and it is the only approach that allows us to quantify the skills of the data-reconstruction methods in the entire 3D domain considered for the reconstruction. The assessment approach consisted of three main steps (Figure 5.2). First, the observations that emulate the data obtained from the EuskOOS platforms were extracted from a numerical simulation (for simplicity these “emulated observations” are called “observations” from here on). The extracted simulation data emulate the two vertical current profiles of the ADCPs located in the Matxitxako and Donostia moorings and the surface current fields of the HFR (see locations and coverage in Figure 5.1b). Second, the two data-reconstruction methods were applied to the observations to compute the 3D reconstructed fields. Note that the ROOI method also uses historical data from a simulation to estimate the spatial covariances of the currents in the study area needed for the reconstruction. Finally, the 3D reconstructed fields (outputs of the methods) were compared to the reference field to assess the performances of the data-reconstruction methods.

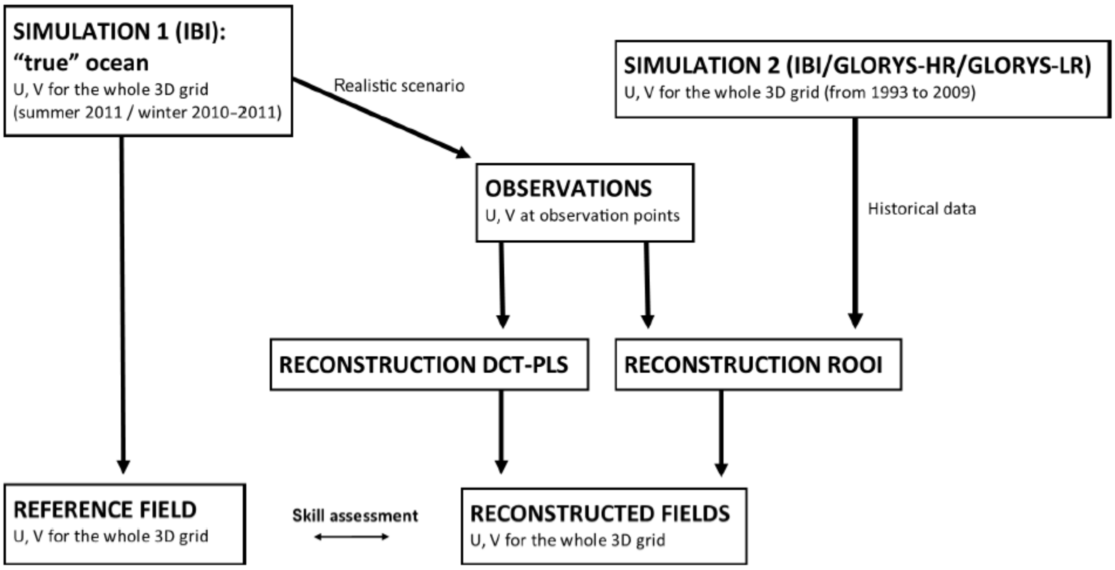

Figure 5.2. *Scheme of the approach used to test the performance of the two data-reconstruction methods described in Section 2.2. The models used for SIMULATION 1 and SIMULATION 2 are presented in Section 2.3.*

Since the current regime is seasonally modulated, the performances of the two data-reconstruction methods were tested for winter and summer periods: November- December-January-February (2010–2011) and June-July-August-September (2011), respectively. The data-reconstruction methods were also analysed in a reduced grid case to evaluate the performance of the reconstructions in areas where the surface currents are highly correlated with the currents at the mooring locations (hereinafter called "well-sampled areas"). Since the moorings are located along the Spanish slope, where the zonal current velocity component (U) prevails over the meridional component (V), the reduced grid was determined only by the correlations obtained for this component (cross-correlation ≥ 0.8). This reduced grid mainly covers the Spanish slope area and slightly differs for the winter and summer periods (black and orange lines, respectively, in Figure 5.1b).

A second scenario with two additional current vertical profiles along the French slope (see Figure 5.1b) was also considered in order to assess the sensitivity of the data-reconstruction methods to different observational configurations (hereinafter called the "4-mooring scenario").

2.2 Data-reconstruction methods

2.2.1 The ROOI method

The ROOI method was first proposed by Kaplan et al. (1997) to reconstruct sea surface temperatures (SSTs) from sparse data, and it has been applied since then for different variables such as sea level pressure (Kaplan et al., 2000), sea level anomalies (Church and White, 2006) or 3D velocity fields (Jordà et al., 2016). It is based on empirical orthogonal function (EOF) decomposition and the details can be found in Kaplan et al. (1997, 2000) or Jordà et al. (2016), so here only the basic elements are presented.

Expressing the 3D velocity field as a matrix $Z(r,t)$, where r is the m-vector of spatial locations and t the n-vector of times, a spatial covariance matrix is first computed as $C = n^{-1}ZZ^T$. Then, an EOF decomposition can be applied:

$$C = U\Lambda U^T \tag{5.1}$$

where U is an m x m matrix whose columns are the spatial modes (EOFs), and Λ is the m x m diagonal matrix of eigenvalues. The velocity field can then be exactly reproduced as

$$Z(r,t) = U(r) \cdot \alpha(t) \tag{5.2}$$

in which the amplitude can be computed as $\alpha = U^T Z$.

In practice, the velocities at every grid point of the 3D analysis grid are not known, but only at a limited set of N locations (being $N << m$). The problem we intend to solve is precisely that of retrieving the whole matrix Z from the available observations (e.g., surface velocities from HFR and velocity profiles at the ADCP locations). The first problem is that the eigenvector U and eigenvalue Λ matrices cannot be computed from actual observations (i.e., there are not enough samples), so a common choice is to use historical data from a realistic numerical simulation to represent the actual velocity statistics. A second aspect to be considered is that fitting high-order modes may introduce unwanted noise into the reconstruction. Thus, the Eq. (5.2) is truncated to include only the M leading EOFs, so that the contribution of the higher-order modes (accounting for local small-scale features) is neglected:

$$Z_M(r,t) = U_M(r) \cdot \alpha_M(t) \tag{5.3}$$

The next problem is that obviously the amplitudes cannot be obtained as in Eq. (5.2), since now we do not know Z. Instead, the M amplitudes can be determined under the constraint that the reconstructed Z_M fits the observations available at each time step. More generally, the amplitudes are obtained by minimizing a cost function that takes into account the observational noise and the role of neglected modes (see Kaplan et al., 1997, 2000, for the complete derivation).

In summary, using the ROOI, the values of the velocity at every grid point of a predefined 3D grid can be obtained by merging the spatial modes of variability computed from a realistic numerical simulation (used as historical data) and the temporal amplitudes obtained using the available observations. Several sensitivity tests have been performed to tune the method and finally, 20 modes have been considered ($M = 20$). Regarding the spatial modes of variability, they have been obtained from different numerical simulations (see *Section 2.3*) to test the sensitivity of the results to the accuracy in the definition of the spatial covariances.

2.2.2 The DCT-PLS method

The DCT-PLS method is a straightforward technique proposed by García (2010), based on a penalized least square regression. Fredj et al. (2016) showcased the method's skills for the 2D reconstruction of HFR surface current fields along the mid-Atlantic coast of the United States with high accuracy. In this section the basic principle of the method is explained; however, for more details, the reader is referred to García (2010) or Fredj et al. (2016).

The main aim of the method is to find the best fitting model, which is based on discrete cosine transforms (DCTs) and one smoothing (fitting) parameter s. Thus, the fitting model that corresponds to each s is tested by cross-validation in order to obtain the best one. The general approach of the method is as follows: for each s (i.e., for each fitting model), the observations are split into two subsets: the training set, which is used to fit the model, and the test set, which is used to test it. This test is carried out by the trade-off (F) between the bias of the fitting (residual sum of squares, RSS) and the variance of the results of the created model (penalty term P):

$$\mathrm{F} = \mathrm{RSS} + \mathrm{P} = ||y - \hat{y}||^2 + s||D\hat{y}||^2 \tag{5.4}$$

where y is the data of the test set, $\hat{y}$ is the data of the created model and D is a second-order difference derivative. Then, for the same s, this procedure is repeated for different training and test sets obtaining different F values at each time. The mean value of F (that is, E [F]) will provide a general cross-validation (GCV) score that corresponds to each fitting model (i.e., to each s):

$$E\,[\mathrm{F}] \rightarrow \mathrm{GCV} \tag{5.5}$$

and the best fitting model will be the one that minimizes the GCV score:

$$min(\mathrm{GCV}) \rightarrow s. \tag{5.6}$$

In conclusion, here we introduce a penalized least square method, based on discrete cosine transforms, with one smoothing parameter approach consisting of minimizing a criterion that balances the fidelity with the current data, measured by the RSS, and a P that reflects the noisiness of the smooth current data.

2.3 Numerical simulations

The Atlantic-Iberian Biscay Irish simulation, and particularly the IBI_REANALYSIS_PHYS_005_002 product (hereinafter IBI), provided by the Copernicus Marine Environment Monitoring Service (CMEMS), was used to obtain the *true* ocean from which the observations and the reference field were extracted, as explained in *Section 2.1*. The IBI reanalysis is based on a realistic configuration of the NEMO model for the Iberian Biscay Irish region (Figure 5.1a), which assimilates in situ and satellite data. For more details, see Table 5.1; a complete description of the product and its validation can be found in Sotillo et al. (2015) and the links shown in Table 5.1. In *Section 3*, the realism of IBI simulations is assessed based on previous knowledge of the circulation in the area and used to provide an overview of the dynamical characteristics of the study area to support the discussion of the results.

The spatial covariances required for the ROOI have been obtained from IBI and two additional numerical simulations (see Figure 5.2) with daily outputs from 1993 to 2009, with the objective of exploring the impact on the reconstruction of an imperfect definition of the covariances. The two additional numerical simulations used for this purpose were the GLORYS high-resolution (GLOBAL_REANALYSIS_PHY_001_030 product, hereinafter called ”GLORYS-HR”) and the low-resolution (GLOBAL_REANALYSIS_ PHY_ 001_025 product, hereinafter called “GLORYS-LR”) reanalyses. The general details of these products are listed in Table 5.1, along with links to additional information about the products and their validation. Thus, the ROOI method was tested both in an optimal configuration, where the covariance matrix was obtained from the same numerical simulation used as the reference field (i.e., IBI), and in two suboptimal configurations: one in which the covariances were obtained from a high-resolution numerical simulation (i.e., GLORYS-HR), which is supposed to capture the same range of processes as IBI although not exactly, and another one from a low-resolution numerical simulation (i.e., GLORYS-LR), which differs from IBI in the numerical code and also in the resolvable spatial scales.

The same 3D grid was considered for the reference field, the covariance matrices, and to extract the observations at the surface layer or in the vertical profiles at the grid points closest to the mooring locations (Figure 5.1b). The horizontal grid spacing was given by the native horizontal grid of IBI and GLORYS-HR (0.083º) (Figure 5.1b). Thus, for the computation of the covariance matrices with GLORYS-LR, the data were linearly interpolated to the IBI grid points. The vertical configuration was adapted to the levels of the real ADCPs with data every 8 m (from 12 to 148 m). Since the surface layer was set at 0.5 m, all the used numerical simulation fields were linearly interpolated to this vertical configuration (i.e., −0.5, −12, −20, −28, . . . −148 m).

Table 5.1. *Details of the numerical simulations used in this study. Note that T and S represent temperature and salinity, respectively.*

	IBI	**GLORYS-LR**	**GLORYS-HR**
Product identifier	IBI_REANALYSIS_PHYS_005_002	GLOBAL_REANALYSIS_PHY_001_025	GLOBAL_REANALYSIS_PHY_001_030
Regional/ global	Regional	Global	Global
Spatial resolution	$0.083^\circ \times 0.083^\circ$	$0.25^\circ \times 0.25^\circ$	$0.083^\circ \times 0.083^\circ$
Temporal resolution	Daily	Daily	Daily
Model	NEMO v3.6	NEMO v3.1	NEMO v3.1
Data assimilation	In situ TS profiles, Sea level, SST	Sea ice concentration and/or thickness; in situ TS profiles, Sea level, SST	Sea ice concentration and/or thickness; in situ TS profiles, Sea level, SST
Atmospheric forcing	ECMWF ERA-Interim	ECMWF ERA-Interim	ECMWF ERA-Interim
Bathymetry	GEBCO_08 + different local	ETOPO1 for deep ocean and GEBCO8on coast and continental shelf	ETOPO1 for deep ocean and GEBCO8 on coast and continental shelf
Initial conditions	January 1992: T, S, velocity components and sea surfaceheight from GLORYS2V4	December 1991: T, S regressed from EN4	December 1991: T, S regressed from EN.4.2.0
Open boundary data	Data from daily outputs from the CMEMS GLOBAL reanalysis eddy-resolving system.	–	–
Application in this study	Observations, reference fields and the covariance matrix for the ROOI	The covariance matrix for the ROOI	The covariance matrix for the ROOI
For a more detailed description:	http://cmems-resources.cls.fr/documents/PUM/CMEMS-IBI-PUM-005-002.pdf	http://cmems-resources.cls.fr/documents/PUM/CMEMS-GLO-PUM-001-025.pdf	http://cmems-resources.cls.fr/documents/PUM/CMEMS-GLO-PUM-001-030.pdf
	http://resources.marine.copernicus.eu/documents/QUID/CMEMS-IBI-QUID-005-002.pdf	http://resources.marine.copernicus.eu/documents/QUID/CMEMS-GLO-QUID-001-025.pdf	http://resources.marine.copernicus.eu/documents/QUID/CMEMS-GLO-QUID-001-030.pdf

2.4 Skill assessment

The skills of the data-reconstruction methods were assessed by means of the root-mean-square difference (RMSD) between the reconstructed fields (x) and the reference fields (y). The RMSDs were computed at each point of the 3D grid for each study period and for U and V. Thus, for one grid point and N time steps,

$$\mathrm{RMSD} = \sqrt{\frac{\sum_{t=1}^{N}(x_t - y_t)^2}{N}} \tag{5.7}$$

where x_t and y_t are the reconstructed and reference fields at each time step, respectively.

The relative RMSD, relative to the root-mean-square (rms) current (hereinafter RRMSD), was also considered, since the strength and variability of the current are different at different locations of the study area and therefore influence the magntude of the RMSDs. Therefore, the considered relative value is

$$\mathrm{RRMSD} = \frac{\mathrm{RMSD}}{\mathrm{rms}} \tag{5.8}$$

where

$$\mathrm{rms} = \sqrt{\frac{\sum_{t=1}^{N}(y_t)^2}{N}}. \tag{5.9}$$

Since RMSD and RRMSDs were computed for each study period and for each velocity component, hereinafter we use RMSD-U and RRMSD-U as RMSD and RRMSD computed for U and RMSD-V and RRMSD-V as RMSD and RRMSD computed for V. When the RRMSD is equal to 1 at one point for a study period, it means that the RMSD equals the rms of the studied period at that point.

Table 5.2. *Seasonal spatial correlation length scales for the emulated current velocity components U and V in the study area, for the summer and winter periods and in zonal and meridional directions. Note that the surface horizontal scales are shown in kilometres and that the vertical scales in depth at Matxitxako and Donostia mooring points are shown in metres.*

Current component	Surface (km)				Depth (m)			
	Summer		Winter		Summer		Winter	
	Zonal direction	Meridional direction	Zonal direction	Meridional direction	Matxitxako mooring	Donostia mooring	Matxitxako mooring	Donostia mooring
U	78	15	79	16	24	23	88	43
V	11	60	12	73	19	15	30	36

3 Describing the spatiotemporal variability in the study area

In this section, the characteristics of the simulated IBI currents are validated against those found in previous studies based on real HFR and ADCP data (e.g., Rubio et al., 2019, 2013a; Solabarrieta et al., 2014). We focus on the comparison of the statistical properties (i.e., spatiotemporal correlations), which are also the basis for the reconstruction methods, and, in particular, on the spatial correlation length scales and temporal cross-correlations (see *Appendix A5* for a detailed description of the computation of the correlations). The main aim is to provide an overview of the currents used to test the data-reconstruction methods as ground information in order to justify the scenarios and to support the discussion on the performances of the data-reconstruction methods. Indeed, the best performances are expected in the areas and periods of higher cross-correlation between currents at different locations and vertical levels.

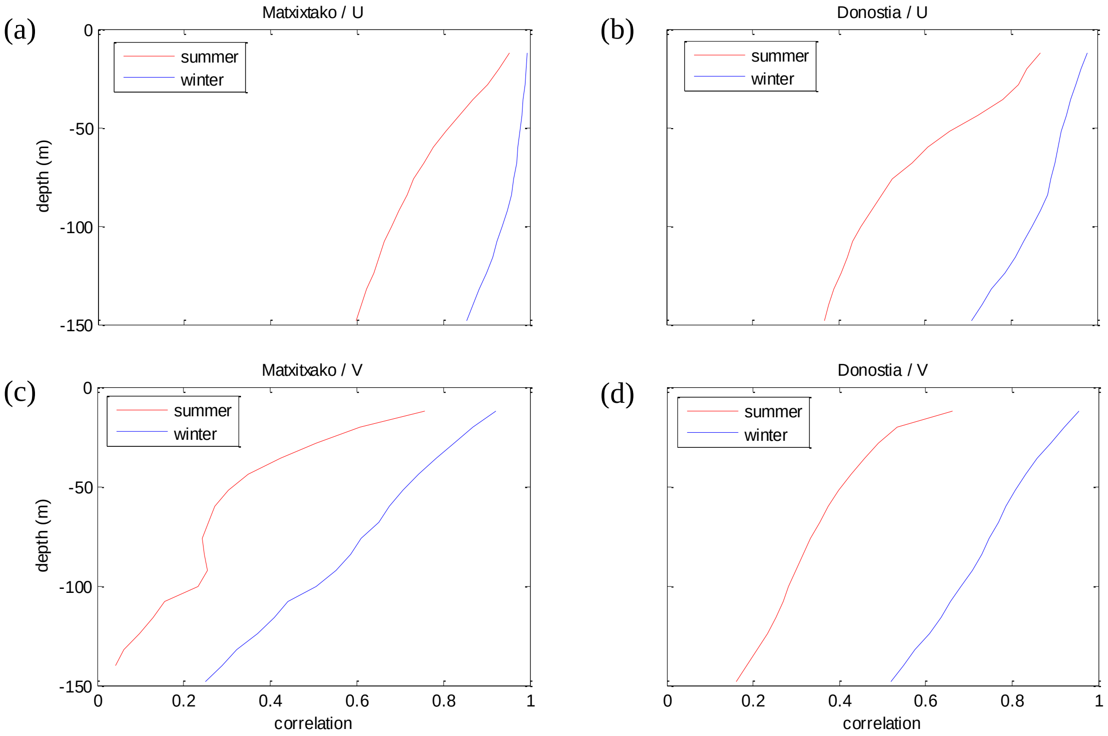

Figure 5.3. *U (a, b) and V (c, d) temporal cross-correlations between the surface and the water column levels for winter (blue) and summer (red) periods. In the Matxitxako location (a, c) and in the Donostia location (b, d).*

As shown in Table 5.2, the spatial correlation length scales along the water column are higher for U than for V, since the profiles of both moorings are located in the Spanish slope, where the slope current prevails. Moreover, the highest correlation values are observed at Matxitxako, which is under a stronger influence of the slope current (Rubio et al., 2013a; Solabarrieta et al., 2014). The scales are larger in winter than in summer when the water column is well mixed (Rubio et al., 2019, 2013a). Regarding surface currents, the horizontal spatial correlation length scales are higher when considering the same direction for the computation of the correlation and the velocity component (i.e., for U in the zonal direction and V in the meridional direction) due to the zonal and meridional slope currents along the Spanish and French coasts, respectively. The highest horizontal spatial correlation length scales are obtained for U and the scales are slightly larger in winter than in summer. These results are coherent with the presence of the along-slope current in the area, which is stronger and more persistent in winter and along the Spanish coastal area (Solabarrieta et al., 2014).

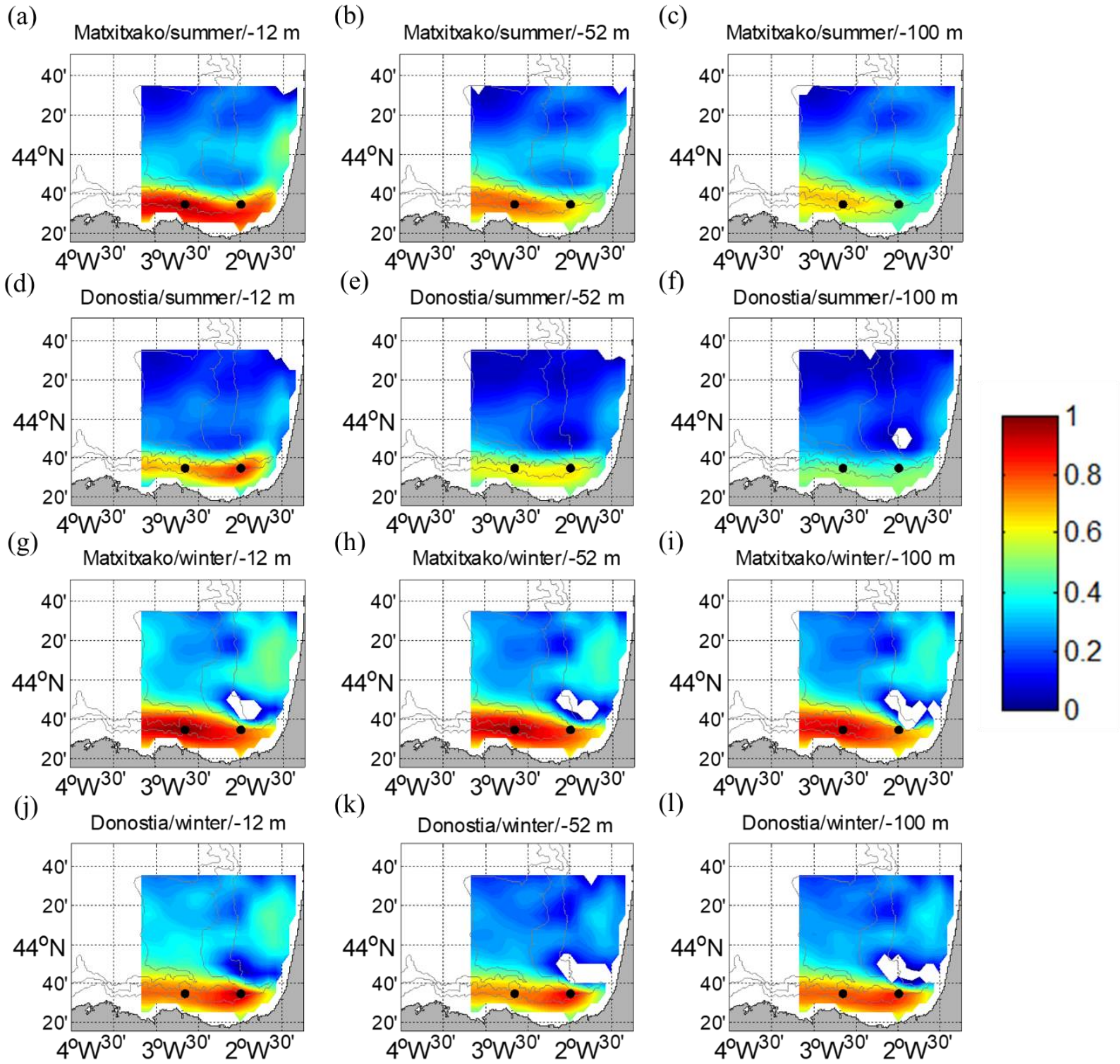

Figure 5.4. *Temporal cross-correlation maps between the water column levels considered and the surface points of the HFR grid for U. (a, b, c, g, h, i) for the Matxitxako mooring and (d, e, f, j, k, l) for the Donostia mooring. Different depths are considered: −12m (a, d, g, j), −52m (b, e, h, k) and −100m (c, f, i, l), for summer (a-f) and winter (g-l). The white gaps are the areas where the confidence level is less than 95 %. The black dots depict the locations of the current vertical profiles.*

Concerning the temporal cross-correlation, the same patterns shown by the spatial correlation length scales are observed. The temporal cross-correlation profiles between the surface and subsurface levels (Figure 5.3) and the temporal cross-correlation maps (Figures 5.4-5.5) show that the highest correlations are observed for the along-slope component of the current in winter (with maximum correlation along the vertical levels at Matxitxako), and that the decrease in the correlation with depth is sharper in summer.

It is worth highlighting that these model-based spatial correlation length scales and temporal cross-correlations are coherent with those obtained from real observations (Rubio et al., 2019; see also *Appendix A1*), validating the use of IBI to emulate the study case of the SE-BoB observatory.

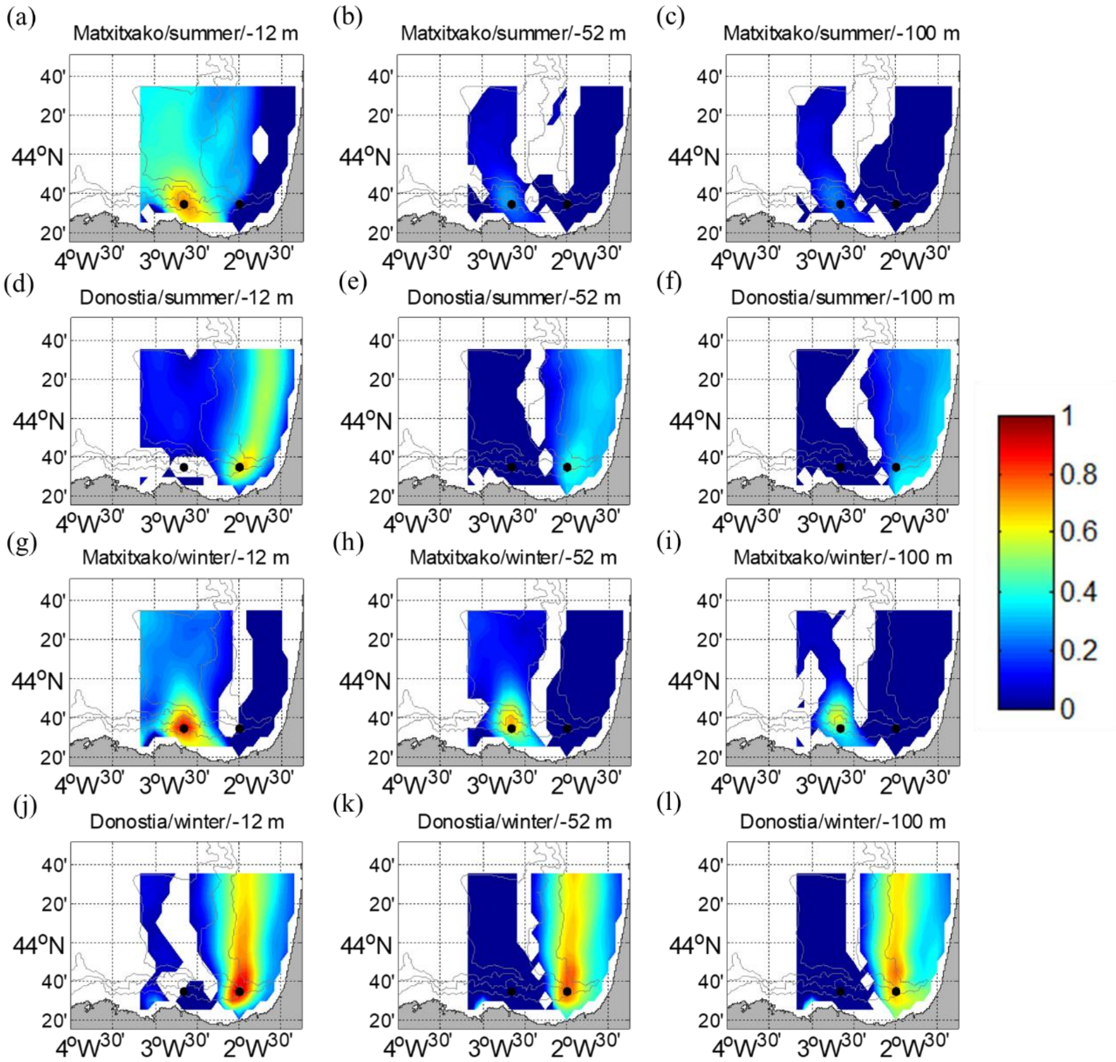

Figure 5.5. *Temporal cross-correlation maps between the water column levels considered and the surface points of the HFR grid for V. (a, b, c, g, h, i) for the Matxitxako mooring and (d, e, f, j, k, l) for the Donostia mooring. Different depths are considered: −12m (a, d, g, j), −52m (b, e, h, k) and −100m (c, f, i, l), for summer (a-f) and winter (g-l). The white gaps are the areas where the confidence level is less than 95 %. The black dots depict the locations of the current vertical profiles.*

4 Results and Discussion

4.1 Data reconstruction

The results, in terms of RMSDs and RRMSDs, are summarized in Table 5.3. It is observed that the RMSDs and the RRMSDs are affected by the spatial and temporal variability of the slope current regime. The mean RMSDs are, in general, higher in winter than in summer due to more intense currents in that period. However, the rms values are also higher and in relative terms, the reconstructions show, overall, better results in winter (lower mean RRMSDs). This dependence of the results on the current regime can be also observed if we compare the reduced and the entire grid cases. For the reduced grid case, which covers an area of intense zonal slope currents, the highest mean RMSDs and lowest mean RRMSDs are generally obtained for U. Since V is much weaker for this grid, it provides the lowest mean RMSDs. Nevertheless, the expected increase in the mean RRMSDs is not so clear compared to the entire grid case due to lower rms values.

Table 5.3. *Summary of the results of the reconstructions with ROOI (with GLORYS-LR) and DCT-PLS in terms of spatial mean RMSDs and RRMSDs for the entire and reduced grids, the summer and winter study periods, and different depths.*

Parameter	Considered grid		ROOI		DCT-PLS	
			Summer	Winter	Summer	Winter
<RMSD> (cm s^{-1})	Whole	U/V −12 m	3.79/5.08	4.46/6.28	3.59/3.62	3.10/2.65
		U/V −52 m	2.84/3.66	4.05/5.45	4.01/4.48	5.69/4.99
		U/V −100 m	2.69/3.14	3.89/5.31	4.10/3.22	8.45/5.32
	Reduced	U/V −12 m	6.35/3.87	8.29/3.91	4.15/2.77	3.92/1.93
		U/V −52 m	4.98/2.02	9.19/2.85	3.10/2.01	4.66/2.67
		U/V −100 m	4.31/1.77	8.38/2.46	2.33/1.75	3.66/2.59
<RRMSD>	Whole	U/V −12 m	0.83/0.83	0.84/0.88	0.88/0.64	0.67/0.38
		U/V −52 m	0.98/1.02	0.94/0.80	1.69/1.33	1.83/0.74
		U/V −100 m	1.05/1.04	0.92/0.80	1.82/1.07	2.79/0.83
	Reduced	U/V −12 m	0.56/0.94	0.53/1.04	0.37/0.74	0.25/0.53
		U/V −52 m	0.79/0.94	0.64/0.88	0.54/1.03	0.33/0.90
		U/V −100 m	0.95/1.04	0.72/0.80	0.54/1.00	0.32/0.95

Regarding the comparison between data-reconstruction methods, at −12 m the DCT-PLS provides lower mean RRMSDs for both grids. At deeper levels, RRMSDs are lower for the ROOI in the entire grid case, whereas for the reduced grid case (of intense zonal slope currents), the mean RRMSD-U(V) values are lower for the DCT-PLS(ROOI). This shows that the DCT-PLS performs better in well-sampled areas, whereas the ROOI performs well also out of them. Indeed, it is observed that the DCT-PLS at −12 m provides lower RMSDs in winter than in summer despite the more intense currents in that season.

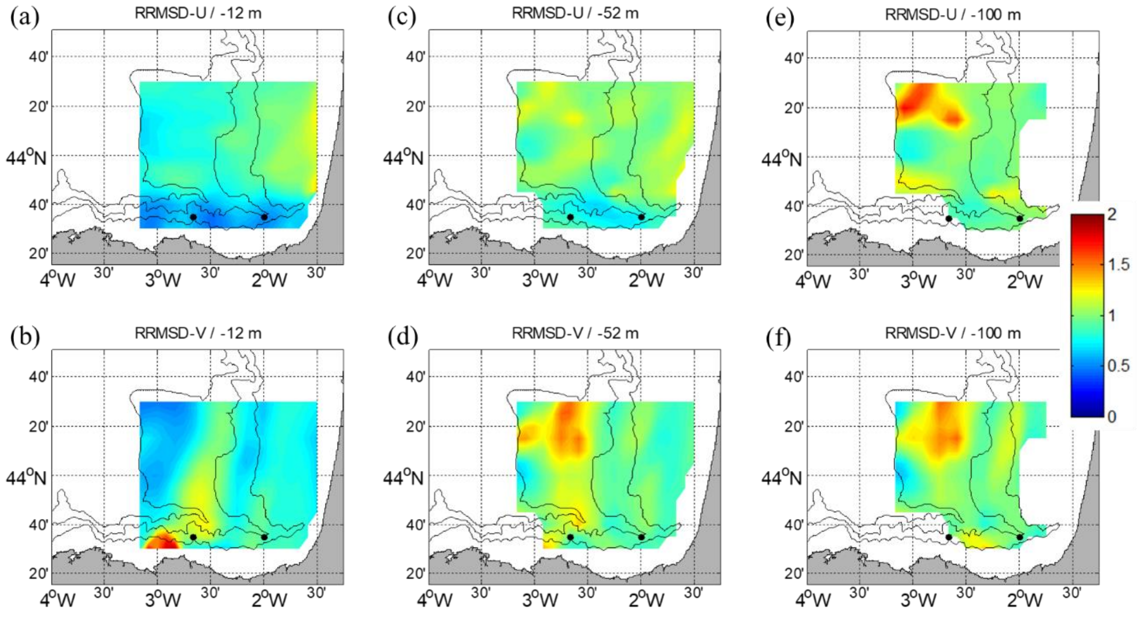

Figure 5.6. *RRMSD maps for the summer period between the reference fields and the outputs of the ROOI with GLORYS-LR for U (a, c, e) and V (b, d, f). Different depths are considered: −12 m (a, b), −52 m (c, d) and −100 m (e, f). The black dots depict the locations of the current vertical profiles.*

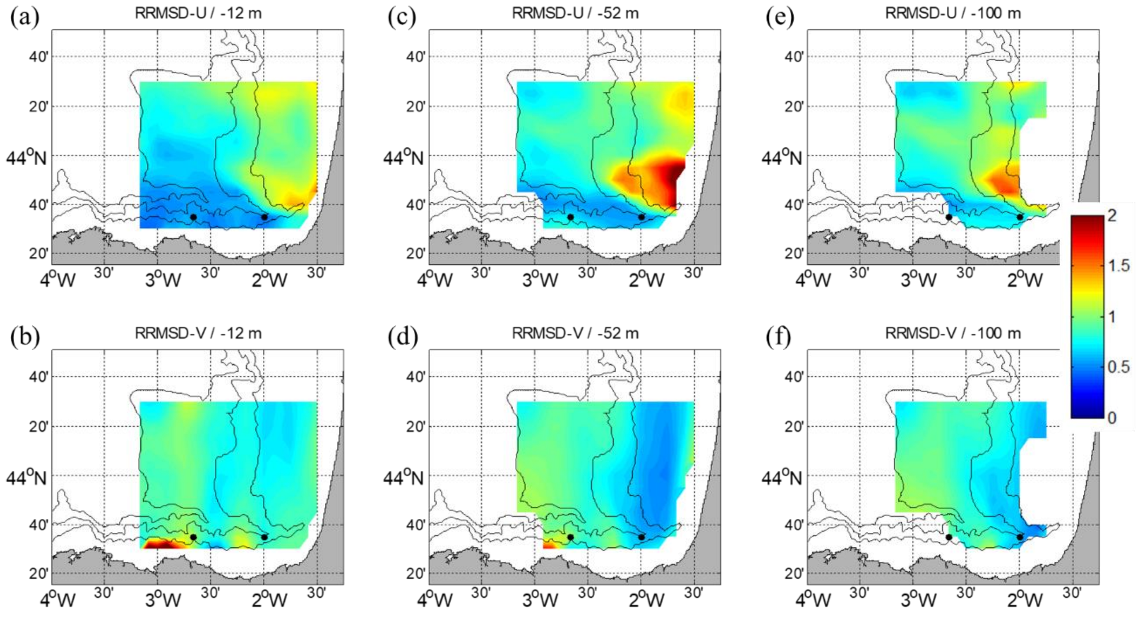

Figure 5.7. *RRMSD maps for the winter period between the reference fields and the outputs of the ROOI with GLORYS-LR for U (a, c, e) and V (b, d, f). Different depths are considered: −12 m (a, b), −52 m (c, d) and −100 m (e, f). The black dots depict the locations of the current vertical profiles.*

All these results, in addition to more specific analyses, are shown herein in terms of RRMSDs by means of maps (Figures 5.6‒5.9) and horizontal mean value profiles along the water column (Figures 5.10‒5.11). The results of the RMSDs are shown in *Appendix A4*. For the ROOI RRMSD maps, only the results with the spatial covariances from GLORYS-LR are presented (Figures 5.6‒5.7), because those are the ones that most challenge the method. In fact, for the ROOI with GLORYS-HR the RRMSDs are even lower (see *Appendix A2*), with the main conclusions being very similar.

For the ROOI, the RRMSD spatial distribution is more uniform in summer (Figure 5.6) than in winter (Figure 5.7) due to the more marked winter slope current regime. The Spanish slope area shows the lowest RRMSD-Us due to the persistent signal of the along-slope current, with lower values in winter than in summer. This suggests that the reconstructed fields are more accurate in well-sampled areas and that U is well resolved in the numerical simulations used for the definition of the spatial covariances. For the RRMSD-V, the French slope and part of its platform show the lowest values in winter, indicating that the slope current is well reconstructed for that period. Since the density of the observations is much higher at the surface, it is expected that the method performs better in the upper layers; in fact, it is observed that the RRMSDs increase with depth. This increase is sharper in summer than in winter, probably due to higher vertical shear in the currents due to the stratification conditions. It is shown that for the ROOI with GLORYS-LR (Figures 5.6‒5.7), the RRMSDs are, in general, below 1.25; that is, the RMSD is below 1.25 times the rms value at each point, except for some concrete areas.

Regarding the DCT-PLS, RRMSD maps (Figures 5.8‒5.9) show that this method works better in well-sampled areas since the lowest values are observed near the surface and the mooring locations. The RRMSDs are lower in winter (Figure 5.9) than in summer (Figure 5.8). For the RRMSD-U, the Spanish slope area shows the lowest values for both periods, whereas low RRMSD-V s are observed over the French slope in winter, showing that this method is also able to reconstruct the slope current. Overall, RRMSDs increase with depth; nevertheless, in summer the RRMSD-V s are higher for –52 m (Figure 5.8d) than for –100 m (Figure 5.8f). This could be due to a stronger vertical shear related to the seasonal thermocline, which in this period is located between –30 and –50 m. For the DCT-PLS, the RRMSDs are not as smooth as for the ROOI, with RMSDs near (off) the observation areas lower (higher) than half (twice) the rms value at each point.

Thus, for both methods, lower RRMSDs are observed in winter than in summer, along the slope for the along-slope component of the velocity and close to the surface. While the DCT-PLS is more effective at well-sampled areas, the ROOI performs better elsewhere. The best performances in the well-sampled areas show that the a priori analysis, shown in *Section 3*, can provide an approximate idea about the areas where the reconstructions could, in principle, perform better.

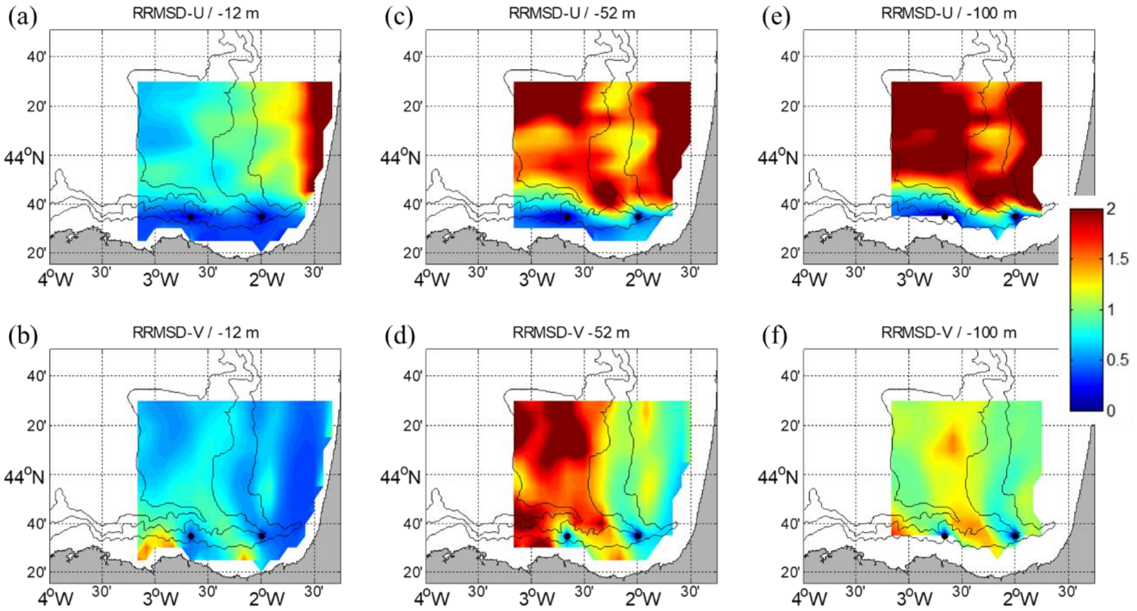

Figure 5.8. *RRMSD maps for the summer period between the reference fields and the outputs of the DCT-PLS for U (a, c, e) and V (b, d, f). Different depths are considered: −12 m (a, b), −52 m (c, d) and −100 m (e, f). The black dots depict the locations of the current vertical profiles.*

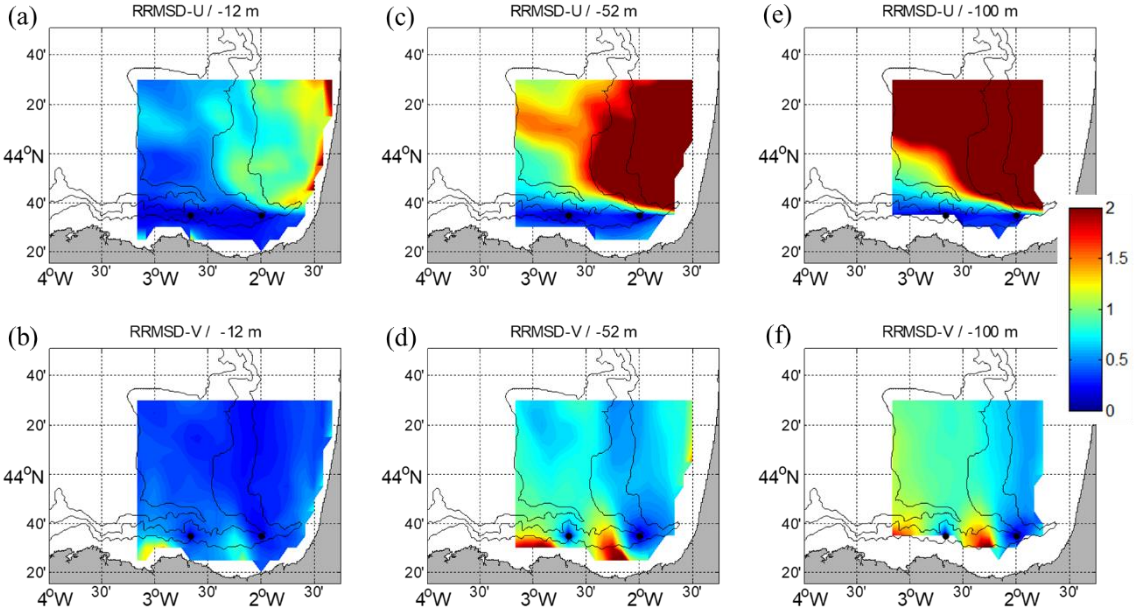

Figure 5.9. *RRMSD maps for the winter period between the reference fields and the outputs of the DCT-PLS for U (a, c, e) and V (b, d, f). Different depths are considered: −12 m (a, b), −52 m (c, d) and −100 m (e, f). The black dots depict the locations of the current vertical profiles.*

It is observed that the results for the DCT-PLS worsen quickly as we get away from the observation points. Considering the −52 m depth layer, we observe that RRMSD values obtained with the DCT-PLS method increase from 0 to 0.25 at 31 km (6.3 km) for the U (V) component in the zonal (meridional) direction from the mooring points.

An analysis of the spatial mean of the RRMSDs with depth (Figures 5.10−5.11) was performed to evaluate the methods' skills, regardless of the spatial variability shown in previous figures. Note that the same grid points were considered for both data-reconstruction methods and that the ROOI with IBI, GLORYS-LR, and GLORYS-HR are shown in this analysis. The analysis was carried out in the entire grid and the reduced grid (see Figure 5.1b) in order to explore the sensitivity of the results to the choice of different areas.

For the entire grid case (Figure 5.10), the ROOI with GLORYS-LR provides similar results as the DCT-PLS for V (Figure 5.10b and d), whereas it provides much better results for U (Figure 5.10a and c). On the other hand, the ROOI with IBI and GLORYS-HR performs better for both velocity components. As it could be noticed in Table 5.3 and Figures 5.6−5.9, the mean RRMSDs show RMSDs around or less than 1 times the rms value at each point, except for U for the DCT-PLS.

In the reduced grid case (Figure 5.11), the lowest mean RRMSD-Us are observed for the DCT-PLS, performing significantly better than the ROOI. In general, the mean RMSDs are around or less than 0.75 times the rms value at each point, with values around or less than 0.5 times the rms value for the DCT-PLS. This provides quite a satisfactory reconstruction of the along-slope velocity component in the Spanish slope area. The latter results in the water column (Figures 5.11−5.12) again show that the ROOI provides smaller RRMSDs than the DCT-PLS for the entire grid case, whereas the DCT-PLS provides better results in well-sampled areas.

With regard to the seasonal analysis, lower RRMSDs are observed in winter (Figures 5.10−5.11). The only exception is the RRMSD-U in the entire grid case for the DCT-PLS (Figure 5.10a and c) due to the high RRMSDs over the French shelf and slope for that period (see *Appendix A3*) since this method expands the zonal component to that area of meridional regime. Considering all the analysed depths and study periods, satisfactory reconstructions are obtained by both methods. These reconstructions provide mean RMSDs for each depth (Figures 5.10−5.11) ranging from 0.55 (0.7) cm s^{-1} to 10.94 (9.58) cm s^{-1} for the entire (reduced) grid and mean RRMSDs ranging from 0.07 (0.12) to 3.47 (1.31) with typical values around 1 or less, i.e., with reconstructed field errors around the rms value or less at each point. In general, the RRMSDs are increased with depth obtaining RMSDs up to 10.94 cm s^{-1} at −150 m.

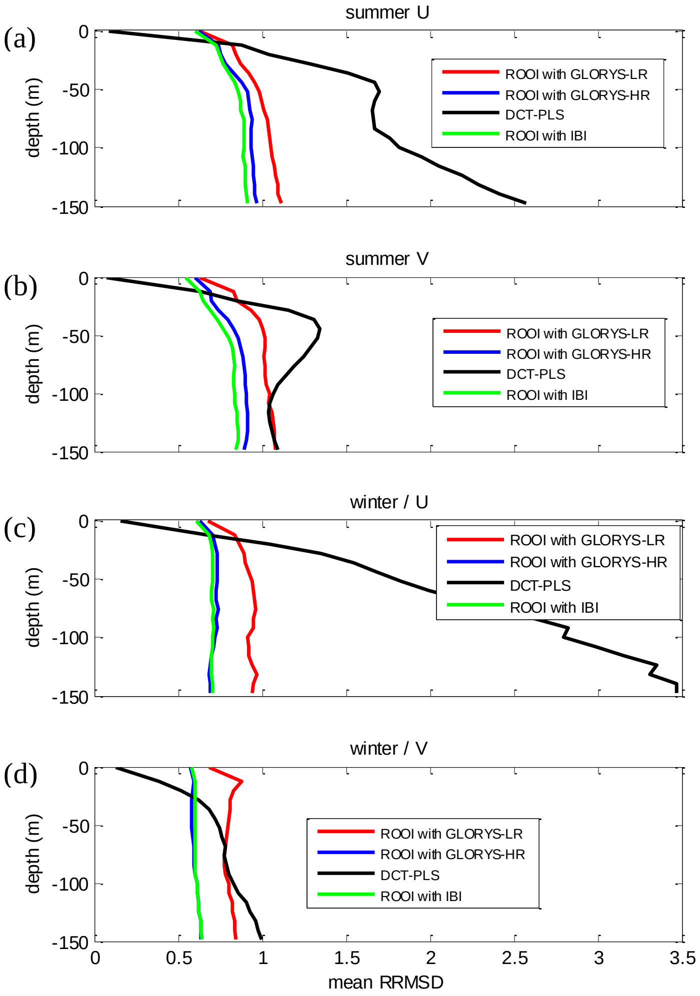

Figure 5.10. *Mean RRMSDs related to all the data-reconstruction methods for each depth considering the entire grid for the summer period (a, b) and for the winter period (c, d). U is shown in (a, c) and V in (b, d).*

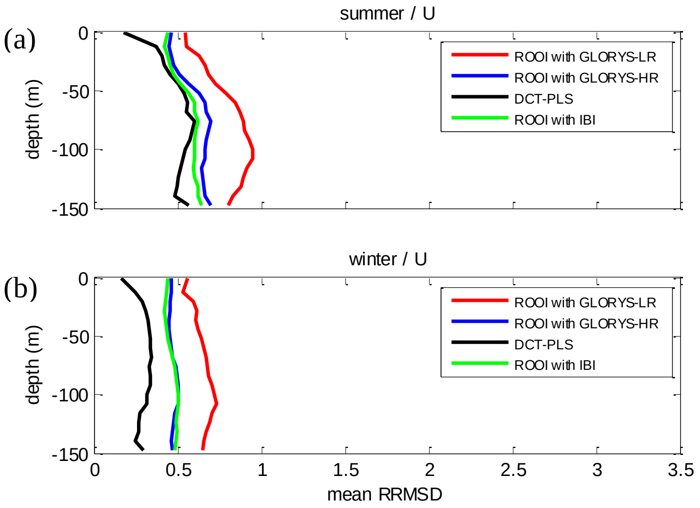

Figure 5.11. *Mean RRMSD-U related to all the data-reconstruction methods for each depth considering the reduced grid domain for the summer period (a) and for the winter period (b).*

4.2 Sensitivity test: increased number of ADCPs

An analysis with two additional ADCPs was carried out in order to evaluate the sensitivity of the data-reconstruction methods to an increased number of observations. The two extra ADCPs were located over the French slope since this could be a strategic area to monitor the winter slope current downstream of the Capbreton Canyon.

Only the winter period is shown, when the slope current is the strongest and the effects of the new scenario are more noticeable. Also, we show here the results obtained for the –52 m layer, due to its representativeness of the entire water column. The performance of the data-reconstruction methods for this configuration is assessed by subtracting the RRMSD maps of the 2-mooring case to the 4-mooring case. Therefore, the negative (positive) values in Figure 5.12 show that the RRMSD is lower (higher) for the 4-mooring configuration, thus showing a better (worse) performance. In general, in this new scenario, the performance of both data-reconstruction methods improves, with smoother changes for the ROOI since it already uses historical information of the covariances in the whole study area.

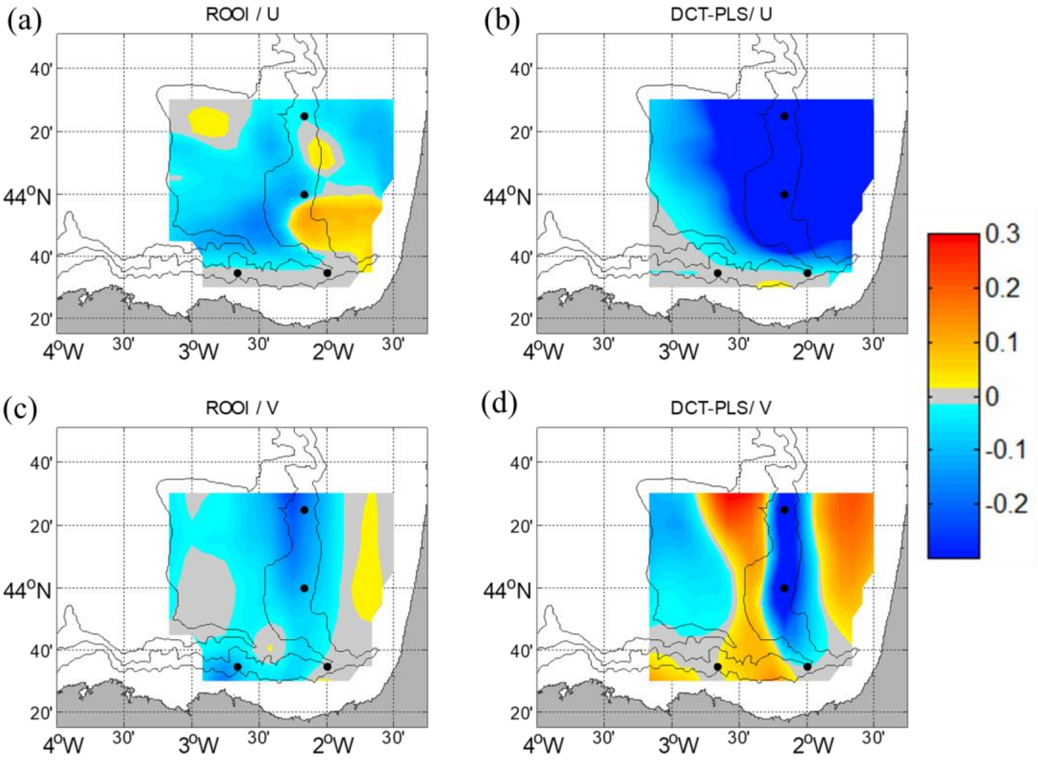

Figure 5.12. *The 4-mooring scenario RRMSD maps subtracted by the 2-mooring scenario RRMSD maps for winter at –52 m. Negative values mean a better performance in the 4-mooring scenario for U (a, b) and for V (c, d) for the ROOI (a, c) and for the DCT-PLS (b, d). The black dots depict the locations of current vertical profiles.*

For U, the addition of two extra ADCP profiles does not affect the Spanish slope area where there are already two moorings that capture the slope current. In the rest of the grid, for the DCT-PLS (Figure 5.12b), the performance of the reconstruction is remarkably improved; whereas, for the ROOI (Figure 5.12a), although in general the reconstruction is improved, there are some specific areas where the RRMSD-U s are slightly increased. For V, the results improve along the French slope, especially for the DCT-PLS (Figure 5.12d). However, for this method, the RRMSD-Vs are increased in the areas close to that slope, probably due to the spread of the information from the slope observations to those nearby areas which are not affected by the slope current regime.

5 Summary and Conclusions

In this chapter, we investigated the feasibility of combining data from multiplatform observing systems to reconstruct 3D velocity fields in the SE-BoB by means of two data-reconstruction methods. More precisely, we assessed the performance of such methods in the case of combining surface current data (as the ones provided by a long-range HFR system) and current vertical profiles (as the ones provided by two moorings equipped with ADCPs) in an emulated scenario based on an existing observatory (being also a typical configuration that can be found in other coastal areas). The performances of the methods were assessed through a classical approach conceptually similar to OSSEs, where a realistic simulation was regarded as the *true* ocean. This assessment approach allowed for the comprehensive evaluation of the selected methods as a first step towards their application to real data in the study area. Besides, it provides a best-practice methodology for the evaluation of the challenges and limitations of this kind of method in a broader way, prior to their applications to real data in other study cases. An interesting further step, out of the scope of the present chapter, would be to evaluate the robustness of the reconstruction methods for different observational errors.

We obtained satisfactory reconstruction results with spatial mean RMSDs typically ranging between 0.55 and 7 cm s^{-1}, for the first 150 m depth, with mean relative errors of 0.07–1.2 times the rms current at each point for most of the cases. The main feature of the region, the slope current, was well reconstructed by both methods, and it significantly improved when the information of two additional moorings was added.

Regarding the data-reconstruction methods, each one has its pros and cons. The DCT-PLS is only fed with the observations with no extra information about the study area, so its configuration is simpler. It performs well in well-sampled areas, but its quality is quickly degraded elsewhere. On the other hand, the ROOI is a robust data-reconstruction method that uses additional historical information, and thus provides better results in undersampled areas. The shortcoming of this method is that it needs accurate historical information of the study area. This is typically obtained from a realistic numerical simulation of the region, although it does not need to be contemporary to the observational period (i.e., from a hindcast simulation). Also, the method requires more tuning, so its implementation demands a careful testing of the parameters.

The tested methods have proven to be reliable, showing that it would be feasible to use them to reconstruct 3D current fields in the study area. In addition, they also could be used in a wide range of applications, due to their low computational cost. As, for instance, to obtain new operational products, combining data from different sources and complementary spatial coverage in near real-time. Moreover, through OSSEs and observing system experiments (OSEs), an optimization of existing observing networks can be proposed, providing a potential decision-making tool for future planning of coastal observatories or to set-up optimal operational data assimilation strategies. The use of these methods can be an alternative to data assimilation approaches (more expensive computationally and more complex to set-up) as far as they do not require users to run a numerical model. This is especially appealing for the marine rapid environmental assessment (MREA). The 3D reconstructed velocity fields can also be used for model validation, as well as for broadening the utility of coastal observing systems to biological, geochemical and environmental issues.

CHAPTER 6

3D characterization of a coastal mode-water eddy from multiplatform observations and a data-reconstruction method

Abstract

Coastal mesoscale eddies are important oceanic structures partially responsible for regulating ocean-shelf exchanges. However, their description and characterization are challenging; observations are often too scarce for studying their physical properties and environmental impacts at the required spatiotemporal resolution. Therefore, models and data extrapolation methods are key tools for this purpose. Observations from high-frequency radar, one satellite and two gliders, are used here to better characterize the three-dimensional structure of a coastal mode-water eddy from a multiplatform approach in the southeastern Bay of Biscay in spring 2018. After the joint analysis of the observations, a three-dimensional data reconstruction method is applied to reconstruct the eddy current velocity field and estimate the associated water volume transport. The target eddy is detected by surface observations (high-frequency radar and satellite) for two weeks and presents similar dimensions and lifetimes as other eddies studied previously in the same location. However, this is the first time that the water column properties are also observed for this region, which depicts a mode-water eddy behaviour, i.e., an uplift of the isopycnals in the near-surface and a downlift deeper in the water column. The reconstructed upper water column (1−100 m) eddy dynamics agree with the geostrophic dynamics observed by one of the gliders and result in cross-shelf inshore (offshore) volume transports between 0.04 (−0.01) and 0.15 (−0.11) Sv. The multiplatform data approach and the data reconstruction method are here highlighted as useful tools to characterize and three-dimensionally reconstruct coastal mesoscale processes in coastal areas.

The contents of this chapter were published as:

Manso-Narvarte, I., Rubio, A., Jordà, G., Carpenter, J., Merckelbach, L., Caballero, A., 2021. Three-Dimensional Characterization of a Coastal Mode-Water Eddy from Multiplatform Observations and a Data Reconstruction Method. Remote Sens. 13, 674. https://doi.org/10.3390/rs13040674

1 Introduction

In recent years, several studies have investigated the impact of coastal eddies on ocean-shelf exchanges (e.g., Akpınar et al., 2020; Cherian and Brink, 2016; Combes et al., 2013; Peliz et al., 2004; Rubio et al., 2018; Shapiro et al., 2010), coastal water retention (Brzezinski and Washburn, 2011; Rubio et al., 2018), as well as the eddy contribution to nutrient and phytoplankton transport in coastal areas (e.g., Campbell et al., 2013; Moore et al., 2007; Peliz et al., 2004) as a key element for primary production. These studies show that knowledge of the coastal eddy field is crucial for a good understanding of physical and ecological processes in the coastal ocean. However, the characterization and prediction of such eddies are difficult due to their interactions with topography and coastal dynamics, which exhibit turbulent and chaotic currents and waves of various sorts.

Huthnance et al. (2009) highlighted the importance of numerical models as a methodological tool to extrapolate sparse observations to three-dimensional (3D) fields for use in determining ocean-shelf exchanges in western European shelf seas. At the same time, numerous studies use models that reproduce coastal eddies to assess the coastal water ocean-shelf exchanges (e.g., Akpınar et al., 2020; Campbell et al., 2013; Combes et al., 2013; Dietze et al., 2009; Mizobata et al., 2006). In this context, observations are crucial to support numerical models via data assimilation, the validation of results, or as benchmarks to overcome the uncertainties from which models suffer. Indeed, De Mey-Frémaux et al. (2019) highlighted the potential of integrating coastal observations and numerical models for a more complete characterization of coastal areas. In addition, observations can be used to simply inter/extrapolate information in areas of interest.

This study is focused on the southeastern Bay of Biscay (SE-BoB), which is characterized by the presence of canyons (e.g., Capbreton canyon), an abrupt change in the orientation of the coast, and a narrow shelf (Figure 6.1). The slope current is the main driver of the circulation in the region that in winter flows in the upper 300 m of the water column, advecting warm surface waters eastwards along the Spanish coast and northwards along the French coast (as shown by the solid arrows in Figure 6.1a), and with a reversed flow in summer that is weaker and less persistent (Charria et al., 2013; Le Cann and Serpette, 2009; Solabarrieta et al., 2014). Several studies have investigated open water mesoscale eddies in the southern part of the Bay of Biscay, also called SWODDIES (Slope Water Oceanic eDDIES; e.g., Caballero et al., 2016b, 2014, 2008b; Pingree and Le Cann, 1992b), which are observed to be generated along the slope by the interaction of the winter slope circulation with the abrupt changes in bathymetry. Some of these eddies display mode-water eddy behaviour, i.e., an uplift of the isopycnals in the near-surface and a downlift deeper in the water column (McGillicuddy et al., 1999). However, the vertical structure of coastal SWODDIES in the SE-BoB has not been well studied. In the comprehensive study of Rubio et al. (2018), the surface signatures of several coastal anticyclonic SWODDIES were observed in the study area centered around 43.8°N−2.5°W. These SWODDIES originated mainly in winter after the relaxation of strong winter slope current events and had diameters of ~40−60 km and lifetimes of ~1−5 weeks. Rubio et al. (2018) studied the eddy-induced surface cross-shelf water transport in the study area, concluding that coastal eddies might effectively induce offshore export of coastal waters, as well as their retention in the area. Nevertheless, their analysis was limited to the surface layer, although they suggested the potential importance of a 3D characterization of the transports.

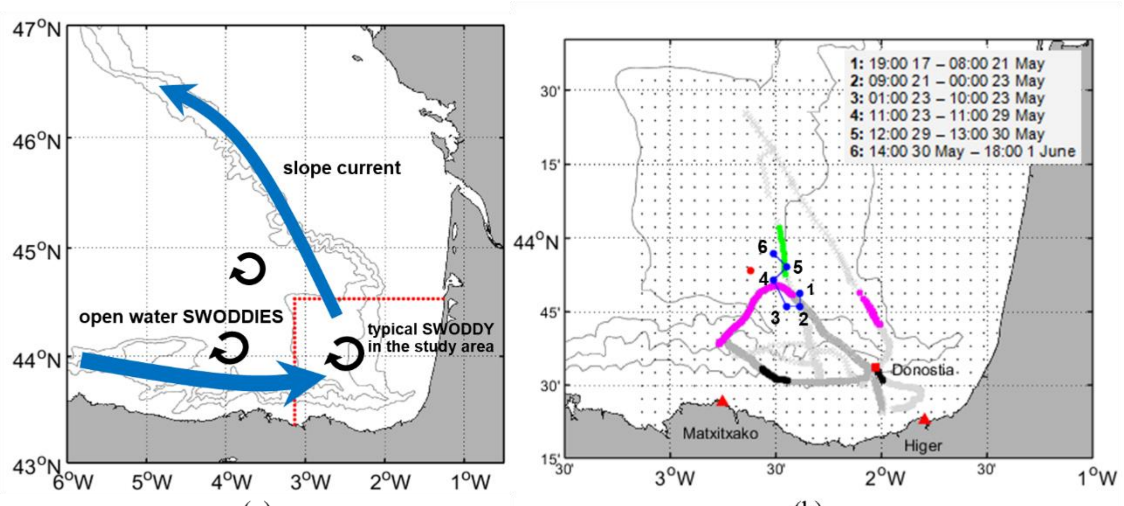

(a) (b)

Figure 6.1. *(a) Location of the study area (dashed red square). The winter slope current is represented by blue solid arrows, whereas the black arrows depict the usual location of anticyclonic eddies. (b) Close-up map of the study area. The grid points used to compute total high-frequency radar (HFR) currents are shown by gray dots, and the red triangles show the location of the HFR stations. The red square provides the location of the Donostia mooring. The dark and bright gray crosses show the shallow and deep gliders' trajectories, respectively; while the black, magenta, and green ones show the position of the gliders during the three reconstruction periods (P1, P2, and P3 respectively). The blue dots and numbers show the positions of the anticyclonic eddy core (from the location of the maximum vorticity values). The point used for extracting the wind time series is depicted by the red point. The gray lines show the 200, 1000, and 2000 m isobaths.*

In this work, we study a coastal SWODDY from a 3D perspective for the first time in the study area. This SWODDY, analyzed using multiplatform data, is located over the slope and shows a mode-water eddy behaviour. This work has a three-fold objective: (i) to characterize the 3D properties of the coastal mode-water eddy, since only the surface signatures of eddies have been described previously in the study area; (ii) to use and assess the skills of a 3D data reconstruction method to reconstruct these kinds of structures and to quantify the cross-shelf transport in the water column; and (iii) to showcase the use of multiplatform multivariable observations for an integrated study of mesoscale processes in a coastal region.

To this end, the data from a high-frequency radar (HFR) system and satellite observations are used to describe the surface signature of the eddy, whereas glider data provide information in the water column at the eddy's periphery and core. HFR and glider data are also used together with a slope mooring and a realistic numerical simulation data to obtain 3D reconstructed fields by means of the reduced order optimal interpolation (ROOI) method in three selected periods. The skills of the ROOI method were already analyzed in Manso-Narvarte et al. (2020) for this study area.

2 Data and Methods

2.1 Multiplatform and multivariable data approach

Table 6.1. *Summary of the observing platforms and datasets where* θ *denotes potential temperature,* σ_θ *denotes potential density anomaly, Vgeos denotes geostrophic current velocity, U (V) denotes the zonal (meridional) current velocity component, LP denotes low pass filtered and x, y, and z denote the zonal, meridional, and vertical directions, respectively.*

Observing Platforms/ Dataset	**Purpose**	**Variable**	**Spatial Resolution**	**Temporal Resolution**
Glider	Eddy analysis Reconstruction Validation	θ, Salinity, σ_θ, Chl-a, Vgeos σ_θ Vgeos	3D grid z: 1m x, y: uneven	Uneven Uneven (24 h LP) Uneven
HFR	Eddy analysis Reconstruction	U, V	2D grid x, y: 5 km	Daily + Hourly (10d LP) Average
Mooring	Reconstruction	U, V, σ_θ	1D profile z: 8 m (uneven for σ_θ)	Average
Sentinel-3A (satellite)	Eddy analysis	Chl-a	2D grid x, y: 1 km	Daily
WRF (model)	Eddy analysis	Wind U, V	Pointwise	Hourly
IBI (model)	Reconstruction	U, V, σ_θ	3D grid x, y: 0.083° z: uneven	Daily

Several datasets were used in this study to support the analysis of the mode-water eddy detected (objective (i)). Specifically, 2 gliders, a two-station HFR system, the output from the Weather Research and Forecasting (WRF) model and Sentinel-3A satellite data were used for this purpose.

Moreover, HFR and glider data were also used for reconstructing the eddy 3D current velocity fields along with numerical simulation and mooring data (objective (ii)). Details of the different observing platforms and datasets used are summarized in Table 6.1.

2.1.1 Temperature, salinity, pressure and chlorophyll-a from glider profiles

Temperature, salinity, pressure and chlorophyll-a (Chl-a) data were recovered from two Teledyne Webb Slocum Electric G2 gliders' Conductivity Temperature Depth devices (CTDs, Seabird SBE41 at 1 Hz) and fluorescence sensors (Wetlabs FLNTU at 1 Hz) and used to study the vertical characteristics of the eddy. From these data, potential temperature (θ) and potential density anomaly (σ_θ) referenced to the surface and across-track geostrophic current velocities (Vgeos) were also estimated for characterizing the eddy; whilst σ_θ was additionally used as input for the 3D reconstruction of the eddy current velocity fields (for which it was 24-h low pass filtered). Thanks to the differences between the glider and position fixes (measured with GPS) along their trajectories, the average water column current velocities or integrated current velocities were obtained, which were used as reference to estimate the Vgeos.

The gliders were deployed in the region (see Figure 6.1b) from 16 May until 14 June, 2018, during the BB-Trans glider mission run by AZTI (Pasaia, Spain) in collaboration with the Helmholtz-Zentrum Geesthacht (HZG) (Geesthacht, Germany) in the frame of the JERICO-Next European project Transnational Actions (https://www.jerico-ri.eu/ta/selected-projects/second-call/bb-trans/). During this mission, a shallow-water glider (0−100 m depth, hereinafter shallow glider) and a deep-water glider (0−1000 m depth, hereinafter deep glider) were deployed. The shallow glider comprises data from 16 May to 29 May, while the deep glider comprises data from 17 May to 14 June. After the glider mission, the data were processed, quality controlled, and made freely available by the Everyone's Gliding Observatories (EGO; https://www.ego-network.org/) project and the national programs that contribute to it. The data flagged as bad data were removed, as well as the data corresponding to excessive or low glider vertical velocities, setting a few gaps within the glider's datasets. In addition, transects were linearly interpolated in the water column to the mean latitude and longitude (of each transect), obtaining vertical profiles with a vertical resolution of 1 m.

2.1.2 Surface currents from HFR

Hourly fields of surface current velocities from the Basque Operational Oceanography System (EuskOOS, https://www.euskoos.eus/en/) HFR (CODAR Seasonde) were used both for studying the surface characteristics of the detected eddy and as input for the 3D reconstruction of the eddy current velocity fields. The current velocity data were quality controlled using procedures based on velocity and variance thresholds, signal-to-noise ratios, and radial total coverage, following standard recommendations (Mantovani et al., 2020). To isolate the most persistent signals in the HFR surface current velocity fields, the 10-day low pass filtered fields (hereinafter LP fields) were computed using an 8th order Butterworth filter. The daily averages were also used for characterizing the eddy at 3 days. Moreover, HFR data were averaged to be used as input for the 3D reconstruction.

The EuskOOS HFR system consists of two sites, one in Cape Higher and another one in Cape Matxitxako (see Figure 6.1b). It works at a central frequency of 4.46 MHz with an operational bandwidth of 30 kHz. The footprint area covers ~150 km off the coast and the integration depth is ~1.5 m. The system has provided hourly current velocity fields gridded onto a 5 km resolution regular orthogonal mesh since 2009, with some interruptions mostly due to maintenance stops or malfunctioning related to severe atmospheric conditions. The performance of this system and its potential for the study of ocean processes and transport patterns have already been demonstrated by previous works (e.g., Rubio et al., 2018, 2011; Solabarrieta et al., 2016, 2015, 2014).

2.1.3 Vertical profiles of potential density anomaly and currents from a moored buoy

Current velocities from the acoustic Doppler current profiler (ADCP) and σ_θ computed from the conductivity temperature devices (CTs) along the first 100 m of the water column at the Donostia slope mooring were used only for the 3D reconstruction of the eddy current velocity fields. To that end, the ADCP data were quality controlled by beam amplitude and correlation magnitudes, and velocity errors following (Bender and DiMarco, 2009), whereas CT data were controlled following standard procedures (Petit de la Villéon et al., 2005). In addition, as with the glider and HFR data, mooring data were adapted (averaged) to be used as input for the 3D reconstruction.

The EuskOOS Donostia mooring (Wavescan Buoy WS169) is anchored in a water depth of 550 m on the Spanish slope (at 43.56°N−2.03°W, see Figure 6.1b) and has been providing data since 2007. Among the oceanographic sensors, a downward-looking ADCP (RDI Workhorse), operating at a frequency of 150 kHz, measures hourly current velocities with bins of 8 m depth starting at a depth of 12.26 m and extending down 200 m into the water column. In addition, several CTs (Seabird SBE37IM at hourly measurements) along the mooring line provide hourly temperature and salinity data at −10, −20, −30, −50, −75, −100 and −200 m (note that the CT located at −200 m also contains a pressure sensor). The performance of these sensors and the quality of the data have already been demonstrated (e.g., Ferrer et al., 2009; Rubio et al., 2013a; Solabarrieta et al., 2016, 2014).

2.1.4 Chl-a images and wind data

Chl-a images and wind data were used for studying the surface characteristics of the detected eddy. Daily level 3 Chl-a images (1 km resolution) were provided by the Ocean and Land Colour Instrument (OLCI) airborne in the Sentinel-3A satellite during the BB-Trans mission. However, cloud-free images were only obtained for 20, 21, and 24 May due to cloudy conditions during the glider mission period.

The hourly wind data were extracted from the Weather Research and Forecasting model (WRF) provided by the meteorological agency of Galicia (MeteoGalicia) at 43.89°N−2.62°W (Figure 6.1b). This model, with a native resolution of 12 km, reproduces the offshore wind fields of the SE-BoB with reasonable accuracy (Ferrer et al., 2010).

2.1.5 Numerical simulations

As in Manso-Narvarte et al. (2020), the covariance matrix needed for the 3D reconstruction using the ROOI method was built upon the IBI_REANALYSIS_PHY_005_002 product (hereinafter IBI), provided by the Copernicus Marine Environment Monitoring Service for the period 1992−2016. The IBI reanalysis is based on a realistic configuration of the NEMO model for the Iberian Biscay Irish region, which assimilates in situ and satellite data. For more details on the simulations, the reader is referred to (Manso-Narvarte et al., 2020) (Table 1). A complete description of the product and its validation can be found in (Sotillo et al., 2015) and the following links: http://cmems-resources.cls.fr/documents/PUM/CMEMS-IBI-PUM-005-002.pdf and http://resources.marine.copernicus.eu/documents/QUID/CMEMS-IBI-QUID-005-002.pdf.

The temporal resolution of the dataset used was daily, and the horizontal spatial resolution was 0.083° × 0.083° (~6−9 km). The vertical levels used were unevenly distributed with separations between 1 and 3 m in the first meters and an increasing separation with depth.

2.2 Method for the 3D reconstruction of the observed fields

In this section, the 3D data reconstruction method and its implementation in our specific case are explained. Note that to allow the blending of datasets with different temporal and spatial resolution, a specific preprocessing was needed as explained in *Section 2.2.2*.

2.2.1 The ROOI method

The ROOI method was used to reconstruct the 3D current velocity fields from HFR surface fields, mooring, and glider observations. In Manso-Narvarte et al. (2020), after reviewing several methods to expand the HFR data to subsurface layers, two data reconstruction methods, namely the discrete cosine transform-penalized least square (DCT-PLS; Fredj et al., 2016) and the ROOI

(Kaplan et al., 1997) were tested and compared in the study area. The ROOI provided better results in areas far from the observations, thus being more suitable for the present study since it allowed taking advantage of the complementarity of the available datasets. More quantitatively, the ROOI provided mean spatial reconstruction errors between 0.55 and 7 cm s^{-1} and mean relative errors of 0.07−1.2 times the root mean square value for the first 150 m depth. The ROOI is based on Empirical Orthogonal Function (EOF) decomposition and was first proposed by Kaplan et al. (1997) to reconstruct sea surface temperatures. Since then, it has been used to reconstruct several variables such as sea level pressure (Kaplan et al., 2000), sea level anomalies (Church and White, 2006), or 3D current velocity fields (Jordà et al., 2016). The details of the method can be found in Kaplan et al. (2000, 1997) and Jordà et al. (2016), so here, only the basics are presented to understand the method and support the discussion of the results.

The 3D current velocity field we want to obtain can be expressed as a $m\ x\ n$ matrix $Z(r,t)$, where r is the m-vector of spatial locations and t is the n-vector of times. However, the observations only cover a small part of the 3D domain (a few N locations, being $N \ll m$). In order to obtain current velocities in all m locations, an EOF decomposition approach is considered. If a spatial covariance matrix is computed as $C = n^{-1}ZZ^T$, an EOF decomposition can be applied:

$$C = U\Lambda U^T \tag{6.1}$$

where U is an $m\ x\ m$ matrix whose columns are the spatial modes (EOFs) and Λ is the $m\ x\ m$ diagonal matrix of eigenvalues. Then, the velocity field can be exactly reproduced as:

$$Z(r,t) = U(r) \cdot \alpha(t) \tag{6.2}$$

in which the temporal amplitude α can be computed as $\alpha = U^T Z$, since U is orthogonal.

Since there are not enough observations for directly computing Z, historical data from a realistic numerical simulation are used to represent the current velocity statistics (C) between all m locations. Then, U is inferred by applying the EOF decomposition. In addition, Eq. (6.2) is truncated to include only the M leading EOFs that reproduce the features that we intend to reconstruct, avoiding introducing noise from the higher-order modes. Thus:

$$Z_M\,(r,t) = U_M\,(r) \cdot \alpha_M(\,t) \tag{6.3}$$

Then, the α_M can be determined under the constraint that the reconstructed Z_M fits the observations available at each time step, while minimizing a cost function that takes into account the observational error and the role of neglected modes (see Kaplan et al. (2000, 1997) for the complete derivation). In summary, the values of the current velocities of a 3D grid can be obtained by merging (i) the spatial modes of variability computed from a realistic numerical simulation, and (ii) the temporal amplitudes obtained using the available observations.

Note that the m-vector of spatial locations (each row of Z) corresponds to the grid points at which we want to reconstruct the currents as well as the grid points where we have the observations. Each grid point only corresponds to one velocity component. Thus, if instead of using only one component both horizontal components are jointly used, there will be twice the number of grid points. However, more variables can also be used, and the way to incorporate them is simply enlarging the matrix Z with additional rows: one for each grid point at which the new variable is available.

2.2.2 Implementation of the ROOI method

Current velocity (zonal (U) and meridional (V)) and σ_θ observations were used to reconstruct current velocities at the IBI grid points (see *Section 2.1.5*). Moreover, the ROOI also reconstructs the observations at their own locations (fitting the reconstruction to the observation). For that, first, spatial covariances were set from IBI between current velocities at the IBI grid points and current velocities and σ_θ at the location of the observations (interpolated from the IBI grid). Then, based on these covariances and the observations, the reconstructions were obtained following the methodology explained in *Section 2.2.1*.

Current velocity fields were reconstructed for three different periods (hereinafter called P1, P2, and P3), as indicated in Table 6.2. The criteria for selecting the periods was to have the eddy or its near field measured simultaneously by at least the HFR and one glider. In P1 and P2, the eddy was detected at the surface by the HFR, while the gliders surveyed a frontal area to the south of the eddy (P1) and the eddy periphery (P2). In P3, the HFR detected a weak anticyclonic signal at the surface, while the deep glider crossed the eddy core. The relative positions of the gliders with the overall locations of the eddy cores for each period can be seen in Figure 6.1b; more accurate relative positions are provided in Figure 6.2a for P1, Figure 6.2b for P2, and Figure 6.2c for P3. P3, in addition to the reconstruction, is used to study the hydrographic vertical properties of the eddy, since it is the period when the deep glider crossed the eddy core.

Table 6.2. *Definition of the three periods in 2018 used for the reconstruction, with all times in UTC. Period P3 was also used for the vertical description of the eddy.*

	From	**To**
P1	17:00 20 May	17:00 21 May
P2	00:00 25 May	23:59 26 May
P3	02:37 2 June	02:06 3 June

Note that apart from current velocity data (from HFR and ADCP), σ_θ from the mooring and glider CTDs was also used as an input variable for the 3D reconstruction of the current velocity field. σ_θ was selected because it presented significant covariances with the current velocities and gathered the effect of salinity and θ. Note that another variable that presented significant covariances was the across-track Vgeos; however, it was not used as an input variable but as reference to validate the results.

Considering that the historical (hindcast) data from IBI were provided on a daily basis and the covariances could not resolve features corresponding to shorter temporal scales, all the observations were averaged or low-pass filtered and subsampled to a daily scale, accordingly. HFR and mooring CT and ADCP data were averaged for each reconstruction period, making a daily average for P1 and P3, and a 2-day average for P2. Then, glider data were not averaged but 24-h low pass filtered to avoid aliasing of signals, due to the continuous change in position of the glider throughout the time. Note that the adapted observations used for the reconstruction in each of the three periods are shown in *Appendix B1* (Figure B1).

Several sensitivity tests were performed to tune the method's parameters. The main parameters to be adjusted were M, the number of modes, and the error corresponding to velocity and σ_θ observations (ε_{vel}^{obs} and ε_{pd}^{obs}, respectively). After several tests, M = 1000 modes were used, since they provided the necessary variability to describe the structures that were observed during each reconstruction period. Regarding the observational errors (ε^{obs}), the weight given to an input observation in the reconstruction can be partially increased (decreased) by decreasing (increasing) the ε^{obs} associated with it. Therefore, a different choice was made for each period, since different features were detected by each observing platform at each time, and a different weight was given to each variable. Thus, for P1, ε_{vel}^{obs} = 2 cm s^{-1} and ε_{pd}^{obs} = 0.4 kg m^{-3}, whereas for P2 and P3, ε_{vel}^{obs} = 2 cm s^{-1} and ε_{pd}^{obs} = 0.1 kg m^{-3}. However, it is worth mentioning that the sensitivity of the results to different parameterizations is relatively low, as long as the used ε^{obs} values are reasonable for each observing platform. A high ε^{obs} provides results that appeared overly smoothed, whereas a very low ε^{obs} provides noisy results (the sensitivity tests carried out with a set of different values for these two parameters are shown in *Appendix B2*, Figures B2−B14).

Since some observations were limited to the upper 100 m (i.e., the shallow glider observations) and Manso-Narvarte et al. (2020) showed that the skills of the 3D reconstruction decreased with depth, the reconstructions were made for the upper 100 m, and only using observations within that range. Moreover, the deep glider observations under −100 m were used to validate the results.

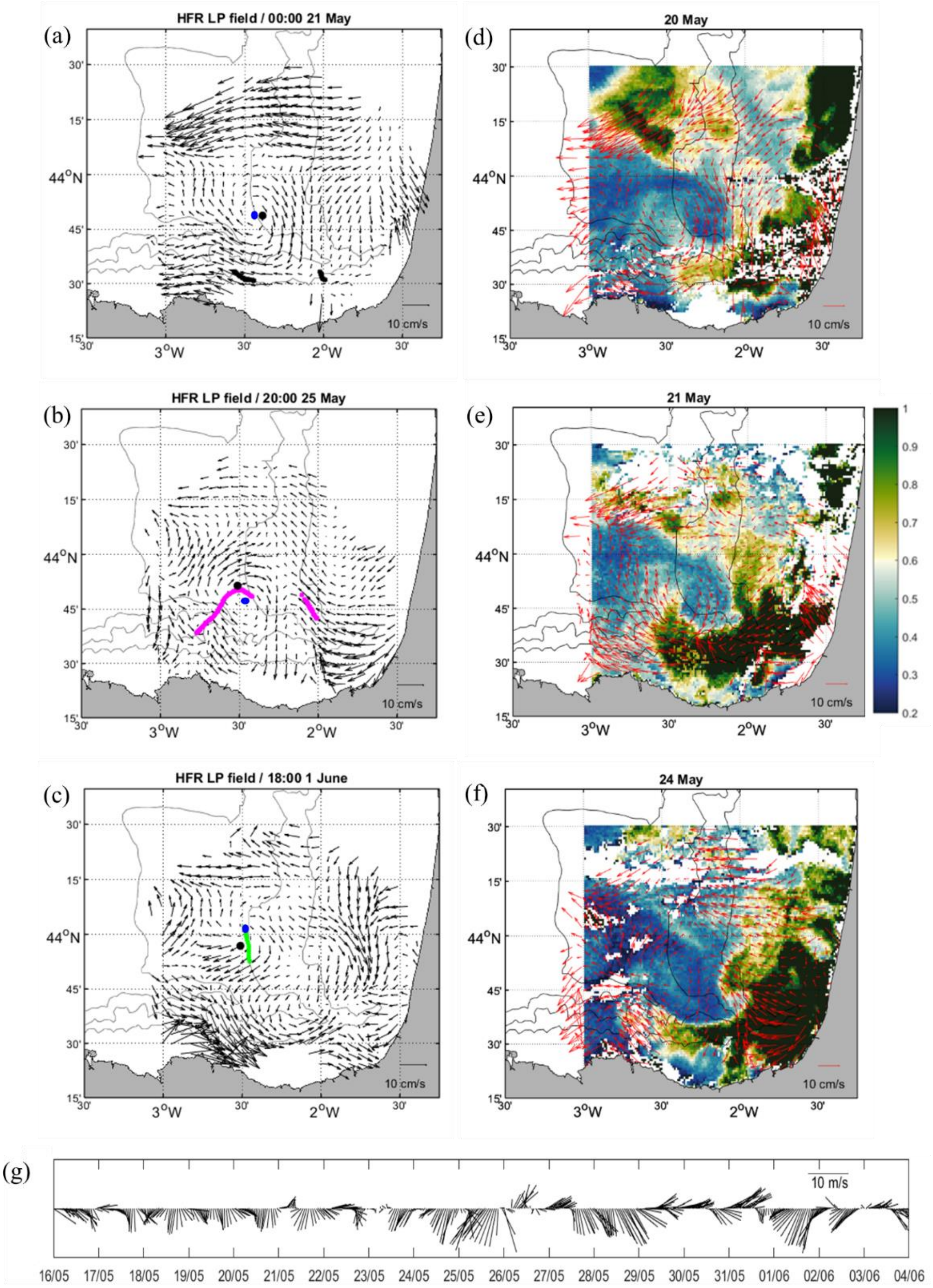

Figure 6.2. *In (a-c) the black dots show the positions of the eddy core, estimated from the location of the maximum of relative vorticity, overlaid to a snapshot of the high-frequency radar (HFR) low pass filtered (LP) field for a date within P1 (a), P2 (b), and the last detection date before P3 (c). In (a-c), the trajectory followed by the gliders is shown in black, magenta, and green colors, respectively, and the blue dots depict the position of the eddy core. (d-f) show satellite Chl-a (mg m*$^{-3}$*) images with the daily mean HFR fields superimposed (red arrows) showing the mentioned anticyclone. The gray lines show the 200, 1000, and 2000 m isobaths. (g) depicts the wind series (see location in Figure 6.1b).*

3 Results

3.1 Observed 3D properties of the eddy

The HFR LP fields were used to study the persistent (~15 days) surface signature of the eddy. The location of the anticyclonic eddy core was tracked in the HFR LP fields by the position of the maximum relative vorticity (Figure 6.1b). It was first observed on 17 May, and its core moved gradually northwestward by 18 km until 1 June. The eddy had a quicker northward displacement (first northeastward and after northwestward) in the last three days when weaker winds from the north were observed (Figure 6.2g). Additionally, Chl-a images show that the Chl-a distribution patterns in the nearby areas of the eddy on 20, 21, and 24 May (Figure 6.2d-f) are in agreement with the daily mean HFR field patterns that are superimposed (red arrows) and with the eddy core locations.

Figure 6.2a-c provides three snapshots of three different moments of the surface evolution of the eddy, showing the position of the eddy cores overlaid to the HFR LP fields and the relative position of the gliders. These three moments correspond to a date within P1, a date within P2, and the last detection date at the surface (the day before P3), respectively. In these snapshots, it is observed that the eddy core locations provided by the maximum relative vorticity (black dot) are approximate; sometimes, they are accurate, as in Figure 6.2a, where the HFR LP field shows that the eddy core (blue dot, determined visually) is almost in the same location as the maximum relative vorticity. Some other times, they are less accurate, as in Figure 6.2b,c, where the maximum vorticity is not precisely on the center of the eddy shown by the HFR LP fields. In any case, the obtained locations with the relative vorticity maximum are accurate enough to track the overall trajectory of the eddy. Note that in Figure 6.2b, it can be observed how the shallow glider passes along the periphery of the eddy in P2. On the other hand, Figure 6.2c shows that the eddy core is detected by the HFR LP fields on 1 June at 44.02°N−2.48°W, where the deep glider passes through on 2 June (green crosses), i.e., in P3, when the surface signature shows a weak anticyclonic flow (as shown in Figure B1h in *Appendix B1*). This indicates that the mode-water eddy observed by the deep glider in P3 is the same as that observed at the surface until 1 June.

As explained before, the hydrographic properties of the eddy have been analyzed for P3, when the deep glider crossed the eddy core. The θ and σ_θ profiles (Figure 6.3b,c) show that at shallow depths, the isotherms and isopycnals are uplifted between −40 and −200 m. In the case of the salinity (Figure 6.3a), the uplifting starts at −100 m, whereas in the Chl-a profile (Figure 6.3d), it starts at around −70 m. The seasonal thermocline is located between −10 and −20 m without any remarkable uplift. The across-track Vgeos retrieved from the hydrography of the upper 100 m (i.e., referenced to a level of no motion at −100 m) clearly shows a cyclonic behaviour (Figure

6.4a). Note that this reference level is only considered to show the dynamics provided by the waters within the first 100 m. We will show that for the whole Vgeos construction, the whole water column should be considered.

In contrast to this uplift observed in shallow depths, in deeper waters, a downlift is observed, showing a structure typical of mode-water eddies. The isotherms and isopycnals downlift approximately from −200 m to −450 m (Figure 6.3f,g), whereas in the case of the isohalines, the downlift starts at −100 m (Figure 6.3e).

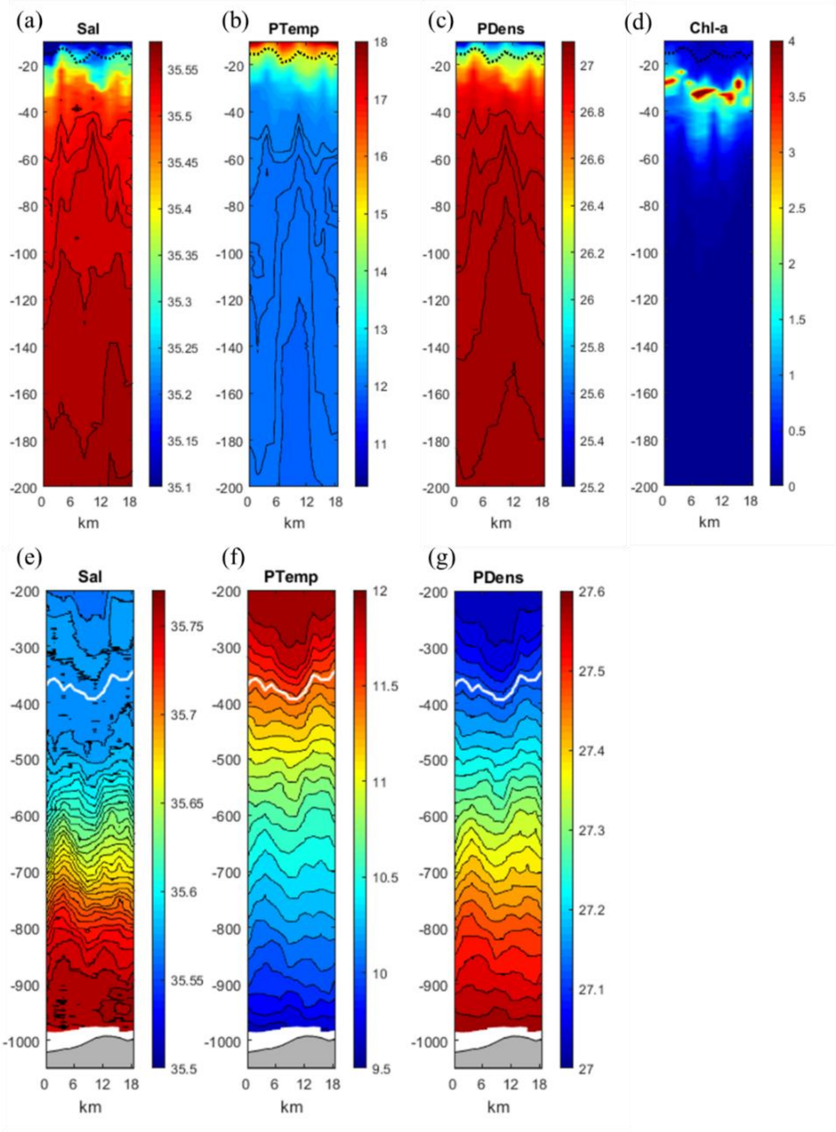

Figure 6.3. *Deep glider (a,e) salinity (psu), (b,f) θ (°C), (c,g)* σ_θ *(kg* m^{-3}*), and (d) Chl-a (mg* m^{-3}*). From −10 to −200 m for (a–d); and from −200 m to the bottom (gray area) for ((e–g), note the change in the color bar). In (a–d), the dashed black line depicts the 15 °C isotherm (representing the form of the seasonal thermocline), whereas in (e–g), the white line depicts the 11.5 °C isotherm (representing the form of the permanent thermocline). The X-axis shows the distance (in km) to the first point of the profile (from north to south in the maps shown in Figures 6.1b and 6.2c) and the Y-axis the depth in m.*

The downlift is shown by a minimum at the core of the eddy, which is deeper than the isoline on the sides of the profile. The 11.5 °C isotherm gives an idea of the shape of the permanent thermocline, which in Figure 6.3e–g shows a downlift at around −400 m and thus shows an anticyclonic signal. In addition, the deep salinity profile (Figure 6.3e) shows a salty water lens with its core centered at around −250 m and its base at around −350 m, which is downlifted by the anticyclone. The across-track Vgeos also shows that the anticyclonic signal extends until around −450 m (Figure 6.4b). Note that the Vgeos is referenced to the integrated currents, thus considering the water properties of the whole water column.

A rough theoretical estimation of the depth of an eddy can be obtained by the factor W·f/N (e.g., Carpenter and Timmermans, 2012; Zhao and Timmermans, 2015), where W is the width (diameter of the eddy), f is the Coriolis frequency, and N is the buoyancy frequency. Based on the measurements taken during P3, when the eddy core is sampled, we find W ~ 16 km (Figure 6.4b) and N ~ $3.4 \cdot 10^{-3}$ s^{-1} beneath the thermocline, leading to the rough depth estimate of −480 m. On the other hand, based on the azimuthal velocity Vr = 9 cm s^{-1} and the radius of the eddy R = 8 km, the obtained Rossby number value, defined as Ro ≡ 2 Vr/(R·f), is 0.22.

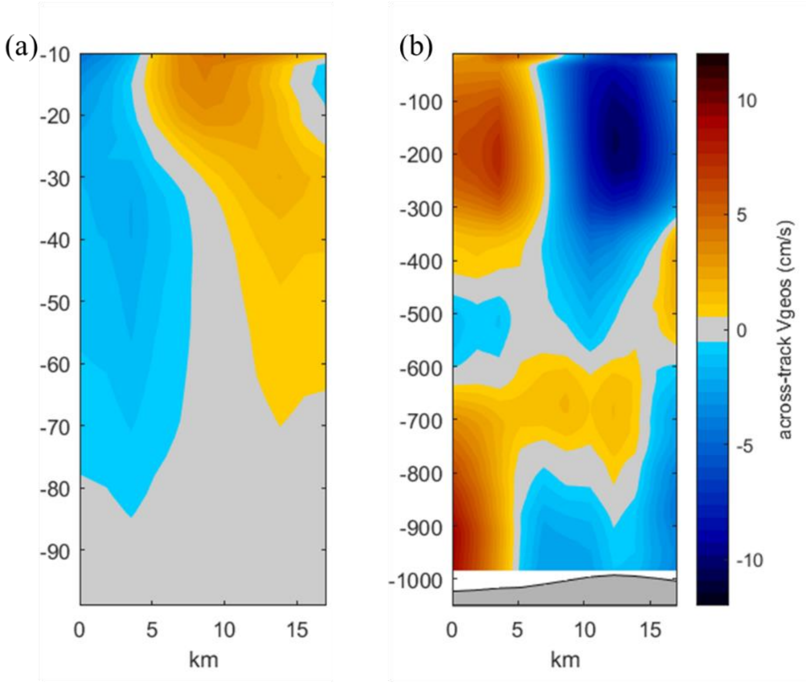

Figure 6.4. *Across-track Vgeos (cm s^{-1}) profiles corresponding to P3. The Vgeos was referenced to a level of no motion at −100 m for (a) and the integrated currents for (b). The positive values cor-respond to the eastward across-track currents, whereas the negative ones correspond to the westward currents. The X-axis shows the distance (in km) to the first point of the profile (from north to south in the maps shown in Figures 6.1b and 6.2c) and the Y-axis the depth in m. In (b) the bottom is depicted by dark gray color.*

3.2 Reconstruction of the 3D eddy current velocity fields

In this section, we focus on the reconstruction of the detected eddy; however, the results over the whole study area are depicted to show the overall variability in the reconstructed fields.

3.2.1 Skill of the reconstruction

Since the skill of the 3D reconstructions cannot be validated with additional external observations of current velocities, one option is to compare the reconstructed current velocity fields with the observations (previously used as inputs) themselves (as in Jordà et al., 2016). Thus, the root mean square differences (RMSDs) between the reconstructed and observed current velocities at the HFR and ADCP observation points were estimated (shown in Table 6.3). Note that the points considered correspond to the whole grid and not necessarily to locations where the eddy is observed. The RMSD at the HFR observation points show values ranging from 1.18 to 1.74 cm s^{-1}, while at the ADCP observation points, RMSD values range from 0.58 to 1.74 cm s^{-1}. The root mean square values range from 3.45 to 5.6 cm s^{-1} and from 0.70 to 3.19 cm s^{-1} at HFR and ADCP observation points respectively, showing that the obtained RMSD values are low.

Table 6.3. *Root mean square differences (RMSDs) between the reconstructed and observed current velocities at the HFR and acoustic Doppler current profiler (ADCP) observation points (in cm s^{-1}).*

	U_{HFR}	V_{HFR}	U_{ADCP}	V_{ADCP}
P1	1.39	1.37	0.58	0.68
P2	1.33	1.18	1.74	0.58
P3	1.72	1.74	1.35	0.92

3.2.2 Reconstructed 3D eddy current velocity fields and associated transports

In P1, the 3D reconstruction of the eddy current velocity fields (Figure 6.5) shows that the anticyclone is centered at 43.75°N–2.33°W in the first 50 m, whereas from −50 to −100 m, it is slightly displaced northwestward and horizontally spread. The eddy signal is weakened with depth and shows progressively weaker relative vorticity. In Figure 6.5d, the reconstructed currents projected across the section shown by the black line in Figure 6.5a–c (hereinafter section A) also show a clear anticyclonic behaviour. The across-track currents are stronger in the first 30 m, thus providing higher anticyclonic (i.e., negative) relative vorticity values.

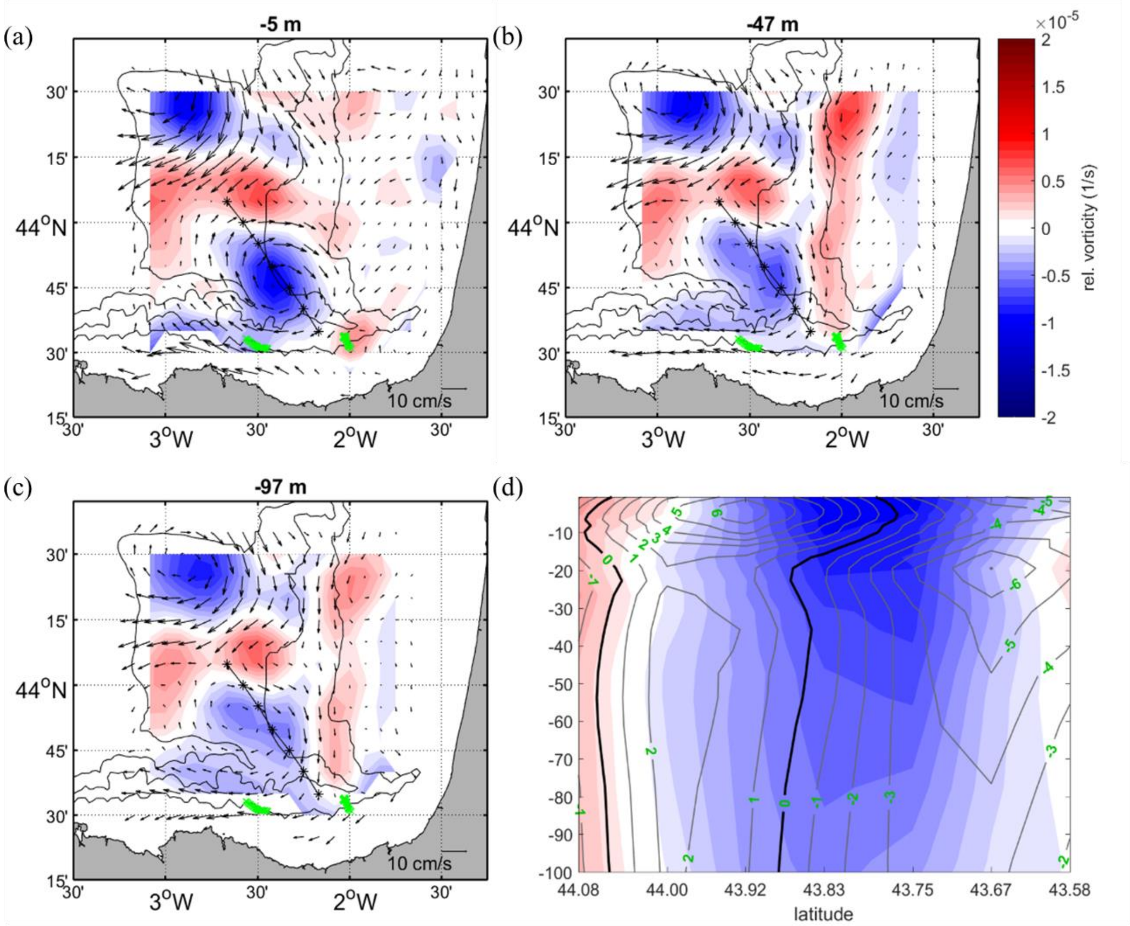

Figure 6.5. Reconstructed fields in P1. (a–c) show the current velocity fields and the relative vorticity for three depth levels. The gray lines show the 200, 1000, and 2000 m isobaths. The green crosses show the position of the gliders and mooring observations. The straight black line depicts section A. In (d), the relative vorticity in section A is shown along with the velocities perpendicular to it (gray contour lines). The values of the velocities are depicted in green in cm s^{-1}, and the 0 cm s^{-1} contour is marked in black. The positive/negative velocities correspond to northeastward/southwestward currents. The Y-axis shows the depth in m.

In P2 (Figure 6.6), the signal is narrower and more intense than in P1 (Figure 6.5). From the surface to −15 m, the eddy is centered at around 43.83°N–2.5°W; however, its core is displaced southeastwards between −15 and −25 m to 43.75°N–2.33°W. This latter position corresponds to the position of the eddy in P1, suggesting a tilting of the eddy, where the first 15 m have been moved northwestward, while the deeper part of the eddy remains in its original place (as shown in Figure 6.6d). The across-track current velocity contours of section A show a clear anticyclonic flow that is weaker at the surface (where the eddy is tilted) and is stronger for subsurface levels.

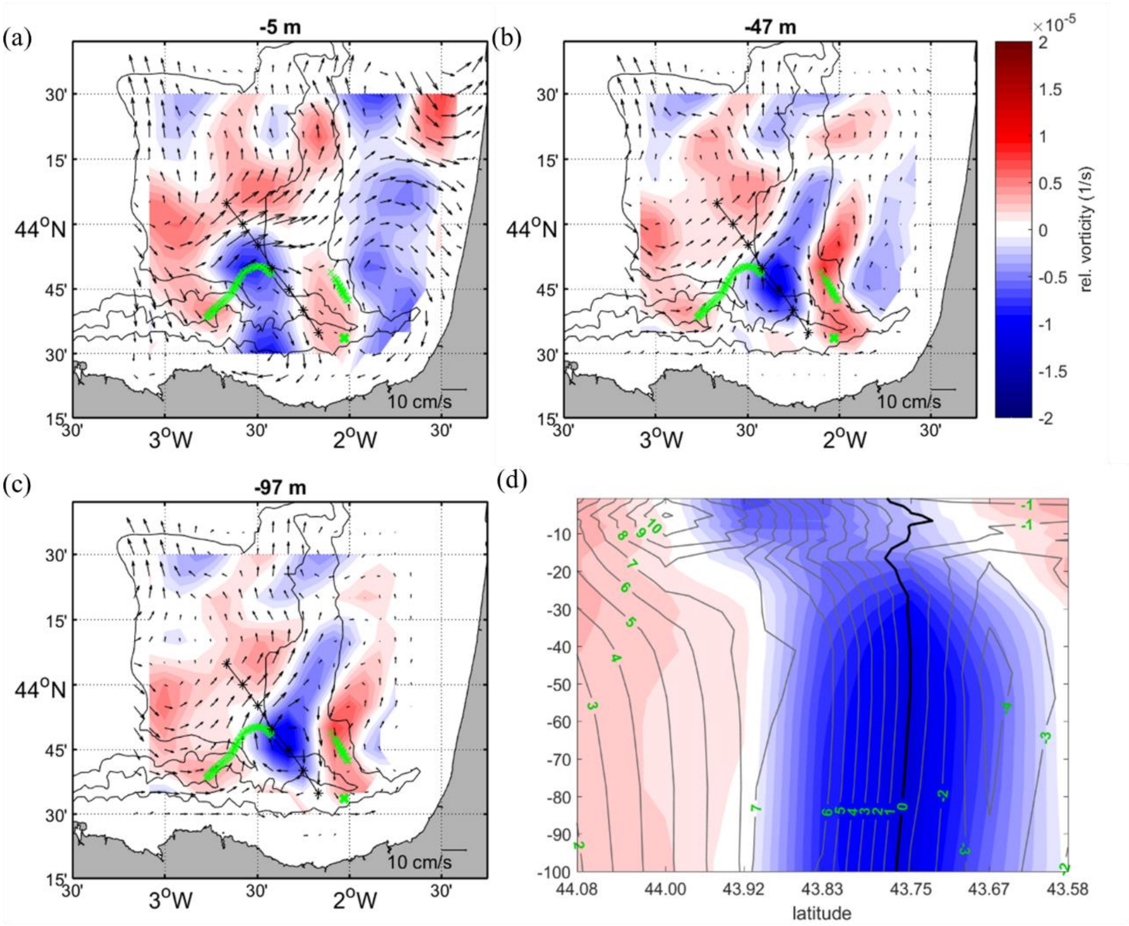

Figure 6.6. *The same as Figure 6.5 but for P2.*

In P3 (Figure 6.7), the weak anticyclonic signal detected at the surface over the trajectory of the deep glider is expanded for the whole water column without any horizontal tilting. Its relative vorticity is the lowest between −20 and −30 m, while it increases at around −10 and −60 m. The across-track current velocity contours with respect to section A also show an anticyclonic flow. The observed across-track Vgeos and the reconstructed currents projected across the trajectory of the deep glider show a similar anticyclonic pattern at −50 and −90 m (Figure 6.8) with eastward currents in the northern part of the trajectory and westward currents in the southern part.

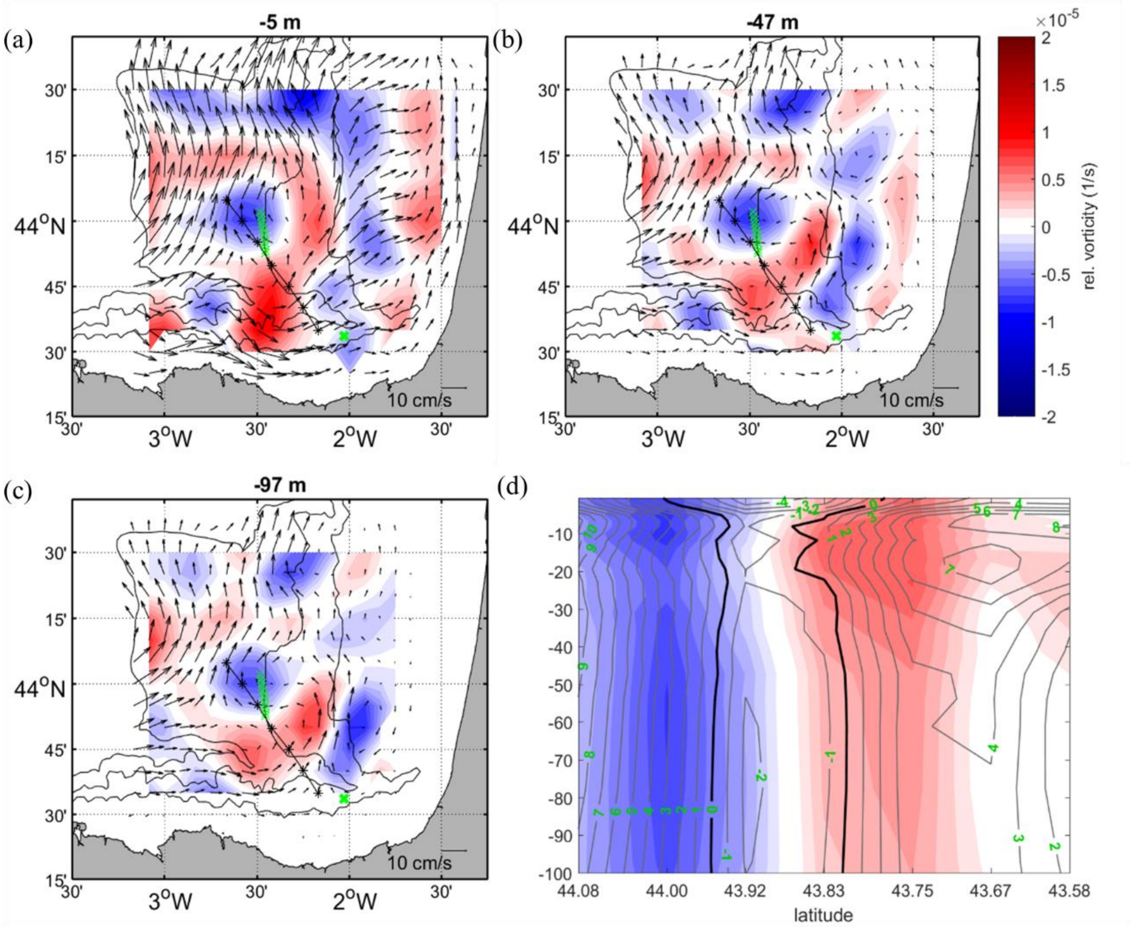

Figure 6.7. *The same as Figure 6.5 but for P3.*

The diameter of the reconstructed eddy (along the section A and taking as a reference the contour of negative relative vorticity) in the three periods considered is around 30 km, 25 km, and 15 km, respectively for P1, P2, and P3. The transport induced by the reconstructed eddy (delimited again by the negative vorticity) was also estimated at each period for the upper 100 m across section A. The positive transports correspond to the northeastward across-track direction (inshore), whereas the negative ones correspond to the southwestward one (offshore). Although this section is not strictly parallel to the shelf, it crosses the cores of the three reconstructed eddies, being useful to provide a rough estimate of cross-shelf transports across the same section. The estimated positive (negative) values are 0.05 Sv (−0.11 Sv), 0.12 Sv (−0.05 Sv), and 0.15 Sv (−0.01 Sv) in P1, P2, and P3, respectively.

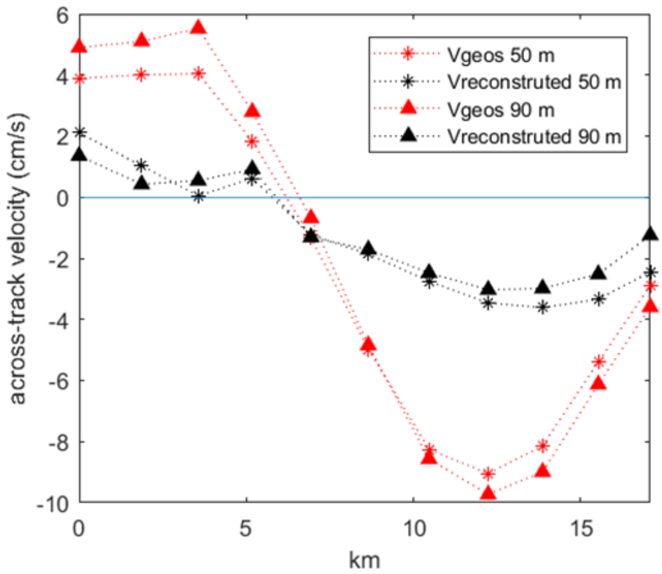

Figure 6.8. *Across-track currents (in cm s^{-1}) along the deep glider trajectory in P3 for −50 m (asterisk) and 90 m (triangle). The red markers correspond to the Vgeos observed by the glider (as in Figure 6.4b), whereas the black markers correspond to the reconstructed current velocities. Eastward currents have positive values whereas westward currents have negative values.*

4 Discussion

Thanks to a multiplatform data approach, combining in situ and remote sensing data, a coastal mode-water eddy was detected and investigated in 3D for the first time in the study area. From the observation of the surface anticyclonic signature of the eddy in the HFR LP fields, we conclude that the structure remained in the area for two weeks. This anticyclonic signature is also coherent with the Vgeos computed along the deep glider's trajectory (Figure 6.4b). The location and the main surface characteristics of the mode-water eddy observed here (Figures 6.1b and 6.2) are in agreement with the characteristics of anticyclonic eddies previously studied at the surface in the area by Rubio et al. (2018) who suggested that eddies with diameters of ~40−60 km and lifetimes of ~1−5 weeks were recurrent in this region. During the period of observation, the eddy showed a slow drift northward along the French shelf-break following a wind change from northerlies to southwesterlies. This behaviour is also coherent with the observations of Rubio et al. (2018), where at least one of the observed structures (i.e., the anticyclonic eddy A1214 in their paper) followed a very similar path.

With regard to the vertical properties of the mode-water eddy, we observe that the waters within the eddy were uplifted between −40 and −200 m and downlifted between −200 and −450 m. In a previous glider mission, an open water mode-water eddy west of the study area was detected by Caballero et al. (2016b). In that study, the mode-water eddy was located in deeper waters and showed larger horizontal and vertical dimensions, being the uplifting and downlifting of the isotherms and isohalines placed at shallower and deeper depths, respectively. The vertical properties of the mode-water eddy observed here extend until depths of around −450 m (Figures 6.3 and 6.4). These observations are coherent with the values obtained from the rough theoretical estimation of the depth of the eddy, based on the width and the f/N ratio (Carpenter and Timmermans, 2012; Zhao and Timmermans, 2015), which provides a depth of −480 m. In addition, the Ro = 0.22 is similar to values found in Carpenter and Timmermans (2012) and indicate that the eddy is largely in geostrophic balance.

The mode-water eddy observed by Caballero et al. (2016b) showed an anticyclonic flow on the surface by sea-level anomaly altimetry maps that was not observed in our case (not shown). This could be related to the closer vicinity of this structure to the coast (Manso-Narvarte et al., 2018), which would affect the altimetry measurements since both HFR surface fields and Chl-a images show the existence of an anticyclonic eddy. The weak surface signature of the eddy in the HFR fields in the last days could be related to the partial compensation between the cyclonic (baroclinic) and anticyclonic (barotropic) signals of the mode-water eddy upper layers as suggested by McGillicuddy (2015). However, in mode-water eddies, the geostrophic velocities are dominated by the permanent pycnocline, obtaining the same direction of rotation as in anticyclones (McGillicuddy et al., 2007). In fact, it is shown that the geostrophy provided by the hydrography of the whole water column (Figure 6.4b) compensates the cyclonic behaviour provided in the shallowest levels (Figure 6.4a). It is also worth mentioning that 3D studies such as this one are key since mode-water eddies are difficult to track by altimetry and HFR due to their smaller surface signal.

An in-depth discussion on the possible mechanisms behind the generation of this eddy and its mode-water structure is not possible, since it can be barely supported by the available observations. However, an approximate description of the history of the eddy could be the following. Before the first detection of its surface signature in the HFR fields, an event of intensified along self/slope current was detected in the study area between 7 May and 13 May (not shown). After this intensification, an anticyclonic meandering on 15 May preceded the day when the eddy was first detected (17 May). The interaction of the intensified slope current with the bathymetry is one of the main drivers of the generation of SWOODIES in the study area (Caballero et al., 2014; Pingree and Le Cann, 1992b; Teles-Machado et al., 2016), which was also suggested to be responsible for the generation of the eddy A1214 studied by Rubio et al. (2018). However, whether the eddy was already formed during the event of intensified along-shelf/slope current remains unclear. Concerning the generation of mode-water eddy in the water column, the observed wind variability in the area might help to develop this kind of structure through the Ekman pumping triggered by the eddy-wind interactions as explained by McGillicuddy (2015).

A rough estimate (following Gaube et al., 2015) of the vertical velocity due to this effect shows values around 18 cm day^{-1}, which are insufficient for the generation of the mode-water eddy in the period where the eddy is detected; however, the permanent underlying mean cyclonic circulation of this coastal area might also reinforce this effect. Further work through additional observations and process-oriented numerical experiments should be addressed to better understand the triggers for the generation of mode-water eddies in the study area, in view of their implications on the vertical and cross-shelf transport of high Chl-a to coastal waters (Caballero et al., 2016b; Rubio et al., 2018).

In the future, in order to better characterize eddies in the study area, an ad hoc sampling strategy would be desirable. HFR and satellite observations could help to detect them before a survey with in situ data, in order to plan the timing and location of the deployments. For instance, an improved strategy could be based on the deployment in the area covered by the HFR of two deep gliders that sample the eddy core and periphery and also cross the slope and shelf-break areas in perpendicular directions. In this way, the vertical properties and the across-track geostrophic currents would be better characterized and provide information about the cross-shelf and along-shelf water transports in the water column. Current measurements provided by gliders or by additional observing platforms such as shipborne downward-looking ADCPs or drifting buoys would also be valuable to analyze the eddy and to validate the reconstruction (which is independent of the data used, so it can accommodate different sampling strategies as shown in Jordà et al. (2016) and Manso-Narvarte et al. (2020)). In addition, turbulence measurements in the core and periphery of the eddies would be very valuable to study eddy-induced mixing processes. These kinds of multiplatform sampling strategies set from mid to long-term temporal frames arise as a helpful approach toward the comprehensive characterization of eddies and their effects on coastal ecosystems.

Building on the work by Manso-Narvarte et al. (2020), this work demonstrates the potential of a data reconstruction method for retrieving the 3D current velocity field associated with eddies in coastal regions. Concerning the methodology used for the reconstruction, one important factor to consider when applying the ROOI is the required input parameters (M, ε_{vel}^{obs}, ε_{pd}^{obs}). Low RMSD values between the reconstructed and observed fields at the observation points (Table 6.3) and a realistic variability of the reconstructed maps have been the criteria used to select the optimal parameters for the reconstruction (sensitivity tests displayed in *Appendix B2*, Figures B2−B14). Note that the sensitivity of the results to the different parameterizations is reduced, as long as the number of selected modes provides the minimum variability needed for the reconstruction of the target processes and the observational errors are reasonable.

The reconstructions were carried out for three different periods where the eddy and its surroundings were sampled in a different manner. In P1, the eddy was only observed by the HFR on the surface, whereas in P2, the HFR observed the eddy, and the shallow glider sampled the periphery. In P3, the surface eddy signal was very weak, but the deep glider sampled its core. The ROOI was able to reconstruct the eddy for the three periods, showing its ability to carry out reconstructions under different scenarios.

The ability of the method to reconstruct the eddy is especially remarkable in P3, taking into account its complex vertical structure in terms of σ_θ fields and its weak surface signature. Indeed, the ROOI reproduces the anticyclonic flow of the eddy in the upper 100 m, extending the weak anticyclonic signature observed at the surface, despite the cyclonic pattern provided by the σ_θ observations in the water column (shown in Figure 6.3c and also noticeable in Figure 6.4a). This anticyclonic flow in P3 is still reconstructed even giving more weight to σ_θ observations (by tuning the ε^{obs} as explained in *Section 2.2.2*; sensitivity tests are shown in Figures B13 and B14 in the *Appendix B2*) and might be explained due to higher covariances between surface and subsurface currents and lower covariances between subsurface currents and σ_θ. The strong covariances between the surface and subsurface currents are also noticeable in P1 when the eddy surface observations are enough for its reconstruction in the water column. However, in that case, the eddy becomes weaker as depth increases (i.e., when moving away from the surface observations). This shows that apart from the observations and the parameters used for the ROOI, the reconstruction is also dependent on the covariances, highlighting the importance of a good historical dataset. The reconstructed anticyclonic flow in P3 agrees with the Vgeos observed by the deep glider (Figure 6.4b), which is dependent on the water properties of the whole water column. In fact, the reconstructed across-track currents along the deep glider trajectory agree well with the across-track Vgeos observed by the deep glider (Figure 6.8), thus providing a first validation of the results. The difference in the intensity between both currents is likely due to the fact that the reconstructed currents have a daily variability.

The reconstructed eddy shows diameters of around 15–30 km, which are slightly smaller than those found in the literature at the surface in the study area (Rubio et al., 2018). The associated inshore transport values range between 0.04 and 0.15 Sv, being anisotropic and weaker when oriented offshore (negative transports). The values obtained here have a similar order of magnitude compared with the eddy-induced across-shelf transports modeled by Akpınar (2020) to the north of our study area in the Bay of Biscay, which were computed across the 500 m isobath for the first 50 m. In the future, the ROOI could be used to better understand the cross-shelf transports in the study area by broadening the EuskOOS slope ADCP data series by filling temporal gaps from surface HFR observations, based on covariances provided by real observations. Indeed, initial cross-validation tests have shown promising results (see *Appendix B3*).

The results of the reconstructions agree with the water column properties measured by the deep glider and with the characteristics of eddies found in the literature. Nevertheless, they are not validated with any other external data sources. Thus, although the ROOI shows promising skills for reconstructing eddy-like structures and for estimating transports in the study area, further analysis and validation with independent observations are needed to ensure a robust reconstruction of such structures.

When using the ROOI, having robust historical data is a prerequisite to any attempt of 3D reconstruction of current velocity fields in order to ensure reliable relationships between the variables we want to use in the reconstruction and to be able to reproduce the target processes or features we want to reconstruct. The sensitivity to the main parameters used in the ROOI must be analyzed carefully when applying the method to other study areas. The choice of the parameters also depends on the structure or features that require reconstruction and the relative importance that should be given to each input variable. In addition, as mentioned, validation of the results with additional observations is necessary to assess the skill.

5 Conclusions

This study continues with previous efforts to analyze coastal eddies in the SE-BoB (Rubio et al., 2018), shedding some light on the 3D characteristics of these structures that have been analyzed only from surface observations until now. A coastal mode-water eddy has been characterized in 3D and, despite showing slightly smaller scales, the general characteristics were similar to those found in the literature at open water regions nearby. The mode-water eddy was characterized by the joint analysis of multiplatform observations, highlighting the potential of this kind of approach for a better characterization of the different oceanic features, especially in coastal areas, where satellite observations present several limitations.

In addition, a 3D data reconstruction method was used to assess its capability to reconstruct eddy-like structures and estimate the associated cross-shelf transports in the upper 100 m. The results show that the method is able to reconstruct mesoscale eddies in different scenarios and that their associated cross-shelf transports provide reasonable first results. Therefore, the ROOI is here presented as a compelling tool for reconstructing coastal 3D circulation and transports. However, further validation with external data sources of current velocities or transport estimations would be valuable to ensure the robustness of the results.

In the future, the analysis of the main physical drivers responsible for the generation and evolution (e.g., migration, decay) of these recurrent coastal eddies would be interesting for better understanding the origin and progression of such structures in the study area. This could be carried out by means of numerical simulations and additional observations, for which ad hoc sampling strategies would be desirable. A better depiction of these types of structures would constitute an advance in the understanding of their impact on the surrounding ecosystem. Additionally, the ROOI approach could have several applications. The first application would be to reconstruct current velocity fields to study 3D coastal transports from a Lagrangian approach. This can have interesting ecological applications, such as for instance, the estimation of the residence areas of passive particles, such as marine litter at different layers, or for studying the distribution of eggs and larvae of different pelagic fish species. In fact, previous studies suggested that within the SE-BoB, the coincidence in space and time of SWODDIES with anchovy spawning could favour its recruitment by advecting eggs and larvae to off-shelf areas of lower predation risk but still productive enough to support them (Irigoien et al., 2007). Another future application could be to use the ROOI operationally in near real-time and at different depths in order to continuously reconstruct 3D current velocity fields from the HFR and mooring observations to complement the surface information for supporting the correct follow-up and integrated management of the SE-BoB.

CHAPTER 7

Anchovy eggs and larvae advection in the southeastern Bay of Biscay

1 Introduction

Coastal transport and retention processes are crucial from an environmental and ecological perspective. They are the main drivers of pollutants such as floating marine litter (FML) or oil spills but also affects to the biological component of the ecosystem, contributing to the advection of phytoplankton and nutrient-rich coastal waters, which are key for supporting primary production and sustaining the trophic chain and also contribute to the advection of fish larvae, which affects to survival rates and population dynamics. These processes are strongly dependent on the oceanic hydrodynamics of the coastal areas. In the southeastern Bay of Biscay (SE-BoB), water parcel retention conditions at the surface vary at interannual, seasonal and even daily scales, influenced by the variability of the general circulation as well as by several mechanisms such as wind-driven currents, mesoscale processes and fronts (Rubio et al., 2020).

The SE-BoB is characterized by an abrupt change in the orientation of the coast that separates the narrow Spanish shelf and the wider French shelf, with the Capbreton canyon in between (Figure 7.1). The slope current is one of the main drivers of the circulation that strongly flows poleward in late autumn and winter and with a weaker and more variable reversed flow in summer (e.g., Charria et al., 2013; Solabarrieta et al., 2014). The interaction of the slope current with the abrupt bathymetry often triggers the so-called SWODDIES (Slope Water Oceanic eDDIES; e.g., Pingree and Le Cann, 1992b). At the surface, the circulation is also driven by winds (e.g., Solabarrieta et al., 2015) with prevailing southwesterlies in autumn and winter that induce a northward and eastward drift over the shelf. During spring, the wind regime changes to northeasterlies inducing a westward and southwestward drift, being the situation in summer similar. However, weak and variable winds make wind-driven currents more uncertain in spring and summer. Over the shelf, wind-driven currents prevail over tidal or density-driven currents due to the narrow shelves and the low influence of rivers that induce significant density currents. River discharges are mainly subject to oceano-meteorological conditions (Ferrer et al., 2009), being the main river the Adour (see Figure 7.1). Additionally, freshwater discharges of the Gironde river, slightly to the north of the study area, could reach the study area.

Transport and retention processes regulate the fate of eggs and larvae at early life stages (ELS) of different pelagic fish species in the Bay of Biscay (BoB), as occurs with the European anchovy (Engraulis encrasicolus). Anchovy fishery activity is considered to be one of the pillars of the economy of the Basque fishing sector and the entire Cantabrian coast. The spawning peak occurs around May-June and the main spawning areas are the Gironde and Adour river plumes and to a less extent the shelf-break areas nearby (Motos et al., 1996). Anchovy eggs and larvae are mainly set along the first 30 m in the water column (e.g., Boyra et al., 2003; Palomera, 1991). Food availability and risk of predation are important factors in the recruitment of anchovy, as well as the oceanic transport patterns. Anchovy eggs and larvae are usually transported from the shelf to the off-shelf (i.e., shelf-break, slope and open-ocean) areas, mainly southwestwards driven by the seasonal northeasterly winds (e.g., Cotano et al., 2008; Irigoien et al., 2008; Uriarte et al., 2001), before developing swimming abilities at around 30 days after hatching (e.g., Irigoien et al., 2008). Then they remain in those areas until they return to the shelf as mobile juveniles (e.g., Boyra et al., 2016; Cotano et al., 2008; Irigoien et al., 2008; Uriarte et al., 2001).

The advection patterns observed in the latter references are based on the Eulerian approach, which describes oceanic properties in time at given locations. Indeed, such patterns were deduced comparing eggs, larvae and juveniles' positions with the corresponding averaged wind or current regimes in the area. These patterns provided valuable information, but only considered low-frequency advections. In order to describe how anchovy eggs and larvae are advected, the Lagrangian approach is the appropriate one since it describes the trajectory of a water parcel and its properties in time and enables to find out the effects of instantaneous advections. In Allain et al. (2007, 2001) the advection patterns of eggs and larvae were simulated forced by currents averaged in the upper 30 m derived from models. However, in those studies the simulation period clearly exceeded the period where larvae are considered passive, potentially biasing the results, as Irigoien et al. (2008) already highlighted. In Caballero et al. (2016a) the advection of larvae was simulated forced with numerically simulated currents at −5 m for simulation periods (in 2008 and 2010) where larvae are considered passive, observing that distributions are highly dependent on the variability of the current regime and that in general larvae do not tend to disperse towards open ocean.

In the study area, the available observations offer the possibility of performing Lagrangian simulations of the advection of eggs and larvae for peak spawning periods for several years for the first time, based on surface current velocities obtained from a high-frequency radar (HFR) system. This is an interesting approach since HFRs have proven to be suitable for different environmental and ecological applications (e.g., Cianelli et al., 2017; Declerck et al., 2019; Sciascia et al., 2018). Moreover, current velocity observations can be expanded to 3D fields by the reduced order optimal interpolation (ROOI) method, thus allowing Lagrangian simulations also at subsurface levels. Although further validations would be valuable, the ROOI has demonstrated to be a compelling method (Manso-Narvarte et al., 2021, 2020), and enables simulating the advection of eggs and larvae at different depths. The initial egg distributions for the simulations can be set from BIOMAN observations, which is a survey conducted every year in May that covers the shelf and slope areas, providing the most complete anchovy egg abundance dataset in the area, along with other environmental parameters.

The main aim of this study is two-fold: (i) to simulate the advection of anchovy eggs and larvae for the first time from in situ current velocity observations at different depths during this species ELS for several years, to better understand the role played by hydrodynamics in those periods, and at the same time (ii) to showcase the utility of multiplatform observations for 3D Lagrangian applications. For these purposes, the origin and fate of anchovy eggs and larvae were simulated from a Lagrangian approach, starting from the egg distributions observed during the BIOMAN surveys in 2011, 2012, 2013, 2014, 2016, 2017 and 2018 (2015 was not included due to the lack of enough current velocity data).

The study is organized as follows: In *Section 2* the used data is presented, whereas in *Section 3* the implementation of the ROOI method and the Lagrangian model used are explained. The reconstructed 3D current velocity fields were obtained by the ROOI method from HFR and acoustic Doppler current profiler (ADCP) observations (hereinafter called ROOI data). Since, as mentioned, further ROOI validation is valuable, in *Section 3* the ROOI validation exercises are also depicted, as well as the approach used in eggs and larvae advection simulations shown in the following section. Then, in *Section 4* the results and discussion of such simulations are shown, and finally, in *Section 5* conclusions are presented.

2 Data

In this section, the data used for 3D reconstructing current velocity fields, the ROOI validation exercises, and the eggs and larvae advection simulations are presented. Details of the different observing platforms and datasets used are summarized in Table 7.1.

Table 7.1. *Summary of the observing platforms and datasets used. LP means low pass filtered.*

	Data reconstruction (ROOI)	**ROOI validation**	**Advection simulations**
HFR	Input observations (hourly 24h LP)	Test data (hourly (HFRtot) / hourly 24h LP (HFR))	Forcing (hourly (HFRtot))
Donostia ADCP	Input observations (hourly 24h LP)	-	-
Matxitxako ADCP	-	Benchmark data (hourly / hourly 24h LP)	-
IBI reanalysis	Input covariances (daily)	Test data (daily)	-
ROOI data	Output data (hourly 24h LP)	Test data (hourly 24h LP)	Forcing (hourly 24h LP)
Drifter	-	Benchmark data (hourly)	-
BIOMAN	-	-	Egg abundance (initial distribution)

2.1 HFR and ADCP data

HFR and ADCP data correspond to the Basque Operational Oceanography System (EuskOOS, https://www.euskoos.eus/en/) that continuously monitors the study area (Figure 7.1). The HFR system is composed of two sites, one in Cape Higher and another one in Cape Matxitxako and works at a central frequency of 4.46 MHz with an operational bandwidth of 30 kHz. It provides hourly surface current velocity fields grided onto a regular orthogonal mesh of 5 km resolution covering ~150 km off the coast. This system has provided data since 2009 with some interruptions mostly due to severe atmospheric conditions and its validity to study coastal processes and transport patterns have been widely demonstrated (e.g., Rubio et al., 2011, 2018; Solabarrieta et al., 2014, 2015, 2016).

Within EuskOOS, two ADCPs co-located at Donostia and Matxitxako moorings working at a central frequency of 150 kHz provided hourly current velocity data from −12.26 m extending down 200 m in the water column with bins every 8 meters from 2007 to 2013. From 2013 on only Donostia mooring has provided data. The performance of these ADCPs have been demonstrated in several works (e.g., Rubio et al., 2013a; Solabarrieta et al., 2016, 2014).

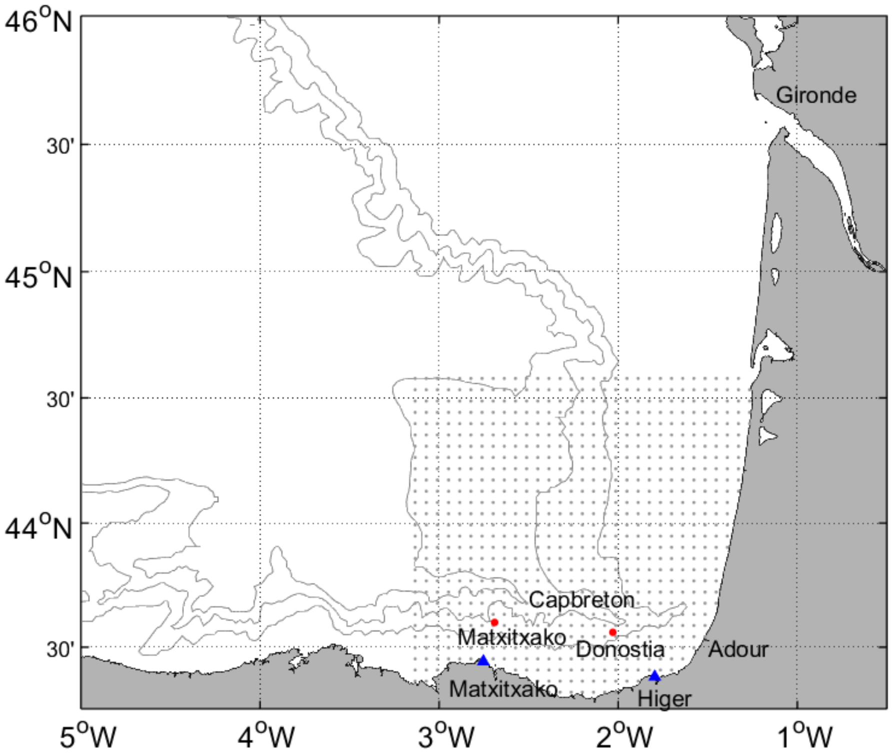

Figure 7.1. *Location of the HFR antennas (blue triangles), the HFR grid points (grey points) that cover the study area and the location of the moorings (red points). Capbreton canyon, and Gironde and Adour rivers are also depicted. The grey lines show the 200, 1000 and 2000 m isobaths.*

In this study, HFR and Donostia ADCP data were used as input observations for the 3D reconstructions by the ROOI method. In addition, HFR and Matxitxako ADCP data were used in the ROOI validation exercises as test dataset and benchmark data, respectively. HFR data were also used as forcing data in the eggs and larvae advection simulations.

The HFR data were spatially gap-filled since spatiotemporal continuity in the current fields is a prerequisite to perform accurate Lagrangian simulations. The data-gap filling was carried out by the open-mode analysis (OMA) method (Kaplan and Lekien, 2007). To that end, 85 OMA modes, built setting a minimum spatial scale of 20 km, were used. HFR data were quality controlled using procedures based on velocity and variance thresholds, signal-to-noise ratios, and radial total coverage, following standard recommendations (Mantovani et al., 2020). The used ADCP data ranged from surface until −100 m and were quality controlled by beam amplitude and correlation magnitudes and velocity errors following Bender and DiMarco (2009).

2.2 IBI data

The IBI_REANALYSIS_PHYS_005_002 product data (hereinafter IBI reanalysis) provided by Copernicus Marine Environment Monitoring Service (CMEMS) were used as historical data to estimate the covariance matrix needed for the 3D reconstruction by the ROOI method. Additionally, the data were used in the ROOI validation exercise as test dataset (along with ROOI and HFR data). The IBI reanalysis is based on a realistic configuration of the NEMO model for the Iberian Biscay Irish region and assimilates in situ and satellite data. For more information, the reader is referred to Manso-Narvarte et al. (2020; Table 1) and a complete description of the product and its validation can be found in Sotillo et al. (2015) and the following links: http://cmems-resources.cls.fr/documents/PUM/CMEMS-IBI-PUM-005-002.pdf and http://resources.marine.copernicus.eu/documents/QUID/CMEMS-IBI-QUID-005-002.

IBI reanalysis provides daily data with unevenly distributed vertical levels with separations between 1−3 m in the first meters and an increasing separation with depth. Regarding the horizontal resolution, it has a resolution of 0.083º x 0.083º (~6-9 km).

2.3 Drifter data

The data (trajectories in longitude and latitude) from 3 drifters (Figure 7.2) were used in the ROOI validation exercises as benchmark against the simulated advection. The trajectories were quality controlled by velocity thresholds and visual inspection of the positions. One of them (drifter-1) was operated by the SHOM (Service Hydrographique et Océanographique de la Marine, France), whereas the other two (drifter-2 and drifter-3) corresponded to a set of campaigns run in the Bay of Biscay (Charria et al., 2013).

The drifters were linked to a holey sock drogue centred at −15 m and their positions were hourly transmitted by the ARGOS localization system.

2.4 BIOMAN data

As stated before, BIOMAN is an oceanographic survey run in the Bay of Biscay every year around May, with the aim of evaluating the anchovy population at the end of spring. Several samples are collected along 15 nautical miles (nmi)-separated transects (7.5 nmi in areas of high abundance) perpendicular to the coast (see Figure 7.4). Among other parameters, anchovy egg abundances are estimated, which were used in this study to set the initial particle distribution in the eggs and larvae advection simulations.

Anchovy eggs are sampled by means of two systems. On the one hand, the Continuous Underway Fish Egg Sampler (CUFES; Checkley, 1997) pumps the water at −3 m onboard and record the eggs with a net of 350 μm mesh size. Then, samples are immediately checked thus providing real-time estimations of the volumetric abundance each 1.5 mi. On the other hand, vertical hauls are made every 3 nmi (6 nmi when eggs are absent) along the survey transects using a PairoVET net (i.e., 2-CalVET nets; Smith et al., 1985) with a 150 μm mesh. After lowering the net until −100 m, it is lifted back and anchovy eggs are sorted, identified and counted onboard. Note that the CUFES samples represent the egg abundances at −3 m, whereas PairoVET samples integrate the upper 100 m of the water column. In the water column, eggs are mainly located in the upper 30 m (e.g., Palomera, 1991; Boyra et al., 2003) with a higher abundance in the shallowest depths as the mean profiles shown in Figure 4b in Boyra et al. (2003) depict. Based on those distributions, here the PairoVET samples are allocated at −10 m.

3 Methods

In this section, the implementation of the ROOI method to 3D reconstruct current velocity fields is first explained. Then, the Lagrangian model used to simulate the advection of particles is presented. Thereafter, two validation exercises are shown to further validate the ROOI data (from a Eulerian and a Lagrangian approach, respectively). Finally, the setting up of the anchovy eggs and larvae advection simulations is depicted.

Note that IBI reanalysis and ROOI data had a daily variability, whereas the HFR, ADCP and drifter data had hourly variability. For carrying out the reconstructions, HFR and ADCP observations were 24 hours low-pass filtered (LP) in order to agree with the variability of the covariances obtained from IBI reanalysis needed for the reconstructions. In the ROOI validation exercises, HFR data were tested with both hourly (i.e., non-filtered, hereinafter HFRtot) and daily (i.e., 24h LP, hereinafter simply HFR) variability to compare them at the same variability level as other datasets and at its highest possible variability level, respectively. The Matxitxako ADCP data used as benchmark in the mentioned exercises were adapted to the resolution of the dataset to be validated (i.e., hourly against HFRtot data and daily against IBI reanalysis, ROOI and HFR data). The drifter hourly location data were not modified.

3.1 Implementation of the ROOI method

In order to reconstruct 3D current velocity fields from multiplatform data, the ROOI method was used. Its feasibility was previously tested in the study area in Manso-Narvarte et al. (2020) obtaining mean spatial reconstruction errors between 0.55 and 7 cm s^{-1} and mean relative errors of 0.07–1.2 times the root mean square value for the first 150 m depth. Additionally, in Manso-Narvarte et al. (2021) it was used to reconstruct 3D eddy current velocity fields concluding that although further validations would be valuable, it is a compelling method to reconstruct these kinds of processes. This method was first used by Kaplan et al. (1997) and it is based on Empirical Orthogonal Function (EOF) decomposition. Historical data of the grid points where we want to make the reconstructions and of the points where we have the available observations are needed, usually extracted from a model, to set the spatial covariances between all those points. Then an EOF decomposition is applied to that covariance matrix and only the N leading modes are kept (ignoring high order modes). The reconstructed fields are obtained extending the available observations to all the grid points based on those modes and by minimizing the deviation between the reconstructions and observations. For a more complete description of the method see Kaplan et al. (1997), Jordà et al. (2016) or Manso-Narvarte et al. (2021).

ROOI data were obtained from HFR and Donostia ADCP current velocity observations while the covariances were obtained from the 1992−2016 historical data of IBI reanalysis. Since the covariances had a daily variability, the hourly HFR and ADCP observations were adapted (24h LP) providing hourly ROOI data with a daily variability and with the same spatial resolution as IBI reanalysis in the upper 100 m of the water column.

The tunning parameters of the method were the N number of modes and the observational error. For all the reconstructions herein presented, the number of modes selected was N=100 and the observational error of the current velocities 2 cm s^{-1}. This configuration led to reasonable results in Manso-Narvarte et al. (2021) and the tests carried out against Matxitxako ADCP data showed that it was still a good option (see *Appendix C1*). Note that, as in Manso-Narvarte et al. (2021), the sensitivity of the reconstructions to the selected observational error parameters is small as long as reasonable values are selected.

3.2 The Lagrangian model

In order to simulate the advection of anchovy eggs and larvae as passive particles the MOHID ("MOdelo HIDdrodinamico") modelling system (Neves, 2013) was used. More precisely, the Lagrangian module (Leitão, 1996) of the MOHID Water tool. This module was previously used in Declerck et al., (2019) to simulate trajectories at the surface in the study area, providing satisfactory results.

In our case, the spatial resolution of the simulation grid was set to 2.25 x 3.1 km, covering the same area in all the simulations presented hereinafter. At the coastal boundaries (south and east) a particle slip condition was set, thus avoiding the removal of particles (i.e., the particles return to the domain when they reach the coast); whereas, at the two open boundaries (north and west) particles were allowed to leave the domain. The slip condition was set since the available forcing data do not have enough resolution nor coverage in the coastal area to properly parametrize the complex hydrodynamics there. The used integration scheme was based upon an explicit Euler scheme.

The value of the diffusion coefficient (D) varies depending on the spatial resolution of the forcing data. Several sensitivity tests on the performance of the Lagrangian simulations are shown in *Appendix C2* comparing the results obtained with different current velocity forcings and depths. Moreover, different forcings were also tested in the ROOI validation exercises from a Lagrangian perspective (in the next section). Although the used forcings have different spatial resolutions, the same $D = 4\ \mathrm{m}^2\ \mathrm{s}^{-1}$ value was considered for all the simulations in order to compare the results. This value was the mean diffusion corresponding to all the different forcings, estimated based on Okubo (1971). This value was kept in the eggs and larvae advection simulations.

3.3 ROOI validation

Although in Manso-Narvarte et al. (2020, 2021) the ROOI demonstrated to be a compelling method to reconstruct current velocity fields, further validations with additional data sources were carried out in this study. In this section, those validations are shown. ROOI data were compared with Matxitxako ADCP observations (Eulerian validation) and used as forcing to simulate the trajectories of 3 drifters at −15 m (Lagrangian validation). In addition, in order to assess the performance of ROOI data against other datasets, IBI reanalysis, HFR and HFRtot data were also compared with Matxitxako ADCP and drifter observations.

Concerning the comparison with the Matxitxako ADCP observations, IBI reanalysis and ROOI data were interpolated to the ADCP observation points in the water column from −12.26 to −100.26 m depth. In the case of the HFR, data were interpolated to the Matxitxako mooring location at the surface. 11,211 timesteps were considered, when Matxitxako ADCP, ROOI, HFR and IBI reanalysis data were available at once from 2009 to 2013. The metrics used to compare the results were, for each velocity component, the root mean square difference (RMSD), the relative RSMD (RRMSD) normalized with the root mean square (RMS) of the observations and the temporal correlations (with a confidence level of 99%).

Table 7.2. *RMSD (in cm s^{-1}), RRMSD and correlations between the Matxitxako ADCP observations and IBI reanalysis, ROOI, HFR and HFRtot data for both current components. HFRtot denotes the original non-filtered HFR data. General values are shown as well as values for different depths. Note that in the case of the HFR, comparisons are carried out between the surface and the water column.*

	RMSD				**RRMSD**				**CORRELATION**			
	IBI		**ROOI**		**IBI**		**ROOI**		**IBI**		**ROOI**	
	U	**V**	**U**	**V**	**U**	**V**	**U**	**V**	**U**	**V**	**U**	**V**
General	7.70	5.10	6.81	4.49	0.74	1.04	0.65	0.91	0.69	0.02	0.75	0.37
-12.26 m	9.15	6.35	7.37	5.57	0.93	1.04	0.75	0.91	0.58	0.09	0.64	0.43
-20.26 m	8.86	6.27	7.12	5.35	0.89	1.06	0.71	0.90	0.59	NaN	0.68	0.42
-28.26 m	8.25	5.85	6.86	5.02	0.81	1.05	0.68	0.90	0.64	NaN	0.72	0.42
-36.26 m	7.73	5.35	6.62	4.62	0.75	1.05	0.65	0.91	0.68	-0.02	0.75	0.41
-44.26 m	7.50	5.06	6.52	4.49	0.72	1.06	0.62	0.94	0.71	-0.03	0.77	0.36
-52.26 m	7.41	4.85	6.52	4.38	0.70	1.05	0.61	0.95	0.72	NaN	0.78	0.32
-60.26 m	7.29	4.64	6.53	4.28	0.68	1.03	0.61	0.95	0.73	0.02	0.78	0.30
-68.26 m	7.25	4.59	6.60	4.23	0.68	1.03	0.62	0.95	0.74	0.02	0.78	0.30
-76.26 m	7.24	4.50	6.61	4.12	0.69	1.03	0.63	0.94	0.73	NaN	0.77	0.31
-84.26 m	7.16	4.43	6.63	4.08	0.68	1.02	0.63	0.94	0.73	NaN	0.77	0.30
-92.26 m	7.13	4.41	6.70	4.08	0.68	1.01	0.64	0.94	0.73	0.02	0.77	0.30
-100.26 m	7.09	4.36	6.75	4.02	0.68	1.01	0.65	0.93	0.73	NaN	0.76	0.31
	HFR		**HFRtot**		**HFR**		**HFRtot**		**HFR**		**HFRtot**	
	U	**V**	**U**	**V**	**U**	**V**	**U**	**V**	**U**	**V**	**U**	**V**
General	8.62	6.89	13.08	12.18	0.83	1.40	1.05	1.55	0.57	0.20	0.4	0.11
-12.26 m	8.23	7.06	11.98	10.84	0.84	1.15	0.96	1.13	0.57	0.34	0.50	0.42
-20.26 m	8.33	7.24	12.49	11.71	0.83	1.22	0.99	1.28	0.57	0.28	0.45	0.28
-28.26 m	8.36	7.13	12.97	12.28	0.82	1.28	1.03	1.40	0.58	0.25	0.41	0.17
-36.26 m	8.41	6.90	13.30	12.52	0.82	1.36	1.06	1.51	0.58	0.23	0.38	0.09
-44.26 m	8.53	6.83	13.35	12.62	0.81	1.43	1.06	1.61	0.58	0.20	0.38	0.03
-52.26 m	8.68	6.86	13.31	12.56	0.82	1.48	1.06	1.66	0.58	0.16	0.38	NaN
-60.26 m	8.69	6.82	13.24	12.43	0.82	1.52	1.06	1.69	0.58	0.16	0.38	NaN
-68.26 m	8.81	6.86	13.28	12.38	0.82	1.53	1.06	1.70	0.58	0.14	0.38	NaN
-76.26 m	8.83	6.78	13.26	12.25	0.84	1.55	1.08	1.73	0.57	0.15	0.38	0.02
-84.26 m	8.82	6.74	13.19	12.21	0.84	1.55	1.08	1.73	0.56	0.16	0.38	0.02
-92.26 m	8.88	6.75	13.24	12.19	0.84	1.55	1.08	1.73	0.56	0.16	0.38	0.03
-100.26 m	8.89	6.72	13.23	12.11	0.85	1.56	1.09	1.74	0.56	0.16	0.37	0.03

The results (Table 7.2) show lower RMDSs for V than for U since the Matxitxako mooring is located in the area of the slope current, where the zonal component is more intense and persistent. Indeed, RRMSD values are lower and correlation values higher for U, showing that the zonal component is better represented by all the datasets. The lowest RMSD and RRMSD values and the highest correlations are obtained with ROOI data probably because the surface observations of the HFR were robustly expanded in the water column since the covariances from IBI reanalysis reproduce well the slope current. On the other hand, HFR data provide better results than IBI reanalysis in the first 20 meters for U, whereas, for V, IBI reanalysis provides lower RMSD and RRMSD values, despite the almost null correlations. The comparison between ADCP and HFRtot data (of hourly variability) show the highest RMSD and RRMSD values due to the higher variability of the data that leads to bigger discrepancies. Regarding correlations, the lowest values comparing with other (daily variability) datasets are observed for U, whereas for V, at −12.26 m, correlations are similar to those with ROOI and values sharply decrease in deeper levels.

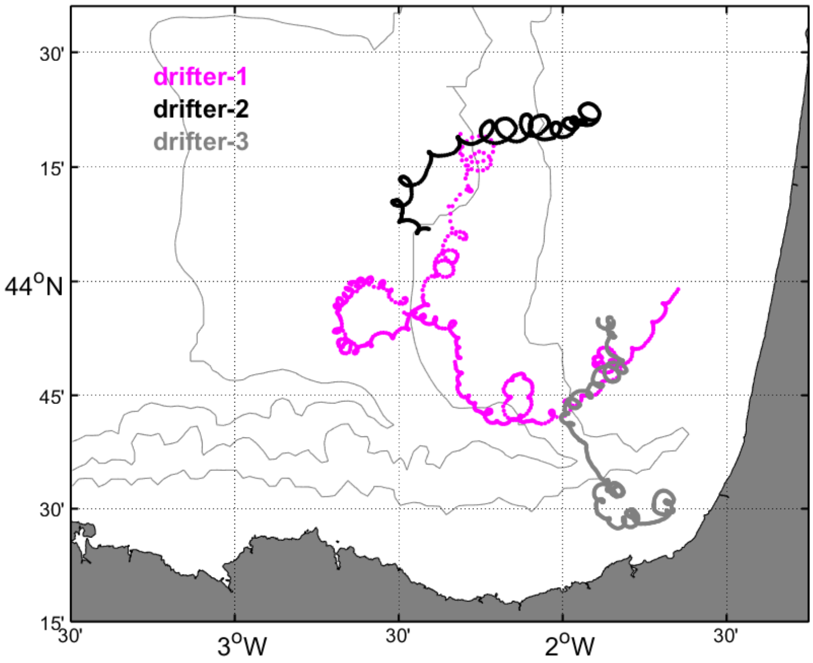

Figure 7.2. *Drifter trajectories: drifter-1, drifter-2 and drifter-3 are depicted by magenta, black and grey points, respectively. The light grey lines show the 200, 1000 and 2000 m isobaths.*

For the comparison between simulated and observed drifter trajectories, numerical particles were launched every day at the position of the drifters and advected for 6 days. The observed and simulated trajectories were compared by estimating the mean distance between them as a function of the duration of the simulation. In addition, the normalized distances (normalized by the total distance travelled by the drifter) were also estimated. The dates for the simulations were selected when drifter, ROOI, HFR and IBI reanalysis data were available at once. The considered periods range from 2011-09-23 to 2011-10-28 for drifter-1, from 2009-07-21 to 2009-07-31 for drifter-2, and from 2009-09-25 to 2009-10-14 for drifter-3. The drifters travelled around the French shelf and open ocean, where the current variability is in general higher and does not present persistent current patterns as the ones observed at Matxitxako mooring (Figure 7.2).

The results show that at −15 m HFR(tot) data provide the lowest mean distance with respect to the drifters with values around 10 and 20 km after two and six days, respectively (Figure 7.3a). Note that both HFR and HFRtot datasets provide similar results. ROOI data, which were fed with

HFR observations, show lower mean distances (11 and 27 km after two and six days) than IBI reanalysis (16 and 41 km after two and six days). Similar values to the observed distances with HFR(tot) and ROOI data after 2 days were detected in the study area in Rubio et al. (2013b) and Solabarrieta et al. (2016), where the trajectories of drifters were compared with the ones simulated with the HFR. Moreover, Declerck et al. (2019) also analysed the trajectories simulated with HFR-derived data, obtaining similar mean normalized distances to the ones obtained here (Figure 7.3b).

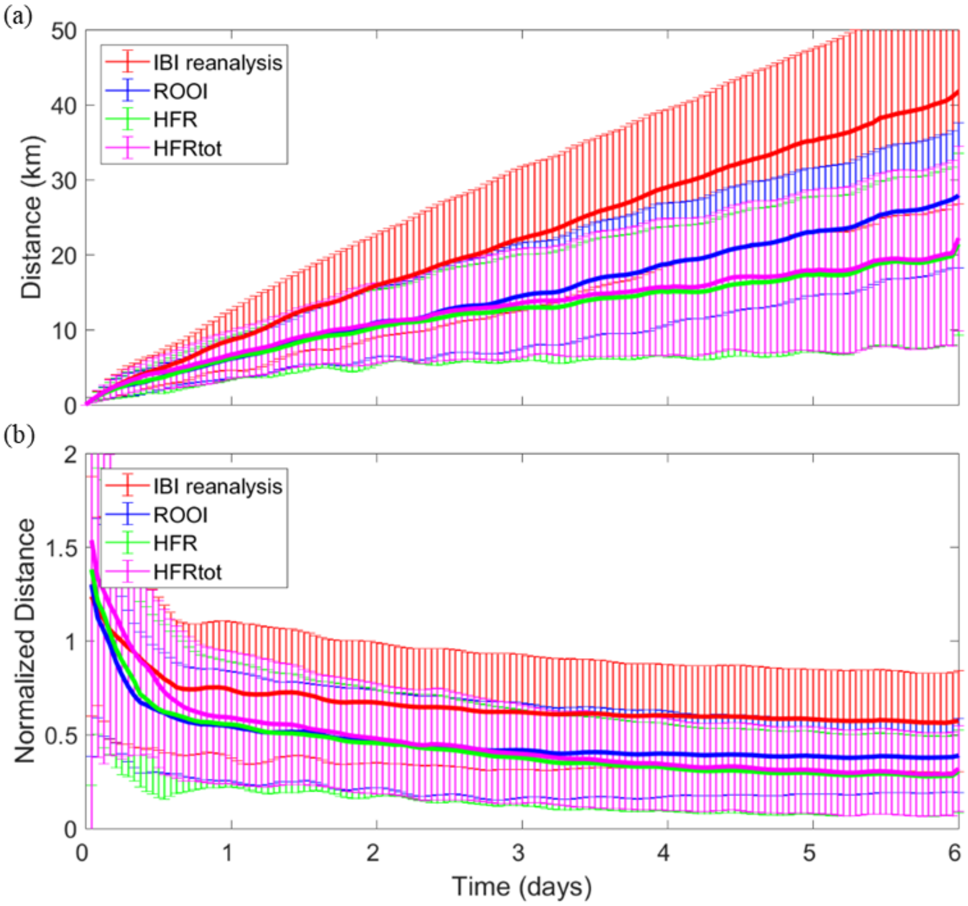

Figure 7.3. *(a) Mean distance in function of time between real drifter trajectories and simulated trajectories using IBI reanalysis, ROOI, HFR and HFRtot data. HFRtot denotes the original non-filtered total HFR data. (b) The same for the distance normalized by the distance travelled by the real drifter. The vertical error bars depict the standard deviation.*

In conclusion, it is observed that the slope current is well represented along the Spanish slope, where the ROOI provides the best characterization from surface to −100 m. Despite the small time coverage of the Lagrangian validation, at −15 m in the areas covered by the 3 drifters, the HFR(tot) provides the best characterization of the dynamics from a Lagrangian point of view, while ROOI data provide the closest results to the HFR(tot) (this similarity was also observed in some sensitivity tests shown in *Appendix C2*). Hence, here, the ROOI is further validated and still arises as a compelling method for the 3D hydrodynamic characterization of the study area. In general, the HFR(tot) also seems a good option for reproducing the hydrodynamics at the shallowest depths. In the anchovy eggs and larvae advection simulations, HFRtot and ROOI data were used as forcing data; however, it is worth mentioning that these kinds of simulations are quite sensitive to the used forcing and depth (see sensitivity tests in *Appendix C2*).

3.4 Eggs and larvae advection simulations

Simulations of the advection of anchovy eggs and larvae were carried out for seven periods corresponding to the BIOMAN surveys of 2011, 2012, 2013, 2014, 2016, 2017 and 2018. Note that 2015 was not included due to the lack of available forcing data. Each simulation started from a scenario where 10,000 particles were released, distributed according to the egg abundance data obtained during the surveys at −3 m (from the CUFES system) and at −10 m (from the PairoVET system) for each year. In Figure 7.4 examples are shown for 2011 and 2013, however, the initial conditions of each simulation are displayed in panels b, h, n, t in Figures 7.5 and 7.7, and in panels b, n, h in Figure 7.8. The starting dates were set as the mean date of the observations (covering periods of 3 days), which are: 10-05-2011, 13-05-2012, 13-05-2013, 08-05-2014, 09-05-2016, 09-05-2017 and 13-05-2018. Trajectories were simulated 3 days backwards, which is the maximum time needed by the eggs to hatch (Frimodt, 1995), and 30 days forward, which is approximately the time needed by the larvae to metamorphose and gain significant swimming abilities (i.e., becoming non-passive particles; Irigoien et al., 2008). Herein, when showing and discussing the results of the forward simulations we will refer to the simulated particles as larvae since eggs will quickly metamorphose, whereas in the backward simulations we will call them eggs.

Two forcing datasets were used in the simulations: the HFRtot data and the ROOI data. HFRtot data were used instead of the filtered ones (i.e., HFR) since they provide a higher (more realistic) variability and provided similar results in the Lagrangian validation in *Section 3.3*. Simulations forced by HFRtot data were run for all the above-mentioned years, and since the depth integration range of the HFR is around 1.5 m, the initial egg distributions were retrieved from CUFES at −3 m. The ROOI data availability depends on the simultaneous HFR and ADCP data availability, being scarce to cover the forward 30 days of the simulations except for 2011 and 2013. Therefore, such years were simulated forced with ROOI at −3 m with the initial egg distributions from CUFES, and at −10 m with initial distributions from PairoVET.

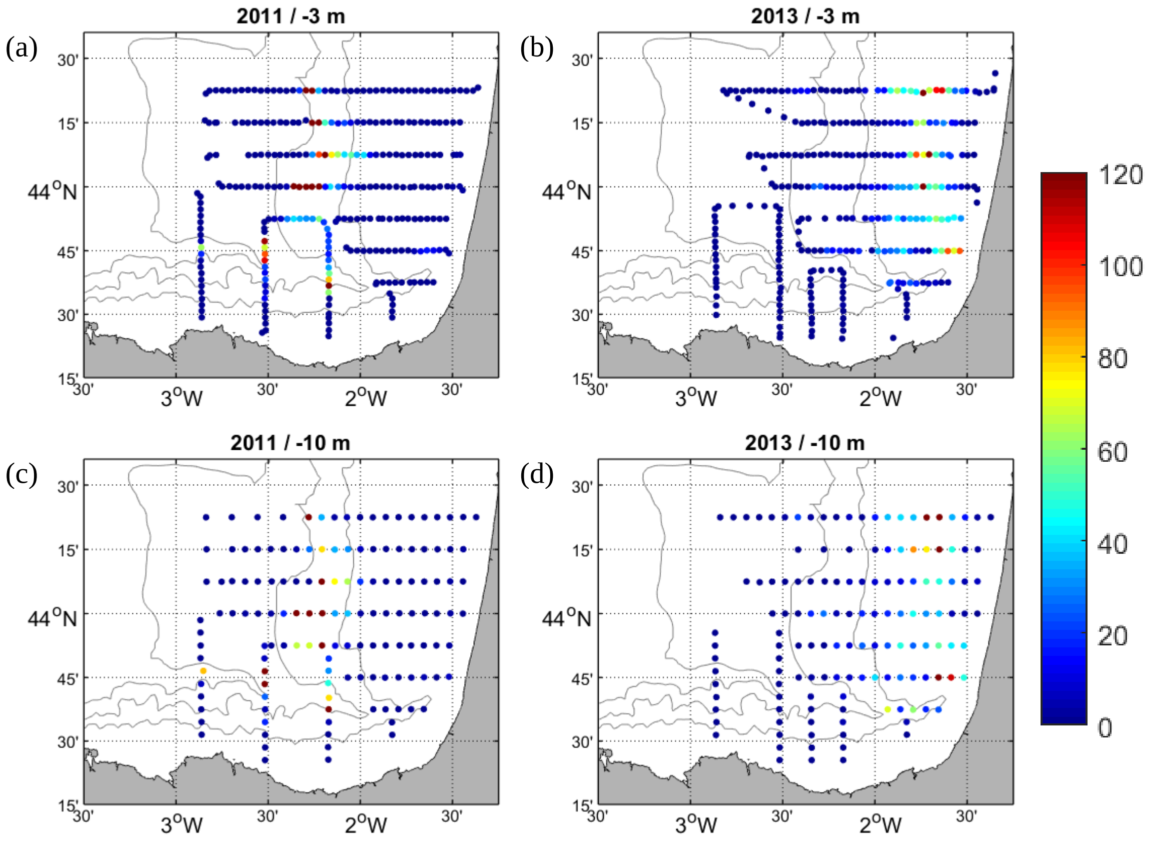

__Figure 7.4.__ Distribution of the 10.000 particles according to observations of the CUFES system at −3 (a, b) and of the PairoVET system at −10 m (c, d). (a) and (c) correspond to the period centred on 10-05-2011, whereas (b) and (d) correspond to the period centred on 13-05-2013. The colorbar depicts the number of particles and the grey lines show the 200, 1000 and 2000 m isobaths.

4 Results

In the next subsections, the results of the simulations forced with ROOI are first presented, then the simulations forced with HFRtot, and finally, the results are discussed.

4.1 Simulations with ROOI

Based on the observed egg distributions, in the simulations eggs are initially located mainly over the French slope in 2011, whereas in 2013 they are located over the French shelf. The backtracking shows that in 2011 eggs move northward in the first 3 days, whereas in 2013 they almost do not move (Figures 7.5a,b, 7.5g,h, 7.5m,n, 7.5s,t and 7.6).

Concerning the fate of the larvae, in 2011, from 3 days of advection on, larvae first move southwestward at −3 m and then southeastwards in the last 10 days (Figures 7.5b-f and 7.6a). At −10 m larvae gradually travel from the French slope to the shelf with a southward advection in the last 10 days (Figures 7.5h-l and 7.6b). Concerning the comparison between the results at −3 and −10 m, it is observed that after 3 days of simulation distributions start to differ. After 30 days the distributions have a slightly similar form but overall are different with larvae located over the French shelf, closer to the coast, at −10 m.

In 2013, larvae mainly remain over the French shelf at −3 and −10 m, although some of them are advected to the slope. Similar patterns are observed in the first 20 days, however, in the last 10 days at −3 m larvae start to drift towards the northwest getting away from the study area, whereas at −10 m they still remain over the shelf (Figures 7.5n-r,t-x). For both analysed years, the centres of mass do not get further west than the French slope from the coast (Figure 7.6).

The percentages of the particles that leave the domain in each simulation are shown in Table 7.3. However, how eggs and larvae leave the domain is not shown for practical reasons since a huge number of snapshots per simulation would be needed. In 2011, a significant number of particles (35.5 % and 40.3 % at −3 and −10 m, respectively) leave the domain mostly through the northwestern boundary, before larvae drift southwestwards. Conversely, in 2013 larvae are far more retained with domain-leaving rates of 10.4 and 0 % at −3 and −10 m, respectively.

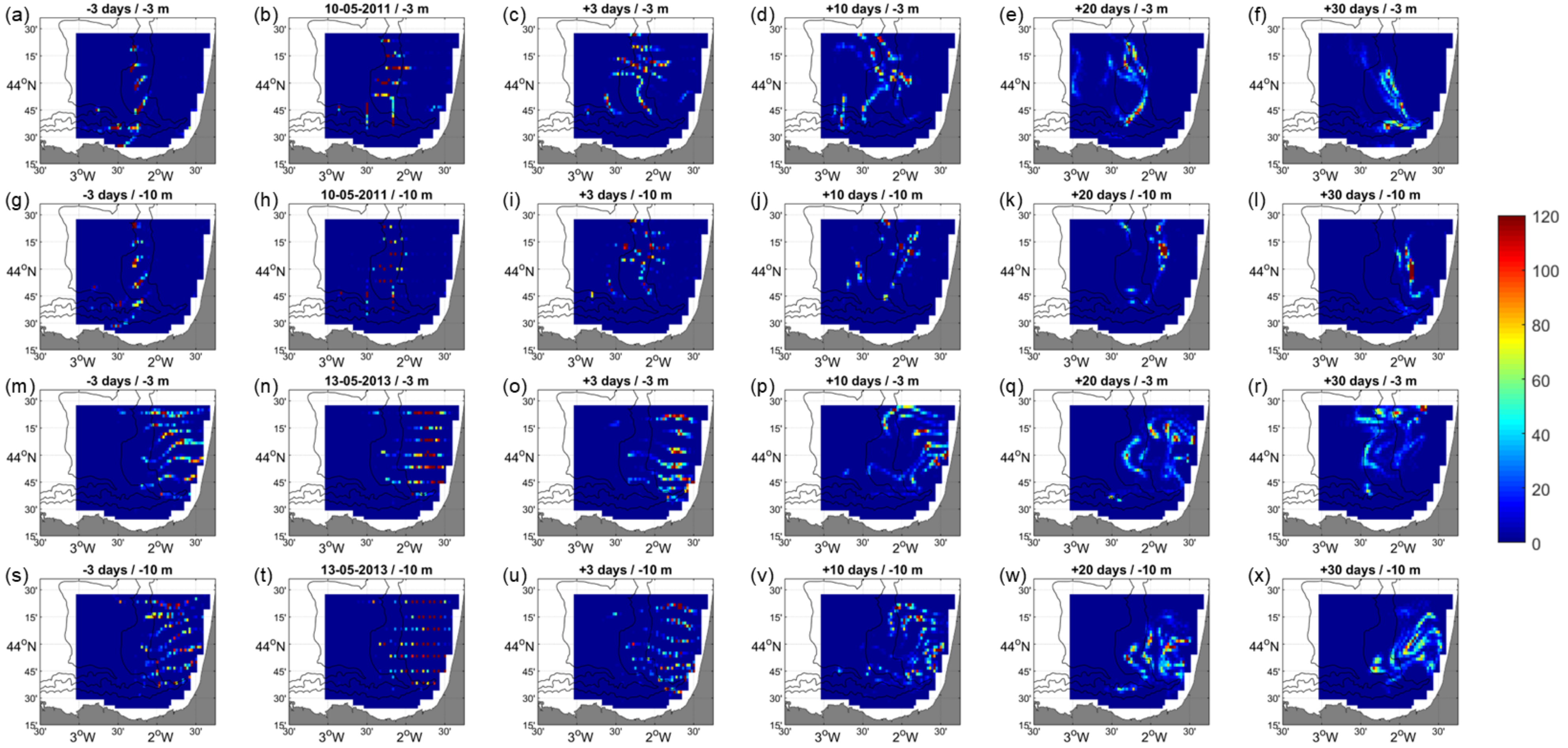

Figure 7.5. *Simulated particle density maps starting from 10-05-2011 (a-l) and 13-05-2013 (m-x) forced with ROOI at −3 and −10 m. −3 days means 3 days backwards and +3, +10, +20 and +30 days mean 3, 10, 20 and 30 days forwards, respectively. The colorbar depicts the number of particles. The grey lines show the 200, 1000 and 2000 m isobaths.*

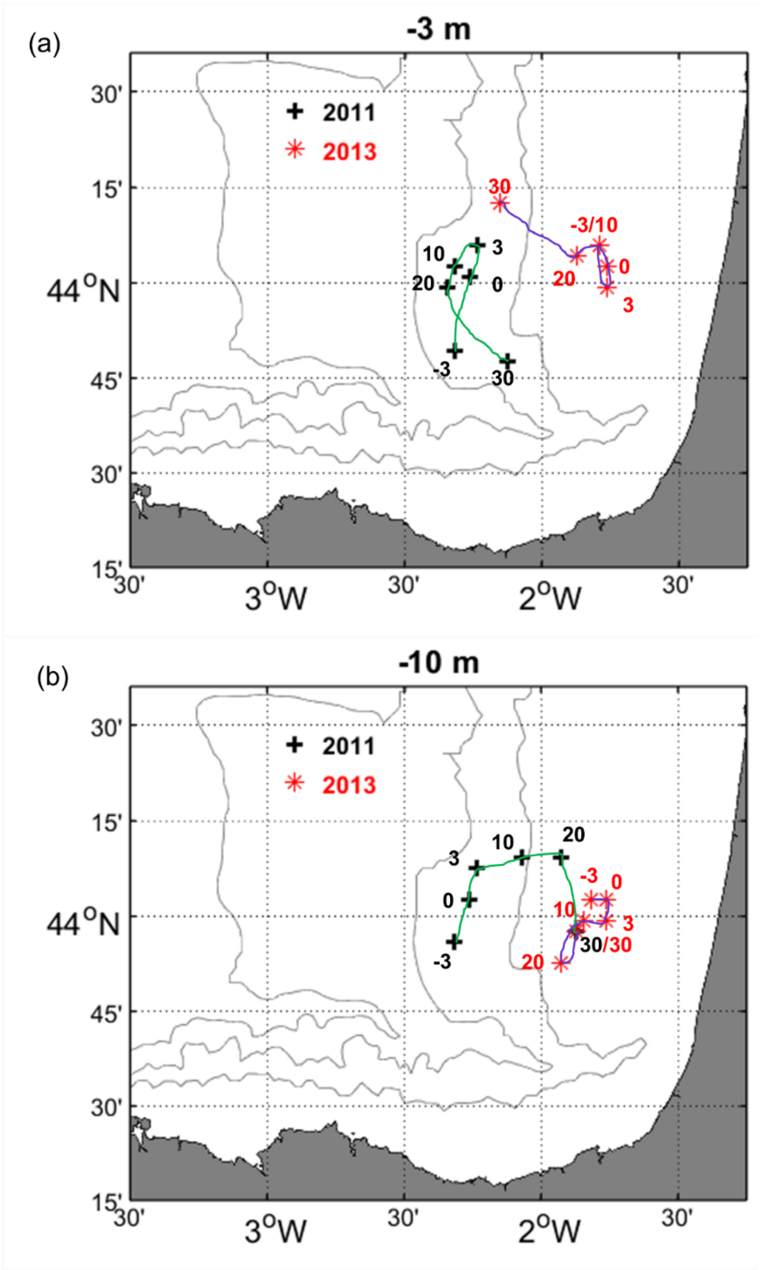

***Figure 7.6**. Location of the centres of mass at −3 (a) and −10 m (b) for 2011 (black crosses) and 2013 (red asterisks), corresponding to simulations forced with ROOI. −3 days means 3 days backwards and +3, +10, +20 and +30 days mean 3, 10, 20 and 30 days forwards, respectively. The green and purple lines show the trajectory of the centres of mass in 2011 and 2013, respectively. The grey lines show the 200, 1000 and 2000 m isobaths.*

***Table 7.3.** Percentage of the particles that leave the domain during the simulations.*

	−3 m	**−10 m**
2011	35.5 %	40.33 %
2013	10.4 %	0 %

4.2 Simulations with HFRtot

The initial distribution in 2011 and 2013 is the same as in the simulations forced with ROOI data, with eggs mainly located on the French slope and shelf, respectively. As in 2013, in 2012, 2014, 2014, 2017 and 2018 eggs are located over the French shelf. In 2016 and 2017 eggs are additionally located over the Spanish slope and also off the shelf in 2017.

The 3-day backtracking in 2011, 2012, 2016 and 2017 shows that eggs move northward (Figures 7.7a,b, 7.7g,h, 7.8a,b, 7.8g,h and 7.9), whereas for the rest of the years, eggs almost do not move in 3 days (Figures 7.7m,n, 7.7s,t, 7.8m,n and 7.9).

Concerning the 30-day forward simulations, in 2011 and 2013 similar results to the simulations at −3 m forced with ROOI are obtained. In 2011 larvae first travel southwestwards, where most of the larvae that leave the simulation get out of the domain (almost 30.3 % of the larvae) through the southwestern boundary. Then, larvae are advected southeastwards in the last 10 days (Figures 7.7b-f and 7.9). In 2013, larvae remain over the French shelf for the first 20 days, and then, travel northwestward in the last 10 days (Figures 7.7n-r and 7.9) losing 18.3 % of the larvae through the northern boundary. Comparing with the simulation forced with ROOI, in this case, larvae tend to gather much more.

In 2012 larvae gather and remain mainly over the French shelf and partially over the shelf-break and slope without travelling long distances (Figures 7.7h-l and 7.9). Indeed, few larvae get out of the domain for this period (2.2 %). In 2016 larvae also remain over the French shelf, however, they tend to drift southwards (Figures 7.8b-f and 7.9).

In 2014, although eggs are initially set over the French platform and the centre of mass remains there during the 30 days of simulation (Figure 7.9), part of the larvae are advected to the shelf-break and slope area and the other part towards the coast. Then larvae remain around those areas until the 30th day of the simulation (Figure 7.7t-x). The number of larvae that leave the domain is relatively low (9.7 %).

In 2017, the larvae that are set in the northern part of the domain are advected out of it after the third day of the simulation, losing a big percentage of the larvae that finally leave the domain and changing the position of the centre of mass to the south (Figure 7.9). The rest of the larvae tend to move slightly southwards but remaining around their initial area over the French shelf and the Spanish shelf and slope (Figures 7.8h-l and 7.9).

In 2018, the eggs initially set over the Spanish slope drift eastwards, whereas the eggs set over the French shelf drift southwestwards, ending up (as larvae) around the Spanish and French shelf-break and slope areas near the Capbreton canyon (Figure 7.8n-r and Figure 7.9). Eggs initially set at the northern part of the domain over the French shelf are advected off-shelf and get out of the domain through the northwestern boundary, losing 24.3 % of the larvae.

2011 and 2017 are the years when initially there are more eggs at the shelf-break, slope or even at off-shelf areas. After 30 days of simulation, these are the years with the highest percentages of larvae that leave the domain, that is, 30.3 and 35.5 %, respectively.

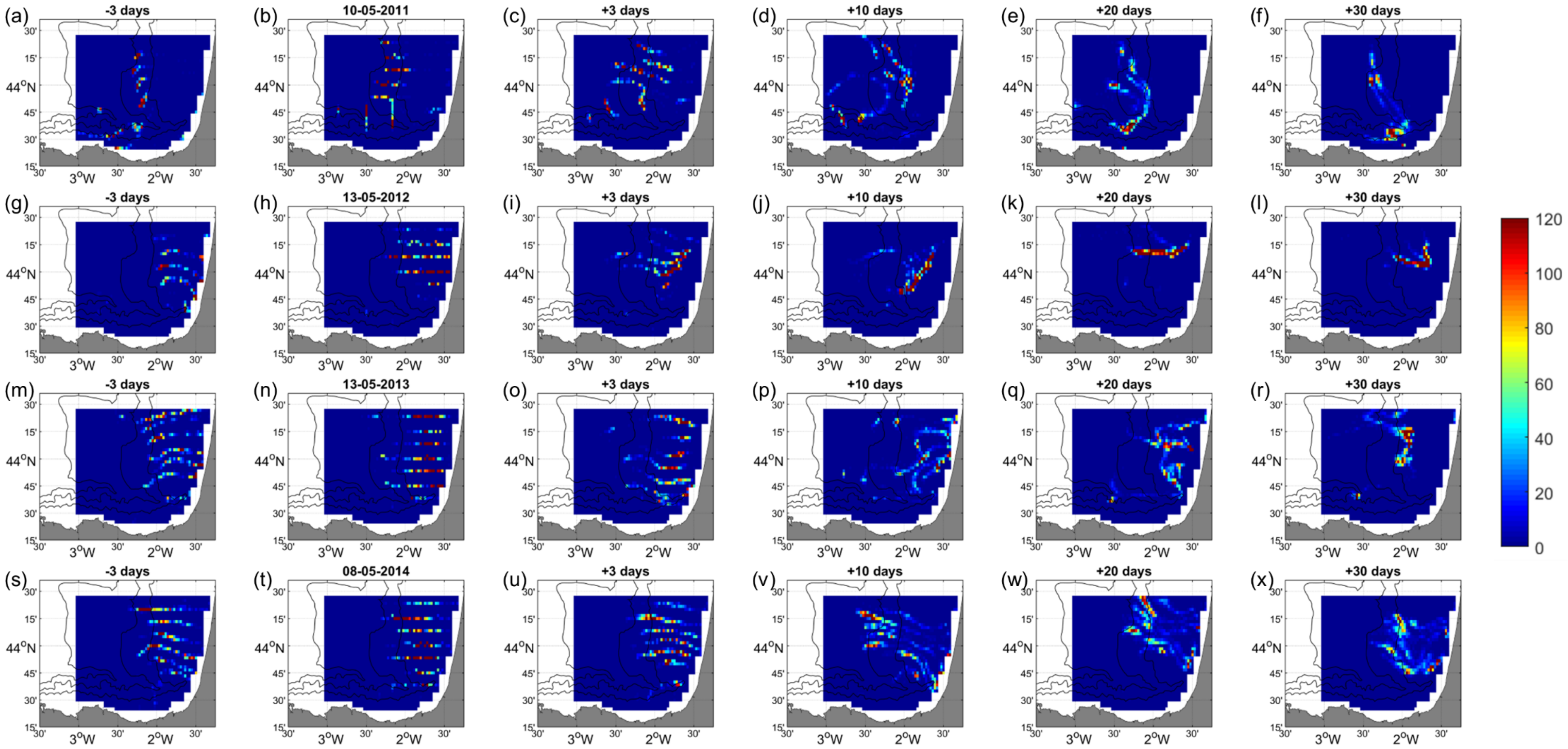

Figure 7.7. Simulated particle density maps starting from 10-05-2011 (a-f), 13-05-2012 (g-l), 13-05-2013 (m-r) and 08-05-2014 (s-x) forced with HFR data at −3 and −10 m. −3 days means 3 days backwards and +3, +10, +20 and +30 days mean 3, 10, 20 and 30 days forwards, respectively. The colorbar depicts the number of particles. The grey lines show the 200, 1000 and 2000 m isobaths.

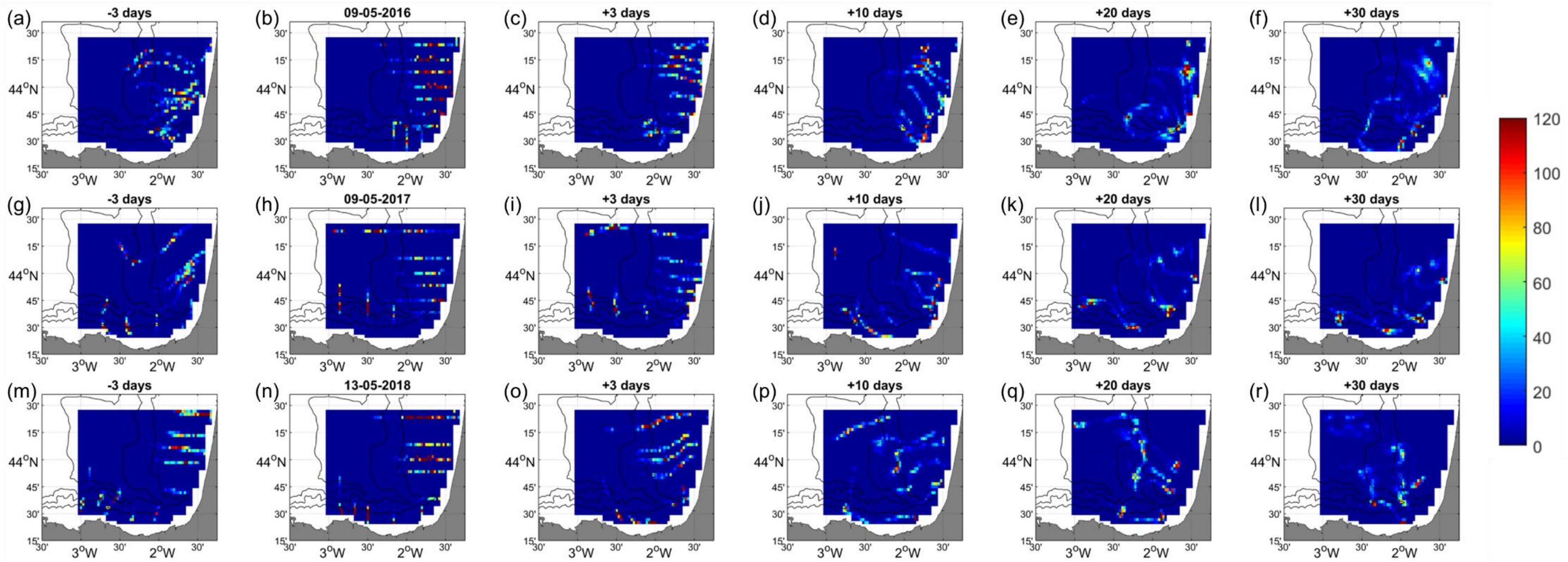

Figure 7.8. *Simulated particle density maps starting from 09-05-2016 (a-f), 09-05-2017 (g-l) and 13-05-2018 (m-r) forced with HFR data at −3 and −10 m. −3 days means 3 days backwards and +3, +10, +20 and +30 days mean 3, 10, 20 and 30 days forwards, respectively. The colorbar depicts the number of particles. The grey lines show the 200, 1000 and 2000 m isobaths.*

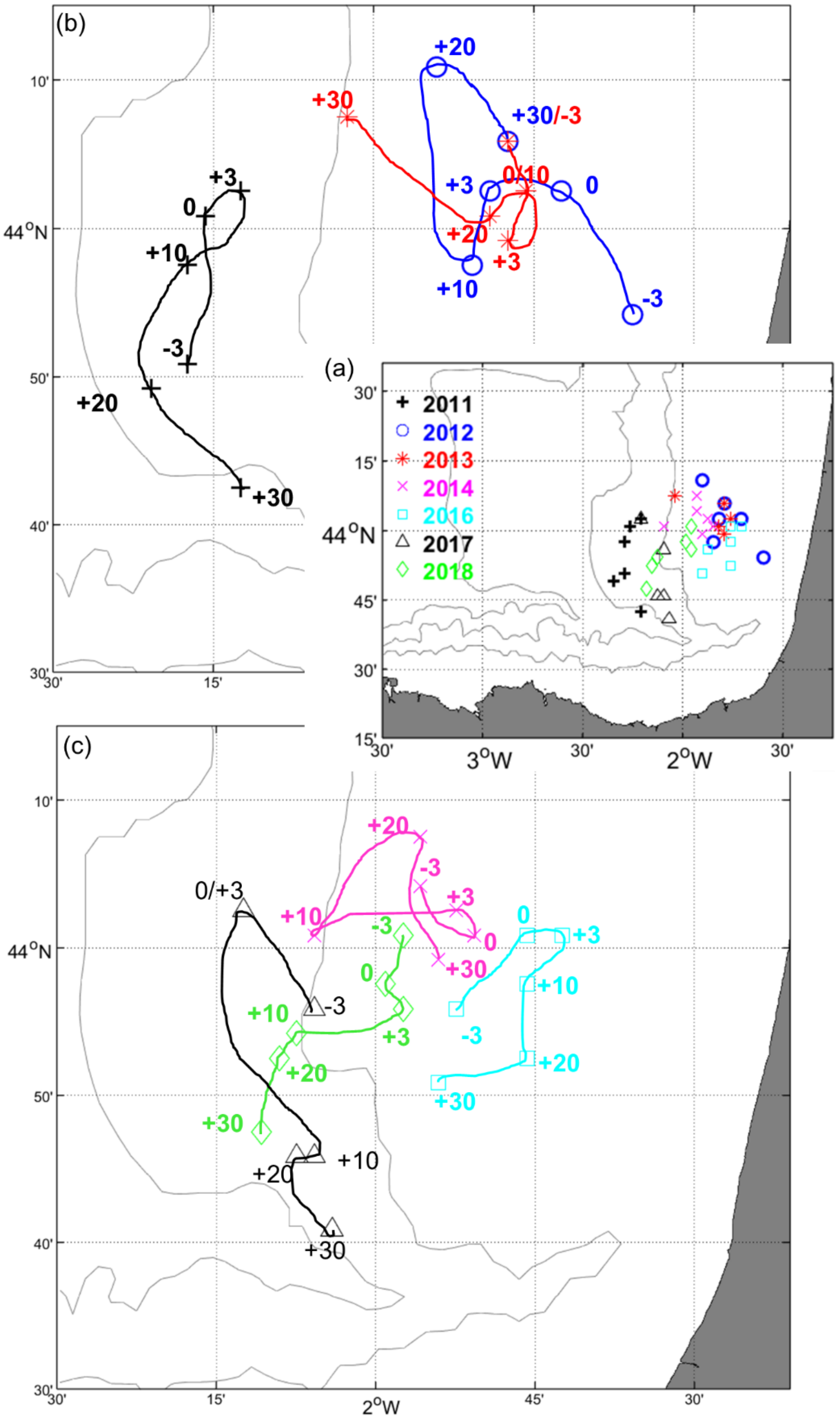

Figure 7.9. *(a) Location of the centre of mass at −3 m for different years, corresponding to simulations forced with HFR data. −3 days means 3 days backwards and +3, +10, +20 and +30 days mean 3, 10, 20 and 30 days forwards, respectively. The lines show the trajectory of the centres of mass. (b) zoomed for 2011, 2012 and 2013. (c) zoomed for 2014, 2016, 2017, 2018. The grey lines show the 200, 1000 and 2000 m isobaths.*

Table 7.4. *Percentage of the particles that leave the domain during the simulations.*

2011	2012	2013	2014	2016	2017	2018
30.3 %	2.2 %	18.3 %	9.7 %	14.6 %	35.5 %	24.3 %

4.3 Discussion

In this study, the origin and fate of anchovy eggs and larvae in the study area have been simulated using a Lagrangian model. Since anchovy eggs need around 1−3 days to hatch (Frimodt, 1995), the 3-day backtracking simulations suggest that in 2011, 2012, 2016 and 2017 eggs were potentially spawned at around 15 km south of the sampled positions, whereas in 2013, 2014 and 2018 eggs were spawned almost in the sampled positions. In the 30-days forward simulations, different distributions and patterns are observed each year. Some years larvae tend to remain over the French shelf, whereas others end up over the shelf-break and slope or distributed between both areas depending on the date. Despite the eggs being spawned over the French shelf, part of the larvae are usually advected to around the shelf-break and slope. Moreover, in 2011 and 2018 larvae drift southwestwards, following the general drifting path suggested in other studies related to seasonal wind patterns (e.g., Uriarte et al., 2001; Irigoien et al., 2008; Cotano et al., 2008). It must be noted that the trajectories shown in the simulated distributions are subjected to a higher hydrodynamic variability (i.e., hourly/daily) compared with the mentioned general southwestward drift (i.e., seasonal). Moreover, Irigoien et al. (2008) already suggested that wind variations within a season or between different years might induce changes in distribution. This variability was also observed in Allain et al. (2007) and Caballero et al. (2016a). Additionally, our study area is smaller than the areas considered in previous studies.

Higher eggs and larvae retention is observed when eggs are spawned over the shelf instead of over the shelf-break, slope, or open ocean areas, highlighting the importance of the spawning location in the later retention of eggs and larvae. In any case, the centres of mass of the distributions do not get further west than the French slope (off the French coast), suggesting that most of the particles do not drift towards the open ocean. In the future, it would be interesting to study which are the factors that contribute to the retention in the area by, for example, analysing the Lagrangian coherent structures. Indeed, Irigoien et al. (2008) already suggested that SWODDIES could favour such retention.

Despite eggs and larvae being located in the upper 30 m of the water column where they migrate vertically (Palomera, 1991), they are mainly located at the shallowest depths as shown in Boyra et al. (2003). Thus, it is interesting to analyse the difference in the advections between those shallow depths. Comparing the results at −3 and −10 m, larvae distributions start to differ after 3 days of simulation, triggered by the slightly different initial egg positions (provided by CUFES and PairoVET) and the different hydrodynamics. The percentage of larvae retained in the domain also changes between depths ranging between 5−10 %. This agrees with the depth-dependent sensitivity shown in *Appendix C2* and highlights the importance of the characterization of subsurface currents and the methodologies to infer them from observational data, such as the ROOI.

Despite some discrepancies, in general, results are similar when simulations are forced with HFRtot and ROOI data at −3 m, indicating that both datasets can be used to represent surface advections. Since the HFRtot data enables a wider time coverage, more years were simulated with it. At −10 m, the ROOI arose as a good option as forcing data since it did not differ too much with respect to the best results obtained with HFRtot in the Lagrangian validation and provided the best results in the Eulerian validation (in *Section 3.3*). However, the lack of simultaneous HFR and ADCP observational data to reconstruct current velocity fields only provided enough ROOI data for 2011 and 2013. Therefore, simulations at −10 m were solely run for those years.

In the future, in order to overcome the scarce data availability of the ROOI, 3D current velocity fields could be reconstructed from only the HFR observations (along with the model data needed) in the dates where there is not ADCP data available. In addition, a higher spatial resolution of the forcing would be desirable to solve small scale features. The use of IBI analysis (presented in *Appendix C2*) instead of IBI reanalysis to estimate the spatial covariances would provide ROOI data with higher spatial resolution. The main inconvenience of this approach is that the availability of IBI analysis time series is not currently long enough (from mid-2018 on) to estimate the covariances robustly. However, this issue will be gradually solved in the future with a larger IBI analysis dataset as time passes or other regional 3D models that could provide data with an adequate time coverage.

The results presented in this study are merely physical in the sense that other factors in the ELS of anchovy such as food availability and risk of predation were not taken into account, providing information about the role played by hydrodynamics on the advection based on in situ current velocity observations for several periods for the first time. In the future, higher spatial resolution and/or wider temporal coverage at −10 m would broaden the analysis and provide further information. Validation of the simulations against larvae abundance data in June would be also valuable, as well as the analysis of the wind regime corresponding to each period in order to find out its relationship with the simulated advection, since in previous studies seemed to be correlated (e.g., Allain et al., 2001; Irigoien et al., 2008; Borja et al., 1996, 1998, 2008).

In this study, the utility of multiplatform observations for 3D Lagrangian analyses by means of the ROOI method has also been showcased. In the future, ROOI data could be used to simulate the advection of eggs and larvae of other fish species such as the sardine (*Sardina pilchardus*) or to assess if the particles sampled along a transect during the BIOMAN survey are resampled along other transects due to the advection. Transport patterns in the water column could be also analysed for different time scales in the study area. These kinds of analyses were already made at the surface by Rubio et al. (2020) who differentiated interannual, seasonal and daily scale variabilities on the water retention patterns due to several oceanic mechanisms such as general circulation, mesoscale processes, wind-driven currents and fronts. Also at the surface, Rubio et al. (2018) observed that eddies can regulate cross-shelf coastal water exchanges. The analysis of transport and retention patterns in the water column would help to better understand the fate of phytoplankton or nutrient-rich waters, which are crucial for primary production and the sustainability of the trophic chain. To that end, several Lagrangian techniques could be used such as residence times of different areas, cross-shelf escape rates, Lagrangian connectivity maps or more novel techniques such as path-integrated Lagrangian divergence (Hernández-Carrasco et al., 2018a), vorticity and eddy kinetic energy (Hernández-Carrasco et al., 2020).

5 Conclusions

In this study, the origin and fate of anchovy eggs and larvae were simulated at −3 and −10 m in peak spawning periods in the SE-BoB, from the spawning until they develop considerable swimming abilities. These simulations were carried out for several years based on in situ observations for the first time, providing information about the role played by instantaneous (i.e., in our context: hourly/daily) variability hydrodynamics on the distribution of anchovy ELS. The observed patterns are highly influenced by the variability of the forcing data, however, in general, part of the larvae ends up around the shelf-break, slope, or open ocean areas. Overall, larvae are retained in the study area and the retention is lower if there are eggs spawned over off-shelf areas. Simulations are sensitive to depth and results somewhat differ between −3 m and −10 m.

In the future, this study could be broadened by analysing the oceanic structures that induce retention in the area, studying the relationship between the simulated advection and the wind regime corresponding to each period, broadening the observations at −10 m for more years and reconstructing current velocity fields with a higher resolution.

The power of multiplatform observations for 3D Lagrangian studies has also been shown, and the reconstructed 3D current velocity fields could be used for further applications in the study area. For instance, a similar analysis could be carried out with other fishing species. ROOI data could be also used for assessing the potential resampling of eggs during BIOMAN surveys or for studying the transport patterns in the water column by means of Lagrangian techniques for a better understanding of biophysical interactions.

CHAPTER 8

Conclusions and Thesis

Conclusions

The first objective of this thesis was: “To obtain a diagnosis of the agreement between surface currents measured by altimetry and HFR over the SE-BoB and to evaluate the observability of certain seasonal and mesoscale processes by both measuring systems in the study area” (*Chapter 3*). The main conclusions in relation to this objective are:

1. Altimetry-derived across-track geostrophic and HFR surface current velocities agree in the SE-BoB with correlations up to 0.64 and with the best agreement along the slope, where the slope current (IPC) provides a more persistent geostrophic signal than in other areas more affected by ageostrophic currents (e.g., wind-driven currents).
2. The addition of wind-induced ageostrophic currents to the altimetry-derived across-track geostrophic ones improves the agreement with HFR total (i.e., ageostrophic + geostrophic) surface currents by an increase in correlation of around 10 %.
3. Altimetry and HFR measurements show a quantitative agreement when detecting seasonal and mesoscale processes in the study area, such as the slope current and especially its intensification, and mesoscale eddies.

The second objective was: “To showcase the combination of HFR and ADCP data for monitoring the slope current (IPC) and its seasonal variability in the SE-BoB” (*Chapter 4*). The main conclusions from this objective are:

4. Surface current velocity measurements by HFR and current velocities in the water column measured by ADCPs co-located at two slope moorings can jointly resolve the seasonality of the slope current and its intensification.
5. Current velocity fluctuations which are subject to strong wind pattern changes are detected by the HFR at the surface and the ADCPs along the water column.
6. The spatial agreement of the along slope currents measured by the HFR at the mooring locations with the rest of the HFR nodes, and the agreement in the water column between currents measured by ADCPs at different depths, in addition to the agreement between both observing systems, show that their data can be blended to 3D monitor the study area.

The third objective was: “To assess and compare the skills of two data-reconstruction methods in terms of current velocities to evaluate the feasibility of using such methods in the study area for blending multiplatform observations” (*Chapter 5*). The main conclusions from this objective are:

7. Both the DCT-PLS and ROOI methods have provided acceptable error levels in the upper 150 m of the water column, spatially in agreement with the main circulation patterns of the area, when reconstructing 3D current velocity fields from multiplatform observations,

showing the feasibility of using such methods to blend data from different observing platforms.

8. The DCT-PLS method works better in areas near the observations and has a simpler configuration, whereas the ROOI needs accurate historical information as well as careful testing of the tuning parameters providing better results in undersampled areas, thus being more suitable to study wider areas.

The fourth objective was: “To characterize the 3D properties of a coastal mode-water eddy and quantify the induced cross-shelf transport by means of a multiplatform data approach and a data-reconstruction method, while assessing the skills of the method for reconstructing mesoscale processes in the study area” (*Chapter 6*). The main conclusions from this objective are:

9. An eddy was 3D characterised for the first time in the study area by multiplatform observations showing a mode-water eddy behaviour that, although depicting smaller scales, had similar characteristics to eddies previously found in the study area and nearby regions.
10. 3D eddy current velocity fields were reconstructed in the upper 100 m from multiplatform and model data by the ROOI method under different observation-availability configurations. The reconstructions showed high agreement with glider observations. Thus, the ROOI showed strong skills for reconstructing mesoscale processes in the study area although further validation with additional data sources would be valuable.
11. The combination of multiplatform observations has enabled to better characterize the eddy and its induced inshore/offshore transport by providing information about different aspects at the surface and in the water column, showcasing the utility of this kind of approach for a more complete understanding of different oceanic processes.

The fifth objective was: “To simulate the advection of European anchovy eggs and larvae in the study area for several periods forced with current velocity observations, from HFR data and reconstructed fields, for the first time for a better understanding of the effect of the hydrodynamics in the ELS of this species.” (*Chapter 7*). The main conclusions from this objective are:

12. Simulations, run for periods where larvae are considered passive and starting at around mid-May, show that interannual larvae distribution patterns are highly variable as they are subject to the instantaneous current regimes. However, part of the larvae usually end-up around the shelf-break and slope agreeing with the main advection pattern suggested in the literature.
13. Although, in general, larvae are not dispersed towards open ocean, their retention in the study area seems to be sensitive to the spawning location with a higher retention if eggs

are spawned over the shelf and a lower retention if part of the eggs are located over the shelf-break or off-shelf areas.

14. Final larvae distributions are also sensitive to different hydrodynamics along the water column.
15. Multiplatform observations are showcased as useful data for 3D Lagrangian applications thanks to data-reconstruction methods such as the ROOI.

The research carried out and the results and conclusions obtained throughout the thesis open the way to future lines of work as presented in *Appendix D*.

Thesis

The results obtained in this thesis allowed working towards the validation of the enunciated working hypothesis, being the thesis that:

"*The combination of multiplatform and model data enables the characterization of the complex 3D hydrodynamics from submesoscale to seasonal coastal physical processes and their associated transports in the SE-BoB, which were only partially resolved until now. Such combination contributes towards a higher synergy between the different observing systems, enhancing the value of the available data. The methods and approaches shown in this thesis enable a better understanding of the effects of hydrodynamic processes on different ecological and environmental matters, arising as potential tools for marine applications.*"

REFERENCES

Akpınar, A., Charria, G., Theetten, S., Vandermeirsch, F., 2020. Cross-shelf exchanges in the northern Bay of Biscay. J. Mar. Syst. 205, 103314. https://doi.org/https://doi.org/10.1016/j.jmarsys.2020.103314

Allain, G., Petitgas, P., Lazure, P., 2007. The influence of environment and spawning distribution on the survival of anchovy (Engraulis encrasicolus) larvae in the Bay of Biscay (NE Atlantic) investigated by biophysical simulations. Fish. Oceanogr. 16, 506–514.

Allain, G., Petitgas, P., Lazure, P., Grellier, P., 2001. The transport of anchovy larvae and juveniles across the Bay of Biscay studied using otolith increments and a 3D hydrodynamic model. ICES C. 2001, 1.

Alvera-Azcárate, A., Barth, A., Beckers, J.M., Weisberg, R.H., 2007. Multivariate reconstruction of missing data in sea surface temperature, chlorophyll, and wind satellite fields. J. Geophys. Res. 112. https://doi.org/https://doi.org/10.1029/2006JC003660

Alvera-Azcárate, A., Barth, A., Parard, G., Beckers, J.-M., 2016. Analysis of SMOS sea surface salinity data using DINEOF. Remote Sens. Environ. 180, 137–145.

Alvera-Azcárate, A., Barth, A., Rixen, M., Beckers, J.-M., 2005. Reconstruction of incomplete oceanographic data sets using empirical orthogonal functions: application to the Adriatic Sea surface temperature. Ocean Model. 9, 325–346.

Ardhuin, F., Marié, L., Rascle, N., Forget, P., Roland, A., 2009. Observation and estimation of Lagrangian, Stokes, and Eulerian currents induced by wind and waves at the sea surface. J. Phys. Oceanogr. 39, 2820–2838.

Barrick, D., 1972. First-order theory and analysis of MF/HF/VHF scatter from the sea. IEEE Trans. Antennas Propag. 20, 2–10. https://doi.org/https://doi.org/10.1109/TAP.1972.1140123

Barth, A., Beckers, J.-M., Troupin, C., Alvera-Azcárate, A., Vandenbulcke, L., 2014. divand-1.0: n-dimensional variational data analysis for ocean observations. Geosci. Model Dev. 7, 225–241. https://doi.org/doi:10.5194/gmd-7-225-2014

Barth, A., Troupin, C., Reyes, E., Alvera-Azcárate, A., Beckers, J.-M., Tintore, J., 2021. Variational interpolation of high-frequency radar surface currents using DIVAnd. Ocean Dyn. 71, 293–308.

Baschek, B., Schroeder, F., Brix, H., Riethmüller, R., Badewien, T.H., Breitbach, G., Brügge, B., Colijn, F., Doerffer, R., Eschenbach, C., Friedrich, J., Fischer, P., Garthe, S., Horstmann, J., Krasemann, H., Metfies, K., Ohle, N., Petersen, W., Pröfrock, D., Röttgers, R., Schlüter, M., Schulz, J., Schulz-Stellenfleth, J., Wollschläger, J., Stanev, E., Winter, C., Wirtz, K., Zielinski, O., Ziemer, F., 2017. The coastal observing system for northern and arctic seas (COSYNA). Ocean Sci. 13, 379–410.

Bastos, L., Bio, A., Iglesias, I., 2016. The importance of marine observatories and of RAIA in particular. Front. Mar. Sci. 3, 140.

Beckers, J.M., Rixen, M., 2003. EOF calculations and data filling from incomplete oceanographic datasets. J. Atmos. Ocean. Technol. 20(12), 1839–1856. https://doi.org/https://doi.org/10.1175/1520-0426(2003)020%3C1839:ECADFF%3E2.0.CO;2

Bender, L.C., DiMarco, S.F., 2009. Quality Control Analysis of Acoustic Doppler Current Profiler Data Collected on Offshore Platforms of the Gulf of Mexico. New Orleans, LA.

Borja, A., Fontán, A., Sáenz, J., Valencia, V., 2008. Climate, oceanography, and recruitment: the case of the Bay of Biscay anchovy (Engraulis encrasicolus). Fish. Oceanogr. 17, 477–493.

Borja, A., Uriarte, A., Egaña, J., Motos, L., Valencia, V., 1998. Relationships between anchovy (Engraulis encrasicolus) recruitment and environment in the Bay of Biscay (1967-1996). Fish. Oceanogr. 7, 375–380.

Borja, A., Uriarte, Andrés, Valencia, V., Motos, L., Uriarte, Adolfo, 1996. Relationships between anchovy (Engraulis encrasicolus L.) recruitment and the environment in the Bay of Biscay. Sci. Mar. 60, 179–192.

Bouffard, J., Pascual, A., Ruiz, S., Faugère, Y., Tintoré, J., 2010. Coastal and mesoscale dynamics characterization using altimetry and gliders: A case study in the Balearic Sea. J. Geophys. Res. Ocean. 115.

Boyra, G., Peña, M., Cotano, U., Irigoien, X., Rubio, A., Nogueira, E., 2016. Spatial dynamics of juvenile anchovy in the Bay of Biscay. Fish. Oceanogr. 25, 529–543.

Boyra, G., Rueda, L., Coombs, S.H., Sundby, S., Ådlandsvik, B., Santos, M., Uriarte, A., 2003. Modelling the vertical distribution of eggs of anchovy (Engraulis encrasicolus) and sardine (Sardina pilchardus). Fish. Oceanogr. 12, 381–395.

Brasseur, P.P., 1991. A variational inverse method for the reconstruction of general circulation fields in the northern Bering Sea. J. Geophys. Res. Ocean. 96, 4891–4907. https://doi.org/https://doi.org/10.1029/90JC02387

Braunschweig, F., Leitao, P.C., Fernandes, L., Pina, P., Neves, R.J.J., 2004. The object-oriented design of the integrated water modelling system MOHID, in: Developments in Water

Science. Elsevier, pp. 1079–1090.

Broche, P., Forget, P., De Maistre, J.C., Devenon, J.L., Crochet, M., 1987. VHF radar for ocean surface current and sea state remote sensing. Radio Sci. 22, 69–75. https://doi.org/https://doi.org/10.1029/RS022i001p00069

Brown, G. 977, 1977. The average impulse response of a rough surface and its applications. IEEE Trans. Antennas Propag. 25, 67–74.

Brzezinski, M.A., Washburn, L., 2011. Phytoplankton primary productivity in the Santa Barbara Channel: Effects of wind-driven upwelling and mesoscale eddies. J. Geophys. Res. Ocean. 116. https://doi.org/https://doi.org/10.1029/2011JC007397

Caballero, A., Espino, M., Sagarminaga, Y., Ferrer, L., Uriarte, A., González, M., 2008a. Simulating the migration of drifters deployed in the Bay of Biscay, during the Prestige crisis. Mar. Pollut. Bull. 56, 475–482.

Caballero, A., Ferrer, L., Rubio, A., Charria, G., Taylor, B.H., Grima, N., 2014. Monitoring of a quasi-stationary eddy in the Bay of Biscay by means of satellite, in situ and model results. Deep Sea Res. Part II Top. Stud. Oceanogr. 106, 23–37. https://doi.org/https://doi.org/10.1016/j.dsr2.2013.09.029

Caballero, A., Pascual, A., Dibarboure, G., Espino, M., 2008b. Sea level and Eddy Kinetic Energy variability in the Bay of Biscay, inferred from satellite altimeter data. J. Mar. Syst. 72, 116–134. https://doi.org/https://doi.org/10.1016/j.jmarsys.2007.03.011

Caballero, A., Rubio, A., Ferrer, L., Cotano, U., Aldanondo, N., Le Cann, B., 2016a. Impacto de remolinos oceánicos MESOescalares en la distribución, abundancia y crecimiento de la ANCHOA europea (Engraulis encrasicolus). Pasaia.

Caballero, A., Rubio, A., Ruiz, S., Le Cann, B., Testor, P., Mader, J., Hernández, C., 2016b. South-Eastern Bay of Biscay eddy-induced anomalies and their effect on chlorophyll distribution. J. Mar. Syst. 162, 57–72. https://doi.org/https://doi.org/10.1016/j.jmarsys.2016.04.001

Campbell, R., Diaz, F., Hu, Z., Doglioli, A., Petrenko, A., Dekeyser, I., 2013. Nutrients and plankton spatial distributions induced by a coastal eddy in the Gulf of Lion. Insights from a numerical model. Prog. Oceanogr. 109, 47–69. https://doi.org/https://doi.org/10.1016/j.pocean.2012.09.005

Carpenter, J.R., Timmermans, M., 2012. Deep mesoscale eddies in the Canada Basin, Arctic Ocean. Geophys. Res. Lett. 39. https://doi.org/https://doi.org/10.1029/2012GL053025

Chapman, R.D., Shay, L.K., Graber, H.C., Edson, J.B., Karachintsev, A., Trump, C.L., Ross, D.B., 1997. On the accuracy of HF radar surface current measurements: Intercomparisons with ship-based sensors. J. Geophys. Res. Ocean. 102, 18737–18748. https://doi.org/https://doi.org/10.1029/97JC00049

Charria, G., Lazure, P., Le Cann, B., Serpette, A., Reverdin, G., Louazel, S., Batifoulier, F., Dumas, F., Pichon, A., Morel, Y., 2013. Surface layer circulation derived from Lagrangian drifters in the Bay of Biscay. J. Mar. Syst. 109, S60–S76. https://doi.org/https://doi.org/10.1016/j.jmarsys.2011.09.015

Chavanne, C.P., Klein, P., 2010. Can oceanic submesoscale processes be observed with satellite altimetry? Geophys. Res. Lett. 37.

Checkley, D.M., Ortner, P.B., Settle, L.R., Cummings, S.R., 1997. A continuous, underway fish egg sampler. Fish. Oceanogr. 6, 58–73.

Chenillat, F., Blanke, B., Grima, N., Franks, P.J.S., Capet, X., Rivière, P., 2015. Quantifying tracer dynamics in moving fluids: a combined Eulerian-Lagrangian approach. Front. Environ. Sci. 3, 43.

Cherian, D.A., Brink, K.H., 2016. Offshore transport of shelf water by deep-ocean eddies. J. Phys. Oceanogr. 46, 3599–3621. https://doi.org/https://doi.org/10.1175/JPO-D-16-0085.1

Church, J.A., White, N.J., 2006. A 20th century acceleration in global sea-level rise. Geophys. Res. Lett. 33. https://doi.org/https://doi.org/10.1029/2005GL024826

Cianelli, D., D'Alelio, D., Uttieri, M., Sarno, D., Zingone, A., Zambianchi, E., d'Alcalà, M.R., 2017. Disentangling physical and biological drivers of phytoplankton dynamics in a coastal system. Sci. Rep. 7, 1–15.

Cianelli, D., Falco, P., Iermano, I., Mozzillo, P., Uttieri, M., Buonocore, B., Zambardino, G., Zambianchi, E., 2015. Inshore/offshore water exchange in the Gulf of Naples. J. Mar. Syst. 145, 37–52. https://doi.org/https://doi.org/10.1016/j.jmarsys.2015.01.002

Cleveland, W.S., Devlin, S.J., 1988. Locally weighted regression: an approach to regression analysis by local fitting. J. Am. Stat. Assoc. 83, 596–610.

Combes, V., Chenillat, F., Di Lorenzo, E., Rivière, P., Ohman, M.D., Bograd, S.J., 2013. Cross-shore transport variability in the California Current: Ekman upwelling vs. eddy dynamics. Prog. Oceanogr. 109, 78–89. https://doi.org/https://doi.org/10.1016/j.pocean.2012.10.001

Corgnati, L., Mantovani, C., Novellino, A., Rubio, A., Mader, J., 2018. Recommendation Report 2 on improved common procedures for HFR QC analysis. JERICO-NEXT WP5-Data

Management, Deliverable 5.14, Version 1.0.

Cotano, U., Irigoien, X., Etxebeste, E., Álvarez, P., Zarauz, L., Mader, J., Ferrer, L., 2008. Distribution, growth and survival of anchovy larvae (Engraulis encrasicolus L.) in relation to hydrodynamic and trophic environment in the Bay of Biscay. J. Plankton Res. 30, 467–481.

Craven, P., Wahba, G., 1978. Smoothing noisy data with spline functions. Numer. Math. 31, 377–403.

Cushman-Roisin, B., Beckers, J.-M., 2011. Introduction to geophysical fluid dynamics: physical and numerical aspects. Academic press.

D'Assaro, E.A., Eriksen, C.C., Levine, M.D., Niiler, P., Van Meurs, P., 1995. Upper-ocean inertial currents forced by a strong storm. Part I: Data and comparisons with linear theory. J. Phys. Oceanogr. 25, 2909–2936.

Davies, A.M., 1985a. On determining the profile of steady wind-induced currents. Appl. Math. Model. 9, 409–418. https://doi.org/https://doi.org/10.1016/0307-904X(85)90106-4

Davies, A.M., 1985b. Three dimensional modal model of wind induced flow in a sea region. Prog. Oceanogr. 15, 71–128. https://doi.org/https://doi.org/10.1016/0079-6611(85)90032-1

Davies, A.M., 1985c. On determining current profiles in oscillatory flows. Appl. Math. Model. 9, 419–428. https://doi.org/https://doi.org/10.1016/0307-904X(85)90107-6

Davis, R.E., DeSzoeke, R., Niiler, P., 1981. Variability in the upper ocean during MILE. Part II: Modeling the mixed layer response. Deep Sea Res. Part A. Oceanogr. Res. Pap. 28, 1453–1475.

Davis, R.E., Eriksen, C.C., Jones, C.P., 2002. Autonomous buoyancy-driven underwater gliders. Technol. Appl. Auton. Underw. Veh. 37–58.

De Mey-Frémaux, P., Ayoub, N., Barth, A., Brewin, R., Charria, G., Campuzano, F., Ciavatta, S., Cirano, M., Edwards, C.A., Federico, I., Gao, S., Garcia-Hermosa, I., Garcia-Sotillo, M., Hewitt, H., Hole, L.R., Holt, J., King, R., Kourafalou, V., Lu, Y., Mourre, B., Pascual, A., Staneva, J., Stanev, E., Wang, H., Zhu, X., 2019. Model-observations synergy in the coastal ocean. Front. Mar. Sci. 6:436.

De Valk, C.F., 1999. Estimation of 3-D current fields near the Rhine outflow from HF radar surface current data. Coast. Eng. 37, 487–511. https://doi.org/https://doi.org/10.1016/S0378-3839(99)00040-X

Declerck, A., Delpey, M., Rubio, A., Ferrer, L., Basurko, O.C., Mader, J., Louzao, M., 2019.

Transport of floating marine litter in the coastal area of the south-eastern Bay of Biscay: A Lagrangian approach using modelling and observations. J. Oper. Oceanogr. 12, S111–S125.

Destang-Quelen, T., Basurko, O.C., Rubio, A., 2019. Microplastic concentrations in the South-East Bay of Biscay (SE BoB): From observations and estimations to distribution of floating microplastic particles (a Lagrangian approach). AZTI-University of the Basque Country.

Dewey, J., 1938. Logic: the theory of Enquiry Holt Rinehart & Winston. New York, London.

Dietze, H., Matear, R., Moore, T., 2009. Nutrient supply to anticyclonic meso-scale eddies off western Australia estimated with artificial tracers released in a circulation model. Deep Sea Res. Part I Oceanogr. Res. Pap. 56, 1440–1448. https://doi.org/https://doi.org/10.1016/j.dsr.2009.04.012

Dussurget, R., Birol, F., Morrow, R., Mey, P. De, 2011. Fine resolution altimetry data for a regional application in the Bay of Biscay. Mar. Geod. 34, 447–476.

Ekman, V.W., 1905. On the influence of the earth’s rotation on ocean-currents. Ark. för Mat. Astron. och Fys. 2, 1–53.

Esnaola, G., Sáenz, J., Zorita, E., Fontán, A., Valencia, V., Lazure, P., 2013. Daily scale wintertime sea surface temperature and IPC-Navidad variability in the southern Bay of Biscay from 1981 to 2010. Ocean Sci. 9, 655–679. https://doi.org/https://doi.org/10.5194/os-9-655-2013

Farcy, P., Durand, D., Charria, G., Painting, S.J., Tamminen, T., Collingridge, K., Grémare, A.J., Delauney, L., Puillat, I., 2019. Toward a European coastal observing network to provide better answers to science and to societal challenges; the JERICO research infrastructure. Front. Mar. Sci. 6, 529.

Fernández, E., Álvarez, F., Anadón, R., Barquero, S., Bode, A., García, A., García-Soto, C., Gil, J., González, N., Iriarte, A., 2004. The spatial distribution of plankton communities in a Slope Water anticyclonic Oceanic eDDY (SWODDY) in the southern Bay of Biscay. Mar. Biol. Assoc. United Kingdom. J. Mar. Biol. Assoc. United Kingdom 84, 501.

Ferrer, L., Fontán, A., Mader, J., Chust, G., González, M., Valencia, V., Uriarte, A., Collins, M.B., 2009. Low-salinity plumes in the oceanic region of the Basque Country. Cont. Shelf Res. 29, 970–984. https://doi.org/https://doi.org/10.1016/j.csr.2008.12.014

Ferrer, L., Liria, P., Bolaños, R., Balseiro, C., Carracedo, P., González-Marco, D., González, M., Fontán, A., Mader, J., Hernández, C., 2010. Reliability of coupled meteorological and wave models to estimate wave energy resource in the Bay of Biscay, in: Proceedings of the 3rd International Conference on Ocean Energy (ICOE). Bilbao (Spain), pp. 6–8.

Ferrer, L., Zaldua-Mendizabal, N., Del Campo, A., Franco, J., Mader, J., Cotano, U., Fraile, I., Rubio, A., Uriarte, A., Caballero, A., 2015. Operational protocol for the sighting and tracking of Portuguese man-of-war in the southeastern Bay of Biscay: Observations and modeling. Cont. Shelf Res. 95, 39–53.

Fredj, E., Roarty, H., Kohut, J., Smith, M., Glenn, S., 2016. Gap filling of the coastal ocean surface currents from HFR data: Application to the Mid-Atlantic Bight HFR Network. J. Atmos. Ocean. Technol. 33, 1097–1111. https://doi.org/https://doi.org/10.1175/JTECH-D-15-0056.1

Frimodt, C., 1995. Multilingual illustrated guide to the world’s commercial warmwater fish. Fishing News Books Ltd., Oxford.

Frouin, R., Fiúza, A.F.G., Ambar, I., Boyd, T.J., 1990. Observations of a poleward surface current off the coasts of Portugal and Spain during winter. J. Geophys. Res. Ocean. 95, 679–691. https://doi.org/https://doi.org/10.1029/JC095iC01p00679

Fujii, S., Heron, M.L., Kim, K., Lai, J.-W., Lee, S.-H., Wu, Xiangbai, Wu, Xiongbin, Wyatt, L.R., Yang, W.-C., 2013. An overview of developments and applications of oceanographic radar networks in Asia and Oceania countries. Ocean Sci. J. 48, 69–97. https://doi.org/http://dx.doi.org/10.1007/s12601-013-0007-0

Gandin, L.S., 1965. Objective Analysis of Meteorological Fields. Israel Program for Scientific Translations. Jerusalem, Isr. QJR Meteorol. Soc.

Gangopadhyay, A., Shen, C.Y., Marmorino, G.O., Mied, R.P., Lindemann, G.J., 2005. An extended velocity projection method for estimating the subsurface current and density structure for coastal plume regions: An application to the Chesapeake Bay outflow plume. Cont. Shelf Res. 25, 1303–1319. https://doi.org/https://doi.org/10.1016/j.csr.2005.03.002

García-Soto, C., 2004. ’Prestige’oil spill and Navidad flow. Mar. Biol. Assoc. United Kingdom. J. Mar. Biol. Assoc. United Kingdom 84, 297.

Garcia-Soto, C., Pingree, R.D., 2012. Atlantic Multidecadal Oscillation (AMO) and sea surface temperature in the Bay of Biscay and adjacent regions. Mar. Biol. Assoc. United Kingdom. J. Mar. Biol. Assoc. United Kingdom 92, 213.

Garcia-Soto, C., Pingree, R.D., Valdés, L., 2002. Navidad development in the southern Bay of Biscay: climate change and swoddy structure from remote sensing and in situ measurements. J. Geophys. Res. Ocean. 107, 28-1-28–29.

Garcia, D., 2010. Robust smoothing of gridded data in one and higher dimensions with missing values. Comput. Stat. Data Anal. 54, 1167–1178.

https://doi.org/https://doi.org/10.1016/j.csda.2009.09.020

Gaube, P., Chelton, D.B., Samelson, R.M., Schlax, M.G., O'Neill, L.W., 2015. Satellite observations of mesoscale eddy-induced Ekman pumping. J. Phys. Oceanogr. 45, 104–132.

González, M., Ferrer, L., Uriarte, A., Urtizberea, A., Caballero, A., 2008. Operational Oceanography System applied to the Prestige oil-spillage event. J. Mar. Syst. 72, 178–188.

González, M., Uriarte, A., Fontán, A., Mader, J., Gyssels, P., 2004. Marine dynamics. Oceanogr. Mar. Environ. Basqu. Ctry. 70, 133–157.

Groom, S., Sathyendranath, S., Ban, Y., Bernard, S., Brewin, R., Brotas, V., Brockmann, C., Chauhan, P., Choi, J., Chuprin, A., 2019. Satellite ocean colour: current status and future perspective. Front. Mar. Sci. 6, 485.

Gurgel, K.-W., 1994. Shipborne measurement of surface current fields by HF radar, in: Proceedings of OCEANS'94. IEEE, pp. III–23.

Ha, K.-J., Jeon, E.-H., Oh, H.-M., 2007. Spatial and temporal characteristics of precipitation using an extensive network of ground gauge in the Korean Peninsula. Atmos. Res. 86, 330–339. https://doi.org/https://doi.org/10.1016/j.atmosres.2007.07.002

Haynes, R., Barton, E.D., 1990. A poleward flow along the Atlantic coast of the Iberian Peninsula. J. Geophys. Res. Ocean. 95, 11425–11441. https://doi.org/https://doi.org/10.1029/JC095iC07p11425

Herbert, G., Ayoub, N., Marsaleix, P., Lyard, F., 2011. Signature of the coastal circulation variability in altimetric data in the southern Bay of Biscay during winter and fall 2004. J. Mar. Syst. 88, 139–158.

Hernández-Carrasco, I., Alou-Font, E., Dumont, P.-A., Cabornero, A., Allen, J., Orfila, A., 2020. Lagrangian flow effects on phytoplankton abundance and composition along filament-like structures. Prog. Oceanogr. 189, 102469.

Hernández-Carrasco, I., Orfila, A., Rossi, V., Garçon, V., 2018a. Effect of small scale transport processes on phytoplankton distribution in coastal seas. Sci. Rep. 8, 1–13.

Hernández-Carrasco, I., Solabarrieta, L., Rubio, A., Esnaola, G., Reyes, E., Orfila, A., 2018b. Impact of HF radar current gap-filling methodologies on the Lagrangian assessment of coastal dynamics. Ocean Sci. 14, 827–847. https://doi.org/https://doi.org/10.5194/os-14-827-2018

Holt, J., Hyder, P., Ashworth, M., Harle, J., Hewitt, H.T., Liu, H., New, A.L., Pickles, S., Porter, A., Popova, E., others, 2017. Prospects for improving the representation of coastal and shelf seas in global ocean models. Geosci. Model Dev. 10, 499–523.

Huthnance, J.M., Holt, J.T., Wakelin, S.L., 2009. Deep ocean exchange with west-European shelf seas. Ocean Sci. 5, 621–634. https://doi.org/https://doi.org/10.5194/os-5-621-2009

Ibañez, M., 1979. Hydrological studies and surface currents in the coastal area of the Bay of Biscay. Lurralde Investig. y Espac. 37–75.

Irigoien, X., Cotano, U., Boyra, G., Santos, M., Alvarez, P., Otheguy, P., Etxebeste, E., Uriarte, A., Ferrer, L., Ibaibarriaga, L., 2008. From egg to juvenile in the Bay of Biscay: spatial patterns of anchovy (Engraulis encrasicolus) recruitment in a non-upwelling region. Fish. Oceanogr. 17, 446–462.

Irigoien, X., Fiksen, Ø., Cotano, U., Uriarte, A., Alvarez, P., Arrizabalaga, H., Boyra, G., Santos, M., Sagarminaga, Y., Otheguy, P., 2007. Could Biscay Bay Anchovy recruit through a spatial loophole? Prog. Oceanogr. 74, 132–148.

Ivonin, D. V, Broche, P., Devenon, J., Shrira, V.I., 2004. Validation of HF radar probing of the vertical shear of surface currents by acoustic Doppler current profiler measurements. J. Geophys. Res. Ocean. 109. https://doi.org/https://doi.org/10.1029/2003JC002025

Jordà, G., Sánchez-Román, A., Gomis, D., 2016. Reconstruction of transports through the Strait of Gibraltar from limited observations. Clim. Dyn. 48, 851–865. https://doi.org/DOI 10.1007/s00382-016-3113-8

Kaplan, A., Kushnir, Y., Cane, M.A., 2000. Reduced space optimal interpolation of historical marine sea level pressure: 1854-1992. J. Clim. 13, 2987–3002. https://doi.org/10.1175/1520-0442(2000)013<2987:RSOIOH>2.0.CO;2

Kaplan, A., Kushnir, Y., Cane, M.A., Blumenthal, M.B., 1997. Reduced space optimal analysis for historical data sets: 136 years of Atlantic sea surface temperatures. J. Geophys. Res. Ocean. 102, 27835–27860. https://doi.org/https://doi.org/10.1029/97JC01734

Kaplan, D.M., Lekien, F., 2007. Spatial interpolation and filtering of surface current data based on open-boundary modal analysis. J. Geophys. Res. Ocean. 112. https://doi.org/https://doi.org/10.1029/2006JC003984

Kohonen, T., 1997. Self-Organizing Maps , 2nd ed. Springer, Heidelberg, Germany.

Kohut, J.T., Glenn, S.M., 2003. Improving HF radar surface current measurements with measured antenna beam patterns. J. Atmos. Ocean. Technol. 20, 1303–1316.

Koutsikopoulos, C., Le Cann, B., 1996. Physical processes and hydrological structures related to the Bay of Biscay anchovy. Sci. Mar. 60, 9–19.

Large, W.G., Pond, S., 1981. Open ocean momentum flux measurements in moderate to strong winds. J. Phys. Oceanogr. 11, 324–336.

Lavín, A., Valdes, L., Sanchez, F., Abaunza, P., Forest, A., Boucher, J., Lazure, P., Jegou, A.-M., 2006. The Bay of Biscay: the encountering of the Ocean and the Shelf (18b, E). Combridge, MA, Harvard University Press.

Laws, K.E., 2001. Measurements of near surface ocean currents using HF radar. University of California, Santa Cruz.

Lazure, P., 1997. La circulation des eaux dans le Golfe de Gascogne. 10émes rencontres Interreg. lAGLIA. Saint Jean Luz 83–88.

Le Cann, B., 1990. Barotropic tidal dynamics of the Bay of Biscay shelf: observations, numerical modelling and physical interpretation. Cont. Shelf Res. 10, 723–758.

Le Cann, B., Serpette, A., 2009. Intense warm and saline upper ocean inflow in the southern Bay of Biscay in autumn–winter 2006–2007. Cont. Shelf Res. 29, 1014–1025. https://doi.org/https://doi.org/10.1016/j.csr.2008.11.015

Le Hénaff, M., Roblou, L., Bouffard, J., 2011. Characterizing the Navidad current interannual variability using coastal altimetry. Ocean Dyn. 61, 425–437.

Le Traon, P.Y., Faugère, Y., Hernandez, F., Dorandeu, J., Mertz, F., Ablain, M., 2003. Can we merge GEOSAT Follow-On with TOPEX/POSEIDON and ERS-2 for an improved description of the ocean circulation? J. Atmos. Ocean. Technol. 20, 889–895.

Le Traon, P.Y., Morrow, R., 2001. Ocean currents and eddies, in: Fu, L.-L., Cazenave, A. (Eds.), Satellite Altimetry and Earth Sciences A Handbook of Techniques and Applications. Elsevier, pp. 171–215.

Lebreton, L.-M., Greer, S.D., Borrero, J.C., 2012. Numerical modelling of floating debris in the world's oceans. Mar. Pollut. Bull. 64, 653–661.

Leitão, P.C., 1996. Modelo de dispersão lagrangeano tridimensional. Technical University of Lisbon.

Lipa, B., Barrick, D., 1983. Least-squares methods for the extraction of surface currents from CODAR crossed-loop data: Application at ARSLOE. IEEE J. Ocean. Eng. 8, 226–253.

Liu, Y., Kerkering, H., Weisberg, R.H., 2015. Coastal ocean observing systems. Academic Press.

Liu, Y., Weisberg, R.H., Vignudelli, S., Roblou, L., Merz, C.R., 2012. Comparison of the X-TRACK altimetry estimated currents with moored ADCP and HF radar observations on the

West Florida Shelf. Adv. Sp. Res. 50, 1085–1098.

Manso-Narvarte, I., Caballero, A., Rubio, A., Dufau, C., Birol, F., 2018. Joint analysis of coastal altimetry and high-frequency (HF) radar data: observability of seasonal and mesoscale ocean dynamics in the Bay of Biscay. Ocean Sci. 14, 1265–1281.

Manso-Narvarte, I., Fredj, E., Jordà, G., Berta, M., Griffa, A., Caballero, A., Rubio, A., 2020. 3D reconstruction of ocean velocity from high-frequency radar and acoustic Doppler current profiler: a model-based assessment study. Ocean Sci. 16, 575–591. https://doi.org/10.5194/os-16-575-2020

Manso-Narvarte, I., Rubio, A., Jordà, G., Carpenter, J., Merckelbach, L., Caballero, A., 2021. Three-Dimensional Characterization of a Coastal Mode-Water Eddy from Multiplatform Observations and a Data Reconstruction Method. Remote Sens. 13, 674.

Mantovani, C., Corgnati, L., Horstmann, J., Rubio, A., Reyes, E., Quentin, C., Cosoli, S., Asensio, J.L., Mader, J., Griffa, A., 2020. Best practices on High Frequency Radar deployment and operation for ocean current measurement. Front. Mar. Sci. 7:210. https://doi.org/https://doi.org/10.3389/fmars.2020.00210

Marmorino, G.O., Shen, C.Y., Evans, T.E., Lindemann, G.J., Hallock, Z.R., Shay, L.K., 2004. Use of ‘velocity projection’to estimate the variation of sea-surface height from HF Doppler radar current measurements. Cont. Shelf Res. 24, 353–374. https://doi.org/https://doi.org/10.1016/j.csr.2003.10.011

McGillicuddy, D.J., 2015. Formation of intrathermocline lenses by eddy–wind interaction. J. Phys. Oceanogr. 45, 606–612. https://doi.org/https://doi.org/10.1175/JPO-D-14-0221.1

McGillicuddy, D.J., Anderson, L.A., Bates, N.R., Bibby, T., Buesseler, K.O., Carlson, C.A., Davis, C.S., Ewart, C., Falkowski, P.G., Goldthwait, S.A., 2007. Eddy/wind interactions stimulate extraordinary mid-ocean plankton blooms. Science (80-.). 316, 1021–1026. https://doi.org/10.1126/science.1136256

McGillicuddy, D.J., Johnson, R., Siegel, D.A., Michaels, A.F., Bates, N.R., Knap, A.H., 1999. Mesoscale variations of biogeochemical properties in the Sargasso Sea. J. Geophys. Res. Ocean. 104, 13381–13394. https://doi.org/https://doi.org/10.1029/1999JC900021

Mizobata, K., Wang, J., Saitoh, S., 2006. Eddy-induced cross-slope exchange maintaining summer high productivity of the Bering Sea shelf break. J. Geophys. Res. Ocean. 111. https://doi.org/https://doi.org/10.1029/2005JC003335

Moore, T.S., Matear, R.J., Marra, J., Clementson, L., 2007. Phytoplankton variability off the Western Australian Coast: Mesoscale eddies and their role in cross-shelf exchange. Deep

Sea Res. Part II Top. Stud. Oceanogr. 54, 943–960. https://doi.org/https://doi.org/10.1016/j.dsr2.2007.02.006

Morrow, R., Carret, A., Birol, F., Nino, F., Valladeau, G., Boy, F., Bachelier, C., Zakardjian, B., 2017. Observability of fine-scale ocean dynamics in the northwestern Mediterranean Sea. Ocean Sci. 13, 13–29.

Motos, L., Uriarte, A., Valencia, V., 1996. The spawning environment of the Bay of Biscay anchovy (Engraulis encrasicolus L.). Sci. Mar. 60, 117–140.

Neves, R., 2013. The MOHID concept, in: Neves, R., Mateus, M. (Eds.), Ocean Modelling for Coastal Management-Case Studies with MOHID. IST Press, Lisbon, pp. 1–11.

O'Carroll, A.G., Armstrong, E.M., Beggs, H.M., Bouali, M., Casey, K.S., Corlett, G.K., Dash, P., Donlon, C.J., Gentemann, C.L., Høyer, J.L., 2019. Observational needs of sea surface temperature. Front. Mar. Sci. 6, 420.

O'Donncha, F., Hartnett, M., Nash, S., Ren, L., Ragnoli, E., 2015. Characterizing observed circulation patterns within a bay using HF radar and numerical model simulations. J. Mar. Syst. 142, 96–110. https://doi.org/https://doi.org/10.1016/j.jmarsys.2014.10.004

Okubo, A., 1971. Oceanic diffusion diagrams, in: Deep Sea Research and Oceanographic Abstracts. Elsevier, pp. 789–802.

OSPAR, O.C. for the P. of the M.E. of the N.-E., 2000. Quality Status Report 2000: Region IV: Bay of Biscay and Iberian Coast. OSPAR Commission for the Protection of the Marine Environment of the North-East Atlantic.

Paduan, J.D., Graber, H.C., 1997. Introduction to high-frequency radar: reality and myth. Oceanography 10, 36–39. https://doi.org/https://doi.org/10.5670/oceanog.1997.18

Paduan, J.D., Washburn, L., 2013. High-frequency radar observations of ocean surface currents. Ann. Rev. Mar. Sci. 5, 115–136. https://doi.org/https://doi.org/10.1146/annurev-marine-121211-172315

Palomera, I., 1991. Vertical distribution of anchovy larvae Engraulis encrasicolus in Western Mediterranean. ICES C. 50, 31.

Paris, C.B., Cowen, R.K., Claro, R., Lindeman, K.C., 2005. Larval transport pathways from Cuban snapper (Lutjanidae) spawning aggregations based on biophysical modeling. Mar. Ecol. Prog. Ser. 296, 93–106.

Paris, C.B., Hénaff, M. Le, Aman, Z.M., Subramaniam, A., Helgers, J., Wang, D.-P., Kourafalou, V.H., Srinivasan, A., 2012. Evolution of the Macondo well blowout: simulating the effects of the circulation and synthetic dispersants on the subsea oil transport. Environ. Sci. Technol. 46, 13293–13302.

Pascual, A., Lana, A., Troupin, C., Ruiz, S., Faugère, Y., Escudier, R., Tintoré, J., 2015. Assessing SARAL/AltiKa data in the coastal zone: comparisons with HF radar observations. Mar. Geod. 38, 260–276.

Peliz, A., Santos, A.M.P., Oliveira, P.B., Dubert, J., 2004. Extreme cross-shelf transport induced by eddy interactions southwest of Iberia in winter 2001. Geophys. Res. Lett. 31. https://doi.org/https://doi.org/10.1029/2004GL019618

Pereiro, D., Souto, C., Gago, J., 2019. Dynamics of floating marine debris in the northern Iberian waters: A model approach. J. Sea Res. 144, 57–66.

Petihakis, G., Petersen, W., Nair, R., Faimali, M., Pavanello, G., Boukerma, K., Delauney, L., Puillat, I., Farcy, P., Greenwood, N., 2015. Harmonization in the joint European research infrastructure network for coastal observatories - JERICO, in: OCEANS 2015 - MTS/IEEE Washington. pp. 1–8. https://doi.org/10.23919/OCEANS.2015.7404554

Petit de la Villéon, L., Coatanoan, C., Edwards, M., Karstensen, J., Cardin, V., 2005. In-situ real-time data quality control. Mar. Environ. Secur. Eur. Area-Integrated Proj. Doc. id. WP03-IFR-UMAN-001-01A.

Phelps, J.J.C., Polton, J.A., Souza, A.J., Robinson, L.A., 2015. Behaviour influences larval dispersal in shelf sea gyres: Nephrops norvegicus in the Irish Sea. Mar. Ecol. Prog. Ser. 518, 177–191.

Pingree, R.D., 2005. North Atlantic and North Sea climate change: curl up, shut down, NAO and ocean colour. J. Mar. Biol. Assoc. United Kingdom 85, 1301–1315.

Pingree, R.D., 1997. The eastern subtropical gyre (North Atlantic): flow rings recirculations structure and subduction. J. Mar. Biol. Assoc. United Kingdom 77, 573–624.

Pingree, R.D., 1993. Flow of surface waters to the west of the British Isles and in the Bay of Biscay. Deep Sea Res. Part II Top. Stud. Oceanogr. 40, 369–388.

Pingree, R.D., Le Cann, B., 1992a. Anticyclonic eddy X91 in the southern Bay of Biscay, May 1991 to February 1992. J. Geophys. Res. Ocean. 97, 14353–14367. https://doi.org/https://doi.org/10.1029/92JC01181

Pingree, R.D., Le Cann, B., 1992b. Three anticyclonic Slope Water Oceanic eDDIES (SWODDIES) in the southern Bay of Biscay in 1990. Deep Sea Res. Part A. Oceanogr. Res. Pap. 39, 1147–1175. https://doi.org/https://doi.org/10.1016/0198-0149(92)90062-X

Pingree, R.D., Le Cann, B., 1990. Structure, strength and seasonality of the slope currents in the Bay of Biscay region. J. Mar. Biol. Assoc. United Kingdom 70, 857–885. https://doi.org/https://doi.org/10.1017/S0025315400059117

Pingree, R.D., Le Cann, B., 1989. Celtic and Armorican slope and shelf residual currents. Prog. Oceanogr. 23, 303–338.

Pollard, R.T., Griffiths, M.J., Cunningham, S.A., Read, J.F., Pérez, F.F., Ríos, A.F., 1996. Vivaldi 1991-A study of the formation, circulation and ventilation of Eastern North Atlantic Central Water.

Pollard, R.T., Millard, R.C., 1970. Comparison between observed and simulated wind-generated inertial oscillations, in: Deep Sea Research and Oceanographic Abstracts. Elsevier, pp. 813–821.

Pond, S., Pickard, G.L., 1983. Introductory Dynamical Oceanography, 2nd Edn., Butterworh.

Prandle, D., 1991. A new view of near-shore dynamics based on observations from HF radar. Prog. Oceanogr. 27, 403–438. https://doi.org/https://doi.org/10.1016/0079-6611(91)90030-P

Prandle, D., 1987. The fine-structure of nearshore tidal and residual circulations revealed by HF radar surface current measurements. J. Phys. Oceanogr. 17, 231–245. https://doi.org/https://doi.org/10.1175/1520-0485(1987)017%3C0231:TFSONT%3E2.0.CO;2

Prandle, D., 1982. The vertical structure of tidal currents. Geophys. Astrophys. fluid Dyn. 22, 29–49. https://doi.org/https://doi.org/10.1080/03091928208221735

Pujol, M.-I., Faugère, Y., Taburet, G., Dupuy, S., Pelloquin, C., Ablain, M., Picot, N., 2016. DUACS DT2014: the new multi-mission altimeter data set reprocessed over 20 years. Ocean Sci. 12, 1067–1090.

Ralph, E.A., Niiler, P.P., 1999. Wind-driven currents in the tropical Pacific. J. Phys. Oceanogr. 29, 2121–2129.

Ren, L., Nash, S., Hartnett, M., 2015. Observation and modeling of tide-and wind-induced surface currents in Galway Bay. Water Sci. Eng. 8, 345–352. https://doi.org/https://doi.org/10.1016/j.wse.2015.12.001

Restano, M., Passaro, M., Vignudelli, S., Benveniste, J., 2020. 12th COASTAL ALTIMETRY WORKSHOP FINAL REPORT, in: 12th COASTAL ALTIMETRY WORKSHOP FINAL REPORT.

Rio, M., Hernandez, F., 2003. High-frequency response of wind-driven currents measured by drifting buoys and altimetry over the world ocean. J. Geophys. Res. Ocean. 108.

Rio, M., Mulet, S., Picot, N., 2014. Beyond GOCE for the ocean circulation estimate: Synergetic use of altimetry, gravimetry, and in situ data provides new insight into geostrophic and Ekman currents. Geophys. Res. Lett. 41, 8918–8925.

Roarty, H., Cook, T., Hazard, L., George, D., Harlan, J., Cosoli, S., Wyatt, L., Fanjul, E.A., Terrill, E., Otero, M., Largier, J., Glenn, S., Ebuchi, N., Whitehouse, B., Bartlett, K., Mader, J., Rubio, A., Corgnati, L., Mantovani, C., Griffa, A., Reyes, E., Lorente, P., Flores-Vidal, X., Saavedra-Matta, K.J., Rogowski, P., Prukpitikul, S., Lee, S.-H., Lai, J.-W., Guerin, C.-A., Sanchez, J., Hansen, B., Grilli, S., 2019. The Global High Frequency Radar Network. Front. Mar. Sci. 6, 164. https://doi.org/https://doi.org/10.3389/fmars.2019.00164

Roesler, C.J., Emery, W.J., Kim, S.Y., 2013. Evaluating the use of high-frequency radar coastal currents to correct satellite altimetry. J. Geophys. Res. Ocean. 118, 3240–3259.

Rubio, A., Caballero, A., Orfila, A., Hernández-Carrasco, I., Ferrer, L., González, M., Solabarrieta, L., Mader, J., 2018. Eddy-induced cross-shelf export of high Chl-a coastal waters in the SE Bay of Biscay. Remote Sens. Environ. 205, 290–304. https://doi.org/https://doi.org/10.1016/j.rse.2017.10.037

Rubio, A., Fontán, A., Lazure, P., González, M., Valencia, V., Ferrer, L., Mader, J., Hernández, C., 2013a. Seasonal to tidal variability of currents and temperature in waters of the continental slope, southeastern Bay of Biscay. J. Mar. Syst. 109, S121–S133. https://doi.org/https://doi.org/10.1016/j.jmarsys.2012.01.004

Rubio, A., Hernández-Carrasco, I., Orfila, A., González, M., Reyes, E., Corgnati, L., Berta, M., Griffa, A., Mader, J., 2020. A lagrangian approach to monitor local particle retention conditions in coastal areas. copernicus marine service ocean state report. J. Oper. Ocean. 13, 10–1080.

Rubio, A., Mader, J., Corgnati, L., Mantovani, C., Griffa, A., Novellino, A., Quentin, C., Wyatt, L., Schulz-Stellenfleth, J., Horstmann, J., 2017. HF radar activity in European coastal seas: next steps toward a pan-European HF radar network. Front. Mar. Sci. 4, 8. https://doi.org/https://doi.org/10.3389/fmars.2017.00008

Rubio, A., Manso-Narvarte, I., Caballero, A., Corgnati, L., Mantovani, C., Reyes, E., Griffa, A., Mader, J., 2019. The seasonal intensification of the slope Iberian Poleward Current. In: Copernicus Marine Service Ocean State Report. J. Oper. Oceanogr. 3, 13–18.

Rubio, A., Reverdin, G., Fontán, A., González, M., Mader, J., 2011. Mapping near-inertial variability in the SE Bay of Biscay from HF radar data and two offshore moored buoys. Geophys. Res. Lett. 38. https://doi.org/https://doi.org/10.1029/2011GL048783

Rubio, A., Solabarrieta, L., González, M., Mader, J., Castanedo, S., Medina, R., Charria, G., Aranda, J.A., 2013b. Surface circulation and Lagrangian transport in the SE Bay of Biscay from HF radar data, in: 2013 MTS/IEEE OCEANS-Bergen. IEEE, pp. 1–7.

Rudnick, D.L., 2016. Ocean research enabled by underwater gliders. Ann. Rev. Mar. Sci. 8, 519–541.

Ruiz, I., Basurko, O.C., Rubio, A., Delpey, M., Granado, I., Declerck, A., Mader, J., Cózar-Cabañas, A., 2020. Litter windrows in the south-east coast of the Bay of Biscay: an ocean process enabling effective active fishing for litter. Front. Mar. Sci. 7:308.

Schmidt, R., 1986. Multiple emitter location and signal parameter estimation. IEEE Trans. Antennas Propag. 34, 276–280.

Sciascia, R., Berta, M., Carlson, D.F., Griffa, A., Panfili, M., Mesa, M. La, Corgnati, L., Mantovani, C., Domenella, E., Fredj, E., 2018. Linking sardine recruitment in coastal areas to ocean currents using surface drifters and HF radar: a case study in the Gulf of Manfredonia, Adriatic Sea. Ocean Sci. 14, 1461–1482.

Shapiro, G.I., Stanichny, S. V, Stanychna, R.R., 2010. Anatomy of shelf–deep sea exchanges by a mesoscale eddy in the North West Black Sea as derived from remotely sensed data. Remote Sens. Environ. 114, 867–875. https://doi.org/https://doi.org/10.1016/j.rse.2009.11.020

Shen, C.Y., Evans, T.E., 2002. Dynamically constrained projection for subsurface current velocity. J. Geophys. Res. Ocean. 107, 21–24.

Shen, C.Y., Evans, T.E., 2001. Surface-to-subsurface velocity projection for shallow water currents. J. Geophys. Res. Ocean. 106, 6973–6984.

Shields, P.M., Tajalli, H., 2006. Intermediate theory: The missing link in successful student scholarship. J. public Aff. Educ. 12, 313–334.

Shrira, V.I., Ivonin, D. V, Broche, P., de Maistre, J.C., 2001. On remote sensing of vertical shear of ocean surface currents by means of a Single-frequency VHF radar. Geophys. Res. Lett. 28, 3955–3958. https://doi.org/https://doi.org/10.1029/2001GL013387

Skamarock, W.C., Klemp, J.B., Dudhia, J., Gill, D.O., Barker, D.M., Wang, W., Powers, J.G., 2005. A Description of the Advanced Research WRF Version 2. NCAR Tech. Note 468STR, 88.

Smith, P.E., Flerx, W., Hewitt, R.P., 1985. The CalCOFI vertical egg tow (CalVET) net, in: Lasker, R. (Ed.), An Egg Production Method for Estimating Spawning Biomass of Pelagic Fish: Application to the Northern Anchoy (Engraulis Mordax). US Department of Commerce NOAA Tech. Rep., pp. 27–32.

Solabarrieta, L., Frolov, S., Cook, M., Paduan, J., Rubio, A., González, M., Mader, J., Charria, G., 2016. Skill assessment of hf radar–derived products for lagrangian simulations in the bay of biscay. J. Atmos. Ocean. Technol. 33, 2585–2597. https://doi.org/https://doi.org/10.1175/JTECH-D-16-0045.1

Solabarrieta, L., Rubio, A., Cárdenas, M., Castanedo, S., Esnaola, G., Méndez, F.J., Medina, R., Ferrer, L., 2015. Probabilistic relationships between wind and surface water circulation patterns in the SE Bay of Biscay. Ocean Dyn. 65, 1289–1303. https://doi.org/10.1007/s10236-015-0871-5

Solabarrieta, L., Rubio, A., Castanedo, S., Medina, R., Charria, G., Hernández, C., 2014. Surface water circulation patterns in the southeastern Bay of Biscay: New evidences from HF radar data. Cont. Shelf Res. 74, 60–76. https://doi.org/https://doi.org/10.1016/j.csr.2013.11.022

Somavilla, R., González-Pola, C., Rodriguez, C., Josey, S.A., Sánchez, R.F., Lavín, A., 2009. Large changes in the hydrographic structure of the Bay of Biscay after the extreme mixing of winter 2005. J. Geophys. Res. Ocean. 114.

Sotillo, M.G., Cailleau, S., Lorente, P., Levier, B., Aznar, R., Reffray, G., Amo-Baladrón, A., Chanut, J., Benkiran, M., Alvarez-Fanjul, E., 2015. The MyOcean IBI Ocean Forecast and Reanalysis Systems: operational products and roadmap to the future Copernicus Service. J. Oper. Oceanogr. 8, 63–79. https://doi.org/https://doi.org/10.1080/1755876X.2015.1014663

Stewart, R.H., 2008. Introduction to physical oceanography. Robert H. Stewart.

Stewart, R.H., Joy, J.W., 1974. HF radio measurements of surface currents, in: Deep Sea Research and Oceanographic Abstracts. Elsevier, pp. 1039–1049. https://doi.org/https://doi.org/10.1016/0011-7471(74)90066-7

Taillandier, V., Griffa, A., Molcard, A., 2006. A variational approach for the reconstruction of regional scale Eulerian velocity fields from Lagrangian data. Ocean Model. 13, 1–24. https://doi.org/https://doi.org/10.1016/j.ocemod.2005.09.002

Teague, C.C., Vesecky, J.F., Hallock, Z.R., 2001. A comparison of multifrequency HF radar and ADCP measurements of near-surface currents during COPE-3. IEEE J. Ocean. Eng. 26, 399–405. https://doi.org/https://doi.org/10.1109/48.946513

Teles-Machado, A., Peliz, Á., McWilliams, J.C., Dubert, J., Le Cann, B., 2016. Circulation on the northwestern Iberian margin: Swoddies. Prog. Oceanogr. 140, 116–133. https://doi.org/https://doi.org/10.1016/j.pocean.2015.09.011

Tintoré, J., Vizoso, G., Casas, B., Heslop, E., Pascual, A., Orfila, A., Ruiz, S., Martínez-Ledesma, M., Torner, M., Cusí, S., Diedrich, A., Balaguer, P., Gómez-Pujol, L., Álvarez-Ellacuría, A., Gómara, S., Sebastian, K., Lora, S., Beltrán, J.P., Renault, L., Juzà, M., Álvarez, D., March, D., Garau, B., Castilla, C., Cañellas, T., Roque, D., Lizarán, I., Pitarch, S., Carrasco, M.A., Lana, A., Mason, E., Escudier, R., Conti, D., Sayol, J.M., Barceló, B., Alemany, F., Reglero, P., Massuti, E., Velez-Belchí, P., Ruiz, J., Gómez, M., Álvarez, A., Ansorena, L., Manríquez, M., 2013. SOCIB: the Balearic Islands coastal ocean observing and forecasting system responding to science, technology and society needs. Mar. Technol. Soc. J. 47, 101–117.

Troupin, C., Pascual, A., Valladeau, G., Pujol, I., Lana, A., Heslop, E., Ruiz, S., Torner, M., Picot, N., Tintoré, J., 2015. Illustration of the emerging capabilities of SARAL/AltiKa in the coastal zone using a multi-platform approach. Adv. Sp. Res. 55, 51–59.

Uriarte, A., Sagarminaga, Y., Scalabrin, C., Valencia, V., Cermeño, P., De Miguel, E., Gómez Sánchez, J.A., Jiménez, M., 2001. Ecology of anchovy juveniles in the Bay of Biscay 4 months after peak spawning: do they form part of the plankton. ICES C. 20.

Valencia, V., Franco, J., Borja, A., Fontán, A., 2004. Hydrography of the southeastern Bay of Biscay. Oceanogr. Mar. Environ. Basqu. Country. Elsevier Oceanogr. Ser. 70, 159–194.

Van Sebille, E., England, M.H., Froyland, G., 2012. Origin, dynamics and evolution of ocean garbage patches from observed surface drifters. Environ. Res. Lett. 7, 44040.

Van Sebille, E., Griffies, S.M., Abernathey, R., Adams, T.P., Berloff, P., Biastoch, A., Blanke, B., Chassignet, E.P., Cheng, Y., Cotter, C.J., 2018. Lagrangian ocean analysis: Fundamentals and practices. Ocean Model. 121, 49–75.

Wyatt, L.R., 2014. High frequency radar applications in coastal monitoring, planning and engineering. Aust. J. Civ. Eng. 12, 1–15.

Yaremchuk, M., Sentchev, A., 2009. Mapping radar-derived sea surface currents with a variational method. Cont. Shelf Res. 29, 1711–1722. https://doi.org/https://doi.org/10.1016/j.csr.2009.05.016

Zhao, M., Timmermans, M., 2015. Vertical scales and dynamics of eddies in the Arctic Ocean's Canada Basin. J. Geophys. Res. Ocean. 120, 8195–8209. https://doi.org/https://doi.org/10.1002/2015JC011251

APPENDICES

CHAPTER 5 – APPENDIX A

Appendix A1: HFR and ADCP observations temporal cross-correlations

Real HFR and ADCP observations data. Temporal cross-correlations with a confidence level of 99%. All the available data series of each dataset were used. The results presented here complement the results shown in Rubio et al. (2019).

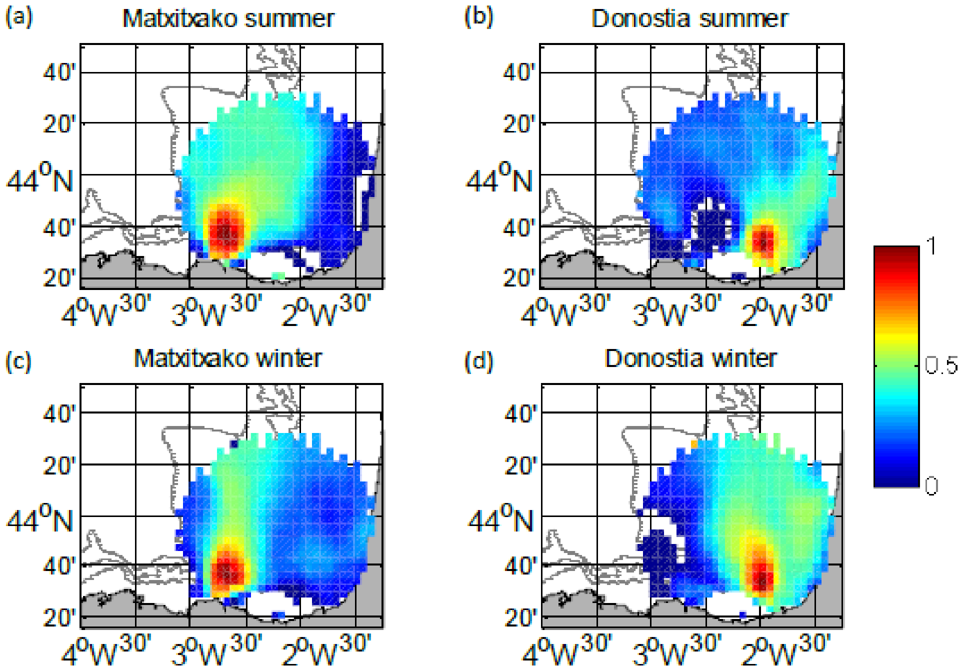

Figure A1. *Temporal cross-correlation maps between the 48h-low-pass filtered time series of the HFR at Matxitxako (a, c) and Donostia (b, d) locations and the rest of the nodes within the HFR footprint area for V and for each season: summer (a, b) and winter (c, d). The results for the U component are shown in Rubio et al. (2019).*

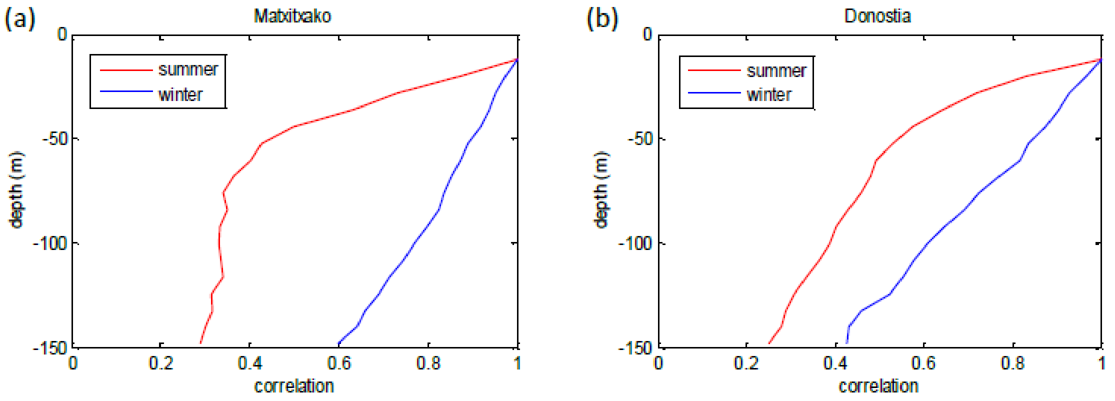

Figure A2. *Low-pass filtered ADCP temporal V cross-correlations between the first bin (-12.26 m) and the rest of the bins along the water column for Matxitxako (a) and Donostia (b) for the summer (stratified) and winter (well-mixed) periods. The results for U are shown in Rubio et al. (2019).*

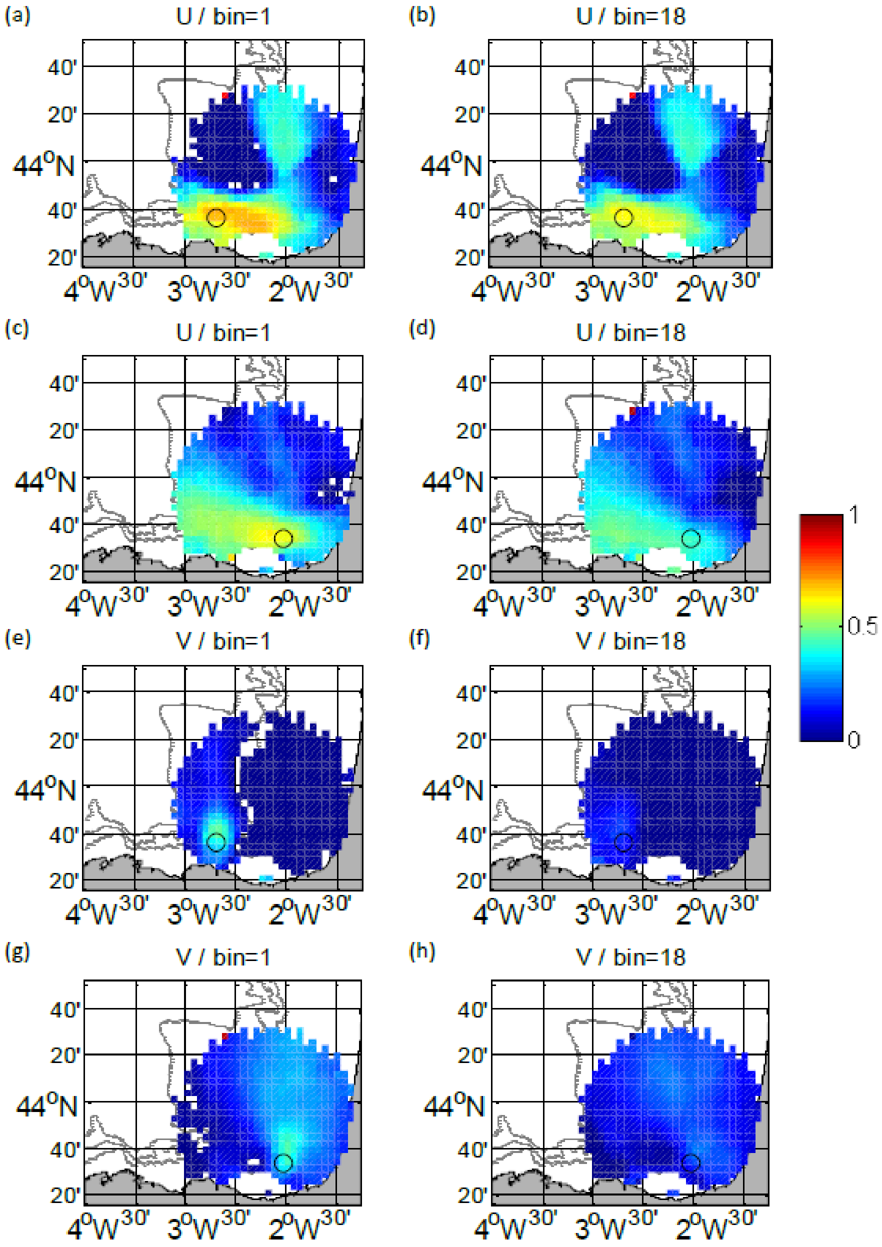

Figure A3. *Temporal cross-correlation maps between the low-pass filtered time series of the HFR at the surface and the low-pass filtered ADCP time series for the bin 1 (-12.26m) (a, c, e, g) and 18 (-148.26m) (b, d, f, h) at Matxitxako (a, b, e, f) and at Donostia (c, d, g, h) and for U (a, b, c, d) and V (e, f, g, h). The black circles depict the positions of the ADCPs.*

Appendix A2: RRMSD maps for ROOI with GLORYS-HR

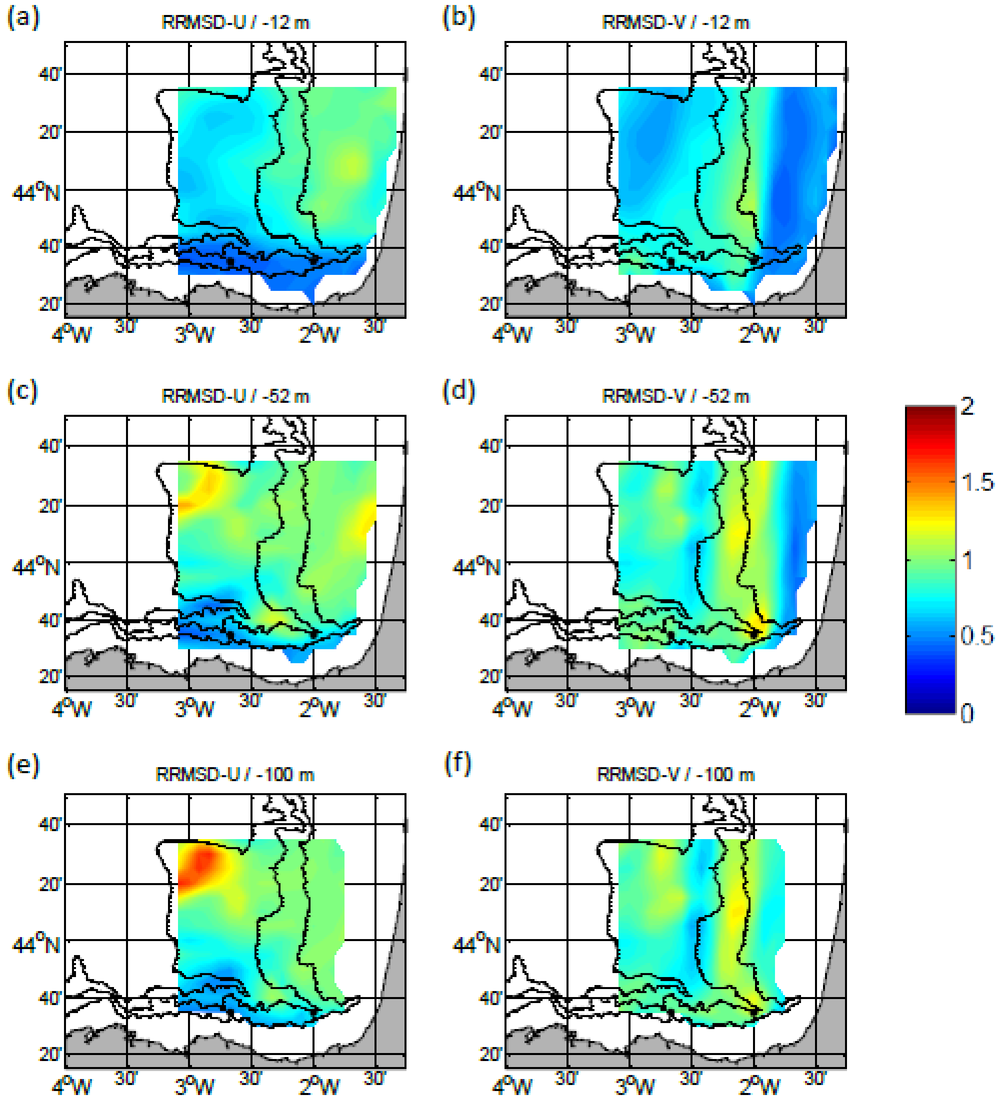

Figure A4. *RRMSD maps for the summer period between the reference fields and the outputs of the ROOI with GLORYS-HR for U (a, c, e) and V (b, d, f). Different depths considered: -12 m (a, b), -52 m (c, d) and -100 m (e, f). The black dots depict the locations of the current vertical profiles.*

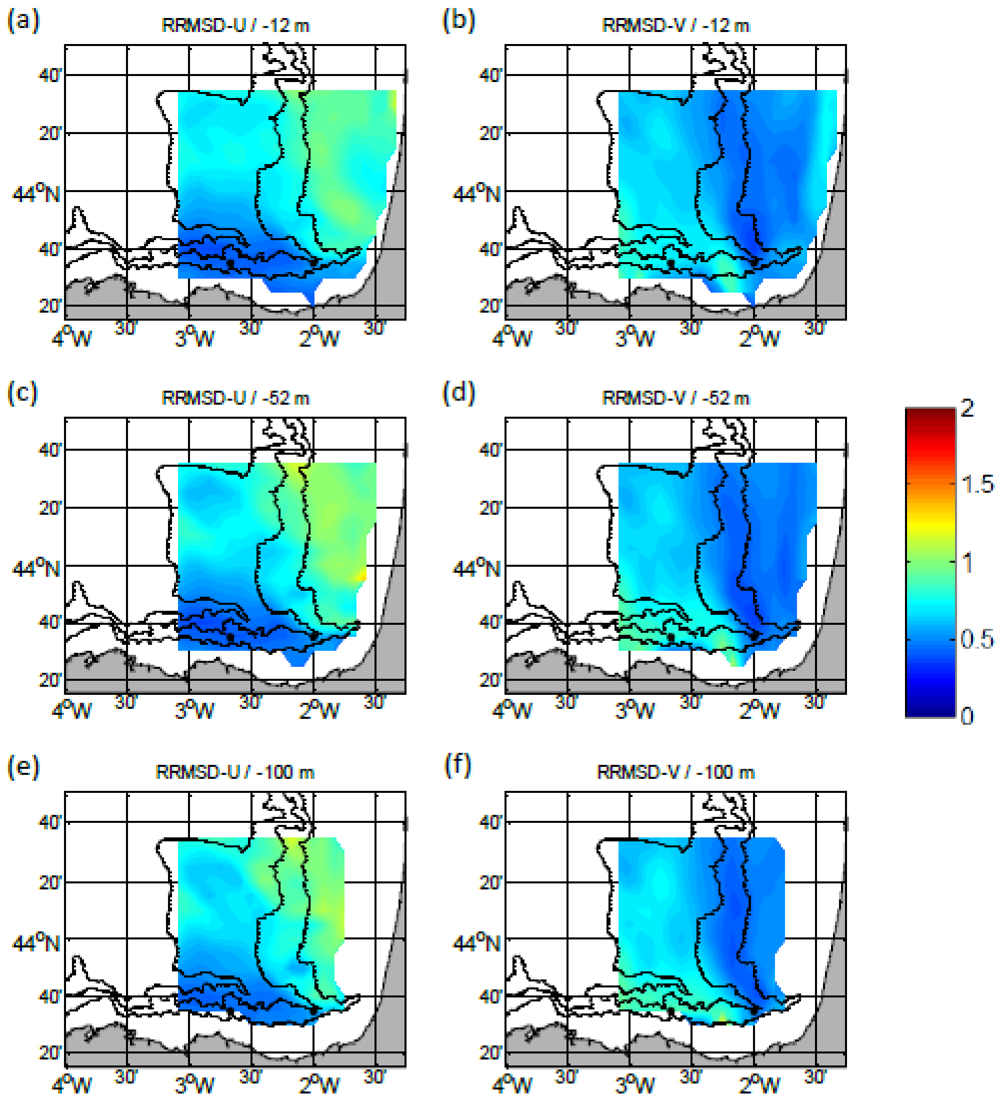

Figure A5. *RRMSD maps for the winter period between the reference fields and the outputs of the ROOI with GLORYS-HR for U (a, c, e) and V (b, d, f). Different depths considered: -12 m (a, b), -52 m (c, d) and -100 m (e, f). The black dots depict the locations of the current vertical profiles.*

Appendix A3: DCT-PLS RRMSD-U maps with higher colorbar values

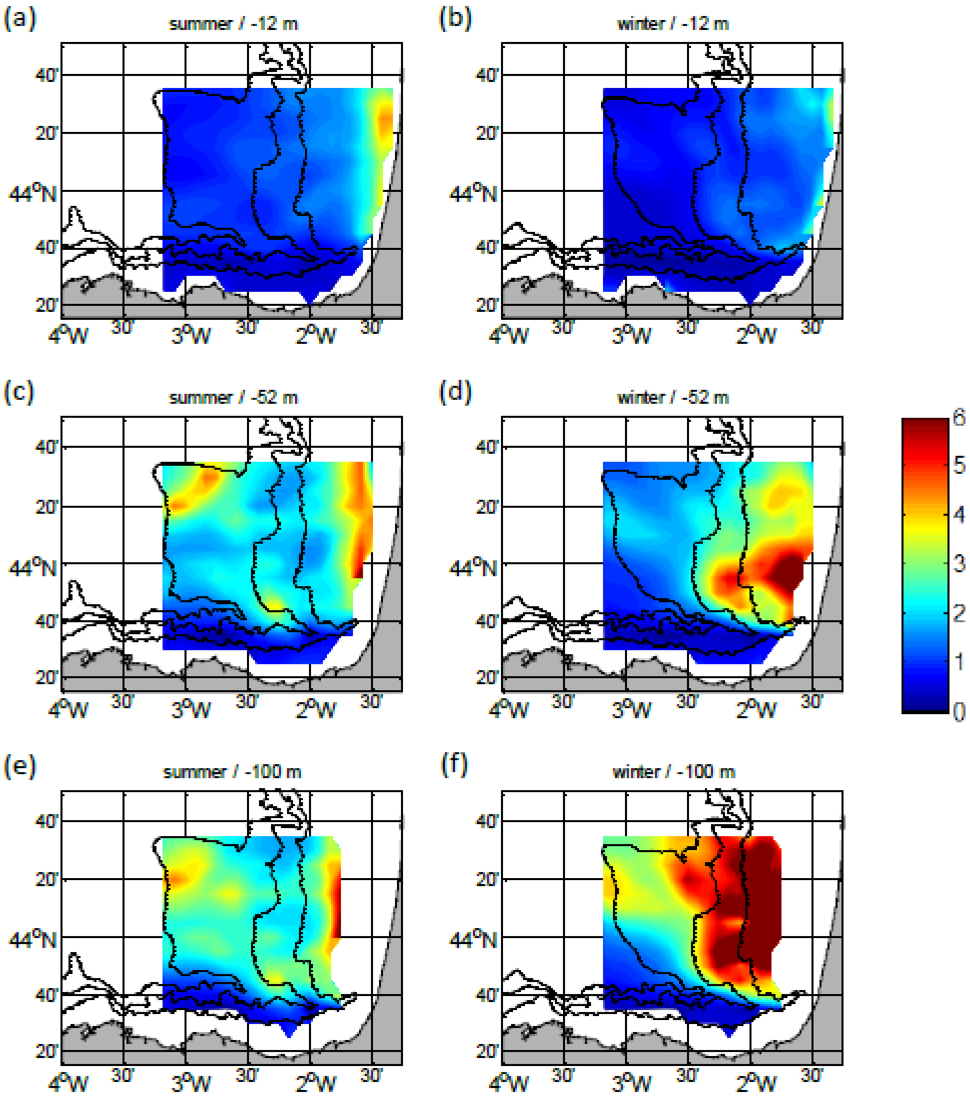

Figure A6. RRMSD-U maps for DCT-PLS for the summer period (a, c, e) and for the winter period (b, d, f).

Appendix A4: RMSD maps and spatial mean RMSD graphs

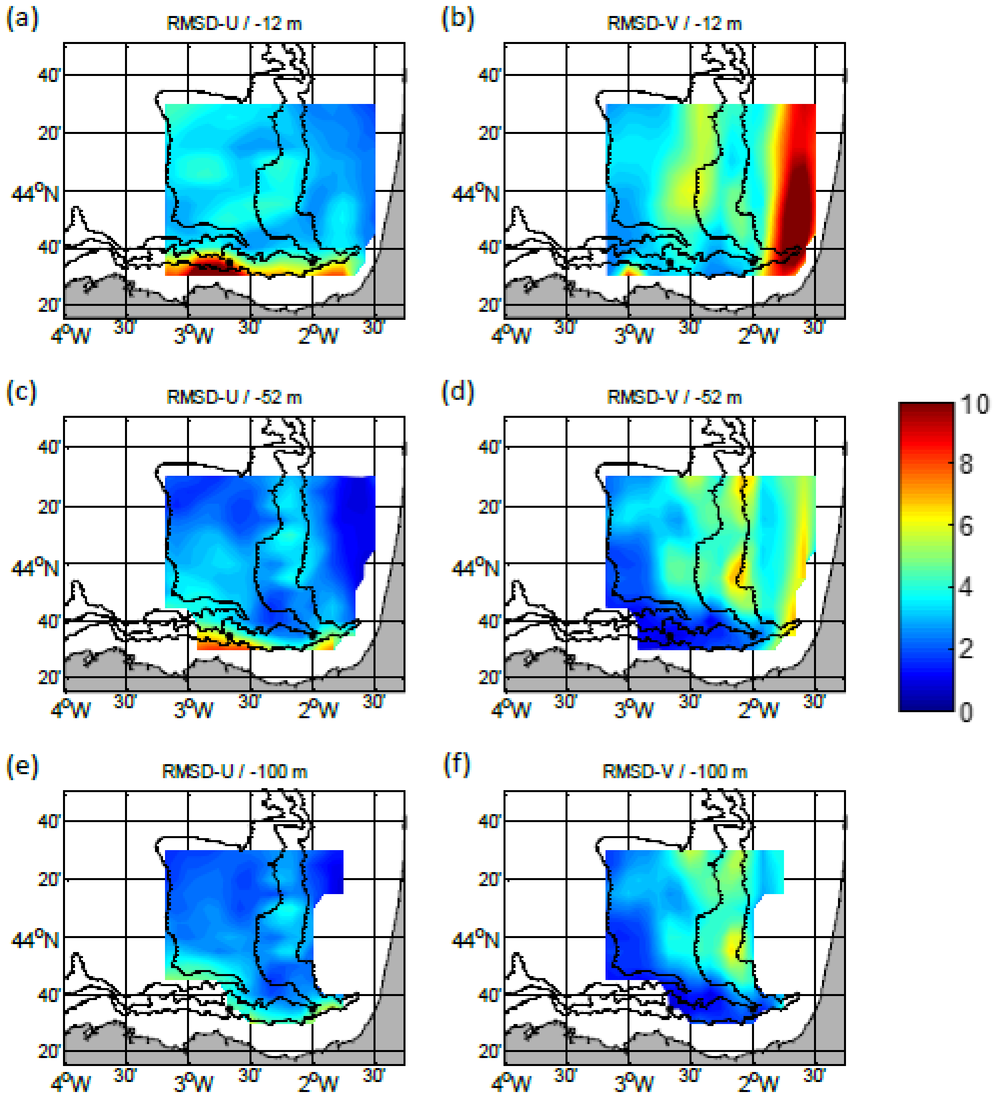

Figure A7. *RMSD maps for the summer period between the reference fields and the outputs of the ROOI with GLORYS-LR for U (a, c, e) and V (b, d, f). Different depths considered: -12 m (a, b), -52 m (c, d) and -100 m (e, f). The black dots depict the locations of the current vertical profiles.*

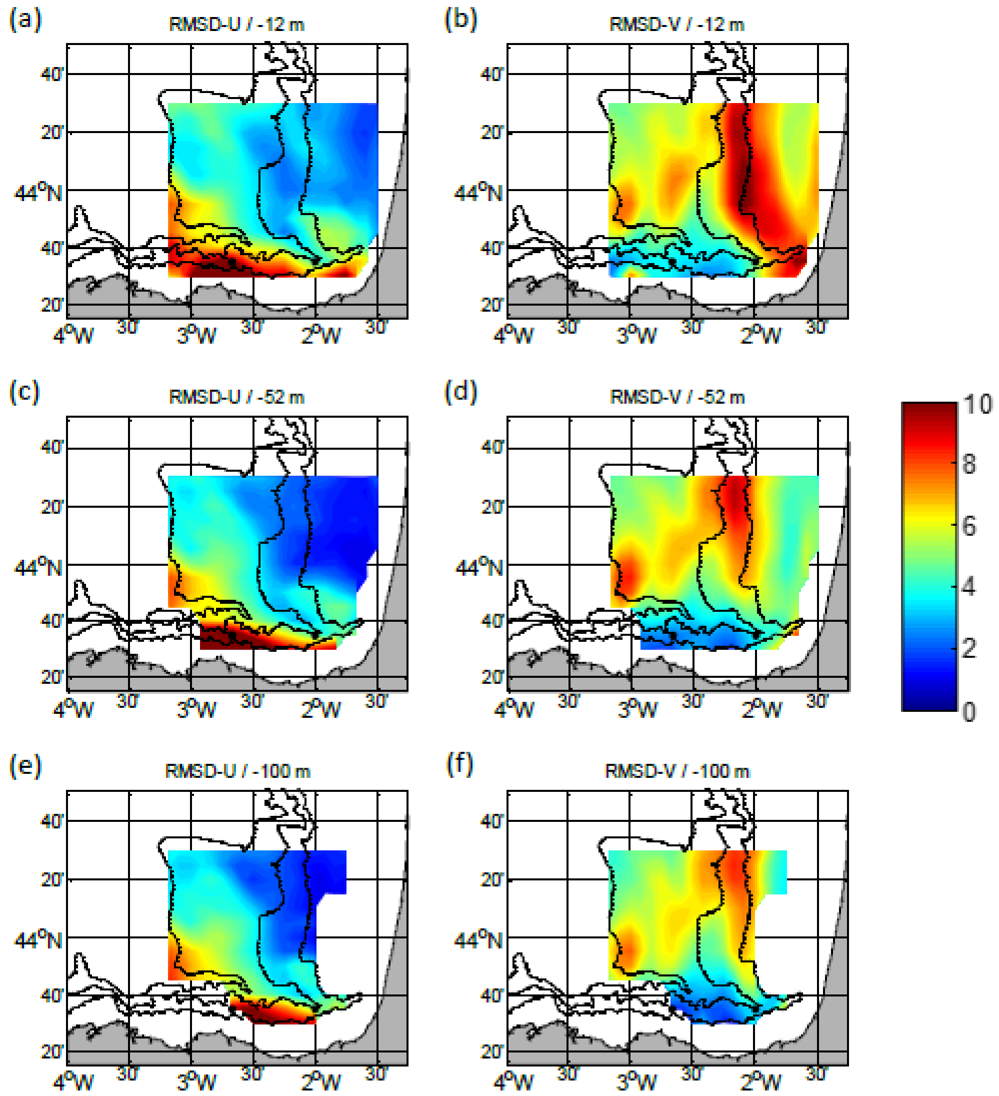

Figure A8. *RMSD maps for the winter period between the reference fields and the outputs of the ROOI with GLORYS-LR for U (a, c, e) and V (b, d, f). Different depths considered: -12 m (a, b), -52 m (c, d) and -100 m (e, f). The black dots depict the locations of the current vertical profiles.*

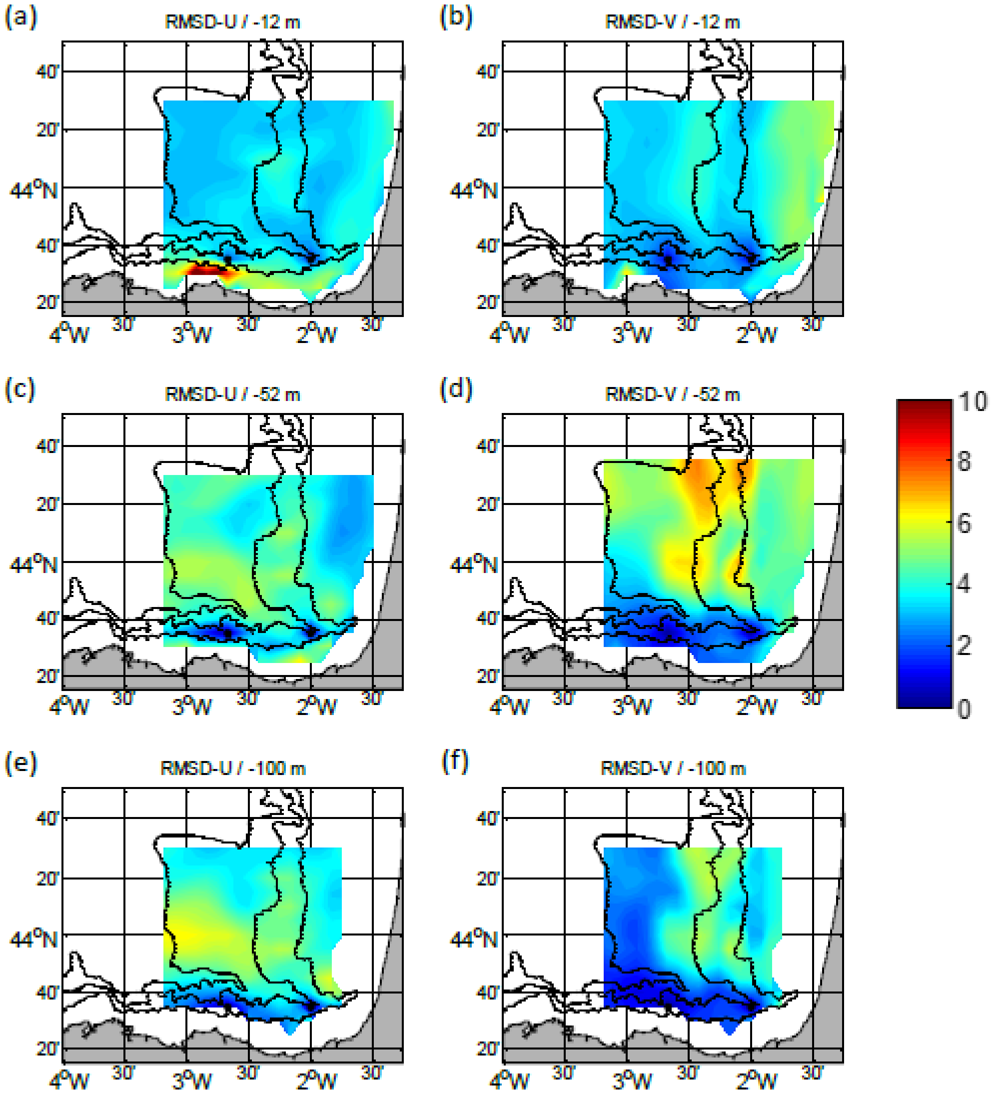

Figure A9. *RMSD maps for the summer period between the reference fields and the outputs of the DCT-PLS for U (a, c, e) and V (b, d, f). Different depths considered: -12 m (a, b), -52 m (c, d) and -100 m (e, f). The black dots depict the locations of the current vertical profiles.*

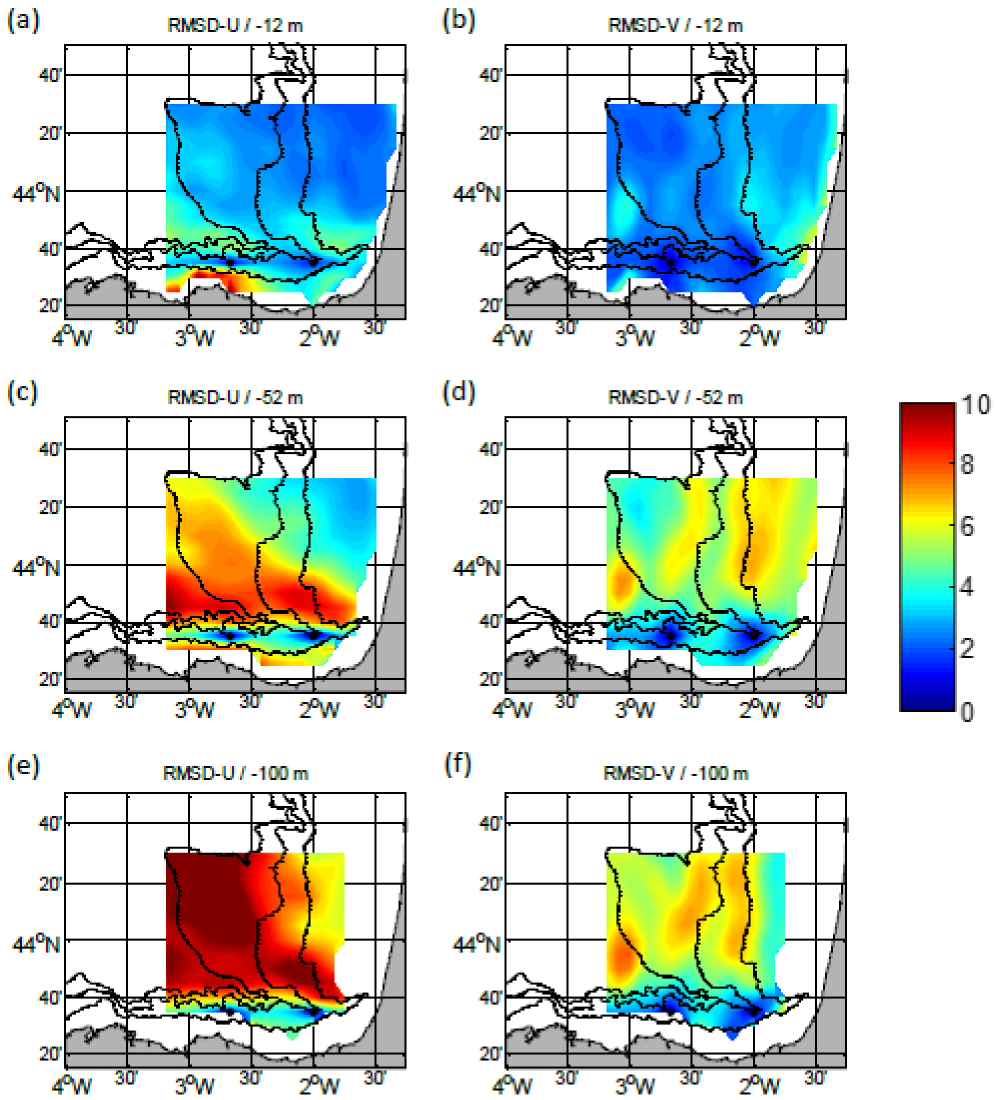

Figure A10. *RMSD maps for the winter period between the reference fields and the outputs of the DCT-PLS for U (a, c, e) and V (b, d, f). Different depths considered: -12 m (a, b), -52 m (c, d) and -100 m (e, f). The black dots depict the locations of the current vertical profiles.*

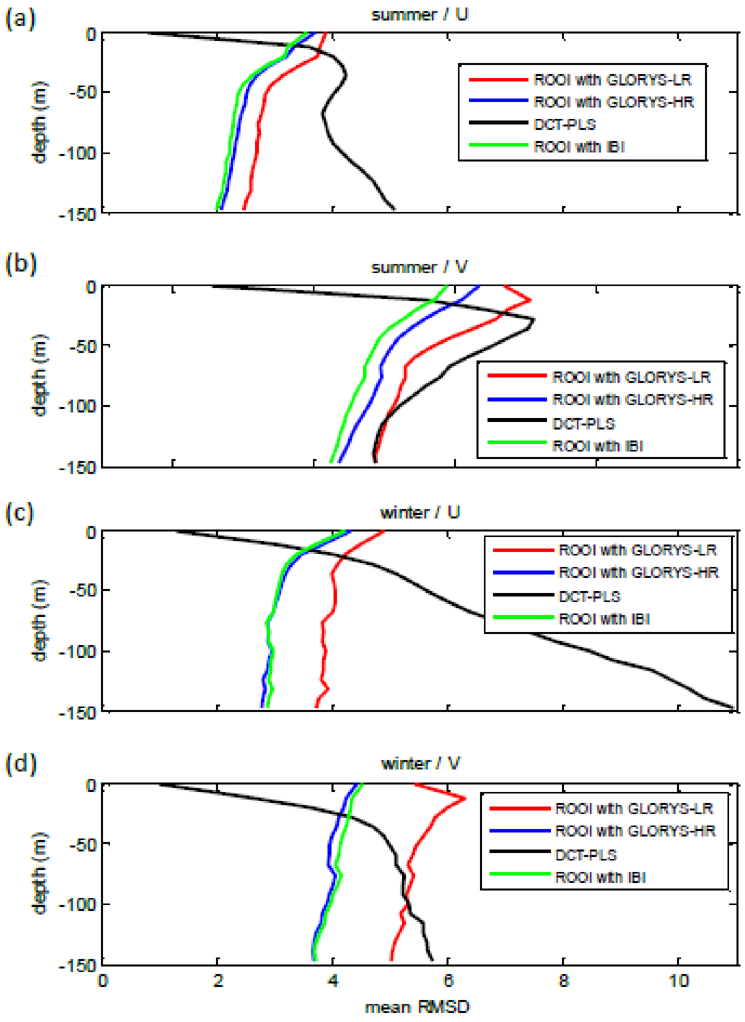

Figure A11. *Mean RMSDs related to all the data-reconstruction methods for each depth considering the entire grid. For the summer period (a, b) and for the winter period (c, d). U in a, c and V in b, d.*

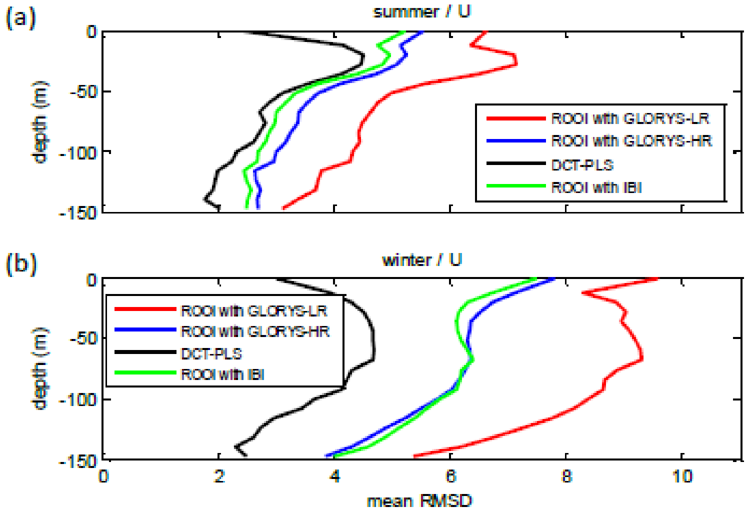

Figure A12. *Mean RMSD-U related to all the data-reconstruction methods for each depth considering the reduced grid domain. For the summer period (a) and for the winter period (b).*

Appendix A5: Correlation between two variables

The correlation (R) between two variables x_1 and x_2 is defined as follows:

$$R(x_1,x_2) = \frac{E[(x_1-\mu_1)\cdot(x_2-\mu_2)]}{\sqrt{E[(x_1-\mu_1)\cdot(x_1-\mu_1)]\cdot E[(x_2-\mu_2)\cdot(x_2-\mu_2)]}}$$

where μ_i is the mean value of x_i, that is, $\mu_i = E[x_i]$. In this study, the correlation was used to estimate the relationships between the emulated horizontal currents in two different ways: by means of spatial relationships, determined by spatial correlation length scales (horizontal and vertical), and by means of temporal relationships, determined by temporal cross-correlations between two different points for a certain period of time. Note that for all the correlations presented here the confidence level considered is 95 %.

The spatial correlation length scales are the maximum distances between the grid points where the currents can be considered that are related. These scales were calculated for each velocity component, considering meridional and zonal directions for the computation by means of the e-folding method (described in Ha et al., 2007). If we consider one grid, one velocity component and one direction for the computation we can obtain one R value for each fixed distance between the grid points. That is, if we consider the zonal direction and the U component, x_1 will be the value of U at each grid point and x_2 will be the value of U at the grid point that is at a fixed distance away (a certain number of grid points in the zonal direction) from the grid point where x_1 is evaluated. Therefore, we will obtain one R value for a fixed distance. Then, R is estimated for all the possible distances, thus obtaining correlation values depending on the distance between the grid points. This operation can be repeated for different time steps through a time period, obtaining a correlation vs distance profile for each time step. All these profiles are then averaged for the time period that interests us, obtaining an averaged correlation vs distance profile. In order to determine the spatial correlation length scale, as explained in Ha et al. (2007), a cut-off point is assumed in the averaged profile where the correlation coefficient decrease to e^{-1} times its original value.

Regarding the temporal relationships, the temporal cross-correlation is defined as the correlation of a variable (or two different variables) between two different points of a grid for a period of time, that is, the correlation value R between a variable at one point (x_1) and a variable at another point (x_2) throughout the period of time analysed.

CHAPTER 6 – APPENDIX B

Appendix B1: Input variables

Figure B1 shows how the observations at each period (P1, P2, P3) look like. Note that only the current velocities of the HFR and the σ_θ of the gliders are depicted here, since the mooring provides data (ADCP and CT) in a distant point and therefore is less relevant for the reconstruction. As explained in *Section 2.2.2*, the observations were adapted to a maximum temporal resolution of a day.

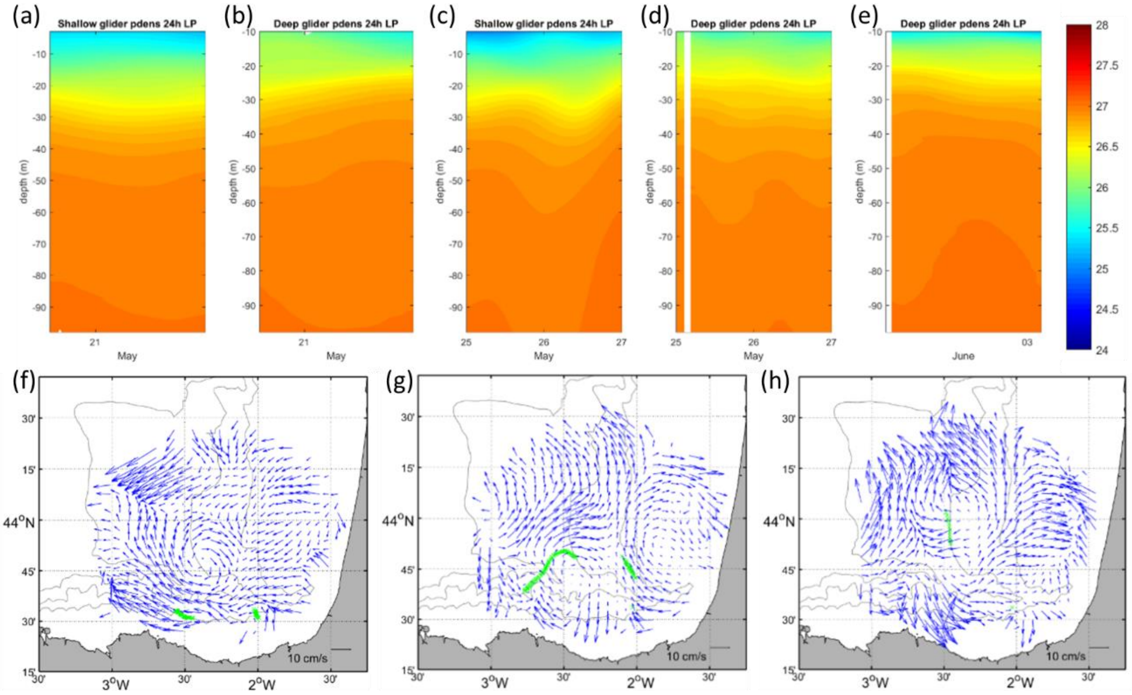

Figure B1. *(a-e) Glider σ_θ (kg m^{-3}) and (f-h) HFR current velocity (cm s^{-1}) observations used for the 3D reconstruction for the 3 periods. (a) and (b) are the filtered shallow and deep glider profiles used in P1, respectively. (c) and (d) are the filtered shallow and deep glider profiles used in P2, respectively. (e) is the filtered deep glider profile used in P3. (f), (g), and (h) are the mean HFR fields used in P1, P2, and P3, respectively. The green crosses show the locations of the glider observations at each period and the position of the mooring. The gray lines show the 200, 1000, and 2000 m isobaths.*

Appendix B2: Sensitivity tests

In this section, the results of some sensitivity tests carried out with different error parameters are shown for each period. Finally, in P1, ε_{vel}^{obs}= 2 cm s^{-1} and ε_{pd}^{obs}= 0.4 kg m^{-3} seem to be the best options, whereas in P2 and P3, ε_{vel}^{obs}= 2 cm s^{-1} and ε_{pd}^{obs}= 0.1 kg m^{-3}. In P1, ε_{pd}^{obs} was higher than for the other periods since the eddy signal was only on the HFR observations and therefore it was necessary to give more weight to those observations for a clearer reconstruction of the eddy.

For P1:

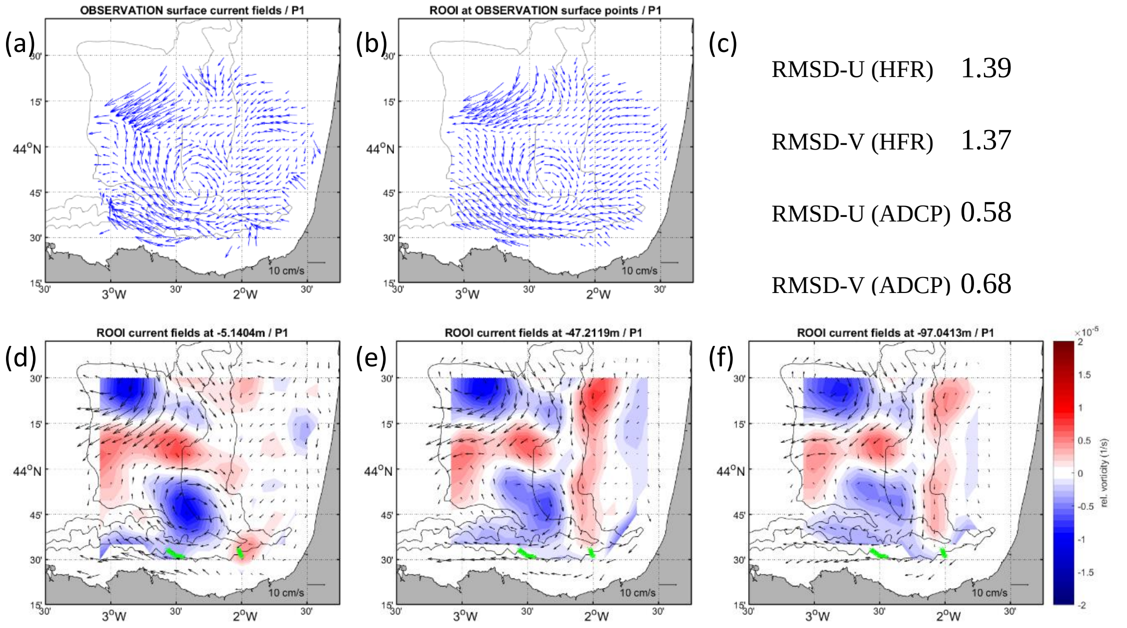

RMSD-U (HFR)	1.39
RMSD-V (HFR)	1.37
RMSD-U (ADCP)	0.58
RMSD-V (ADCP)	0.68

Figure B2. *Reconstructions with* ε_{vel}^{obs}= 2 cm s^{-1} *and* ε_{pd}^{obs}= 0.4 kg m^{-3}. *(a) HFR observation at P1. (b) reconstructed field at HFR observation points. (d-f) reconstructed current velocity fields at −5, −47, and −97 m depth levels respectively with the relative vorticity overlaid. The green crosses show the position of the gliders and mooring observations. The gray lines show the 200, 1000, and 2000 m isobaths. (c) RMSDs between the reconstructed and observed current velocities at the HFR and ADCP observation points (in cm* s^{-1}*).*

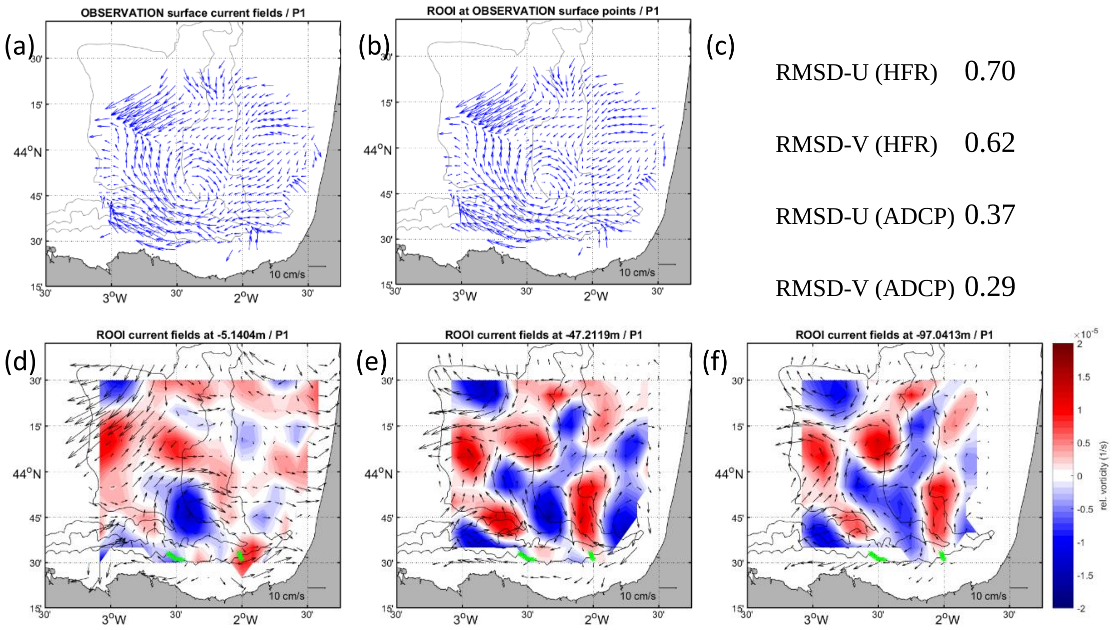

Figure B3. *The same as Figure B2 with* $\varepsilon_{vel}^{obs} = 0.2$ *cm s*$^{-1}$ *and* $\varepsilon_{pd}^{obs} = 0.1$ *kg m*$^{-3}$.

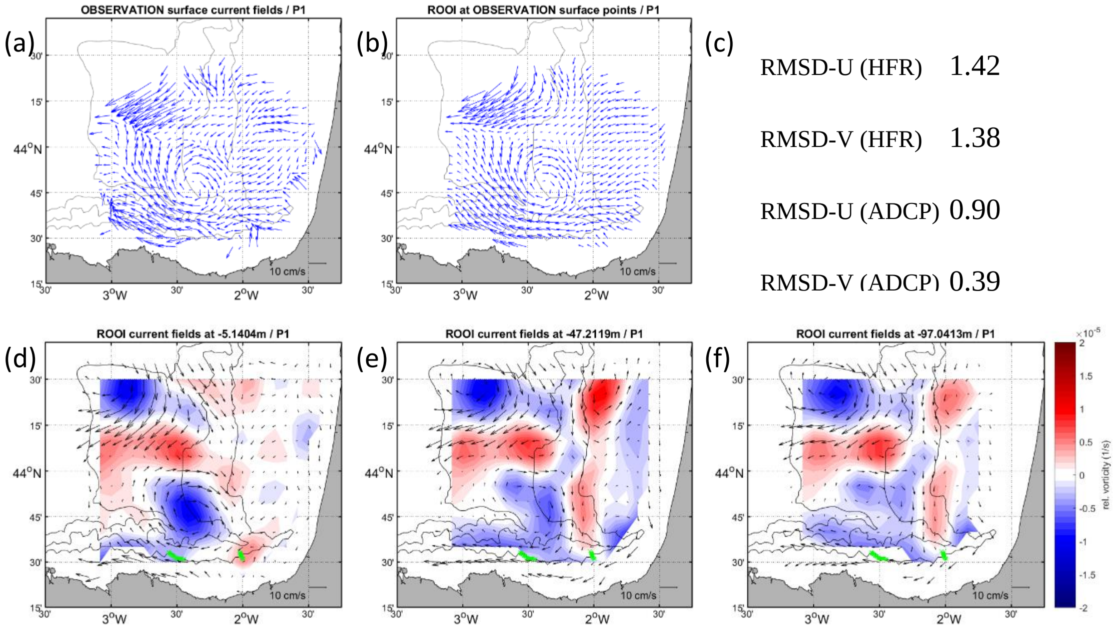

Figure B4. *The same as Figure B2 with* $\varepsilon_{vel}^{obs} = 2$ *cm s*$^{-1}$ *and* $\varepsilon_{pd}^{obs} = 0.1$ *kg m*$^{-3}$.

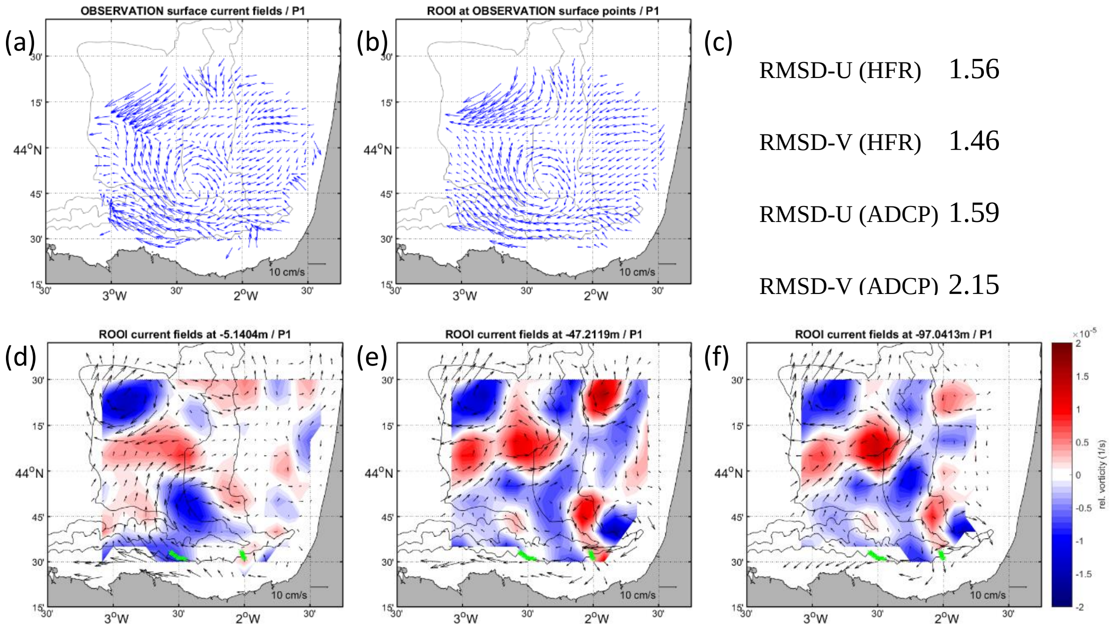

RMSD-U (HFR)	1.56
RMSD-V (HFR)	1.46
RMSD-U (ADCP)	1.59
RMSD-V (ADCP)	2.15

Figure B5. *The same as Figure B2 with* $\varepsilon_{vel}^{obs} = 2$ *cm* s^{-1} *and* $\varepsilon_{pd}^{obs} = 0.01$ *kg* m^{-3}.

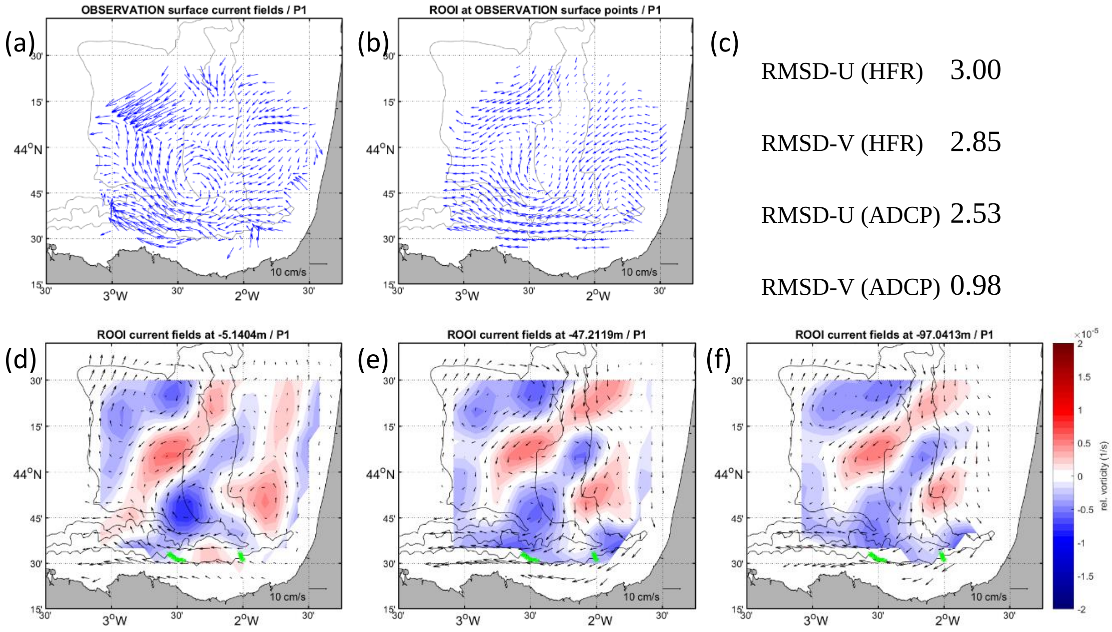

RMSD-U (HFR)	3.00
RMSD-V (HFR)	2.85
RMSD-U (ADCP)	2.53
RMSD-V (ADCP)	0.98

Figure B6. *The same as Figure B2 with* $\varepsilon_{vel}^{obs} = 20$ *cm* s^{-1} *and* $\varepsilon_{pd}^{obs} = 0.1$ *kg* m^{-3}.

For P2:

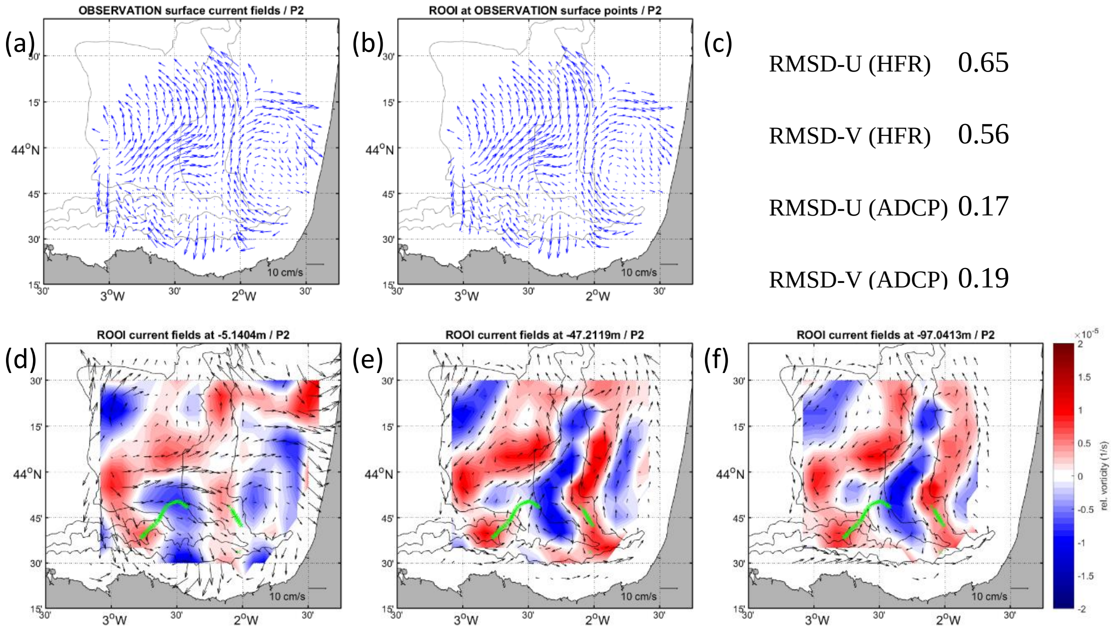

Figure B7. *The same as Figure B2 with* $\varepsilon_{vel}^{obs} = 0.2$ *cm* s^{-1} *and* $\varepsilon_{pd}^{obs} = 0.1$ *kg* m^{-3} *and for P2.*

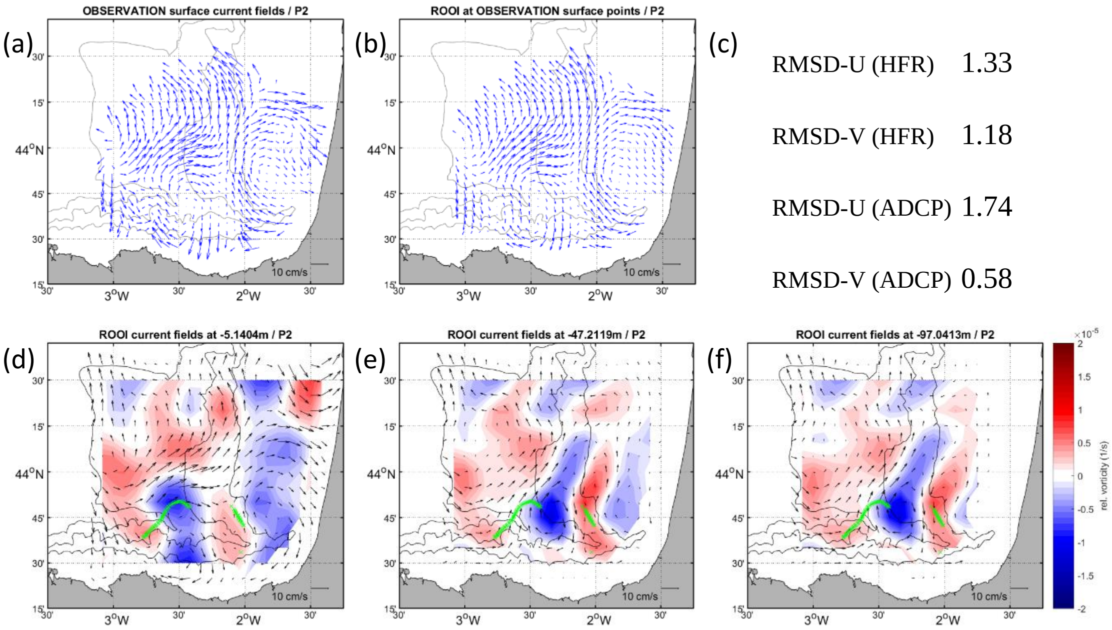

Figure B8. *The same as Figure B2 with* $\varepsilon_{vel}^{obs} = 2$ *cm* s^{-1} *and* $\varepsilon_{pd}^{obs} = 0.1$ *kg* m^{-3} *and for P2.*

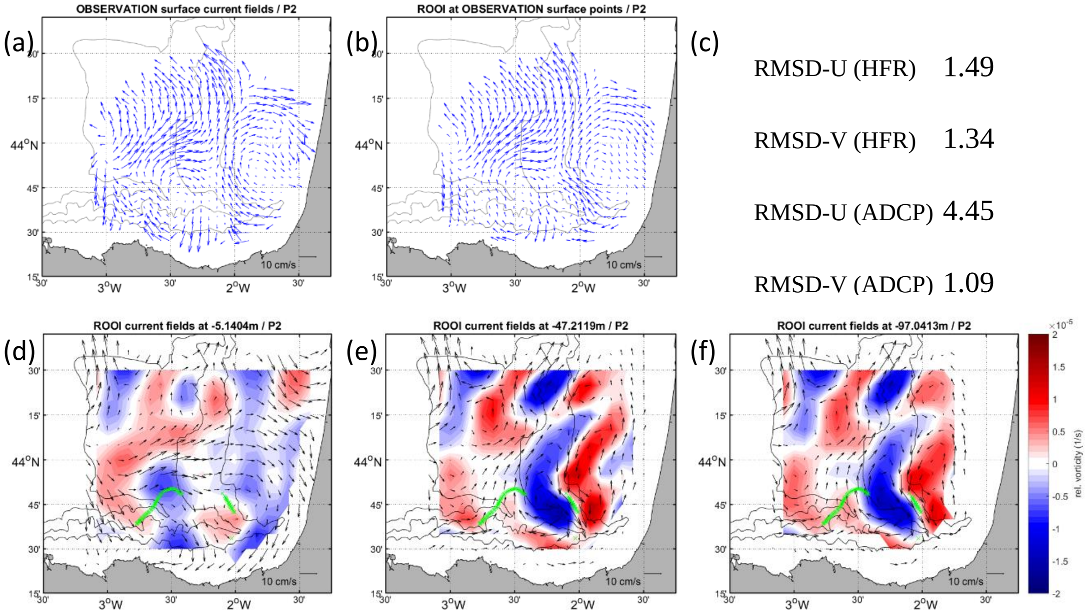

RMSD-U (HFR)	1.49
RMSD-V (HFR)	1.34
RMSD-U (ADCP)	4.45
RMSD-V (ADCP)	1.09

Figure B9. *The same as Figure B2 with* ε_{vel}^{obs} *= 2 cm s*$^{-1}$ *and* ε_{pd}^{obs} *= 0.01 kg m*$^{-3}$ *and for P2.*

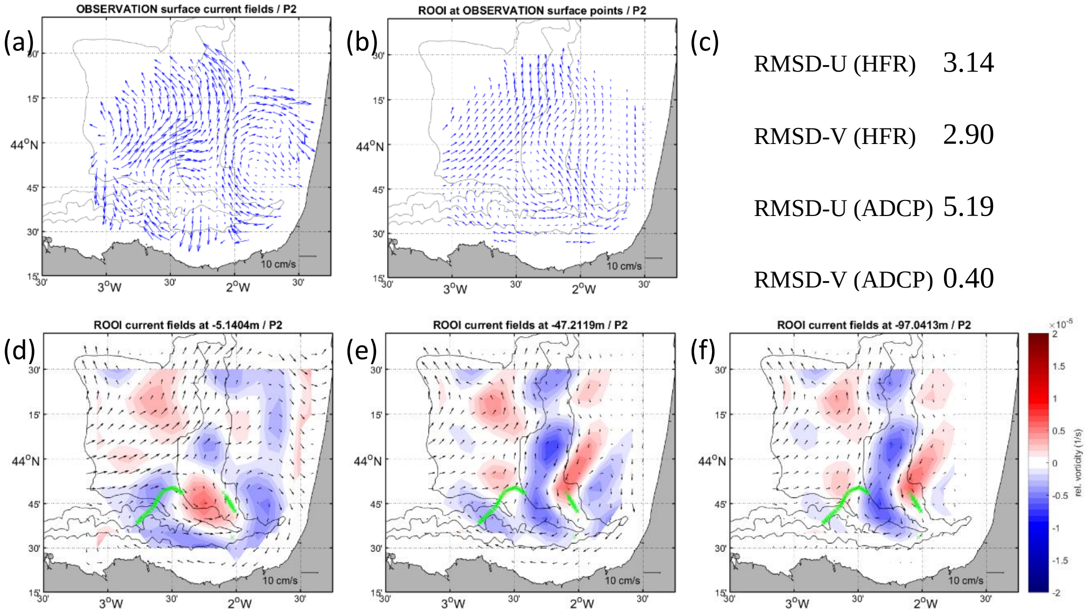

RMSD-U (HFR)	3.14
RMSD-V (HFR)	2.90
RMSD-U (ADCP)	5.19
RMSD-V (ADCP)	0.40

Figure B10. *The same as Figure B2 with* ε_{vel}^{obs} *= 20 cm s*$^{-1}$ *and* ε_{pd}^{obs} *= 0.1 kg m*$^{-3}$ *and for P2.*

For P3:

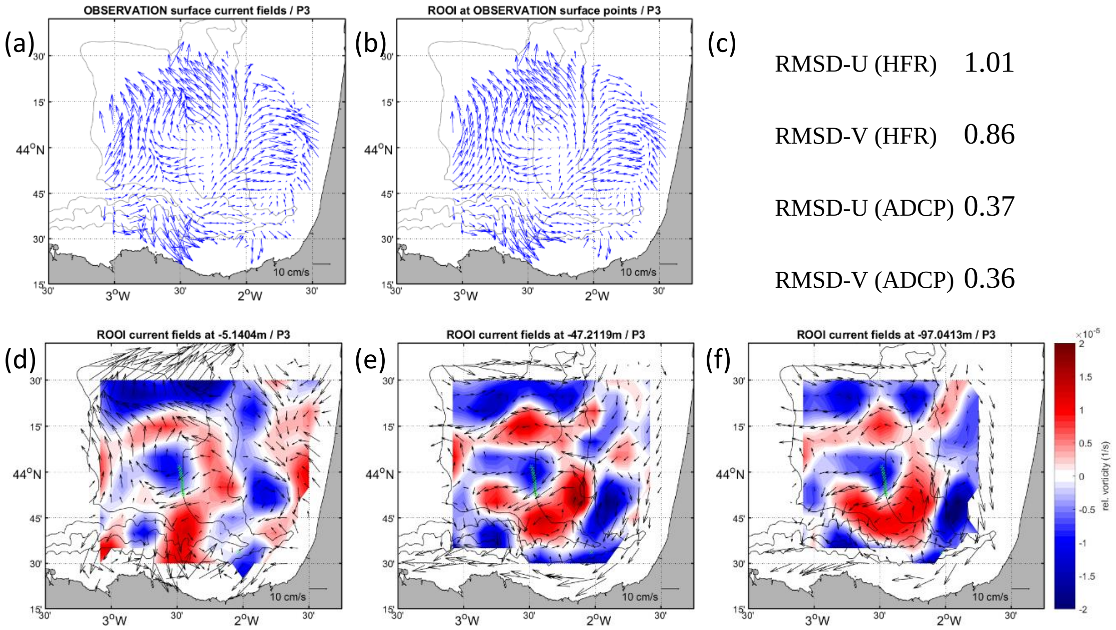

RMSD-U (HFR)	1.01
RMSD-V (HFR)	0.86
RMSD-U (ADCP)	0.37
RMSD-V (ADCP)	0.36

Figure B11. *The same as Figure B2 with* $\varepsilon_{vel}^{obs} = 0.2\ \mathrm{cm\ s^{-1}}$ *and* $\varepsilon_{pd}^{obs} = 0.1\ \mathrm{kg\ m^{-3}}$ *and for P3.*

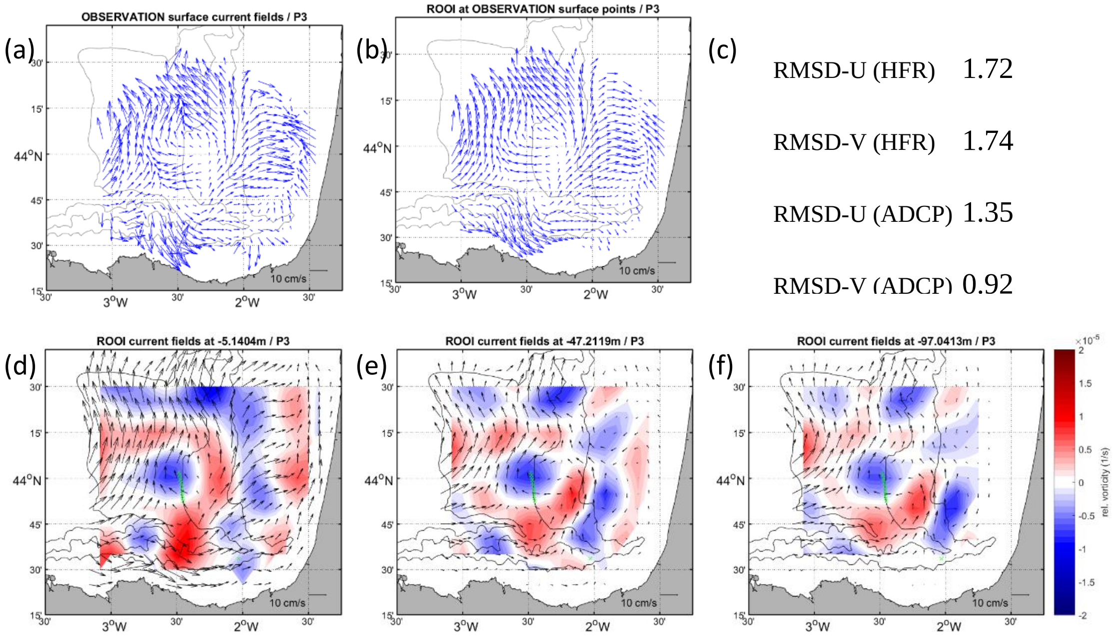

RMSD-U (HFR)	1.72
RMSD-V (HFR)	1.74
RMSD-U (ADCP)	1.35
RMSD-V (ADCP)	0.92

Figure B12. *The same as Figure B2 with* $\varepsilon_{vel}^{obs} = 2\ \mathrm{cm\ s^{-1}}$ *and* $\varepsilon_{pd}^{obs} = 0.1\ \mathrm{kg\ m^{-3}}$ *and for P3.*

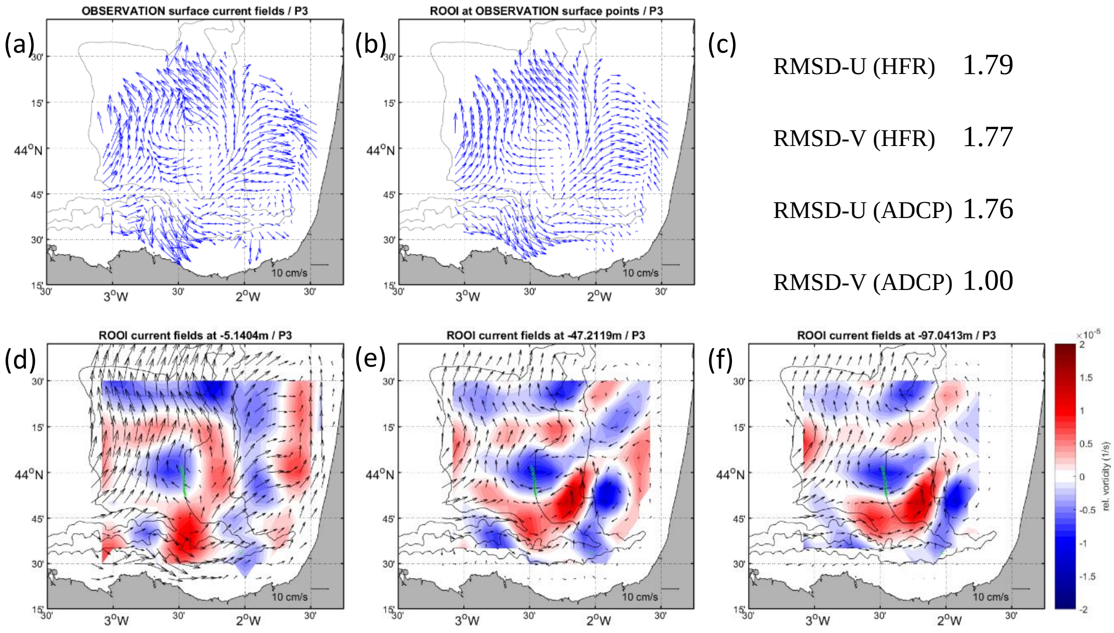

RMSD-U (HFR) 1.79

RMSD-V (HFR) 1.77

RMSD-U (ADCP) 1.76

RMSD-V (ADCP) 1.00

Figure B13. *The same as Figure B2 with* $\varepsilon_{vel}^{obs} = 2\ cm\ s^{-1}$ *and* $\varepsilon_{pd}^{obs} = 0.01\ kg\ m^{-3}$ *and for P3.*

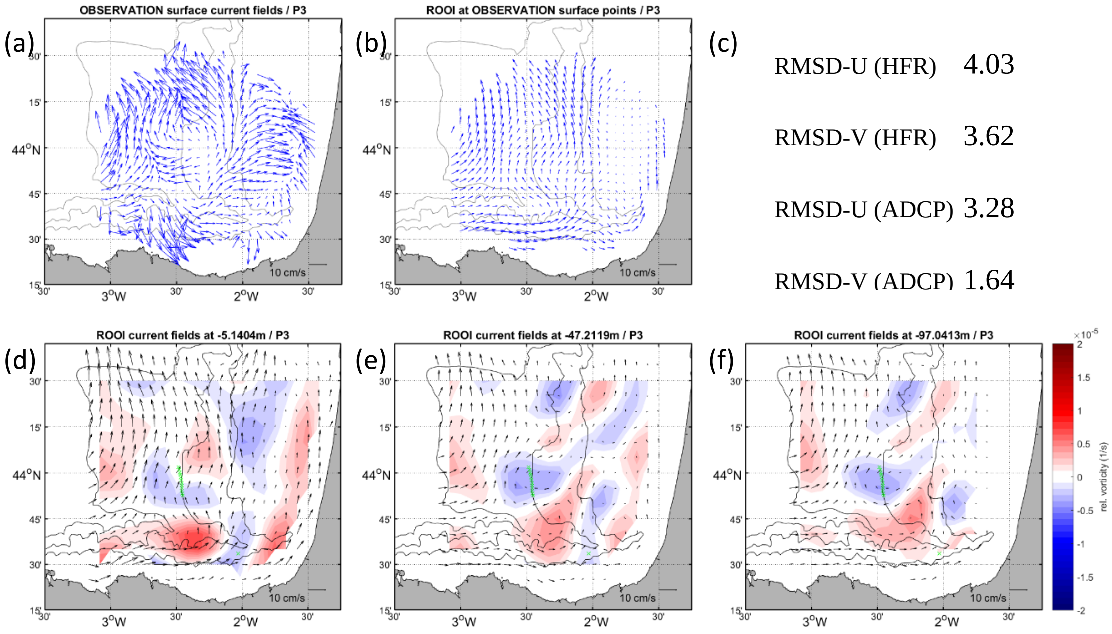

RMSD-U (HFR) 4.03

RMSD-V (HFR) 3.62

RMSD-U (ADCP) 3.28

RMSD-V (ADCP) 1.64

Figure B14. *The same as Figure B2 with* $\varepsilon_{vel}^{obs} = 20\ cm\ s^{-1}$ *and* $\varepsilon_{pd}^{obs} = 0.1\ kg\ m^{-3}$ *and for P3.*

Appendix B3: ADCP data-gap filling

In this section, the assessment of the data-gap filling of the EuskOOS ADCP data series are shown. In addition to the ADCP co-located on the Donostia mooring presented in the text, the ADCP of the Matxitxako mooring was also evaluated located at 43.6º N–2.69º W over the Spanish slope (it worked from 2007 to 2013). To data-gap fill ADCP vertical profiles, the ROOI method was used by expanding the surface HFR observations in the water column since HFR surface current velocities are correlated with the ADCP subsurface currents as shown in Rubio et al. (2019) and Manso-Narvarte et al. (2020).

The assessment consisted of cross-validating the reconstructions with the available ADCP observations. First, the dates when the HFR and ADCP data are simultaneously available were estimated and 1 date every 10 dates was selected to reduce the computational cost (thus overall, 1732 and 2688 hours for Matxitxako and Donostia, respectively). Then, the ADCP data corresponding to one of those dates were used to test the reconstruction, called the test set, whereas the rest of the data, called the train set, were used to calculate the covariances needed for the reconstruction (note that real data were used for estimating the covariances and not model data). Therefore, by means of the HFR surface current observations at that date and the calculated covariances, current velocities were reconstructed in the water column (with N=100 modes and ε^{obs}=2 cm s^{-1}, selected after several sensitivity tests). This process was carried out iteratively for each date finally obtaining RMSD, RMSD relative to the root mean square of the observations (RRMSD) and correlation (with a confidence level of 99%) values between the reconstructed currents and the tests sets. The assessment was carried out for the normal hourly datasets and also for the 48-hour low-pass filtered datasets, which tests the skill of the method in a less exigent scenario enabling to see how the reconstructions perform in this case.

For the non-filtered case (Table B1 and Figure B15a,b), the results show RMSDs between 6.9 and 10.6 cm s^{-1} with higher values for the along-slope component (i.e., U) at Matxitxako due to the more intense slope current. RRMSDs ranged from 0.70 to 0.95, thus showing reconstructions with lower RMSD than the root mean square. Finally, correlations between 0.67 and 0.22 were observed showing much higher values for U. For the filtered case (Table B2 and Figure B15c,d), the results remarkably improve depicting RMSDs between 3.1 and 5.6 cm s^{-1}, RRMSDs between 0.42 and 0.79 and correlations between 0.57 and 0.88. The results display reasonably good error levels, especially for the filtered case, showing that the ROOI could be used to broaden the ADCP data series to the dates where HFR data are available.

Table B1. *RMSD (in cm s^{-1}), RRMSD and correlations between the reconstructed and observed ADCP profiles for both current components (U=zonal, V=meridional) at Matxitxako (M) and Donostia (D) moorings. Data were not filtered and general values are shown as well as values for different depths.*

	RMSD				**RRMSD**				**CORRELATION**			
	M		**D**		**M**		**D**		**M**		**D**	
	U	**V**	**U**	**V**	**U**	**V**	**U**	**V**	**U**	**V**	**U**	**V**
General	10.4	7.5	9.3	7.5	0.72	0.92	0.88	0.93	0.63	0.33	0.45	0.34
-12.26 m	9.80	8	10.2	8.8	0.69	0.84	0.84	0.91	0,67	0.52	0.53	0.39
-20.26 m	10.2	8	10.2	8.4	0.70	0.89	0.87	0.95	0,66	0.40	0.48	0.31
-28.26 m	10.5	8.1	10.2	8.2	0.71	0.92	0.88	0.95	0.64	0.34	0.46	0.30
-36.26 m	10.8	7.9	9.80	8	0.72	0.92	0.88	0.93	0.62	0.31	0.45	0.33
-44.26 m	10.6	7.7	9.70	7.8	0.72	0.93	0.88	0.93	0.62	0.29	0.44	0.34
-52.26 m	10.5	7.4	9.50	7.5	0.72	0.93	0.89	0.93	0.63	0.29	0.44	0.34
-60.26 m	10.4	7.3	9.40	7.4	0.72	0.93	0.88	0.92	0.62	0.26	0.44	0.35
-68.26 m	10.4	7,1	9.30	7.4	0.72	0.93	0.88	0.92	0.63	0.26	0.44	0.35
-76.26 m	10.5	7	9.20	7.3	0.73	0.94	0.88	0.92	0.62	0.24	0.44	0.34
-84.26 m	10.3	7	9.10	7.2	0.74	0.94	0.88	0.92	0.61	0.23	0.43	0.34
-92.26 m	10.2	7	9.10	7.2	0.74	0.94	0.89	0.92	0.62	0.22	0.43	0.33
-100.26 m	10.2	6.9	8.90	7.1	0.75	0.94	0.89	0.92	0.62	0.22	0.42	0.33

Table B2. *The same as Table B1 but with 48h low-pass filtered data.*

	RMSD				**RRMSD**				**CORRELATION**			
	M		**D**		**M**		**D**		**M**		**D**	
	U	**V**	**U**	**V**	**U**	**V**	**U**	**V**	**U**	**V**	**U**	**V**
General	5.5	3.5	4.6	3.5	0.44	0.7	0.64	0.77	0.87	0.64	0.75	0.60
-12.26 m	5.3	3.8	4.7	4.1	0.46	0.66	0.63	0.78	0.86	0.70	0.77	0.60
-20.26 m	5.3	3.7	4.6	3.9	0.44	0.66	0.61	0.78	0.87	0.69	0.78	0.61
-28.26 m	5.4	3.7	4.6	3.8	0.42	0.68	0.62	0.78	0.88	0.67	0.77	0.60
-36.26 m	5.3	3.5	4.5	3.6	0.42	0.69	0.62	0.77	0.88	0.66	0.77	0.61
-44.26 m	5.4	3.4	4.5	3.5	0.42	0.70	0.62	0.76	0.88	0.64	0.77	0.61
-52.26 m	5.5	3.4	4.6	3.5	0.43	0.71	0.63	0.77	0.88	0.62	0.76	0.61
-60.26 m	5.5	3.3	4.6	3.4	0.43	0.72	0.64	0.76	0.88	0.61	0.75	0.61
-68.26 m	5.5	3.3	4.6	3.3	0.43	0.72	0.65	0.76	0.88	0.61	0.74	0.61
-76.26 m	5.6	3.3	4.6	3.3	0.44	0.73	0.65	0.76	0.87	0.60	0.74	0.61
-84.26 m	5.5	3.3	4.6	3.2	0.45	0.73	0.66	0.76	0.87	0.59	0.73	0.60
-92.26 m	5.6	3.3	4.6	3.2	0.46	0.73	0.67	0.77	0.87	0.59	0.72	0.57
-100.26 m	5.6	3.4	4.5	3.1	0.46	0.74	0.67	0.77	0.87	0.57	0.72	0.57

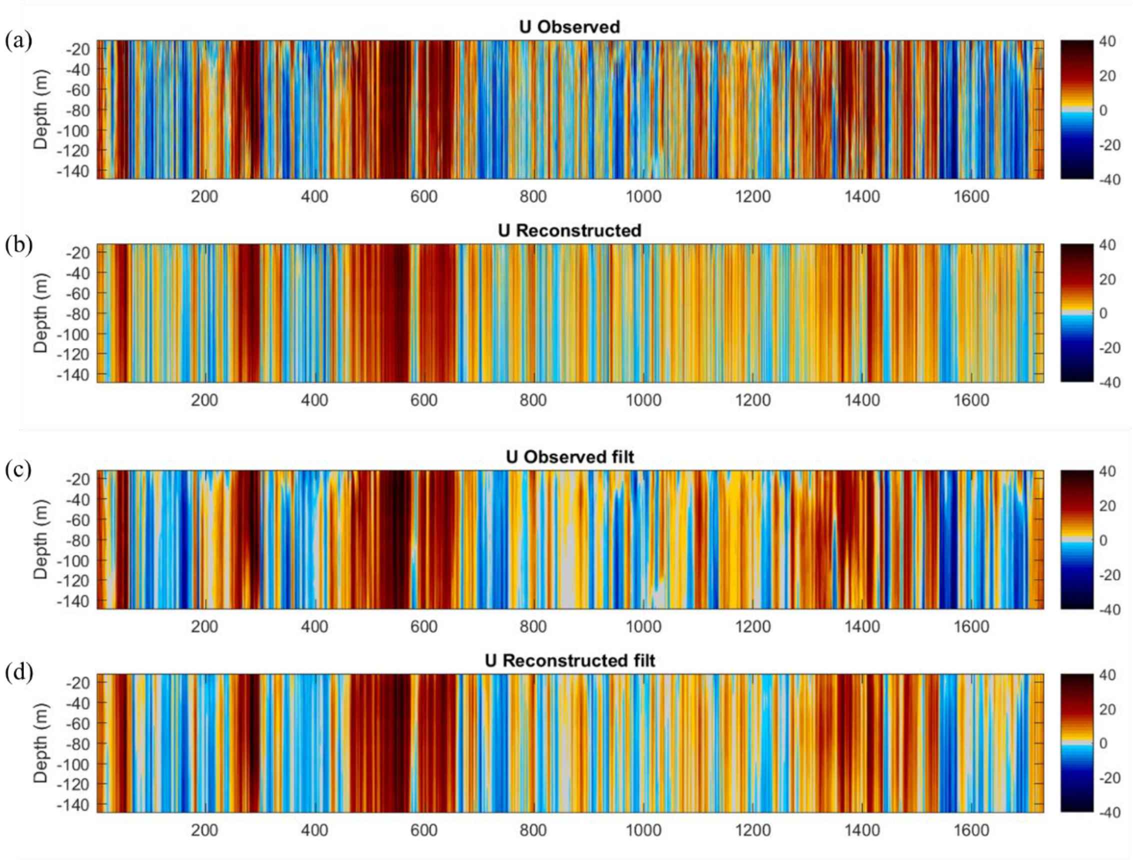

Figure B15. *Observed (a, c) and reconstructed (b, d) zonal current velocity vertical profiles at Matxitxako for the non-filtered (a, b) and filtered (c, d) cases in cm s^{-1} for the dates where HFR and ADCP data are simultaneously available (X-axis show the number of dates) and thus, cross-validated. Positive (negative) values represent eastward (westward) currents. This figure is an example to visually show the comparison between observed and reconstructed profiles.*

CHAPTER 7 – APPENDIX C

Appendix C1: ROOI parameter sensitivity test

Here the sensitivity of the ROOI method when using different numbers of modes and observational errors is tested estimating the RMSD between reconstructed and observed current velocities at Matxitxako ADCP points. The RRMSD with respect to the RMS of the ADCP measurements is also estimated. 11,211 timesteps were considered when ADCP and reconstructed data were available at once between 2009 and 2013.

The results show that N=100 modes and an observational error of 2 cm s^{-1} are a reasonable configuration although the reconstructions are not very sensitive when using parameters with reasonable values (i.e., for instance, results with very low errors as 0.1 cm s^{-1} are remarkably worse).

(a)

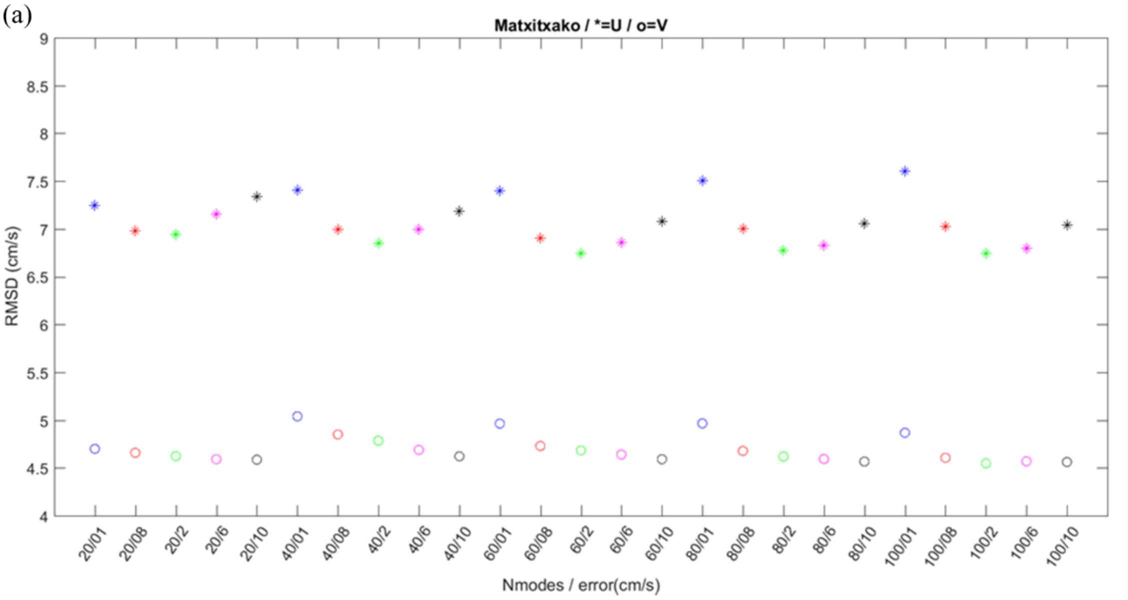

(b)

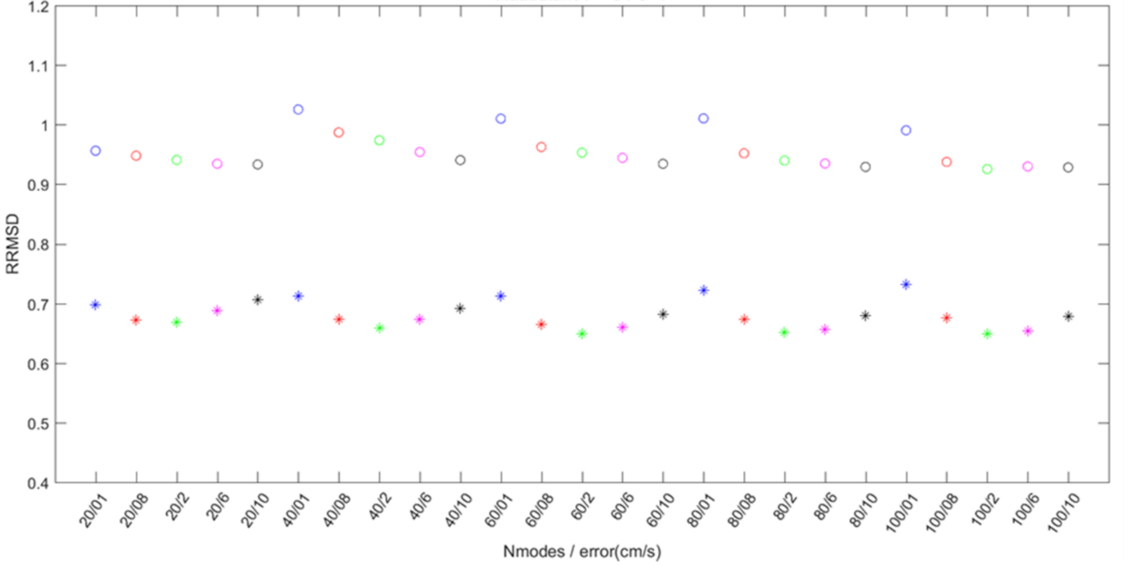

Figure C1. *RMSDs (a) and RRMSDs (b) between reconstructed and observed current velocities at Matxitxako ADCP points for a different number of modes and observational error parameters. 01 and 08 errors in X-axes mean 0.1 and 0.8 cm* s^{-1}*, respectively.*

Appendix C2: Sensitivity of Lagrangian simulations to the used forcing at different depths in the study area

In order to assess the sensitivity of the Lagrangian simulations to the used forcing data and depth, mean particle density maps and residence times were estimated at the surface, at −16 and −55 m forced with the same data as in the simulations in the ROOI validation (i.e., IBI reanalysis, ROOI and HFR data) plus the IBI_ANALYSISFORECAST_PHY_005_001 product (hereinafter IBI analysis) data provided by CMEMS. The latter product is based on an eddy-resolving NEMO model for the Iberian Biscay Irish region which is forced every 3 h at the ocean-atmosphere interface with atmospheric data from ECMWF, whereas lateral open boundaries are forced using daily outputs from the MyOcean Global eddy-resolving system. The validation against independent measurements is shown in Sotillo et al. (2015). For more information about the product see Madec (2008) and Sotillo et al. (2015). As IBI reanalysis it provides daily data with unevenly distributed vertical levels with separations between 1−3 m in the first meters and an increasing separation with depth, however with a much higher spatial resolution of 0.028º x 0.028º (2−3 km). Note that for the HFR forcing, simulations were only run at the surface.

To estimate the above-mentioned mean particle density and residence time maps simulations were run for a period of around 3 months from 8 August to 17 November 2018. The choice of this period was made under the requirement of having available data of all the used datasets at once during at least 3 months to ensure the robustness of the comparisons. Additionally, this is a period where the water column changes from stratified to mixed conditions, thus gathering both situations in the analysis. For estimating the mean particle density maps 1 particle was released every 12 hours every 2 cells and advected within the above-mentioned period. The estimation of residence times was made by releasing 5 particles every 3 cells and measuring the time needed to move 5 km away from the release point. This process was made every 24 hours obtaining mean residence time maps.

The mean density distributions (see Figure C2) show higher densities at deeper depths than at shallow depths due to the weaker dynamics that flush fewer particles. In addition, the deeper the higher the accumulation in the coastal zones. Different distributions are also observed depending on the forcing. At the surface, low densities are observed along the Spanish slope and French platform for IBI reanalysis showing the signal of a marked slope current. However, this signal is weaker for the rest of the forcings. At −16 and −55 m, a much higher accumulation is observed in coastal zones with ROOI data than with IBI products since the ROOI tends to smooth the reconstructions. At −55 m, IBI reanalysis also shows high densities over the French platform and slope. Note that the smallest structures are observed with IBI analysis and HFR data since such products have a higher spatial resolution than the others.

The mean residence time maps (Figure C3) also show the effect of the weakening of the currents with depth since the highest residence times are observed at the deepest levels. The signal of the slope current is also noticeable for IBI reanalysis and the lowest (highest) residence times are observed for IBI analysis (reanalysis). At the surface, ROOI and HFR data show similar patterns since the ROOI is fed with HFR observations. In the water column, the residence time distribution is different for each forcing, however, it is observed that for all of them the residence time remarkably increases with depth along the French coast. Although some mean density maps (Figure C2behi) show that the Spanish coast is an area where particles are accumulated, the residence times are not as high as those along the French coast.

In conclusion, it has been shown that in general the advection of simulated particles changes with depth and forcing, however, common patterns are also observed.

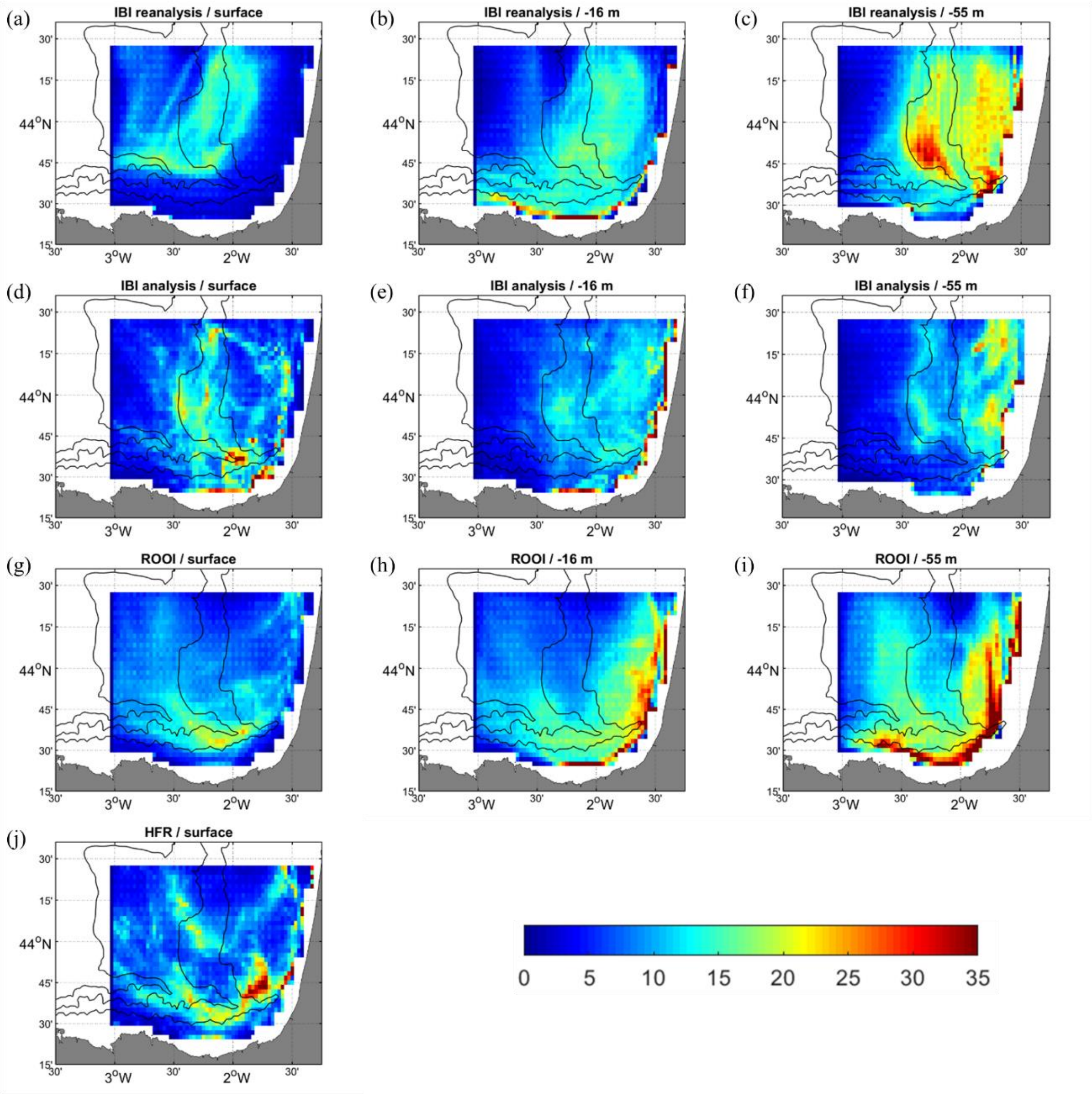

Figure C2. *Mean particle density maps for different forcings at different depths. The colorbar depicts the number of particles and the grey lines show the 200, 1000 and 2000 m isobaths.*

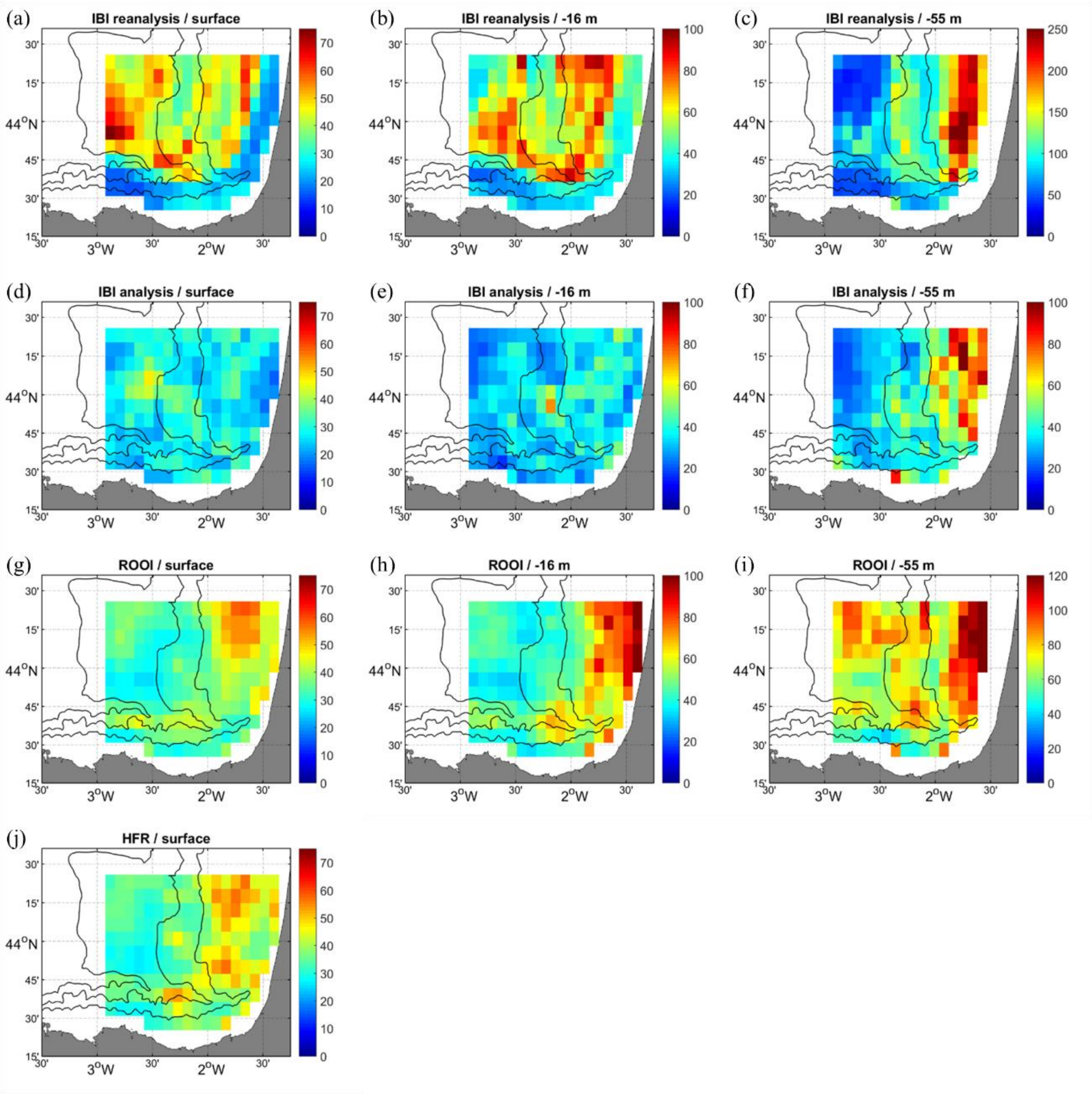

Figure C3. *Mean residence time maps for different forcings at different depths. The colorbar depicts the number of hours and the grey lines show the 200, 1000 and 2000 m isobaths.*

CHAPTER 8 – APPENDIX D

Future Work

The different studies carried out in this thesis pave the way for further applications of the methods and approaches used, and for further investigations on the different oceanic processes in the study area.

Multiplatform data and reconstructed current velocity fields should be used to study transport and retention patterns at different spatiotemporal scales in the water column since only surface patterns have been studied until now (Rubio et al., 2020). This would provide further information about how water masses and its constituents (e.g., nutrients, phytoplankton, eggs, larvae, marine litter) are distributed in 3D enabling to better understand biological, geochemical and environmental processes. Among the different structures and processes that regulate the distribution of such constituents, eddies are considered important features in the study area (e.g., Irigoien et al., 2008; Rubio et al., 2018). Therefore, in addition to the 3D study of the eddy carried out in this thesis, future work should be oriented to better understand their 3D Lagrangian and Eulerian characteristics and the forcing behind their generation and drift. Moreover, the study carried out in this thesis about the effects of hydrodynamics on the ELS of anchovy eggs and larvae in the study area should be further extended.

Although more validation of the ROOI method would be valuable to further assess its skills to reproduce current velocity fields, it would still be an appealing tool for filling gaps in data series (e.g., ADCP) or for covering a wider area by spatially extending the available observations out of the domain considered in this thesis. Moreover, reconstructions could also be improved by using higher spatial resolution data for setting the covariances needed, providing higher spatial resolution current velocity fields. Such applications would enable a more accurate and complete characterization of the hydrodynamic processes which at the same time regulate the above-mentioned transport and retention patterns crucial in biological, geochemical and environmental processes.

In addition, the ROOI could be tested for short-time prediction (i.e., maximum 48 hours) of current velocity fields, based on spatiotemporal covariances and past observations. These forecasts could be applied for search and rescue or pollution-related issues, for example. Another possible application would be to operationally reconstruct 3D current velocity fields in near-real time from the HFR and mooring observations for an improved follow-up and management of the SE-BoB.